Evaporation of Multicomponent Inkjet Printed Droplets

JACK GWILYM JAMES GOODALL

Evaporation of Multicomponent Inkjet Printed Droplets

Jack G. J. Goodall

A Thesis presented for the degree of
Doctor of Philosophy

Department of Chemistry
Durham University
United Kingdom

April 2022

Abstract

Inkjet printing allows for the controlled, contactless deposition of functional picolitre droplets. Industrial applications of droplets are varied and use complex formulations, the motivation of this thesis was to gain an understanding of how different solutes change the evaporation behaviour of drying droplets. To that end I studied solvent mixtures of ethanol, water and ethylene glycol (with and without ethanol vapour) as well as solutions of sucrose, lactose, sodium chloride, sodium nitrate and ammonium sulfate. Thus my experiments spanned volatile, low volatility and involatile solutes with and without crystallisation. In each case I measured the change in droplet profile over time and how that compared to a volume-averaged model of droplet evaporation, the direction and speed of internal (solutal Marangoni) flows by adding tracer particles, and the final deposits.

Using my model I found that all but ethanol-water mixtures developed large concentration gradients, with involatile solutes accumulating at the liquid-vapour interface and suppressing evaporation. Sugar droplets approached a high-viscosity glassy state while salt droplets became supersaturated, leading to fast growing crystalline structures nucleating. By using picolitre rather than microlitre sessile drops I uncovered aerosol-like behaviour where salt droplets would stop nucleating above a certain efflorescence relative humidity.

To directly measure concentration gradients we developed a novel reflectometry experiment, printing droplets on a silica hemisphere and using the evolving refractive index difference between droplet fluid and the substrate to determine the composition. This allowed me to verify the presence of an ethanol residue persisting after the end of solutal Marangoni flows in ethanol-water droplets.

During the solutal Marangoni flows we observed particles migrating across flow streamlines to either the centre or liquid-vapour interface depending on the system in question. From the reversal of migration direction in response to a flipped ethanol concentration gradient we suggest diffusiophoresis as the cause of migration, as a number of other mechanisms were ruled out.

Declaration

The work in this thesis is based on research carried out in the Department of Chemistry at Durham University. No part of this thesis has been submitted elsewhere for any degree or qualification.

MATLAB particle tracking and droplet profile analysis code were composed by Arganthaël Berson and Lisong Yang at the University of Durham and optimised for my uses by myself. Christian Diddens provided some simulations of droplet evaporation in Chapter 3. The SEM images in Chapter 6 were collected with Yilin Wang. Elsewhere where I write "we" I am explicitly acknowledging general contributions from Colin Bain (for theory) or others (Lisong Yang for practical work) in the group to the work.

Acknowledgements

I would like to thank my supervisor Prof. Colin Bain for mentoring and support during my PhD and acknowledge the EPSRC for financially supporting the project (grant number EP/N025245/1) and the Durham University Chemistry Department for my studentship. I would also like to thank other members of the "Evaporative Drying of Droplets and the Formation of Micro-structured and Functional Particles and Films" project in Durham, Bristol and Leeds for useful discussions and cross-pollination of ideas. I also appreciate the useful feedback provided by my examiners David Fairhurst and Halim Kusumaatmaja.

Many thanks go to members of the research group, past and present, for being so welcoming and providing support both in and out of the lab. A special mention goes to Lisong Yang for her expertise and endless generosity with her time without whom I could not have done so much.

Finally I wish to express my sincere appreciation for Jueshan Wu, and my family for their belief, and being there for me during this difficult last year.

In memory of Sian Jones

List of Symbols

Glossary

θ	Drop Contact Angle/°	2
σ	Interfacial Tension/mN m^{-1}	3
h	Drop Height/µm	3
r	Radial Coordinate/µm	3
R	Drop Radius/µm	3
V	Drop Volume/pL	4
Bo	Bond Number	4
ρ	Density/ g mL^{-1}	4
g	Acceleration due to Gravity/m^2 s^{-1}	4
Ca	Capillary Number	4
η	Dynamic Viscosity/ mPa s^{-1}	4
v	Speed (Velocity)/m^2 s^{-1}	4
λ_c	Capillary Length/mm	4
D	Diffusion Coefficient/$m^2\,s^{-1}$	7
τ	Timescale/s	7
c	Concentration (of solute in fluid, etc.)	7
t	Time	8
J	Evaporative Flux	8
$F(...)$	Function of the variable in the brackets	8
M	Mass/g	10
RH	Relative Humidity	10
c_v	Mass Density of Fluid in Vapour	10
x	Mole Fraction	12
p	Vapour Pressure/Pa	12
a	Activity	12
γ	Activity Coefficient	12
Re	Reynolds Number	12
u	Speed (Velocity)/m^2 s^{-1}	14
Ma_T	Thermal Marangoni Number	14
k	Thermal Diffusivity/m^2 s^{-1}	14

Ma_S	Solutal Marangoni Number	15
Ar	Archimedes Number	16
St	Stokes Number	17
Oh	Ohnesorge Number	19
We	Weber Number	19
NA	Numerical Aperture/°	26
ζ	Zeta Potential/mV	28
R_g	Group Radius/µm	33
v_{R_g}	Radial Group Velocity/µm s^{-1}	34
Mr	Molar Mass/g mol^{-1}	39
R'	Ideal Gas Constant	39
n	Refractive Index	49
ϵ_0	Electric Permittivity of Free Space	49
μ_0	Magnetic Susceptibility of Free Space	49
$\mathbf{E}$	Electric Field/V m^{-1}	49
$\mathbf{B}$	Magnetic Field/T	49
θ_i	Angle of Incidence/°	50
θ_r	Angle of Reflection/°	50
θ_t	Angle of Transmission/°	50
R_s	Reflectance of Perpendicularly Polarised Light	51
R_p	Reflectance of Parallel Polarised Light	51
θ_c	Critical Angle/°	52
f	Focal Length/mm	53
I	Laser Intensity/W m^{-2}	54
ϕ	Laser's Angular Spread/°	54
R_p^*	Measurable Reflectance of Parallel Polarised Light	54
w	Gaussian Laser Beam Waist/µm	54
λ	Wavelength of Light/nm	54
R_{exp}	Experimental Reflectance	64
t_0	Time of Droplet Impact on Surface/s	75
k_B	Boltzmann Constant	94
Pe	Péclet Number	140
S	Supersaturation Ratio	162
J_{CNT}	Nucleation Rate from Classical Nucleation Theory	195
ΔG^*	Free Energy Barrier to Nucleation	195
Z	Zeldovich Factor	195
μ	Chemical Potential	196
ERH	Efflorescence Relative Humidity	199
DRH	Deliquescence Relative Humidity	199
m	Molality/mol kg^{-1}	216
a_p	Particle Radius/µm	264

Acronyms

EtOH	Ethanol	xii
Vap	Ethanol Vapour Evaporation Environment	xii
EG	Ethylene Glycol	xii
CCR	Constant Contact Radius (Evaporation Mode)	6
CCA	Constant Contact Angle (Evaporation Mode)	6
FEM	Finite Element Method	8
CRE	Coffee-ring Effect	12
OCT	Optical Coherance Tomography	15
CIJ	Continuous Inkjet	17
DOD	Drop on Demand	18
PG	Propylene Glycol	20
PZ	Piezoelectric	24
PTFE	Polytetrafluoroethylene	24
LED	Light Emitting Diode	25
fps	Frames per Second	26
HMDS	Hexamethyldisilazane	27
OTS	Octamethyldisilazane	27
PS	Polystyrene	28
AMS	Ammonium Sulfate	29
PIV	Particle Image Velocimetry	30
MFS	Mass Fraction	34
IR	Infrared (wavelength of light)	43
PMT	Photomultiplier Tube	56
IPA	Isopropylalcohol	105
E-AIM	Extended Aerosol Inorganic Model	186
CNT	Classical Nucleation Theory	195

List of Videos

Figure	System	Speed	Description
3.27t	50%v EtOH 50%v H_2O	1	20 Drop Reflectometry
4.11	50%v EtOH 50%v H_2O	4	Marangoni Flow and Deposit
4.12	50%v EtOH 50%v H_2O	20	"Propeller"
4.15	H_2O Droplet, Vap	2	Marangoni Flow and Deposit
4.16	50%v EtOH 50%v H_2O, Vap	4	Marangoni Flow and Deposit
4.24	10%v EG 90%v H_2O	5	Marangoni Flow
4.25	5%v EG 95%v H_2O	1	Marangoni Flow
4.26	40%v EG 60%v EtOH	4	Marangoni Flow
4.30	34%v EG 33%v EtOH 32%v H_2O	2	Marangoni Flow
4.32	70%v EG 30%v EtOH, Vap	1	Marangoni Flow
5.11	2 wt% Lactose	10	Slow-starting Marangoni Flow
5.12	16 wt% Sucrose	2	Marangoni Flow and Deposit
6.13	10 wt% NaCl	8	Deposit on HMDS
6.14t	5 wt% NaCl	10	Spike Deposit
6.14b	5 wt% NaCl	2.5	Cubic Deposit
6.15	10 wt% NaCl	5	Deposit on Plasma, Low RH
6.16	10 wt% NaCl	1.25	Deposit on Plasma, High RH
6.18	5 wt% $NaNO_3$	4	Deposit on HMDS
6.19	10 wt% $NaNO_3$	2	Crystalline Layer around Deposit
6.20	10 wt% $NaNO_3$	4	Deposit on Plasma
6.21	10 wt% $(NH_4)_2SO_4$	8	Deposit on HMDS
6.22	10 wt% $(NH_4)_2SO_4$	4	Deposit on Plasma
6.26	10 wt% NaCl	10	Marangoni Flow
6.32	10 wt% $NaNO_3$	10	Jerky Marangoni Flow

The "Speed" header describes how sped up the videos are relative to real time. "HMDS" and "Plasma" refer to substrates which had undergone treatment to become hydrophobic or hydrophilic. "t" for top, "b" for bottom row of a figure showing multiple droplets.

Table of Contents

Chapter 1

Introduction

1.1 Motivation

The study of evaporating drops is useful as drops are abundant in nature and appear in numerous practical applications in graphics, crop spraying[1,2], coatings,[3] inkjet printing and printed electronics,[4–8] biosensors[9,10] and additive manufacturing.[11,12] The formulations for these applications are necessarily complex, containing multiple functional components: solvents, solutes, particles, surfactants and polymers so there are competing effects to study. The drying of drops themselves is also interesting as they are far from equilibria systems where there is coupling of evaporation, diffusion, heat transfer and mass transport. This complexity means that current models are not yet close to achieving predictive design of new products so physical experiments are of great importance. Therefore we were interested in working to close those gaps in understanding with studies of model systems to isolate the behaviour of separate components and develop new characterisation methods.

Inkjet printing is a powerful technique with a lot of possible applications as it allows for the controlled deposition of material without any contact with the substrate.[13] In addition, the vast majority of the literature on drops involves

studies of microlitre drops with radii tens to hundreds of times the size of inkjet-printed droplets. Therefore we chose to study inkjet-printed droplets to work at the most relevant lengthscale for industrial applications and verify results, or not, from the literature at these smaller lengthscales where different mechanisms can become dominant due to differing scaling with size as particles become larger in comparison to the drop radius changing deposition patterns.[14–18]

In this introduction chapter I will give some of the broader background necessary to understand the processes related to drops such as their shape, wetting on surfaces, evaporation, internal flows, the thermodynamics of mixtures and droplet generation with inkjet printing technology.

1.2 Drop Shape

A sessile drop is a drop of non-wetting fluid on a surface that exhibits a finite contact angle. This is in contrast to a wetting system that would spread continuously to cover the surface. On an ideal surface the equilibrium three-phase contact angle θ_{eq} is determined by balancing the surface tension forces at the triple-phase contact line (hereafter the "three-phase" descriptor to contact angle/area/radius shall be dropped for convenience) according to Young's equation

$$\sigma_{lv}\cos(\theta_{eq}) = \sigma_{sv} - \sigma_{sl}, \tag{1.1}$$

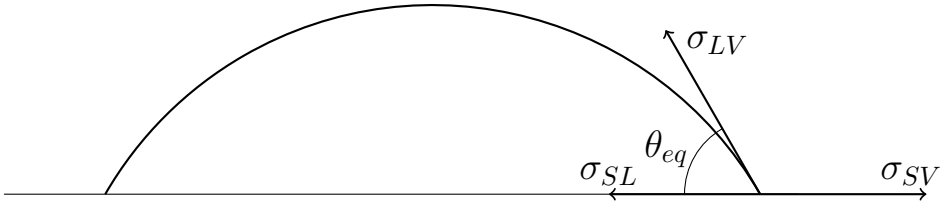

Figure 1.1: The balance of interfacial tensions given by Young's Equation determines the equilibrium contact angle of a drop of fluid on an ideal substrate.

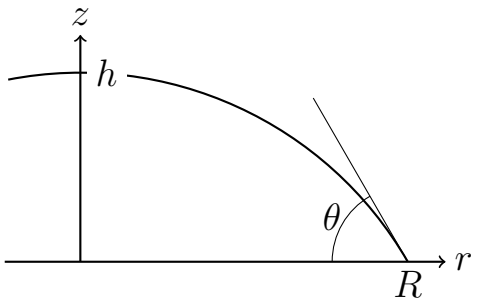

Figure 1.2: Diagram of a drop giving the axes, the contact radius (R), contact angle (θ) at height at some radius ($h(r)$) which define its shape.

where σ_{lv}, σ_{sv} and σ_{sl} are the interfacial tensions between the liquid-vapour, solid-vapour and solid-liquid interfaces and act in directions given in Figure 1.1. Therefore the contact angle of a drop can be changed by altering surface tensions between the substrate and the liquid or vapour phases, such as by silanisation,[19] or changing the liquid surface tensions by using a lower surface tension solvent, or adding a surfactant to change the interaction at the liquid-vapour[20] or liquid-solid interfaces.[21]

Ideal sessile drops have a spherical cap shape, defined as the region of a sphere which lies above (or below) a horizontal plane. A drop on a horizontal surface is axisymmetric so can be described in a cylindrical coordinate system. Figure 1.2 shows a portion of such a shape where the axisymmetric height h as a function of the radial coordinate r can be calculated using the equation

$$h(r) = \sqrt{\frac{R^2}{\sin^2\theta} - r^2} - \frac{R}{\tan\theta}, \tag{1.2}$$

where R is the droplet radius along the surface; therefore at the apex, $r = 0$, and Equation 1.2 reduces to

$$h_0 = R\ \tan\left(\frac{\theta}{2}\right). \tag{1.3}$$

At the contact line $r = R$ and Equation 1.2 reduces to

$$h(r = R) = R\sqrt{\frac{1 - \sin^2\theta}{\sin^2\theta}} - \frac{R}{\tan\theta} = 0. \tag{1.4}$$

The volume, V, of a sessile drop can be determined using

$$V = \frac{\pi h}{6}(3R^2 + h^2) = \pi R^3 \frac{\cos^3\theta - 3\cos\theta + 2}{3\sin^3\theta}. \tag{1.5}$$

In fluid dynamics there are a number of established dimensionless numbers to express the ratio of different forces, times or lengthscales.[22] For instance, for real drops, whether the sessile drop has a true spherical cap shape is conditional on the dominance of surface tension over gravity. Surface tension forces act to minimise the liquid-vapour interfacial area, consistent with a spherical cap shape, however large drops can still experience flattening due to gravity. The Bond number, Bo, compares the relative influence of gravitational and surface tension forces and is defined as

$$Bo = \frac{\rho g R^2}{\sigma_{lv}}, \tag{1.6}$$

where ρ is the density of the liquid, g is the acceleration due to gravity and R is the contact radius as a characteristic lengthscale for the drop.

The Capillary number, Ca, compares the relative importance of viscous effects (at high Ca internal flows may deform the surface, flattening the drop) and surface tension

$$Ca = \frac{\eta\, v_d}{\sigma_{lv}}, \tag{1.7}$$

where η is the dynamic viscosity of the drop and v_d is the characteristic radial velocity induced by evaporation. However it is worth noting that other factors such as Maranagoni flattening[7] or contraction[23] can cause deviations from a spherical cap shape. If both Ca, $Bo \ll 1$ then surface tension effects dominate without surface deformation caused by gravity or viscous flow so a drop is expected to have a spherical cap shape.

An alternative way to predict drop shape is to compare the diameter of the drop against the capillary length, λ_c, where

$$\lambda_c = \sqrt{\frac{\sigma}{\rho g}}. \tag{1.8}$$

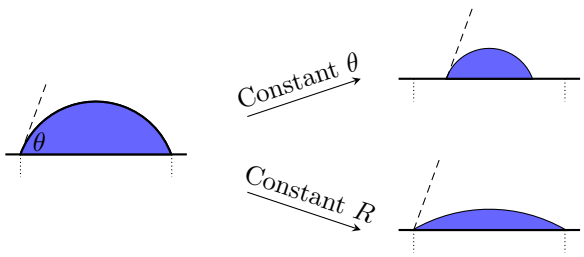

Figure 1.3: Difference between constant contact angle and constant contact radius evaporation. The dotted lines define the starting contact diameter and the dashed line the initial contact angle θ.

This lengthscale is derived from the expression for the Laplace pressure and defines at what lengths gravity effects can result in deformations from an ideal spherical cap. It can also be used to define the Bond number such that

$$Bo = \left(\frac{L}{\lambda_c}\right)^2, \tag{1.9}$$

where L is the curvature of the drop. For water on Earth $\lambda_c = 2.7$ mm which is greater than the lengthscale of most drops in the literature and far larger than the lengthscale of the droplets experimented with in this thesis.

1.3 Evaporation and Wetting

Historically there have been many developments to reach our current understanding of evaporation and dynamic wetting, here I will primarily focus on the developments regarding how the evaporation rate is not proportional to drop surface area as might be expected at first glance.

In practice the surface a drop sits on is not ideal due to roughness and chemical heterogeneity, leading to contact angle hysteresis so the drop is not at equilibrium. During spreading the contact radius increases with a contact angle defined as the advancing contact angle $\theta_A > \theta_{\text{eq}}$. If the drop loses fluid then the contact radius retracts with a contact angle defined as the receding contact angle $\theta_R < \theta_{\text{eq}}$. The contact angle hysteresis θ_{hys} is defined as the difference $\theta_A - \theta_R$.

Picknett and Bexon[24] identified two extreme modes in the evaporation of sessile drops on a smooth surface which are depicted in Figure 1.3. In the first mode the drop would evaporate with a constant contact angle, while the contact line retreated. In the second mode a drop would evaporate with a constant contact area/radius and a diminishing contact angle. In both cases the drop maintained a spherical cap geometry.

These evaporation modes were related to contact angle hysteresis; Picknett and Bexon identified that when the contact angle was greater than the receding contact angle there would be constant contact radius evaporation (CCR), switching to constant contact angle (CCA) evaporation once the receding contact angle was reached. They also reported the existence of mixed modes in which both contact angle and radius could decrease simultaneously in experiments.

Picknett and Bexon also developed an analytical expression for the evaporation rate to fit experiments with methyl acetoacetate drops. This involved making an electrostatic analogy, highlighting parallels between a sessile drop evaporating under diffusional control into a still atmosphere, and the capacitance of an equiconvex lens with the same shape as a sessile drop mirrored along its liquid-solid interface. Their equations could be analytically solved for the two evaporation modes, giving the important result that the mass (or volume) of the drop decreased linearly with time for CCR evaporation. In a CCA evaporation mode drops were found to evaporate more slowly with time as $V^{2/3}$ (or mass$^{2/3}$).

However, while Picknett and Bexon's expressions were useful, they were unwieldy and not straightforwardly linked to the drop dimensions, instead depending on the radius of curvature. Birdi *et al.*[25] were able to usefully demonstrate that the evaporation rate was proportional to the drop radius (rather R^2 with the surface area), verifying that drop evaporation was a gas-diffusion problem.

That the limiting step in evaporation is indeed the molecules' crossing of the liquid-vapour interface can be further validated by considering the magnitude of

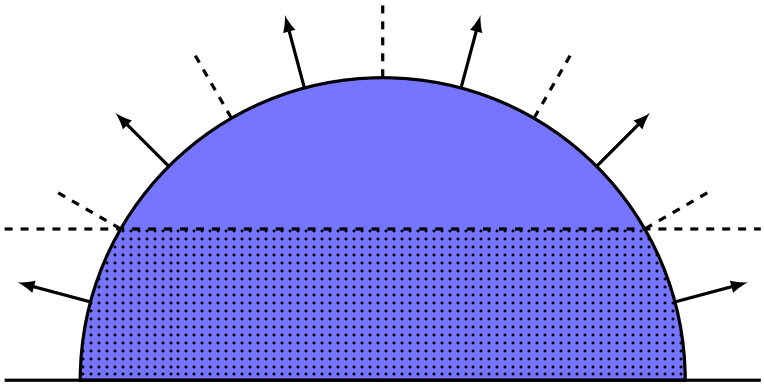

Figure 1.4: An intuitive explanation for faster (diffusion limited) evaporation towards the contact line. First start with a hemispherical drop where the surface is divided into equal angular segments, if one imagines the substrate rising up to the dashed horizontal line (so that the dotted region disappears), otherwise preserving the position of the drop surface then there are regions of air near the drop without any associated liquid interface. This allows evaporated vapour to diffuse away more quickly from near the contact line, enhancing diffusion-limited evaporation towards the contact line.

the timescales for diffusion and a molecule crossing the liquid-vapour interface. The timescale for diffusion can be estimated using the factor[26]

$$\tau_{\text{diff}} = \frac{R^2}{D} \tag{1.10}$$

where D is the diffusion coefficient for the liquid in air. Therefore for a picolitre water droplet of radius 80 µm, $\tau_{\text{diff}} \approx 2 \cdot 10^{-4}$ s whereas the timescale for crossing the interface $\tau_{\text{int}} \approx 10^{-10}$ s.[27] Therefore the diffusion of vapour away from the drop is the slower, limiting step so a quasi-steady description becomes natural where molecules cross the interface in reaction to any change in the vapour field about the drop.

Deegan *et al.*[28] also made the link between sessile drop evaporation and the electrostatic potential about a biconvex lens. They showed that in cylindrical coordinates the vapour field (in units of mass per unit volume), $c(r, z)$, follows

Laplace's equation for the time (t) dependence

$$\nabla^2 c = D\frac{\partial c}{\partial t} = 0 \tag{1.11}$$

with boundary conditions that far away from the drop as $r^2 + z^2 \to \infty$ then $c \to c_\infty$, and that at the drop surface the concentration equalled the saturation concentration $c = c_{\text{sat}}$ (and $\frac{dc}{dz} = 0$ through the impermeable substrate).

From Fick's Law the evaporative flux, J, is

$$J(r,t) = -D\ \nabla c \tag{1.12}$$

which they showed diverges near the edge of the contact line as

$$J(r) \sim (R-r)^{-\lambda_{\text{Deegan}}} \tag{1.13}$$

with a time dependence of

$$J(r,t) \approx J_0 F(\lambda)\left(1-\left(\frac{r}{R}\right)^2\right)^{-\lambda_{\text{Deegan}}} \tag{1.14}$$

where $\lambda_{\text{Deegan}} = (\pi - 2\theta)/(2\pi - 2\theta)$ $(0 < \theta \leq \pi/2)$, and $F(...)$ is some function of λ_{Deegan}. The edge enhancement of the evaporative flux is a key result and arises from an increase in the likelihood of a molecule escaping the drop: due to the greater free space at the edge a random walk of an escaping molecule is less likely to return to the drop (see caption of Figure 1.4). A visual representation of the increasing non-uniformity at lower contact angles is given in Figure 1.5. Due to quasi-steady evaporation the evaporation rate could then be solved by integrating the flux across the drop interface. This was mathematically possible as despite the flux diverging, the exponent $\lambda_{\text{Deegan}} < 1$ so the flux expression is still integrable.

Hu and Larson[30] developed a Finite Element Method (FEM) model to calculate the vapour distribution above a drop to solve for the evaporation rate, comparing it against the analytical solution and experiment. They found that

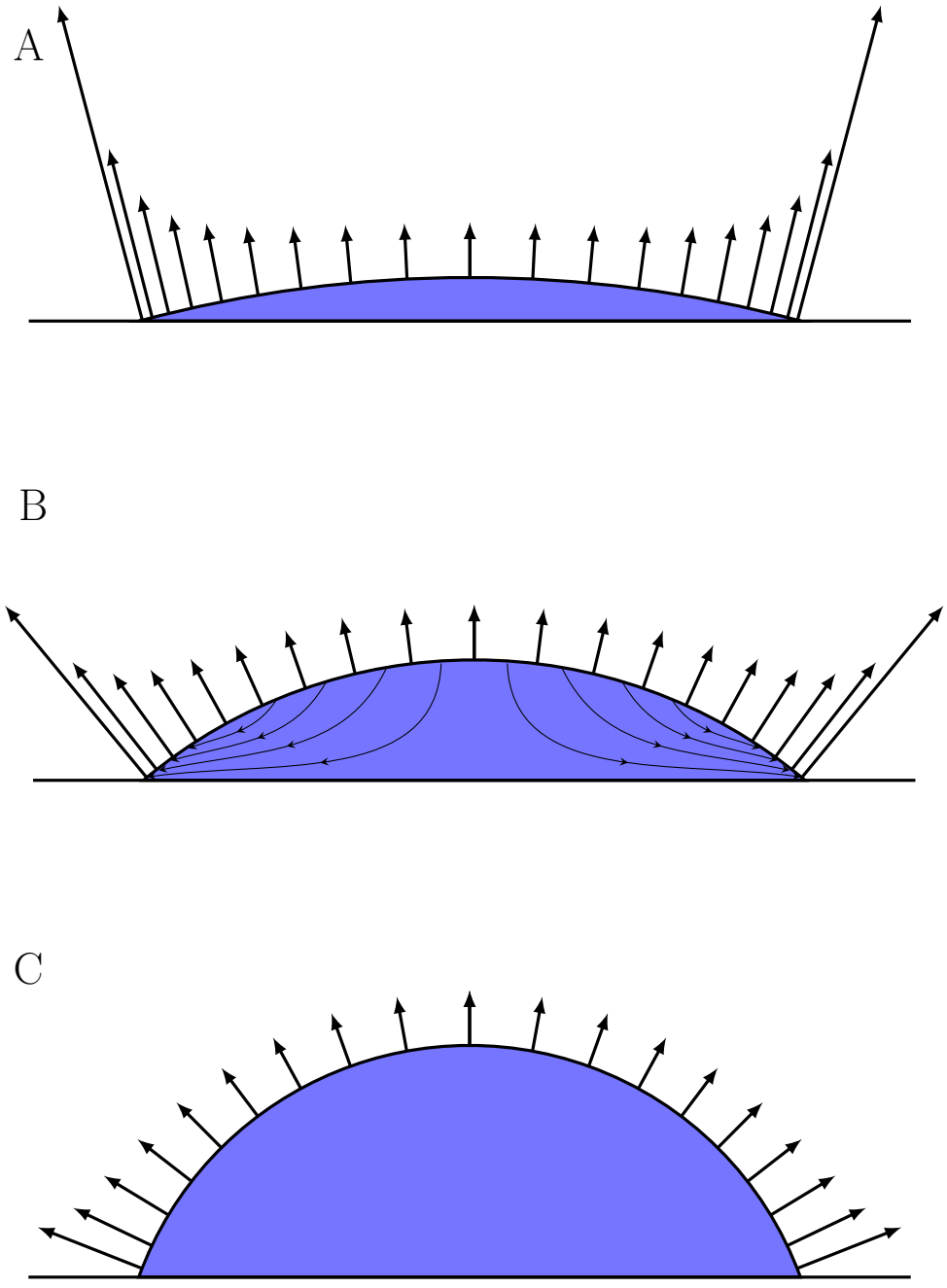

Figure 1.5: Evaporative flux normalised by the value at the apex for drops of different contact angles to show how evaporation from the contact line becomes more enhanced at lower contact angles when applying Equation 1.14 from Ref 28. Contact angles: $\theta_A = 15°$, $\theta_B = 40°$, $\theta_C = 70°$. For drop B I have included some cartoon flows to approximate the radial convective flows from Hu and Larson[29] as a result of the coffee ring effect.

their model performed well and had advantages over the analytical solution as it was not restricted to spherical cap geometries. They also provided convenient semi-empirical equations for the rate of loss of drop mass (M)

$$-\frac{dM}{dt} = \pi RD(1 - RH)\ c_v\ (0.27\theta^2 + 1.30) \tag{1.15}$$

where RH is the relative humidity, describing the amount of water vapour present as a fraction of that when the air is saturated with water, and c_v is the mass density of that fluid in the surrounding vapour at saturation.

Popov[31] worked to calculate the spatial dimensions of the ring deposit in an evaporating droplet at late times, beyond the work of Deegan *et al.* whose time scaling was only appropriate at early times. To do this Popov also worked on the theory of drop evaporation, making a few minor corrections for dropped factors in Hu and Larson's analytical work, giving expressions for the evaporative flux in cylindrical coordinates in the limit of thin drops and a hemisphere, and laying out the analytical solution in terms of integrals when working in toroidal coordinates. The analytical mass loss equations derived by Popov were the foundation of my model and so can be found in Section 2.9. When the drop was pinned Popov developed an equation for the rate of change of contact angle which I modify in Section 5.3. Where there are no competing influences on the surrounding vapour concentration profile (such as due to convection in larger drops[18]) Popov's equations remain the gold standard and have been verified as holding for large contact angles as Gelderblom *et al.*[26] ran experiments with pinned drops on rough superhydrophobic substrates.

The next developments on the theory side of drop evaporation were related to modelling temperature profiles within drops resulting from heated substrates[32,33] and evaporative cooling;[34,35] as a result these works were also closely linked to discussions of thermal Marangoni flows (to be covered in Section 1.5).

More recent developments on the theory of evaporating drops have involved

multicomponent drops. From an interest in protein adsorption Siregar *et al.*[36] modelled evaporation with a solute, adding terms for the convection and diffusion of the solute and reversible protein adsorption at the interface. From this they determined the evolving drop profile in pinned and unpinned cases and calculated the thickness of the deposited solute layer. This was an example of a lubrication model[37] which is popular in the drop literature. In a lubrication model in fluid dynamics, one of the dimensions is much longer than the other, for drops this regime requires the drops are thin so that $R \gg h$. Inertia terms in the Navier-Stokes equation are then ignored reducing it to the Stokes equation and gradients across the drop height are also ignored. From these beginnings Diddens *et al.*[38] developed a much more sophisticated model where multicomponent droplets, and their associated vapour and temperature fields were modelled using a lubrication approach and FEM modelling. The evaporation rates of different components could be calculated and the resulting concentration and temperature fields and internal flows found. However there were many variables that needed to be handled including composition dependent mass density, viscosity, surface tension, mutual diffusion coefficient and thermodynamic activities. The model has now been applied to ethanol-water and glycerol-water across different substrate hydrophobicities[39], ternary mixtures of ouzo (ethanol-water with anise oil)[40] and water with the surfactant 1,2-hexanediol.[41] Other lubrication models for complex droplets have been developed by Stone's group[42] and Karpitschka.[23,43]

1.4 Thermodynamics of Mixtures

In this thesis I will only be discussing the evaporation of droplets of mixtures, therefore it is valuable to discuss how mixtures change the saturated vapour layer above a drop.

For an ideal solution a molecule of A interacts the same with other molecules as

it does itself, then we can apply Raoult's law for the vapour pressure of component A of a mixture

$$p_A = x_A \cdot p_A^* \tag{1.16}$$

where x_A is the mole fraction of component A in the solution and p_A^* is the vapour pressure for pure fluid of component A. The real mixtures in this thesis are not ideal (although binary mixtures of ethylene glycol and water are close to ideal), meaning the molecules interact differently with identical molecules and other molecules, so Raoult's Law cannot be applied, in that case the the activity, a, is introduced and the non-ideality is described by an activity coefficient, γ,

$$a_A = \frac{p_A}{p_A^*} = x_A \cdot \gamma_A. \tag{1.17}$$

1.5 Internal Flows

The Reynolds number, Re, describes the ratio of inertial and viscous forces and is given by

$$Re = \frac{\rho\, v_d R}{\eta}, \tag{1.18}$$

where v_d is the flow velocity in a drop. Low Reynolds numbers are associated with steady, stable flow whereas high values (on the order of a few thousand) indicate turbulence. When $Re \ll 1$ inertia can be ignored.

Deegan *et al.*[44] introduced the coffee-ring effect (CRE): that evaporating drops with pinned contact lines (such as due to surface roughness) leave ring deposits. The origin of this effect is that when an evaporating drop is pinned fluid needs to flow to the contact line to replenish the fluid lost, and these flows transport suspended material (particles or solute) from the interior (see Figure 1.5B). Enhanced evaporation towards the contact line is not necessary for ring deposit, a ring deposit is still generated from a uniform evaporative flux across a drop but not if the flux goes to zero at the contact line, for instance by covering

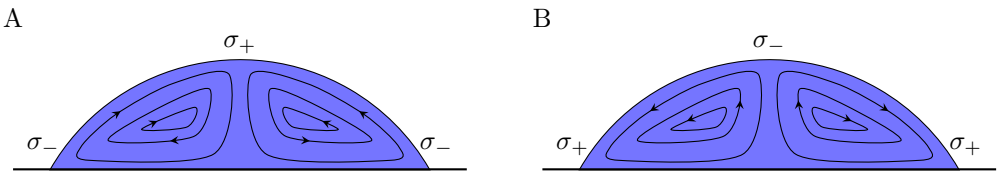

Figure 1.6: Directions of Marangoni flows in response to surface tension gradients where the contact line region has A - a lower surface tension, or B - a higher surface tension, than at the apex.

the drop edge with a mask to block escaping vapour.

For colloidal drops the ring stain's particle mass growth was found to follow a power law dependent on the contact angle,[28] with the fastest flows occurring towards the end of evaporation.[45] These flows have interesting consequences for the end deposits as they can segregate particles according to size,[46,47] leading to multiple concentric rings if the drop goes through pinning cycles,[48,49] as well as leading to regions of deposits with high packing density which can be used to provide high quality connections in printed electronics.[50]

However, highly non-uniform ring stains are typically not desired, with coating applications preferring a uniform deposit. One of the main ways this is achieved in the literature is through recirculatory Marangoni flows which act to keep particles suspended during drying.[51] Marangoni flows are driven by surface tension gradients[52] whose stresses cause fluid flows from regions of low to high surface tension, shown in Figure 1.6 for a drop geometry. When the surface tension is dominant a spherical cap shape is maintained as the flows do not move the contact line, therefore the Marangoni flows are circulatory and act throughout the drop as the non-zero viscosity means that the layers of fluid shear past each other with drag. The flow at the substrate will be zero because of a non-slip boundary condition and Marangoni flows are typically described using a lubrication approximation[37] with a parabolic velocity profile which we discuss in Appendix B.

In a steady-state there cannot be a net force (and so acceleration) at the

interface so the surface tension gradient must be balanced by viscous stress in the fluid. Therefore the surface tension gradient along an interface (liquid-vapour or liquid-liquid) leads to a Marangoni stress described by

$$\frac{d\sigma}{d\hat{s}} = -\eta \frac{du_s}{d\hat{n}} \tag{1.19}$$

where $\hat{s}$ is the unit vector along the surface (droplet liquid-vapour interface), $\hat{n}$ is the unit vector perpendicular to the surface and u_s is the velocity tangential to the surface. Within the lubrication approximation we can work in a cylindrical coordinate system so that

$$\frac{d\sigma}{dr} = -\eta \frac{du_r}{dz} \tag{1.20}$$

where u_r is the velocity tangential to the substrate.

The Marangoni effect can also be described using dimensionless numbers, which compares the magnitude of the cause of the surface tension gradient with diffusion processes that would destroy that gradient. When the surface tension gradient arises from a temperature gradient the thermal Marangoni number, Ma_T, is

$$Ma_T = \frac{d\sigma}{dT} \frac{R\Delta T}{\eta\, k}, \tag{1.21}$$

where $\frac{d\sigma}{dT}$ is the change in surface tension with temperature, R is the drop radius which we have taken as the characteristic lengthscale of the drop, ΔT is the temperature gradient (between the apex and contact) and k is the thermal diffusivity.

Thermally driven Marangoni flows in evaporating drops have two origins: heated substrates and evaporative cooling. Heating the substrate leads to the contact line region being hotter than the apex of the drop (furthest point from the substrate) and strong thermal flows.[33] The temperature gradient arising from evaporative cooling is more subtle, in most cases (as glass substrates are commonly used in experiments and glass is an insulator) evaporative cooling means that the contact line region is slightly colder than the apex as a result of the greater

evaporative flux.[29,35] However on conducting substrates the heat lost from near the contact line can be replenished by conduction from the substrate while the heat lost from the apex is not replenished. Therefore the temperature gradient can change direction based upon the conductivity of the substrate.[53,54]

Alternatively if the surface tension gradient is caused by a concentration gradient of solute the solutal Marangoni number, Ma_S, is

$$Ma_S = \frac{d\sigma}{dc}\frac{R\Delta c}{\eta D}, \tag{1.22}$$

where $\frac{d\sigma}{dc}$ is the change in surface tension with concentration, R is the drop radius which I have chosen as the characteristic lengthscale of the drop, Δc is the concentration gradient (between the apex and contact) and D is the diffusivity of the solute. If this number is large ($Ma > 100$[11]) then the concentration gradient in the radial direction is dominant over diffusive transport and solutal Marangoni flows are expected.

These solutes can be different solvents or humectants (Chapter 4), non-volatile solutes such as sugars (Chapter 5) or salts (Chapter 6). Other common components of inkjet formulations not covered in this thesis which can give rise to solutal Marangoni flows are surfactants[41,55–58] or polymers.[59–61]

As strong Marangoni flows can easily dominate in evaporating drops it is only recently that the relevance of buoyancy driven flows has been widely established. Kang *et al.*[62] suggested their presence in sodium chloride drops but Edwards *et al.*[63] provided convincing experiments with a rotatable Optical Coherence Tomography (OCT) stage, showing that the direction of flow, through the centre of an ethanol−water or water−n-butanol drop from substrate to apex, reversed on changing from a sessile to pendant configuration in opposition to Marangoni driven flow. Following this publication Li *et al.*[64] ran similar experiments comparing sessile and pendant glycerol-water drops and found a similar switch in flow direction. They also introduced the dimensionless Archimedes (equivalently

Grashof) number, Ar, defined as

$$Ar = \frac{gh^3\rho\Delta\rho}{\eta^2} \tag{1.23}$$

where $\Delta\rho$ was the density difference across the drop height. They showed that this number was the relevant control parameter for whether buoyancy effects were prominent and when they could be neglected ($Ar \ll 1$). For their glycerol mixtures they found buoyancy flows were no longer important as they reduced the drop height from 320 to 154 µm. Given the h^3 scaling, and that the density difference is the same order of magnitude as the droplets we study in the thesis, then we do not expect buoyancy-driven flows to be a factor in inkjet-printed droplets with heights of a few tens of microns.

The drop interface can also affect some control over the deposit structure. Yunker *et al.*[65] showed that elliptical particles had strong capillary interactions so that they would form a loosely packed structure at the interface, leading to uniform deposits. Jung *et al.*[66] also demonstrated that in mixtures with microspheres of 0.5 and 5 µm diameter the particles would form a ring deposit and pin the contact line but at late times during depinning the large microspheres would disturb the liquid-vapour interface and experience a strong capillary force sweeping them towards the centre of the drop while the smaller microparticles were left behind at the original position of the contact line.

Within the literature for microlitre drops, particles can be added to act as tracers of the internal flows, with the assumption that the particles faithfully follow flow streamlines. However in this thesis I report particle migration across flow streamlines so it is worth verifying whether the particles should still act as high fidelity tracers of flows in inkjet-printed droplets.

The condition that there are no inertial effects present, for instance particles overshooting turning flow streamlines, is that the dimensionless (reference) Stokes

number, *St*, is low and is defined as[67]

$$St = \frac{\tau_p}{\tau_{\text{flow}}} = \frac{\tau_p \; u_{\text{flow}}}{d_p} \tag{1.24}$$

where on the far right hand side I have applied a common description of the flow timescale τ_{flow}; here u_{flow} is the flow velocity and d_p is the lengthscale of the flow obstruction which I interpret as the particle diameter. The timescale τ_p, is the particle response time, defined as the time required for a particle to react to changes in fluid flow, given by

$$\tau_p = \frac{\rho_p d_p^2}{18\eta}. \tag{1.25}$$

Substituting values for a typical ethanol-water droplet which will have larger Stokes numbers than the other systems studied due to greater particle speeds and lower viscosities:

$$\begin{aligned} St &\approx \frac{1005 \text{ kg m}^{-3} \; (1 \cdot 10^{-6} \text{ m}) \; 3 \cdot 10^{-3} \text{ m s}^{-1}}{18 \times 2.5 \cdot 10^{-3} \text{ Pa s}} \\ &\approx 7 \cdot 10^{-5} \ll 1. \end{aligned} \tag{1.26}$$

Based on this analysis these particles were expected to accurately trace the flows within the inkjet-printed droplets without inertial effects being present.

1.6 Inkjet Printing

In this thesis we will make the distinction between "drops" with microlitre volumes and smaller "droplets" which have been inkjet-printed (or are at inkjet-printed droplet lengthscales, such as aerosol droplets).

There are two main inkjet printing methods to produce droplets (see Figure 1.7).[68] In continuous inkjet printing (CIJ) a jet of the liquid is produced which begins to bulge and separate into discrete droplets as a result of the Plateau-Rayleigh instability (the jet is unstable to perturbations of wavelength greater than jet circumference so is perturbed at a high-enough frequency to cause spontaneous

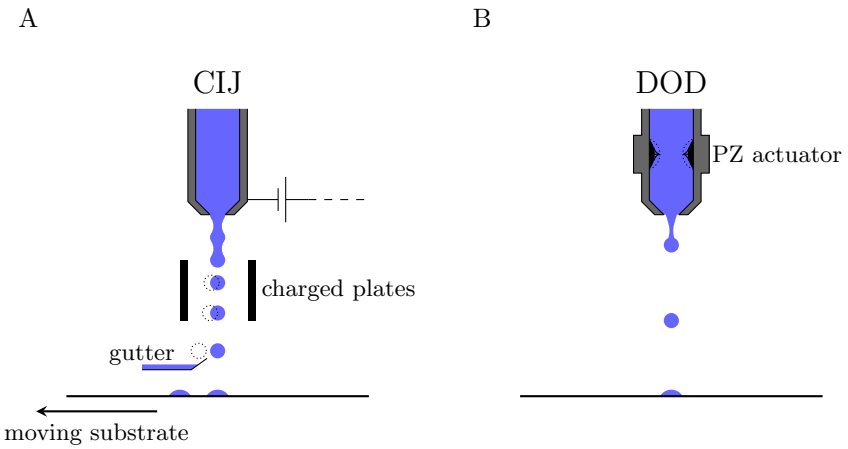

Figure 1.7: A - For continuous inkjet printing (CIJ) a stream of droplets is generated, where the dotted lines show the paths of charged droplets deflected by charged plates into the gutter so they do not impact the surface. B - In drop-on-demand (DOD) printing individual droplets are ejected by an acoustic pulse as a result of movement of piezoelectric (PZ) actuators (dotted lines for maximum extension position.

break-up of the jet). The fluid leaving the nozzle is charged so that during the flight of a droplet it can be deflected to the desired position on the substrate by charged plates. This control over positioning also means that unwanted droplets can be discarded via deflection into a gutter; a necessary feature because the CIJ generates droplets at a high frequency so the printing system may not be able to move quickly enough to deposit all the droplets in position. In contrast to the depiction in Figure 1.7 the deflected droplets are normally directed to the substrate rather than the gutter, as a result CIJ devices may only use a few percent of all the droplets generated.[13] Subsequently there is potential for such processes to be very wasteful if the ink reacts with the environment and so cannot be recycled.

In drop-on-demand (DOD) printing, single droplets are produced by the printhead and positioning of the deposit is controlled by moving the printhead and/or substrate. Such systems rely on the nozzle filling with liquid which stays in the nozzle due to surface tension. Droplets are then generated by applying a pressure

pulse at some resonant frequency to eject a drop with a diameter approximately equal to that of the nozzle. One way in which the pressure pulse can be generated is by using a heating element that boils the adjacent fluid, making a bubble which collapses when the heating element's current is removed. This is the method used in domestic printers although wider applications are restricted by requirements placed upon the printing liquid's vapour pressure.

In this thesis the DOD nozzle used a piezoelectric actuator to mechanically generate the necessary pressure pulse to eject fluid, the actuator acts in reaction to some voltage waveform.[69] While DOD methods have lower throughput than CIJ, control over the waveform shape can change the drop velocity and size while the lack of any need to recycle fluid once ejected means that there is less waste which is useful in high value industrial applications.

It is customary for inkjet printheads/nozzles to be positioned $2-3$ mm above the substrate as when the droplet is generated it is still connected to the nozzle by a thin filament of fluid so a minimum distance is required for breakup. How this filament breaks has an impact on the print quality; if the filament breaks near the nozzle the filament retracts into the drop with minimal effect, similarly if the filament breaks near the drop, the filament can retract back to the nozzle. However if the filament breaks at both ends then "satellite" droplets can result in non-circular deposits or multiple droplets being deposited.

For viscoelastic inks, such as those containing polymers, the filament of fluid may not break at all and the ejected drop is elastically pulled back into the nozzle. Whether a droplet can be jetted can be described by using the dimensionless Ohnesorge (Oh) number. This is defined using the dimensionless Weber (We) and Reynolds numbers (Equation 1.18)

$$We = \frac{v^2 \rho \; d_0}{\sigma_{lv}} \tag{1.27}$$

$$Oh = \frac{\sqrt{We}}{Re} = \frac{\eta}{\sqrt{\sigma_{lv} \rho d_0}} \tag{1.28}$$

where v and d_0 are the velocity and diameter of the drop in flight.

For inkjet printing applications the printability window can be described by upper and lower bounds on the Ohnesorge number (the inverse in Engineering applications). For instance Derby[68] used computational fluid dynamics to suggest $0.1 < Oh < 1$ although the precise lower boundary is less well-defined.[70,71] Broadly the problem outline is that the viscosity and surface tension of the fluid need to be overcome to jet a droplet, while breakup of the liquid thread at high velocities and low viscosities led to satellite droplets which reduce the parameter space for useful printing. This window can be effectively expanded by making use of the high shear rates in the nozzle ($(\approx 10^5\ \mathrm{s}^{-1})$[72]) with shear-thinning fluids.[73,74]

1.7 Droplet Interactions

In inkjet printing applications many droplets are printed near one another while there can also be satellite droplets, this means that a short discussion of coalescence and vapour interactions between droplets is useful.

For coalescence it has been shown that combined drops will try and return to a spherical cap shape,[75,76] however for miscible drops with different surface tensions there can be delayed coalescence and Marangoni flows of fluid from the lower surface tension drop into the higher surface tension drop.[77] Within an inkjet situation these differences in surface tension can arise from multicomponent droplets not being printed simultaneously; the first droplet will partially evaporate during the time taken for the second to be printed and so have a different composition surface tension at the moment of coalescence despite coming from the same fluid.

In Section 1.3 the drops evaporated into free space, however if other drops are present the vapour fields will overlap and there can be interactions, with slower evaporation in between drops.[28] In mixtures such non-uniform evaporation can lead to Marangoni flows. Cira *et al.*[78] studied water-propylene glycol (PG)

drops, despite each fluid wetting the substrate, solutal Marangoni flows led to an apparent contact angle. These drops would sit on a thin film of wetting fluid, reducing substrate interactions and hysteresis effects such that minute forces could lead to drop motion. As a result when two water-PG drops evaporated near one another the water vapour fields would interact, leading to surface tension forces within the film pulling the drops towards one another. Exploring different concentration combinations showed that repulsive behaviour could appear with a low-high combination of PG concentrations with mixed "chasing" behaviour in which the low surface tension drop followed one of higher surface tension.

Rather than using a second drop, Malinowski *et al.*[79] used a needle tip to provide a source of water vapour to interact with PG or PG-water ($x_{H_2O} = 0.95$) drops and induce motion. If the needle was above the drop it would be in an unstable equilibrium and so get repelled until it reached some off-centre radial distance as a result of strong attractive forces at the near side balancing smaller but cumulative attractive forces from the far side of the drop. Therefore the results still followed Cira *et al.* 's observation that the interaction was attractive.

Sadafi *et al.*[80] examined the interactions between pairs of pure, identical fluids (hydrofluoroethers or alkanes). By using a configuration with one sessile drop and one pendant drop on the same substrate they demonstrated that in addition to vapour-mediated interactions there could be short range attractions through the substrate as a result of evaporative cooling. As thermal effects were important for these systems, then rather than drops accelerating towards each other they slowed over time as they experienced an effective drag force to move from their temperature wells, therefore the slow-down behaviour was different between glass and sapphire substrates.

1.8 Thesis Roadmap

In this Chapter I have focused on giving an overview of the important background needed to understand the rest of the thesis. Following the methods chapter each chapter will each have a further literature discussion, tightly focused on the system being studied.

In Chapter 2 I introduce the main experimental rig, how I prepared my substrates and fluids for experiments and the general tools that we developed to analyse results.

In Chapter 3 I discuss the development of a new experimental technique and the corresponding equipment which was applied to study the change in composition over time in model ethanol-water droplets. This technique was only developed at the end of my time in the laboratory, which was cut short by the COVID-19 pandemic, and so was not implemented for other systems.

In the remaining chapters in which experiments are discussed there are a number of points which are repeatedly addressed. These include the evaporation behaviour and how well this is fitted by simple adaptions to Popov's model.[31] I also report the direction of (solutal Marangoni) flows, under what conditions those flows were present, how those flows impacted the deposition and the existence of particle migration across those flows. Chapter 4 discusses these points in relation to ethanol-water and other solvent mixtures with low volatility ethylene glycol. In Chapter 5 I look at solutions where the solute is involatile sugar, therefore I introduce the supersaturation to quantify how evaporation can drive droplets to reach metastable concentrations. In Chapter 6 I study solutions with involatile salts where there is additional complexity as a result of the salts crystallising out of solution once the droplets become concentrated.

Finally in Chapter 7 I compare the particle migration behaviour across all my different droplets, and offer a general conclusion and summarise avenues for future work in Chapter 8.

On readability: in the electronic version of this thesis blue text such as in the Table of Contents or when referring to figures, equations or references are links to elsewhere within the thesis. In addition, the links in the List of Symbols go to the first time a variable or acronym was introduced. When using these links they will naturally take you to a different location so a convenient shortcut to be aware of is `Alt` + ← (left arrow key) to go back to the previous location in the thesis before the link was followed.

In this thesis there are a number of supplementary videos, these show the evaporation of example droplets of each of the solutes studied to show flow behaviour and particle/crystal deposits. Videos are provided in `avi` format for the majority of figures showing frames from "dark-field" videos where droplets are viewed from below. This file type can be played with most free video players although VirtualDub was used during the analysis as it is particularly easy to use to step through individual frames. The videos have been named with their associated figure as well as what the droplet contained and the substrate printed on. The phrase "A.BC x Real Time" in a name details how fast the droplets evaporated relative to the video playback speed of 25 fps. Therefore a video recorded with an effective frame rate of 100 fps would have "4.00 x Real Time" in its filename. The majority of frames from each video have been cut to reduce file sizes to the range of 100 MB each, which gives rise to different playback speeds and faster speeds for smaller droplets where fewer pixels needed to be saved per second.

A folder containing the compressed supplementary videos can be accessed at https://drive.google.com/drive/folders/1zjtWtBG-i1yd6owauTJDMet3onG_kviA?usp=sharing or Durham University's Collections service at doi:10.15128/r11v53jx02v.

Chapter 2

Methods

2.1 Printing Rig

Experiments took place at ambient lab conditions or in a humidity controlled chamber. Lab temperatures were in the range $22 - 24°C$ while uncontrolled humidities were in the range $30 - 50\%$, both values were recorded with a Sensiron SHT31 thermohygrometer with a precision of $T \pm 0.2°C$, $RH \pm 2\%$. The sensors were small, so were positioned in the vicinity of the droplet in open experiments or within the humidity chamber itself.

Droplets were printed from a single drop-on-demand Microfab piezoelectric (PZ) nozzle (MJ-ABP-1, Horizon instruments) with a 50 µm orifice controlled using a Microfab JetDrive III Controller (CT-M3-2). The controller generated an approximate square-wave pulse where the typical durations of each rise, dwell, etc. stage gave a pulse of the form depicted in Figure 2.1. These durations could be tuned to reduce the formation of satellite droplets while the voltage amplitude of the pulse was varied to generate larger or smaller droplets. Fluid was supplied to the nozzle from a 8 mL glass vial with a custom lid with an input and output for Polytetrafluoroethylene (PTFE) tubing. A syringe was used to pressurise the fluid and pump it through the outlet to the tip of the nozzle.

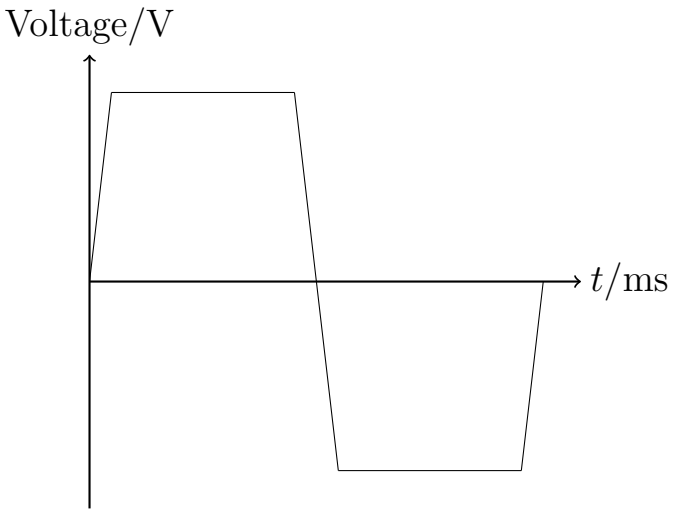

Figure 2.1: To-scale voltage waveform generated by the Microfab Jet-Drive III Controller for the DOD nozzle. The five "rise", "dwell", "fall", "echo" and second "rise" intervals had durations (in ms) of 3, 30, 6, 30 and 3 respectively.

Figure 2.2 presents the schematic of the main experimental rig. The DOD nozzle was mounted on xyz translation stage where the y and z (vertical) directions were manually controlled and the x direction was motorised (Laser2000, T-XYZ-LS13) which could be controlled manually or via ZaberController software. The substrate lay on a horizontal board with a hole in the centre which was positioned by a combination of three of the above motorised stages for full xyz control.

The humidity-controlled cell was a home-made design 3D-printed by the Mechanical Workshop with a holes for input gas and the thermohygrometer and windows for light from LEDs. A nitrogen feed was split, one portion remained dry while the second was passed through a gas bubbler built by the Glassblowers Workshop filled with water which would saturate nitrogen with water vapour. The combined gas lines were passed to a flask to mix with an output into the humidity chamber. The flow of nitrogen through each line was controlled by adjusting two gas flow controllers until the target relative humidity was obtained and remained steady.

The droplet was illuminated by cold uncollimated blue LEDs (Thorlabs) to

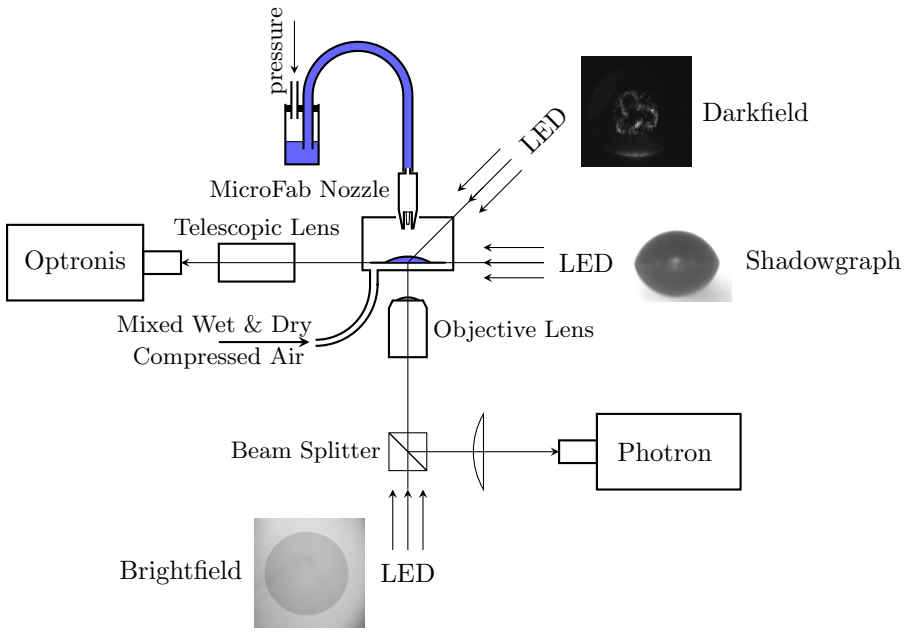

Figure 2.2: Schematic of the experimental rig used to record bright-field recordings of the drying droplet, dark-field recordings of dispersed particles in the drop and bright-field recordings of the drop profile. The Photron and Optronis are brands of high- and mid-speed cameras.

minimise heating of the droplets. Light from the bright-field LED from below the substrate was focused onto the droplet by an objective lens with $50\times$ magnification (Nikon Tu Plan ELWD, numerical aperture $NA = 0.6$), reflected back and collected by a Photron Fastcam SA4 high-speed camera. The angled incident light from the dark-field LED would scatter off particles, crystals, etc. suspended in the droplet or on the substrate; the scattered light could be collected by the objective lens and also focused onto the high-speed camera. Frame rates were varied from $200 - 6000$ frames per second (fps) depending on the system studied. Imaging the particles with scattered light meant that crystals could also be viewed and the tracer particles were not required to be fluorescent; however this came at the cost of a slight background intensity gradient and a bright patch in the videos that would obscure some of a droplet's area. This bright patch was a result of light from the LED being refracted into the objective lens at the far side of the droplet and obscured a larger portion of the droplet at higher contact angles when the

droplet surface had a greater curvature.

Side-view bright-field images of the drop profile were obtained using an LED opposite a mid-speed Optronis camera CR3000×2 into which light was focused by a telescopic lens (LaVision, VZ11-0068, $< 20 \times$ magnification). Recordings of the profile could be taken independently of the Photron camera and frames rates of $500 - 2000$ fps were used.

During experiments the videos were synchronised by having a single trigger from the Fastcam software start both recordings simultaneously then activate the Microfab driver so a droplet was dispensed. Images and recordings were calibrated by comparing the sizes of features relative to those on a glass slide with an array of circles with known diameter and spacing. The bottom-view resolution was $0.398\,\mu\text{m pixel}^{-1}$ and side-view resolution at the maximum magnification was $0.586\,\mu\text{m pixel}^{-1}$.

2.2 Substrate Preparation

The experimental substrates were square Academy glass cover slips (side-length of 22 mm, 0.13-0.16 mm thick) prepared by sonication in 5%v Decon 90 (a non-phosphate laboratory detergent with a mixture of anionic and non-ionic surfactants) twice for 15 minutes with a change of solution. Substrates could be made more hydrophilic by placing them in an air plasma cleaner (Asher E2000) for 30 minutes or more hydrophobic through the vapour deposition of hexamethyldisilazane (HMDS) ($>$ 98% Alfa-Aesar) for at least an hour in a vacuum desiccator. More hydrophobic substrates were prepared by submerging plasma-cleaned substrates in a solution of 1%v octadecyltrichlorosilane (OTS) in toluene for one hour. After any processing step substrates were thoroughly rinsed with ultra-high purity water (Milli-Q, Resistivity > 18 MΩ cm) and blown dry with nitrogen. Finally substrates were covered, placed in a drying oven overnight

and used within 48 hours. Substrates were rarely characterised as a side-view camera was in use to record the contact angles during drying.

2.3 Fluid Preparation

Binary and ternary solvent mixtures were prepared using ultra-high purity water, ethanol (absolute, $\geqslant$ 99.8% High Performance Liquid Chromatography grade, purchased from Fisher Scientific) and ethylene glycol (anhydrous 99.8%, purchased from Sigma-Aldrich). When particles were included in mixtures the volume of the particles was ignored, i.e. a mixture of 50:50 ethanol and water by volume might be made from 100 µL of diluted particle solution, 900 µL of water and 1000 µL of ethanol.

Tracer particles were sourced from The University of Leeds, Leeds, UK (Grace Yow and Simon Biggs, see Ref. 81 for synthesis) and provided in an aqueous suspension with the particles at 16.9%v. These were polystyrene (PS) microspheres with a mean diameter of 977 nm stabilised by poly(ethylene glycol) methacrylate (PEGMA) polymer with a zeta-potential, ζ, of -25 to -39 mV for pHs in the range of $6-9$. Other particles used included 604 nm sterically-stablised PS particles from the same source at Leeds and charge-stablised 520 nm silica particles (SS0N3) and 3110 nm PS particles (PS05N) purchased from Bangs Laboratory Inc.. These particles were sufficiently small that they did not block the nozzle, generate distorted droplets, or settle during the lifetime of a droplet.[82] Low particle concentrations of < 0.02%v were used.

The solutes added to make solutions for printing included:

- Sucrose $\geqslant$ 99.5% (GC) purchased from Sigma Life Sciences,
- Lactose $\geqslant$ 99% $\alpha-$lactose monohydrate (GC) purchased from Sigma Life Sciences,
- Sodium Chloride, $\geqslant$ 99.8% Assay purchased from Fischer Scientific and used

after having been baked in a furnace at the Department's Glassblowers' Workshop to vapourise organic impurities,

- Sodium Nitrate $\geqslant 99\%$, crystalline, purchased from Alfa Aesar,
- Ammonium Sulfate (AMS) $\geqslant 99\%$, purchased from Aldrich Chemical Co..

Solutions were prepared on the day to reduce effects from the evaporation of volatile components or sugars getting eaten by bacteria.

2.4 Video Processing

MATLAB code written by Dr L. Yang was used to calculate the volume of axisymmetric sessile drops using videos of the drop profiles collected by the Optronis camera. The position of the substrate could be manually selected or automatically detected by averaging over the mid-point between the liquid-vapour interface and its reflection in the substrate. The edge of the drop was found by taking maxima along the vertical axis in the differential grayscale going from the bright background to dark drop. A circular arc was fitted to the set of maxima so the height and drop radius could be measured and the contact angle and volume (assuming the drop was axisymmetric) calculated using Equations 1.3 and 1.5.

Our edge detection algorithm worked along the vertical axis rather than perpendicular to the interface (which would have required iterations of fitting), meaning that the radius was less well-defined at high contact angles; other systematic errors could also arise from not considering diffraction effects. Random uncertainties in the volume could be estimated by a χ^2 fit of the edge locations about a circular arc.[83,84] Droplets on hydrophobic HMDS or OTS treated surfaces could have volumes found with a precision of $< 0.5\%$, i.e. less than a picolitre, at early times. On plasma-cleaned cover slips the droplets were thin and a 'halo' in the droplet profile made the position of the interface less certain. If the droplet contact line depinned then initial volumes were precise to $2 - 10\%$ while if the

droplets were pinned and so got thinner over time then uncertainties in the volume could be significant, quickly reaching uncertainties on the order of 20%. When the uncertainty was this large I would not proceed with further analysis of the droplet profile. Larger droplets could be measured with greater precision as an image of the droplet would contain more pixels.

2.5 Particle Tracking

Particle Tracking MATLAB code was written by Dr L. Yang using functions from Georgetown's MATLAB adaption[85] of Crocker and Grier's[86] micro-Particle Image Velocimetry (μPIV) method. The code was applied to dark-field, bottom-view videos where the particles appeared as bright spots with good contrast against the background.

First the position of the drop contact line was found by choosing an appropriate video frame. If the droplet depinned this would be an early frame in which the position of the contact line was obvious. A number of locations around the contact line would then be manually chosen for a circular fit. If the droplet was pinned throughout drying then there would be a well-defined ring deposit at the end of drying, in this case the positions of the outermost particles could be automatically detected for the circular fit. Within the droplet footprint the positions of particles were found by looking for pixels above a threshold intensity and the particles labelled. Between subsequent frames the particles were assumed to have not travelled far so positions were correlated to find the most probable configuration based upon the previous particle positions. The updated positions were then used to calculate velocities between timesteps and the tracks of individual particles. If the particle movements were below a certain magnitude threshold the particle was considered stationary. If algorithm lost track of a particle then resolved it again, the particle would be given a new label leading to incomplete paths of

particle motion. The velocities were binned temporally in twentieths of the time tracked, and radially, in increments of $R_0/10$ (where R_0 is the contact radius at $t = 0$ s); the mean velocity within each bin was then determined.

I made a number of adaptions to this code. Firstly I followed the approach of Talbot[87] to split the binned velocities depending on their radial direction. While the original code worked well for tracking movements in a single direction, when solutal Marangoni flows were present there were inward and outwardly moving particles so the mean velocity would be unrepresentative. Therefore for each bin the mean of the velocities in each radial direction were found.

The bright patch in the videos (see red spot in Figure 2.4) as a result of refraction of the angled LED to the camera also presented a problem. This region was sufficiently bright that the code would label the edge of the region as a set of particles. Most of these movements were small enough that these false particles were classed as stationary however those that were not categorised generated false particle tracks which impacted the mean velocities. Therefore I implemented the intensity gradient function from the drop profile analysis code to find the outline of the bright patch and automated removal of that region from the tracked area in the PIV code. In the bottom right plot of Figure 2.3 the dark red line disappears at later times, this indicates that those velocities were entirely a result of the bright patch's edge being incorrectly assigned as particles. In addition the velocities for $0.5 < R/R_0 \leq 0.7$ were slightly larger as the mean in the bins did not average over false particles with low velocities.

I also averaged velocities within individual particle traces so that small side-to-side motions from Brownian motion would even out. This method also helped cut out artificial particle movements from points along the contact line getting incorrectly classified as particles, or from sub-pixel changes in particle location due to optical artefacts which could lead to nonsensical particle velocities of hundreds of microns per second. While these efforts reduced the amount of noise

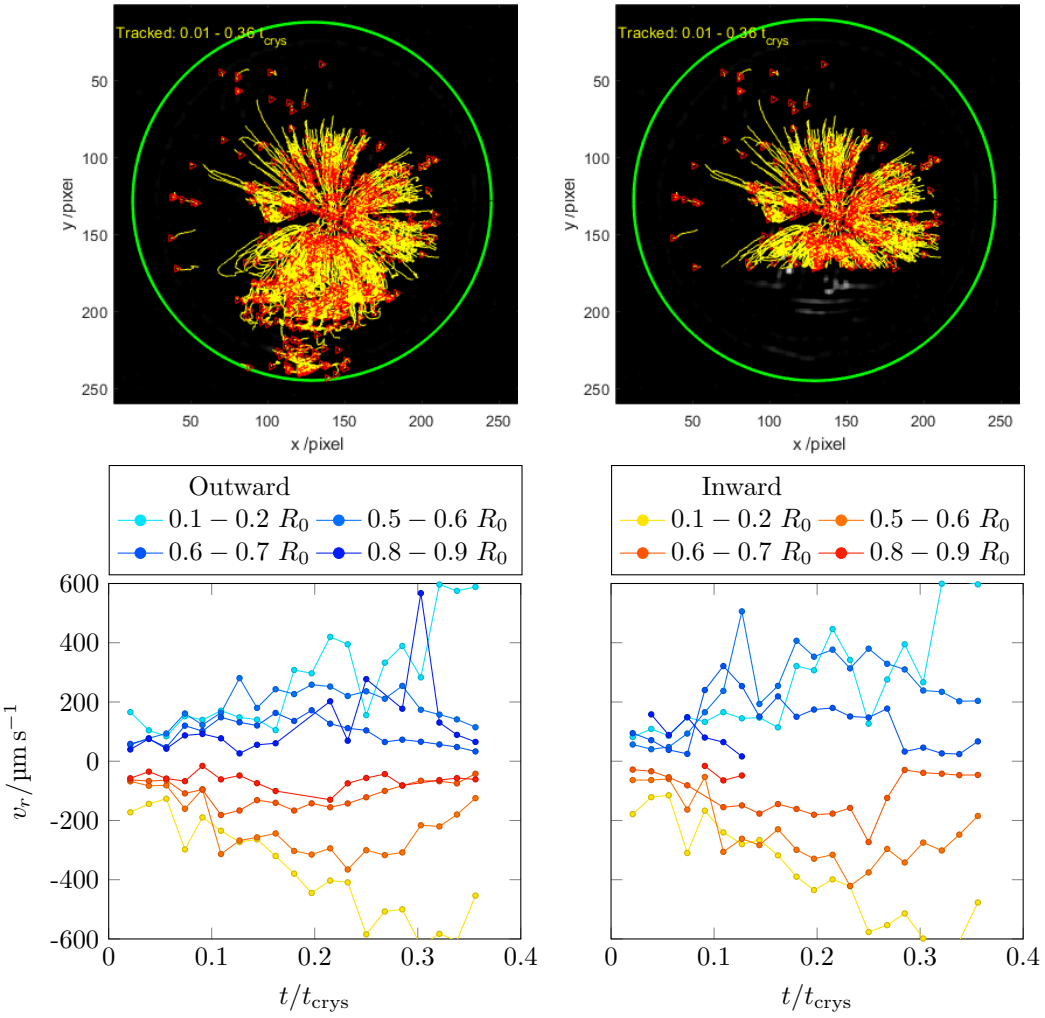

Figure 2.3: Tracked particle traces and binned velocity profiles over time for a 10 wt% NaCl droplet. In the right-hand plots the PIV code was applied with the region of droplet covered by the bright patch from refraction removed.

present it was not fully eliminated. Therefore in the particle velocity plot in Figure 2.3 where the bright patch was eliminated there are still fake particles getting recognised by the algorithm and so leading to a set of measured velocities closer to zero at later times in the $0.8 < R/R_0 \leq 0.9$ interval. Therefore in all the PIV figures in this thesis it is best to ignore tracked velocities on the order of $100\,\mu\mathrm{m\,s^{-1}}$, especially if the value is approximately constant over time.

I also implemented general improvements to automatically save the code inputs and more computationally expensive particle tracks in separate files alongside the

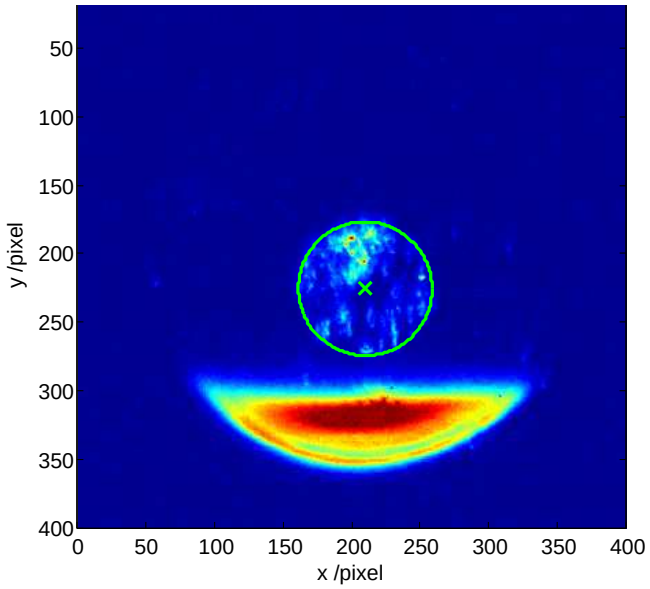

Figure 2.4: Interface for manual fitting of collected group radius. A number of points are selected and following a confirmation step a green circle is generated so the user can assess the quality of the fit. This is from a recoloured dark-field bottom-view image of an ethanol-water droplet where particle migration has collected particles at the centre. There is a bright region due to refraction at the bottom side of the figure.

code inputs such that they were not overwritten unintentionally and make the analysis more transparent to future users.

2.6 Group Radius

The particles suspended in evaporating droplets were observed becoming concentrated in the centre of the droplet when there were solutal Marangoni flows direction inwards along the substrate (and outward along the liquid-vapour interface). To quantify this behaviour we introduced the group radius, R_g, which was defined as the radius of a circle fitted to the outer edge of the group of collected particles. To analyse the change in group radius I wrote a MATLAB script to open a given video and look at predetermined frames corresponding to times up-to and just-after-the-end-of Marangoni convection while the solutal Marangoni flows were axisymmetric without the centre jumping around. For each frame the user

would be asked to fit the contact line of the droplet and radius of the collected group of particles in the centre of the drop by clicking points along the circle to be fitted. This was aided by using a higher particle concentration although this reduced the useful PIV information. The circular fitting algorithm was copied from the PIV code. To aid manual fitting a non-greyscale colourmap was used so the edge of the collected group was more visible by eye (see Figure 2.4). The error in this approach was estimated by repeatedly analysing the same set of data, this gave a fractional standard deviation of $< 2\%$ over six concurrent repeats.

The output of this code was a 2D array of video frame against contact radius and collected group radius, with the radii in pixels. Calibration data and knowledge of the recording's fps could be used to convert the change in R_g with frame into a "migration velocity", v_{R_g}, in $\mu m\, s^{-1}$.

2.7 Hygrometer Calibration

In previous experiments within the group the previous prototypes of the humidity chamber were only used to produce "low" or "high" relative humidity environments for more general exploration of experimental parameters.[88] In order to give a more precise dependence of evaporation on RH a better sensor was needed which would also require calibration.

The water activity and so relative humidities (see Equation 1.17) above saturated salt solutions are described in the literature and given in Table 2.1. Therefore the sensor could be placed in a small airtight container with a dish containing salt solution to check its accuracy. We prepared salt slurries where the mass fraction (MFS) of salt was much higher than the solubility limit which greatly sped up the rate at which the environment inside a container reached equilibrium with the salt and gave more reliable measurements.

The left plot of Figure 2.5 shows that the Sensiron thermohygrometer was

Table 2.1: Saturated salt solution relative humidities at $T = 20°C$ from Ref. 89.

Salt	Relative Humidity/%
Potassium nitrate	94.62
Potassium chloride	85.11
Potassium bromide	81.67
Sodium chloride	75.47
Potassium iodide	69.90
Sodium bromide	59.14
Potassium carbonate	43.10
Magnessium chloride	33.07
Potassium acetate	23.11
Lithium chloride	11.31
Potassium hydroxide	9.32
Lithium bromide	6.61

accurate to within ±2% between 30 and 80% RH, the range of relative humidities in which experiments were conducted. We tested the sensor within the humidity cell with water droplets to see the impact of gas flow on the evaporation. On a HMDS treated substrate, water droplet evaporation is well described by a constant contact angle evaporation mode[90] so that Picknett and Bexon's equation[24] for the drying time applies

$$t_{\text{dry}}^{\text{CCA}} = \frac{3\rho M_0^{2/3}}{4\pi D c_v (1 - RH) E (C/r)} \tag{2.1}$$

where M_0 is the mass of the droplet at the start of drying, E is their description of the volume of the spherical cap in non-cylindrical coordinates

$$E^3 = \frac{3}{\pi(1 - \cos\theta_0)^2(2 + \cos\theta_0)} \tag{2.2}$$

and C/r is related to the "capacitance" of the droplet, where r is the radius of curvature of the droplet and the ratio can be well approximated by the polynomials:

- For $0 \leq \theta < 0.175$ radians:

  $C/r = 0.6366\theta + 0.09591\theta^2 - 0.06144\theta^3$,

- For $0.175 \leq \theta < \pi$ radians:

  $C/r = 0.00008957 + 0.6333\theta + 0.1160\theta^2 - 0.08878\theta^3 + 0.01033\theta^4$,

- $C/r \to 0$ as $\theta \to 0$ (disk),
- $C/r = 1$ when $\theta = \pi/2$ (hemisphere),
- $C/r = 2\ln 2$ when $\theta = \pi/2$ (sphere).

I also used literature values for the density of water's dependence on temperature[91] and Fuller *et al.*[92]'s temperature dependence of the diffusion coefficient for water in air

$$D(T) = D_{298.15}\left(\frac{T}{298.15\ \mathrm{K}}\right)^{1.75} \tag{2.3}$$

where $D_{298.15} = 2.634 \times 10^{-5}\ \mathrm{m^2\ s^{-1}}$.[93] The right-hand plot of Figure 2.5 shows how the ratio of the theoretical drying time to the experimental drying time changed with relative humidity where D was scaled according to the measured temperature for each droplet. The ratio was close to 1 for the majority of the range although the experimental drying times were longer than expected at high relative humidities. This could have been a result of the incoming gas flow holding more water vapour at high relative humidities and reaching the droplet before the humidity sensor, or gas leaks away from the sensor.

As shown in Figure 2.5, the sensor was calibrated in 2019. Before this point during my PhD an Extech thermohygrometer was used with a precision of $\pm 4\%$ *RH*. When the Sensiron thermohygrometer was calibrated for the first time both sensors were placed within the sealed chamber containing the salt solutions so we could correctly map the old relative humidities to the updated values. Where this has been done I will report an approximate relative humidity, for example writing $RH \approx 50\%$ or $RH < 40\%$ rather than $RH = 40 \pm 2\%$. In terms of the results included in the thesis this only impacts limited experiments with ethanol-water droplets printed using the main experimental rig as well as early experiments with sodium chloride.

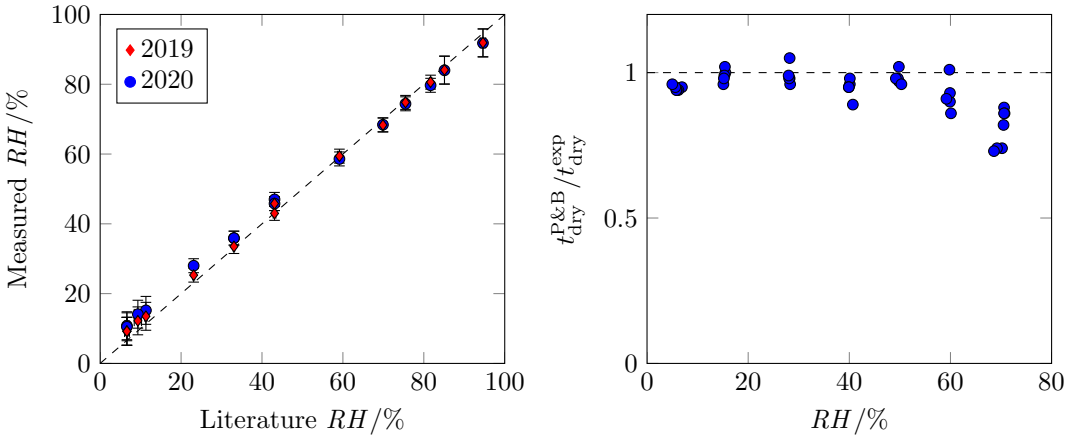

Figure 2.5: Measured vs literature relative humidities for saturated salt solutions and ratio of theoretical and experimental drying times for $100 - 120$ pL water droplets evaporating on HMDS treated substrates. Dr L. Yang developed the salt solution calibration method and collected the 2019 (red) data while I collected the 2020 data (blue).

2.8 Ethanol Vapour

Some experiments with solvent mixtures involved introducing ethanol vapour to the environment into which a droplet was evaporating. In my initial attempts I attached a fitted porous cylinder around the nozzle which had been soaked in ethanol; however a more successful approach used a vapour shroud crafted by the Mechanical Workshop seen in Figure 2.6. A circular well was positioned above the substrate by supporting it with two parallel microscope slides. Lifting the well off the substrate was necessary to use the side-view camera during experiments.

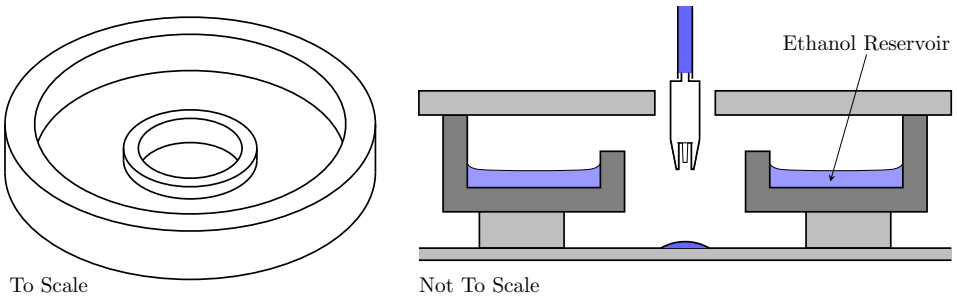

Figure 2.6: Schematic of the stainless steel vapour shroud (outer diameter is 2.5 cm) and diagram of how the vapour shroud was utilised during experiments.

The well within the shroud was then filled with ethanol and capped with a glass plate with a hole drilled through the top for the nozzle to pass through. This approach had the advantage of providing an axisymmetric vapour source that did not require very frequent top-ups of ethanol (and nozzle reallignment). Later experiments involving ethylene glycol systems made use of an updated humidity chamber in which the bubbler fluid (water) was replaced with ethanol and the gas flow kept constant. In all these cases the concentration of ethanol in the vapour phase was approximated by comparing the drying time of pure ethanol droplets in the ethanol-enriched environment to that of a free drying ethanol droplet of the same size, i.e. if an ethanol droplet was printed in air and then one of the same size printed in an ethanol vapour and evaporated in twice (or quadruple) the time then the RH equivalent for ethanol would be 50% (or 75%).

2.9 Modelling Evaporation

I developed a fully (vertically and radially) composition-averaged model to describe the evaporation of droplets over time based upon the mass loss equations derived by Popov.[31] This is a quasisteady model where the evaporation rate depends on the dimensions of the drop and the vapour field about the drop is quasistatic. The core mass loss equation derived by Popov to describe the evaporation of a drop of pure fluid is

$$\frac{dM}{dt} = -\pi R \; D^{air}_{\text{fluid}} \; c_v \; (a_{\text{fluid}} - a_{\text{envir}}) F_{\text{Popov}}(\theta) \tag{2.4}$$

where D^{air}_{fluid} is the diffusion coefficient of the fluid in air, R is the drop radius, c_v is the mass density of the fluid in the vapour, a_{fluid} is the activity of the fluid (equals 1 for pure fluid) and a_{envir} is the activity of the fluid in the environment so that it is equivalent to the relative humidity when the fluid in question is water,

and $F_{\text{Popov}}(\theta)$ contains all the angular dependencies

$$F_{\text{Popov}}(\theta) = \frac{\sin\theta}{1+\cos\theta} + 4\int_0^\infty \frac{1+\cosh 2\theta q}{\sinh 2\pi q}\tanh[(\pi-\theta)q]\ dq. \tag{2.5}$$

In my model this integral was calculated numerically by using the *trapz* function in MATLAB and summing up to some large limit at which the integral converged. The vapour mass density c_v was calculated using the ideal gas law

$$c_v = \frac{Mr\ p_v}{R'T} \tag{2.6}$$

where Mr was the molar mass, p_v was the temperature dependent vapour pressure of the fluid component[94] and R' was the Ideal Gas Constant, $R' = 8.314$ J K^{-1} mol^{-1}. Additional temperature dependence in Equation 2.4 came in through the diffusion coefficient, where Equation 2.3 was again utilised to modify it according to deviations from $T = 25$ °C (i.e. all systems as $T_{\text{exp}} = 21$ to 24 °C).[92]

While these equations were originally derived for pure fluids I extended the model by having each volatile component of the droplet have its own set of mass loss equations[95] where the vapour density of the saturated layer above the droplet was modulated according to the fluid's vapour pressure in a mixture. Therefore for involatile solutes such as sucrose or sodium chloride (see code in Appendix F.1) there would only be a single mass loss equation for the water component with $a_{\text{H}_2\text{O}}$ a function of the solute concentration. While I experimentally found that ethylene glycol would evaporate; it was essentially involatile if I restricted the model to the first few seconds of the evaporation process. Then for something like an ethanol-water system with two volatile components I could describe the evaporation using

$$\frac{dM_{\text{H}_2\text{O}}}{dt} = -\pi R\ D^{air}_{\text{H}_2\text{O}}\ c_v^{H_2O}\ (a_{\text{H}_2\text{O}} - RH)F_{\text{Popov}}(\theta) \tag{2.7}$$

$$\frac{dM_{\text{EtOH}}}{dt} = -\pi R\ D^{air}_{\text{EtOH}}\ c_v^{\text{EtOH}}\ (a_{\text{EtOH}} - a^{\text{EtOH}}_{\text{envir}})F_{\text{Popov}}(\theta) \tag{2.8}$$

where $a^{\text{EtOH}}_{\text{envir}}$ would be zero unless the droplet evaporated in an ethanol enriched

environment and D^{air}_{EtOH} came from Ref 96.

Given the starting composition of a droplet, these mass loss equations meant that I could keep track of the changing average composition throughout the droplet which would be used to update the vapour densities, fluid activities and droplet density with literature values. From the total mass and density I would have the volume of the droplet at any time.

In order to achieve better agreement between my model and experiments I needed to take into account contact line behaviour. Due to contact angle hysteresis, in experiments droplets tended to begin evaporating in a CCR mode. Within the model the new contact angle could be calculated for the new volume and the fixed contact radius by creating a lookup table for the volume of a spherical cap with varying θ and fixed R.

After some time experimental droplets tended to depin, therefore within the model I would force a switch at the experimental depinning time to a mixed mode when both the contact radius and angle would vary (this could be set to occur at $t = 0$ if the droplet never pinned). In my model the change in contact angle was entirely a result of the change in average composition of a droplet as a result of evaporation. In Young's stress balance for the contact angle of a drop (Equation 1.1) σ_{sv} would not change and σ_{sl} was assumed to be constant for the small change over a timestep so that σ_{lv} could be assumed to be the sole driver of changes in contact angle. Therefore the adjusted contact angle after a timestep could be determined using

$$\cos\theta_t = \frac{\sigma_{t-dt}\cos\theta_{t-dt}}{\sigma_t} \tag{2.9}$$

where $t - dt$ refers to the values for the previous time-step and σ is σ_{lv}. The radius could then be found by using Equation 1.5 and more lookup tables. This approach tended to overestimate changes in contact angle during evaporation.

Chapter 3

Reflectometry

Investigations into the evaporation of droplets of different chemical systems detailed in the following chapters made it clear that it would have been useful to have a method to quantitatively determine droplet composition. In terms of the chronological order of experiments in my PhD this was the final project. Therefore while the methods developed could have usefully been applied to all my systems, time limitations as a result of the COVID-19 pandemic meant that further experiments could not be attempted.

In this chapter I first describe the background to this experiment, referring to parts of the literature on the evaporation of model ethanol-water droplets which we hoped to address, before moving onto a comprehensive description of experiments where some kind of composition information has been collected. I then follow with details of what we hoped to achieve with the new technique we designed, the theory underpinning it and how the method was developed. Finally I discuss the results collected for droplets with a range of initial (ethanol) concentrations, an analysis of what we learned from the experiments, and the current limitations of the technique.

3.1 Background

While the amount of work published on the topic of drops has increased dramatically in recent years, researchers typically investigate deposits or drop profiles, commonly changes in volume or spreading. As a result the compositions of mixtures during drying are normally unknown or can only be inferred. For instance in the evaporation of a binary ethanol-water drop, different stages of evaporation have been observed in which the majority of the fluid evaporating in the first stage is ethanol while the majority in the second stage is water.[97,98]

The time evolution of drop profiles in these different stages, compared to those of pure components, led researchers to infer that there was some residue of the volatile ethanol component remaining into later stages of drying. Liu *et al.*[99] noted that the volume remaining at the end of the first stage, at which point most of the ethanol had evaporated, was greater than the expected volume of water within the drop; during the second stage they found the evaporation rate was faster than for pure water. This could be attributed to the lower contact angles observed whose cause could be an ethanol residue lowering the drop surface tension. Ozturk and Erbil[100] also came to a similar conclusion; in experiments on fluoropolymer coated substrates they found that the contact angles even late into drying were different to those of pure water.

Sefiane *et al.*[101] also noted how the contact angles at the end of the first stage were different to that of pure water in the evaporation of binary mixtures of methanol and water, and attributed this to a residue of the volatile alcohol. They rationalised this by a comparison between the characteristic time for methanol to diffuse across the characteristic length of the drop and the drying time. As the diffusion time was longer they suggested a methanol residue could be left after the first stage of evaporation.

In these examples the presence of a residue was inferred by making comparisons to the evaporation dynamics or dimensions of a pure fluid droplet. To

definitively demonstrate the existence of such a residue more direct measurements that explicitly measure the actual concentrations are required. For instance Hopkins and Reid[102] studied the evaporation of free drying ethanol-water aerosol droplets where the liquid-vapour interface could be probed by cavity-enhanced Raman scattering. While this technique utilised Whispering Gallery Modes to be phenomenally sensitive, measuring ±0.2%v ethanol, it was only suitable for the first tens of milliseconds of drying.

Raj *et al.*[103] investigated the drying of pendant drops within a tensiometer allowing them to follow the shape parameter and surface tension over time. This allowed them to estimate the surface composition during the evaporation of aqueous mixtures of 25%v methanol or ethanol down to about 10%v at which point the evolution of composition had approximately flattened out.

Innocenzi *et al.*[104] investigated the evaporation of 50 µL ethanol sessile drops around the azeotropic concentration of 95.5 wt% ethanol with time-resolved infrared spectrometry at a synchotron facility. For their mixtures the absorbance of the ethanol peak constantly decreased, while due to the 50% *RH* environment there was condensation of water onto the drop which would remain after the ethanol fully evaporated.

Chen *et al.*[105] investigated the evaporation of aqueous mixtures of 5, 25 and 50 wt% ethanol or 5 wt% 1-butanol. In their method they had a composition dependent reflection coefficient of an acoustic wave echo from the solid-liquid interface from the fluid's different mechanical impedances relative to the silicon substrate; controlling the acoustic pulse meant they could probe the composition of the nearest 7.5 µm of fluid to the interface in 1 µL drops. This was a powerful approach as simultaneous measurements of the same drop could be made with an infrared (IR) camera from above and the drop profile recorded. As the drops evaporated at ambient temperature Chen *et al.* argued that differences in thermal emissivity across the top surface could be attributed to differing compositions

rather than evaporative cooling, as a result they could estimate when the alcohol had fully evaporated. Comparing these times to acoustic measurements of when the concentration of alcohol at the bottom of the drop went to zero showed that alcohol was present at the bottom for much longer times than at the liquid-vapour interface. This was explained with a similar argument to Sefiane *et al.*[101] in that the lower diffusion coefficient of ethanol in water than air meant that a residue could be present as it would take longer to reach the drop surface than it would to evaporate away. In addition the authors found that the time evolution of ethanol concentration was not linear; at intermediate concentrations the ethanol concentration decreased fastest at the start of evaporation while for pure ethanol evaporating in a chamber of $20 - 56\%$ RH the mass fraction decreased slowly at the start and then more quickly below 70 wt% until a residue of a few wt% remained which evaporated slowly.

Rather than measuring a drop's composition in situ other researchers have taken to relying on the reproducibility of drop generation, printing sets of drops and then collecting different drops after different lengths of time for subsequent analysis. In their investigation into the importance of buoyancy driven flows Edwards *et al.*[63] deposited multiple 10 µL drops spaced apart within their chamber to minimise collective effects. One of the drops would be monitored by Optical Coherence Tomography while the others would be removed at different time intervals and immediately sealed for subsequent Gas Chromatography measurements. They found that the mass fraction of ethanol decreased exponentially with normalised time for 10% ethanol concentration drops. Interestingly the curved appearance of the lower side of the drop during an OCT experiment is dependent on the refractive index of the fluid so there is scope to use that effect to extract information on drop composition.

Simultaneously Kita *et al.*[106] reported using Gas Injection Chromatography for 7 µL ethanol drops dried in a humidity chamber at different temperatures. A

needle would take a 0.2 µL volume for analysis for identical drops after different times. Kita *et al.* found that the volume fraction of ethanol decreased linearly with time, changing more slowly at low RHs because of reduced water adsorption-absorption and/or condensation.

Ozturk and Erbil[107] developed an approach to investigate the change in mean drop composition with time for ethanol-water µL drops. By making use of a syringe to generate reproducible drops they could deposit a drop, allow it to evaporate and then suck it back into the syringe after a defined time. This fluid could then be examined with a refractometer to measure the composition of ethanol using the known dependence of the refractive index for the mixture. Like Kita *et al.*[106] they faced issues making measurements at late times due to minimum fluid volume requirements for the refractometer. Direct measurement of the refractive index and composition of a fluid can also be measured by the degree of deflection of a laser passing through the sample.[108] The curved surface of a three-dimensional sessile drop would make it difficult to apply this method, however it could be useful when applied to a two-dimensional droplet enclosed between parallel non-wetting walls.[109]

A simpler way to view changes in drop composition is to look for phase separating systems and the subsequent segregation of immiscible components. Examples include a body of work from Tan *et al.*[40] on the evaporation of Ouzo droplets. Ouzo is a Greek spirit that is essentially a ternary system of water, ethanol and anise oil. When served as a drink it starts transparent but when water is added it turns "milky" from the solubility of the oil decreasing in the water rich phase. As a result this phase separation also occurs in evaporating Ouzo drops as the faster evaporation of the more volatile ethanol component makes the drop become increasingly water rich. Therefore oil microdroplets nucleate which can be viewed with ordinary optical or confocal microscopy. Eventually the oil microdroplets coalesce to form an oil ring around the contact line leading to a

non-spherical cap geometry. This rim does not prevent further evaporation of water eventually leading to a sessile drop of oil remaining on the substrate.

Li *et al.*[41] have used confocal microscopy to view the nucleation of dyed 1,2-hexanediol from aqueous drops. The surfactant concentration would build up at the contact line, despite mixing from the induced solutal Marangoni flows, and nucleate microdroplets. These could coalesce and grow to eventually cover the liquid-vapour interface and suppress further evaporation.

Segregation was also observed by Dietrich *et al.*[110] who investigated the dissolution of binary oil sessile droplets into a surrounding bath of water. Droplets could be excited at two wavelengths and with emmitted light dependent on the solvent polarity. Therefore in the cases where the mixture components were of different polarities, as when cyclohexane was mixed with a polar alcohol, then the relative concentrations of the components could be viewed. With this method the authors found that a hexanol-cyclohexane mixture became depleted in hexanol over time although the droplet composition stayed homogeneous; meanwhile for a pentanol-cyclohexane mixture the droplet rim became completely depleted of pentanol, fuelling solutal Marangoni flow.

More recently Sadafi *et al.*[111] looked into the demixing of a binary mixture of n-hexane and 2% involatile Diethylene Glycol Monoethyl Ether (DGME). Over time the concentration of DGME increased which, alongside evaporative cooling, resulted in the droplet composition passing through the coexistence curve of its phase diagram and microdroplets of DGME nucleating. These oil droplets could grow and form a ring, and eventually be deposited as a residue of macrodroplets once the solvent evaporated.

Other researchers have been able to give spatio-temporal resolution for the point at which the system passes through some other critical composition. Jalaal *et al.*[112] used Spectral Domain Optical Coherance Tomography to look at the evaporation of an aqueous solution of a thermoresponsive polymer on a heated

substrate. At elevated temperatures the polymer undergoes a reversible sol-gel transition. The drop was viewed from the side and the particles tracked; as the Brownian motion of the tracer particles stopped they could view where in the drop had gelled although the exact concentration for their sol-gel transition was temperature dependent.

Kim and Stone[42] added fluorescent tracer particles to drops of 30 wt% water and 70 wt% 1-Methyl 2-Pyrrolidinone drying at 10% *RH*. This organic component was shown to dissolve the suspended polystyrene particles if the local mass fraction was above 88 wt%. As a result they were able to view particles disappearing from the contact line region as the more volatile water component evaporated more quickly, making it increasingly organic rich. This inward moving front of critical concentration was then compared against a height averaged convection-diffusion model with pleasing agreement.

Whispering Gallery Mode methods such as employed by Hopkins and Reid[102] have been suggested as a way to use evanescent waves to investigate drop compositions non-invasively.[113] However while these techniques utilising resonances are very sensitive at measuring changes in refractive index and thus composition,[114,115] it is hard to imagine how to have cavities present in a sessile drops so the technique seems better suited to aerosol droplets.[102] There are also possibilities to use Raman Spectroscopy to measure droplet (sessile or otherwise) compositions, however the challenge in applying such methods to droplets is that the long acquisition times can limit temporal resolution.

There have also been attempts to measure the composition of the vapour surrounding a drop rather than the drop itself. Kelly-Zion *et al.*[18] passed the IR laser of a FT-IR spectrometer across the region above large 80 µL hexane or 3-methyl pentane drops, measuring the absorbance across horizontal planes at different heights above the substrate to generate a concentration profile assuming axisymmetry. As a result they could find that the vapour concentration profiles

were very different to a diffusion model, being quite flat but peaked above the apex due to the presence of convection in the vapour.

The lack of composition data limits the development of models of droplet evaporation. There is plentiful experimental data to model the evaporation rates in models of binary binary solvent mixtures[38,39] but collecting better composition data is important to thoroughly validate these models.

3.2 Plan

The reported experiments measuring the composition of sessile droplets have all involved µL drops rather than the pL volumes important in inkjet-printing contexts. We proposed to develop a non-invasive method of measuring the compositions of inkjet-printed droplets as existing invasive methods had minimum fluid volume requirements larger than inkjet-printed droplet sizes.[63,106,107]

Therefore we looked at the feasibility of measuring the intensity of reflected laser light from the solid-liquid interface, and using Fresnel's Equations to determine the refractive index and thus composition (see Figure 3.1). The composition measured would be an average over the area examined by the laser spot, either at the centre or edge of a droplet. It would be straightforward to apply such a method for any two component system in which the refractive index dependence was known; however multi-component systems or systems where the refractive index difference was especially low would be challenging. In addition the method would be limited in the choice of substrate as a high quality reflection is required meaning that rough or structured surfaces are not viable.

Commercial reflectometers use Fresnel's Equations to determine the wavelength dependent refractive index of substances for characterisation. Examples of the method in the literature include the work of Räty and Peiponen who measured the reflectance at a fluid-prism interface at UV-Vis wavelengths for industrially

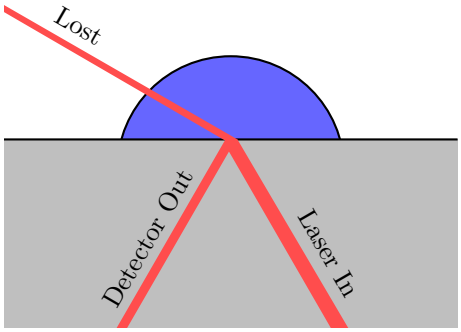

Figure 3.1: Cartoon of our non-invasive experiment where incident light hitting the solid-liquid interface of a sessile drop at an angle below the critical angle leads to reflection at the interface and a drop in laser intensity at the detector due to light being transmitted into the droplet.

relevant turbid fluids[116–118] and time-evolving systems due to a thin film of lignin growing on the prism[119] or the dissolution of a drug-loaded thin film.[120] In comparison our application of reflectometry uses smaller amount of fluid, in a droplet geometry, and which evolves on much faster timescales.

3.3 Theory

The refractive index, n, is defined as the ratio of the speed of light in a vacuum (in all other instances outside this section c will be used for the concentration),[121]

$$c = \frac{1}{\sqrt{\epsilon_0 \mu_0}}; \tag{3.1}$$

where ϵ_0 and μ_0 are the electric permittivity and magentic susceptibility of free space; to that in the optical medium, v,

$$n = \frac{c}{v}. \tag{3.2}$$

Electromagnetic radiation can be described by orthogonally propagating electric, $\mathbf{E}$, and magnetic, $\mathbf{B}$, fields while each $\mathbf{E}$ or $\mathbf{B}$ field can be described as the superposition of two orthogonal polarisations, in which the plane of propagation

is unchanged with time.

These wave properties can be used (see Appendix A) to derive the Law of Reflection for the angles of incidence and reflection, θ_i and θ_r,

$$\theta_i = \theta_r \tag{3.3}$$

and Snell's Law for the angle of transmission, θ_t,

$$n_i \sin\theta_i = n_t \sin\theta_t \tag{3.4}$$

where the subscripts i, r and t refer to the incident, reflected and transmitted light waves as in Figure 3.2, which depicts the direction of the different components of the electric field and directional wavevectors when light is incident at an interface.

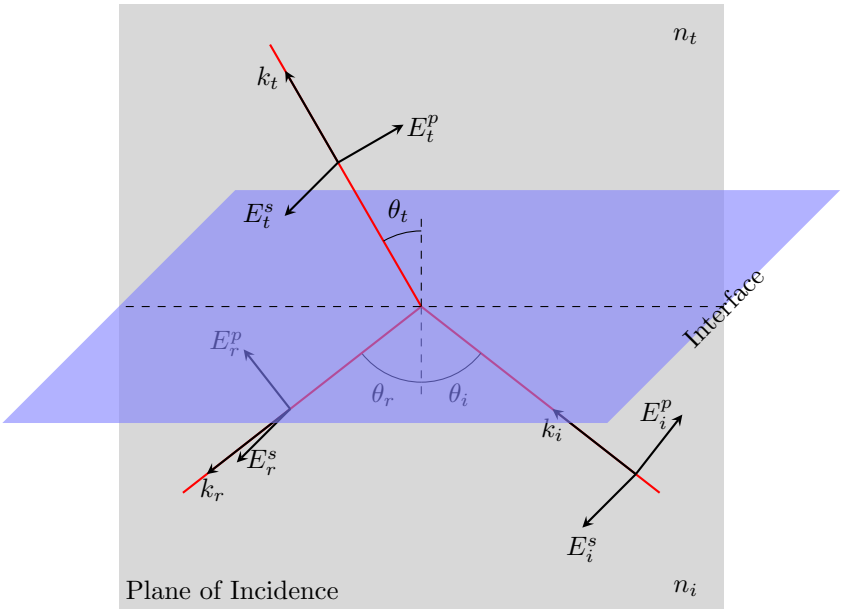

Figure 3.2: Directions of **E** field components of s- and p- polarised laser light where the light is incident (i) on the interface from below and is reflected (r) and transmitted (t) where the refractive indices $n_t > n_i = n_r$.

3.3.1 Fresnel Coefficients

Of great importance here are the Fresnel Coefficients (full derivations can be found in Appendix A). The convention of s- and p- polarised light will be used where 's' is for **E** fields perpendicular ('senkrecht' in German) to the plane of incidence while 'p' is parallel (still 'parallel' in German) to the plane of incidence.

For s-polarised light the Fresnel amplitude reflection and transmission coefficients are

$$r_s = \frac{n_i \cos\theta_i - n_t \cos\theta_t}{n_i \cos\theta_i + n_t \cos\theta_t} \tag{3.5}$$

$$t_s = \frac{2n_i \cos\theta_i}{n_i \cos\theta_i + n_t \cos\theta_t}. \tag{3.6}$$

While for p-polarised light the amplitude reflection and transmission coefficients are

$$r_p = \frac{n_t \cos\theta_i - n_i \cos\theta_t}{n_t \cos\theta_i + n_i \cos\theta_t} \tag{3.7}$$

$$t_p = \frac{2n_i \cos\theta_i}{n_t \cos\theta_i + n_i \cos\theta_t}. \tag{3.8}$$

3.3.2 Reflectance

If we consider a circular beam of light incident on a surface with some power per unit area then we can introduce the reflectance, R_{light}, as the ratio of reflected power to incident power (Appendix A). Similarly the transmittance, T_{light}, is defined as the ratio of the transmitted power to incident power so

$$R_{\text{light}} + T_{\text{light}} = 1. \tag{3.9}$$

The light can be reduced to two polarisations parallel and perpendicular to the plane of incidence giving component forms of the reflectance; R_s and R_p; in terms of the Fresnel amplitude coefficients

$$R_p = r_p^2 \tag{3.10}$$

$$R_s = r_s^2 \tag{3.11}$$

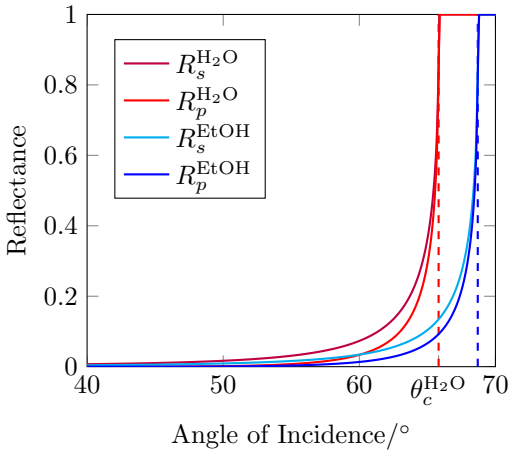

Figure 3.3: Angular dependence of Reflectance for s- and p- polarised light at an interface as a function of the angle of incidence where $n_i = 1.461$ and n_t is 1.333 for water or 1.3614 for ethanol. Dotted lines are for the critical angles for water ($\theta_c^{H_2O}$ red) and ethanol (θ_c^{EtOH} blue).

although $T_s \neq t_s^2$, $T_p \neq t_p^2$ because the relationship between power and field strength depends on the refractive index of the medium (see Appendix A).

Figure 3.3 displays the dependence of R_s and R_p on the angle of incidence for the interface going from silica to water or ethanol. If the angle of incidence is low, then very little of the light's intensity is reflected. However if $n_t < n_i$ there exists some critical angle θ_c, as the angle of incidence approaches the critical angle the reflectance rapidly approaches a value of 1. At the critical angle $R_{\text{light}} = 1$, there is total internal reflection meaning all the light is reflected at the interface. If no fluid is present then the fused silica is in contact with air, $n_t \approx 1$, so the critical angle is lowered to 47°, therefore at the angles of incidence used in these experiments (about 67°) there is total internal reflection before and after a droplet is printed over the laser spot.

Increasing the refractive index of the second medium shifts the critical angle to higher values with $\theta_c \to 90°$ as the difference $(n_i - n_t) \to 0$. Therefore experiments need to take place below the critical angle for water in order to be able to measure a signal for pure water. However to achieve the maximum sensitivity the

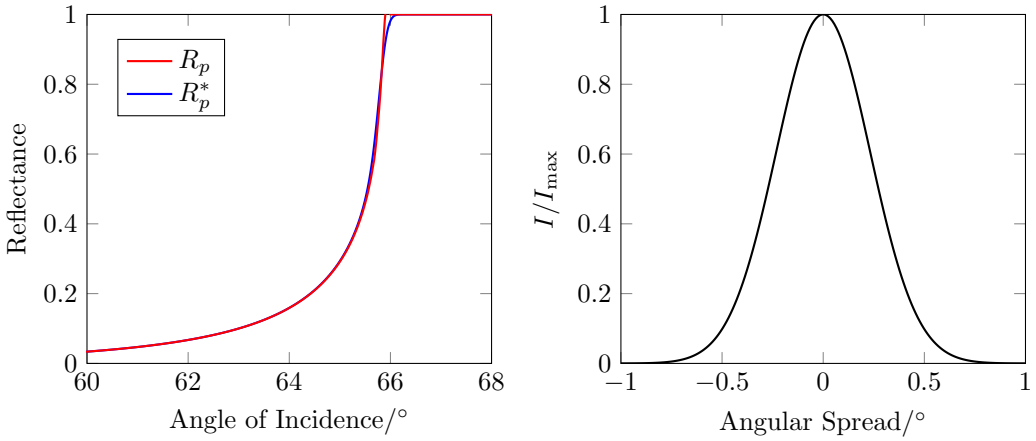

Figure 3.4: Angular dependence of reflectance of p-polarised light at an interface where $n_i = 1.461$ and $n_t = 1.333$. Before (red) and after (blue) convolution with angular intensity profile of incident laser described by Equation 3.13 in the right hand plot.

angle of incidence should be as close to the critical angle as possible to maximise the difference in reflectance between fluid components. Figure 3.3 shows that R_s is always greater than R_p at angles below the critical angle. Close to the critical angle of water $R_s^{H_2O} \approx R_p^{H_2O}$ while $R_p^{EtOH} < R_s^{EtOH}$. Therefore the difference in reflectance between ethanol and water, and so the experimental sensititivity, is greatest when using light polarised parallel to the plane of incidence.

The discussion of reflectance in Section 3.3.2 holds in the case of a non-diverging beam of light. However in reality even a laser will have a small angular divergence; when a beam of light hits an interface it effectively 'sees' a range of angles, given by the angular spread of the beam. In this experiment the range of angles is increased as the laser passes through a focusing lens. The left plot of Figure 3.4 shows the impact of this angular spread on the reflectance curve.

The angular range can be found using the properties of the lens, for a plano-convex lens with a focal length, $f = 50\,\text{mm}$, the numerical aperture (NA),

$$NA = \frac{d_{\text{laser}}}{2f} = 0.46° \tag{3.12}$$

where $d_{\text{laser}} = 0.81$ mm is the beam width of the laser. The decay of intensity

of the laser (I) as a function of angle (ϕ) is then described by the normalised gaussian

$$I(\phi) = \frac{4I_0}{\sqrt{\pi NA^2}} \exp\left(\frac{-2\phi^2}{NA^2}\right) \tag{3.13}$$

given in right plot of Figure 3.4. In order to account for this non-uniform intensity profile I take the convolution (represented by $\circledast$ in my notation) of the reflectance and the normalised angular intensity gaussian to get R_p^*, the measurable reflectance,

$$R_p^* = R_p \circledast \frac{4}{\sqrt{\pi NA^2}} \exp\left(\frac{-2\phi^2}{NA^2}\right). \tag{3.14}$$

where R_p has already been normalised.

At most angles of incidence the convolution only leads to very small deviations, however approaching the critical angle the convolution mixes the reflectance of angles below the critical angle with the reflectance from angles (above the critical angle) at which there is total internal reflection. Hence the reflectance below the critical angle increases while those above decrease. This smooths out the reflectance around the critical angle in Figure 3.4.

When the laser is focused onto the interface it will have a finite size. The beam waist (w) of a Gaussian beam after a lens is related to the wavelength of light, $\lambda = 633\,\text{nm}$, by

$$w = \frac{2\lambda}{\pi NA} \approx 50\,\mu\text{m}; \tag{3.15}$$

although the laser spot itself will not be a circle as the laser does not intersect orthogonally with the surface. For an angle of incidence of 66° the long axis of the oval laser spot is $w/\cos\theta_i \approx 120\,\mu\text{m}$.

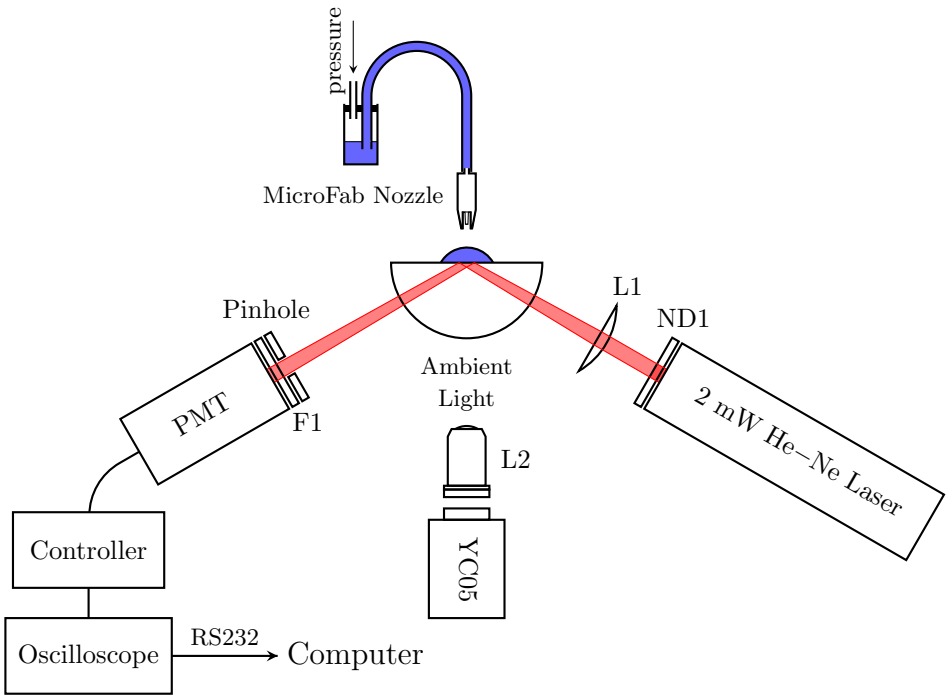

Figure 3.5: Schematic of experimental rig used for reflectometry experiments contained all the functional pieces of equipment.

3.4 Method Development

3.4.1 Equipment

The experimental rig was built from parts of a retired Beaglehole Ellipsometer, where its motorised arms were used to hold optics pieces at controlled angles and its electronics and photomultiplier tube repurposed. Upon the angle of incidence arm I mounted a 2.0 mW 633 nm He-Ne polarised (>500:1) laser manufactured by REO and purchased from Newport (R30989). This light was passed through a neutral density filter (ND1 in Figure 3.5), to reduce the laser intensity by a factor of 10 for safe working, and focused by a $f = 50\,\text{mm}$ plano-convex, uncoated, spherical lens (L1 in Figure 3.5) from Thorlabs, onto the hemisphere. A replacement lens of shorter focal length would produce a smaller laser spot but positioning it any closer to the hemisphere would lead to the arms knocking the objective lens (L2 in Figure 3.5) during alignment.

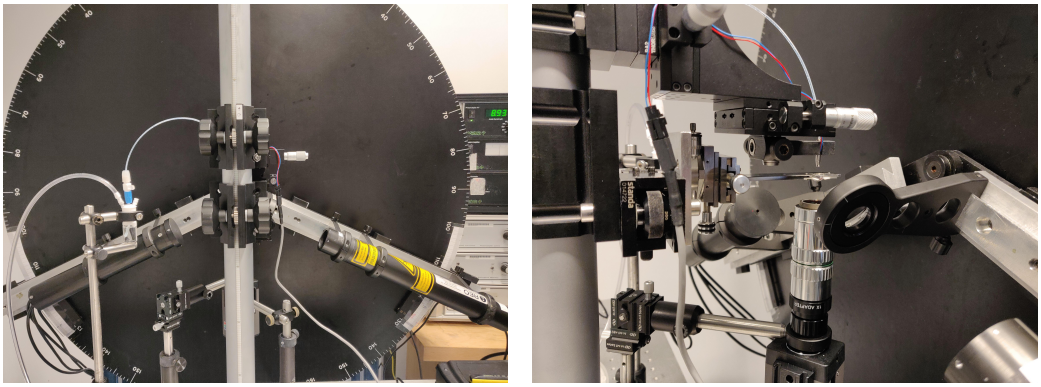

Figure 3.6: Pictures of reflectometry experimental rig "face on" and from the side to avoid the view being blocked by the support pillar.

On the detector arm of the equipment there was a photomultiplier tube (PMT) from the retired ellipsometer fitted with a 633 nm filter and covered with a pinhole to minimise stray reflections. When the detector was blocked the signal did not reach zero; this offset was taken into account in all my measurements of reflectance. The PMT was connected to an ellipsometer controller which displayed a current output and controlled the cathode voltage to accelerate electrons in the PMT. As a result of the ellipsometer circuitry's quirks the cathode voltage was set at less than 10 mA when the full laser intensity reached the PMT. In an ellipsometry experiment the angle of incidence or the plane of polarisation of a motorised polariser in front of the detector would be varied while the ellipsometer controller would use a feedback loop controlling the cathode voltage to maintain a steady current of 10 mA. Therefore in my experiments using this controller if the current was kept below this value the cathode voltage would be constant at a true maximum. If the signal was too high then the voltage would get capped at 10 mA so the signal would no longer be linear with light intensity, invalidating the analysis.

The current output of the signal was converted to a voltage within the controller and then taken to a LeCroy 9304A Quad 200 MHz cathode ray oscilloscope on the first channel. The voltage was negative, becoming more negative as more

light fell on the detector. The cathode voltage was viewed on a second channel to verify the linearity of the PMT's response. Of the available settings a "direct current" coupling of 50 MΩ impedance was used to avoid drawing a current from the controller. The oscilloscope was connected to a computer via a RS232 cable for remote readings via ScopeExplorer software. The output time varying voltage could then be exported as a text file and analysed using my own MATLAB scripts.

The oscilloscope could measure fast signals. However the PMT controller circuitry had an associated capacitance resulting in the first 80 ms or so of any measurement getting lost to the time response of the controller. Figure 3.7 shows an attempt to fit exponentials to the signal as the laser shutter was closed and opened. Such exponentials appear from solving the first order differential equation

$$\frac{dV^{\text{circuit}}}{dt} = \frac{1}{R_{\text{res}}C}(V_0^{\text{circuit}} - V^{\text{circuit}}(t)) \tag{3.16}$$

where the capacitor experiences an applied voltage V_0^{circuit} while the circuit has resistance R_{res} and capacitance C. In Figure 3.7, $R_{\text{res}}C \approx 16$ ms although this time constant was not consistent with fits of signals from droplets so I was unable to make use of this relation to predict V_0^{circuit} and hence the reflectance and composition at very early times. This is relevant because the refractive index would be constantly changing so a linear extrapolation would not be strictly correct.

3.4.2 Hemispheres

Reflectometry experiments used fused silica hemispheres ($n = 1.461$) with a diameter of 1 cm so the angle of incidence could be varied. The hemisphere would be aligned such that the laser path was perpendicular to the curved surface with the laser hitting the centre of the flat side. Printing onto glass coverslips would have severely limited the sensitivity as the incoming light would not be perpendicular to the lower surface so would be refracted; the refractive index of

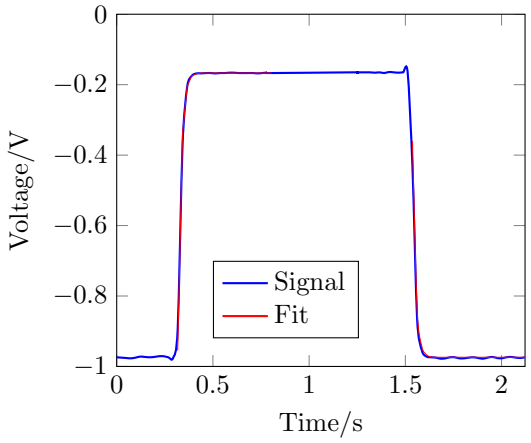

Figure 3.7: Time averaged signal (blue) from the oscilloscope with the laser on, off and then on again with each transition fitted by one of two exponentials (red). The first fit has the form $V_{\text{on}} + (V_{\text{off}} - V_{\text{on}})(1 - \exp((-t - t_1)/RC))$ while the second has the form $V_{\text{on}} + (V_{\text{off}} - V_{\text{on}}) \exp((-t - t_2)/RC)$. Where V_{on} and V_{on} are the circuit voltages where the laser is off or on.

glass is higher than air so incident light would be bent towards the normal to the interface. Putting numbers into Snell's Law

$$\theta_t = \arcsin\left(\frac{n_i \sin\theta_i}{n_t}\right) = \arcsin\left(\frac{1 \sin 90°}{1.5}\right) = 42°, \tag{3.17}$$

i.e. refraction at the lower side of the glass coverslip would lead to an angle of incidence at the upper side of interest far below the target (about 67°) even if the lower face angle of incidence was at its limit. A prism of the correct shape could have been used to avoid this issue; however a hemisphere offered greater flexibility in accessible angles of incidence in this development stage.

The silica hemispheres were silanised by the vapour deposition of HMDS as described in Section 2.2 to avoid low droplet contact angles. If contact angles were low the droplets could be approximated as a thin film of fluid where the liquid-vapour interface of the droplet would be approximately parallel to the substrate. Therefore any light transmitted into the droplet could be reflected back at the liquid-vapour interface and potentially reach the detector, complicating the analysis. While this secondary reflection interfered with measurements using

pure ethanol, as water has a higher surface tension then the HMDS-treatment prevented secondary reflections in most experiments. As the droplets are far below the capillary length they can be taken as spherical caps with some curvature. The focal length of a lens is equal to half the curvature

$$f = \frac{r_{\text{curv}}}{2} = \frac{1}{2}\frac{R^2 + h^2}{2h} \tag{3.18}$$

where R and h are droplet's radius and height. Therefore since R and h are on the order of $10^1 - 10^2$ µm the focal length is extremely short relative to the distance to the detector so any reflection from the liquid-vapour interface of the droplet will be extremely diffuse if the droplet is not thin.

3.4.3 Printing

Large drops of fluids of 3 µL (prepared as in Section 2.3) for calibration (sets of mixtures at fixed angle of incidence) were pipetted by hand. Otherwise droplets were dispensed from a 50 µm MicroFab nozzle as in other experiments (see Section 2.1). A different driving pulse of 3-25-9-25-3 ms was used throughout with maximum and minimum voltages of 60 V and −60 V, leading to larger droplets than in other experiments. The pulse frequency was either 100 or 500 Hz, therefore larger (nanolitre) droplets could be dispensed by printing known multiples of droplets at a high frequencies so that the deposition time was short relative to the time required for the droplet to fully evaporate. This approach was taken because (from Equation 3.15) the diameter of the focused laser spot was approximately 50 µm. As this was similar to the radius of a pL droplet on a silanised substrate this made positioning over the laser spot difficult, and limited the time over which I could take measurements. The hemispheres were silanised and not rough so droplets evaporated in a mixed mode close to constant contact angle evaporation; therefore even if a droplet's footprint covered the laser spot at the start of drying it could quickly retract leaving part of the laser spot exposed which artificially

increased the amount of light reaching the detector.

Figure 3.6 showed that there was no side-view camera to record droplet profiles during drying. In order to estimate the sizes of the droplets printed, the same nozzle and pulse driver were used with the same settings on the main printing rig. The droplets were also dispensed onto treated fused silica hemispheres to view the dynamic contact angles. A single water droplet dispensed at the above settings had a volume of $400 - 450$ pL, and on freshly prepared hemispheres had an initial contact angle of $76 - 77°$ (over 8 drops with the full range of droplet volumes examined), evaporating in a constant contact angle mode. However a disadvantage of using hemispheres in these experiments is that there is only one position which can be printed upon as if the hemisphere is moved to a new position then the laser is deflected. Therefore under the current protocol it is impossible to print on fresh surface. Replacing the hemisphere moves its position relative to the previous one requiring a recalibration and realignment process which necessarily involves depositing drops on the hemisphere to check the nozzle location. That being the case it was useful to view the contact angles of 'used' hemispheres to assess how the printing of droplets and wiping of the substrate with a methanol soaked lint-free tissue degraded the hydrophobicity of the treated surface. On a hemisphere which had been in use for two days and which had been prepared a week prior, the initial contact angles towards the edge of the hemisphere (which would still have been wetted by µL calibration drops) were in the range $52 - 58°$ while the droplets evaporated in a mixed mode. In contrast right at the centre of the hemispheres the contact angles were as low as $23 - 27°$ and droplets were pinned for the majority of their drying times suggesting that wiping removed the bulk of silanes on the surface.

The experiments took place under ambient lab conditions because the humidity cell's walls would deflect the laser. The temperature and relative humidity were measured over a number of days at different times of day. The temperature was

$T = 22 \pm 1°$, relative humidity was $RH = 33 \pm 5\%$ varying from $RH = 28\%$ around midday to $RH = 38\%$ in the evening, consistent across multiple days.

3.4.4 Viewing the Droplets and Alignment

An objective lens-tube lens combination was used to view the position of the droplet on the hemisphere. The magnified image was collected by a Computar YC-05 colour CCTV camera. Access to colour vision helped in finding the position of the laser spot and hence the centre of the hemisphere. The camera output was taken by VGA cable to a computer monitor for viewing, no bottom view videos were recorded although the display monitor itself was occasionally recorded with a personal mobile phone camera.

In order to correctly position the hemisphere an alignment protocol was required. The hemisphere was mounted on an arm with manual micrometer control of all three Cartesian directions where the arm could rotate through 360° along its axis. To mount it, the hemisphere was placed in a groove in the arm with its flat side facing down and then secured with pieces of plastic held down by screws. The laser and detector were switched on and made horizontal before being simultaneously lowered. When the laser was on and the shutter open, light would be totally internally reflected at the hemisphere's flat surface and fall on the pinhole cover of the detector. The hemisphere was then moved so the reflected beam passed through the pinhole. There was a difficulty in that the laser spot could fall anywhere on the detector cover, however for these two degrees of freedom there were three directions in which the hemisphere could be adjusted. As a result the only way to verify that the hemisphere was correctly positioned was to change the angle of incidence and check that the laser still passed through the pinhole.

In practice a perfect alignment was not achieved, the laser would only appear aligned over a small range of angles of incidence (approximately 5°). One problem with achieving perfect alignment was that the hemisphere was not flush with the

upper side of the mounting arm. Therefore while the arm could be checked with a spirit level and adjusted to be horizontal the hemisphere itself could deviate from being horizontal as it rested on two small pieces of plastic screwed into the arm. There were also deviations as a result of the mounting arms: a large screw needed to be tightened on each arm to fix them in position so they would not fall when unpowered overnight. These screws slightly deflected the arms so they were no longer parallel to the plane of the board so spacers were used to restore the arm deflection in the mornings. Despite these procedures, when the hemisphere was moved towards or away from the laser in the plane of incidence, the laser spot in the detector would often move with an additional component indicating that the laser, hemisphere and detector were not all in the same plane parallel to the board. As the experiment's sensitivity relied on the angle of incidence being close to the critical angle then careful calibration was particularly important.

Once the hemisphere was aligned, the centre of the hemisphere and hence the laser spot then needed to be located for the camera, following on from other experiments the laser spot would still be within the alignment camera's field of view; otherwise rather than search for the laser spot on the treated substrate it was more efficient to replace it with a hemisphere with a thick particle deposit. The laser light would scatter off the deposit so the camera's objective lens could be moved to focus on the laser spot which was obvious due to light scattering off particles. Without defects in the hemisphere or particles the interface was hard to notice and the laser near invisible.

Once I knew the laser spot was in the camera's field of view on a fresh hemisphere the nozzle could then be aligned by printing to generate small puddles. The puddles would expand and once they came into view then the direction of the nozzle relative to the centre of the hemisphere could be determined.

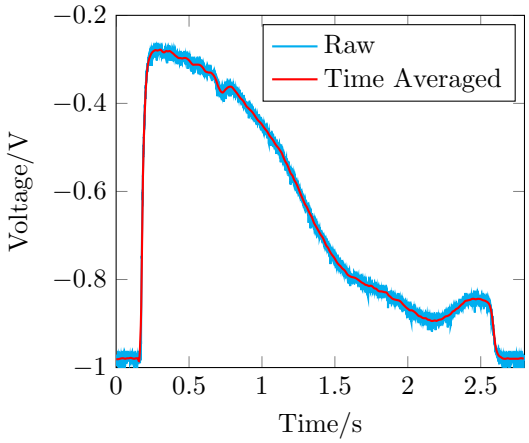

Figure 3.8: Raw signal (cyan) collected from the PMT from printing a single ~ 400 pL 40 wt% ethanol droplet overlayed with time averaged signal (red) to demonstrate noise reduction.

3.4.5 Analysis Tools

The oscilloscope sampled the voltage at sub-millisecond intervals, this combined with the feedback loop of the cathode voltage meant that raw signals could be noisy. To reduce this noise the signal was be binned in time and the mean voltage taken within each bin. While the bin was not too large this would preserve features of the signal hidden by noise and reduce the number of data points in a signal, speeding up further analysis. A full window of the oscilloscope contained an excessive 50,000 points with a fixed frequency depending on the time-base. Therefore all plots except Figure 3.8 will show time-averaged signals or analysis of averaged signals.

Appendix F contains the MATLAB code used to analyse the signals collected. As multiple droplets could be printed within the same signal, the time-averaged signals were cut into multiple sections. In each block the gradient was determined in order to find when the droplet was deposited from the time of maximum increase in signal. The angle of incidence and voltages measured when the shutters were open or closed then needed to be separately inputted. Thus the output reflectance,

R_{exp}, could be determined by the simple ratio of voltages

$$R_{exp} = \frac{V_{exp} - V_{off}}{V_{on} - V_{off}}. \tag{3.19}$$

Given the dependence of refractive index on ethanol composition in Figure 3.9 and Equation 3.14 a set of predicted reflectances for a range of ethanol compositions (below the maximum of refractive index at 80 wt%, see Figure 3.9) could be generated. Approaching the maximum dn/dc decreased so the technique would lose sensitivity to changes in composition. Experimental reflectances were then matched to these predicted reflectances to determine the composition over time.

3.5 Calibration

Before experiments with binary solvent mixtures could be explored, we needed to verify that Fresnel's Equations could be applied for pure fluids. I found it was most time efficient to deposit µL drops and avoid nozzle alignment.

3.5.1 Vary Angle - Pure Fluids

Figure 3.10 shows that the amount of light reflected at the solid-liquid interface for water drops did vary with θ_i. A similar change for ethanol was observed at

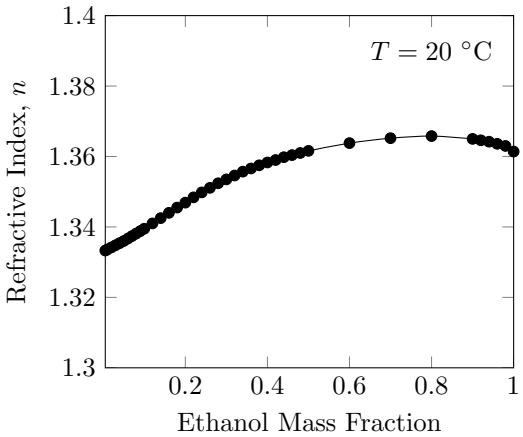

Figure 3.9: Refractive indices of ethanol-water mixtures at a wavelength of 589 nm, data from Ref. 91

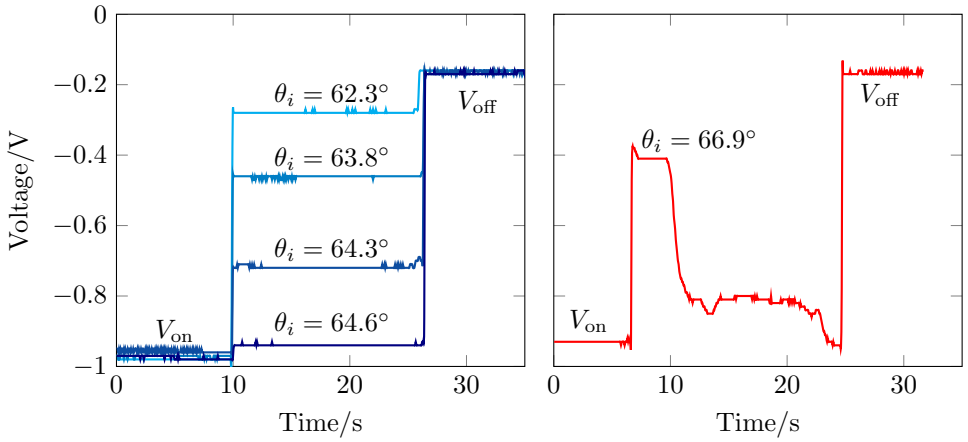

Figure 3.10: Time-averaged signals for water drops (left) at different measured angles of incidence and for an ethanol drop (right). Flat sections are labelled in the plots to distinguish between the on-off baselines and the signal when there was an ethanol or water droplet with angle of incidence given by θ_i

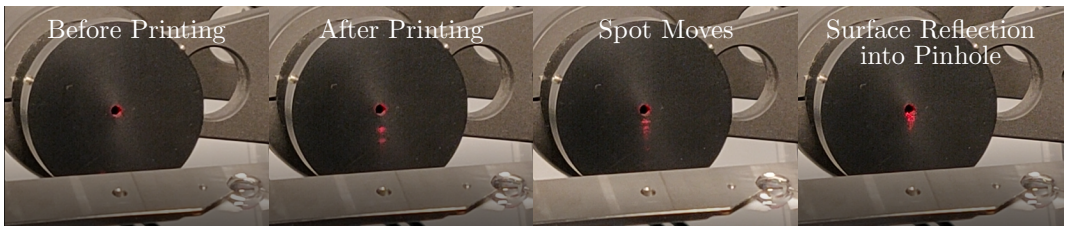

Figure 3.11: Movement of reflected light from the liquid-vapour interface during the evaporation of thin ethanol droplets. The light originally passes through the pinhole, when a droplet is printed more diffuse light reflected from the droplet's liquid-vapour interface lands on the cover, but moves to partially pass through the pinhole at late times leading to unusable signal.

larger angles of incidence, however these signals were not well behaved. Microlitre drops of ethanol spread across the surface of the hemisphere and up the sides of the arm so the system geometry was closer to that of a drop in a well than a spherical cap. As a result light was reflected from the near-flat top interface towards the detector which lead to more negative voltages being detected. This can be seen in Figure 3.11 where the laser spot originating from light transmitted into the droplet eventually made its way through the pinhole, leading to the artificially high reflectances in the right plot of Figure 3.10.

It is worth noting that in Figure 3.10, V_{on} was different between the experiments. While V_{off} did not change, V_{on} was a function of the cathode voltage. Therefore to try keep this variable consistent the cathode voltage was tuned infrequently, or if it was then a signal without any droplet was taken to quantify the change. It was also very important to keep the surface clean, when a drop was printed it would remove and then later redeposit any residue on the surface, however this meant that while the signals during a droplet's evaporation were good, care had to be taken with V_{on} which could be reduced by any residue and make any reflectances appear $1-2\%$ larger and thus make calibration of the angle more difficult.

The ellipsometer came fitted with 1° interval markers and vernier scales to measure angles. Angles of incidence were measured by reading off the angle at a marker and comparing that to the reading when the arms were horizontal at the start of alignment.

Figure 3.12 compares the experimental reflectances for pure water or ethanol as a function of angle of incidence with different markers for different sets of calibration attempts. In the lower plots the angles of incidence of the experimental data have been shifted by arbitrary amounts to give the best fit to the theoretical curves. A different shift is applied for each set of markers, the rationale for this adjustment is to take into account systematic errors resulting from imperfect alignment. That this approach appears successful (consistent shifts across a calibration set) suggests that any error in mounting the hemisphere is much more significant than errors introduced by small adjustments to the position of the hemisphere as the angle of incidence is varied during a set of experiments and that Fresnel's equations could be effectively applied.

In the subplots for water calibration the red circles and black squares corresponded to measurements using single inkjet-printed droplets. The magenta triangles for both water and ethanol were for inkjet-printed drops with volumes

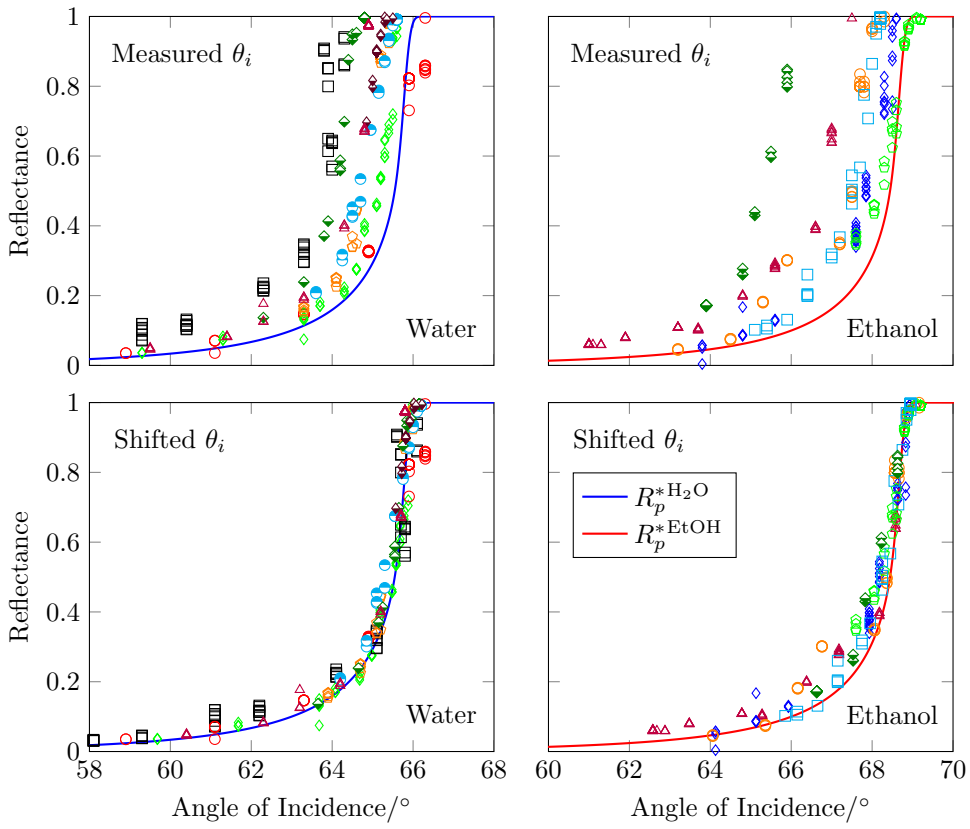

Figure 3.12: Experimental (markers) versus theoretical (curves) reflectances for water drops (left blue) or ethanol drops (right red) on a fused silica hemisphere $n_i = 1.461$. Sets of markers correspond to measurements from different days. In the lower plots arbitrary shifts in angle have been applied to the experimental data to show that they match the curvature of the theoretical curve.

of tens of nanolitres. As all the other data points were for microlitre drops this showed that the Fresnel equations could still be fitted to, as long as the laser spot was entirely within the drop's footprint. These measurements where the drops were generated by nozzle were my first. As such it is not clear whether the increased scatter is a result of having smaller droplets than I eventually studied, or more likely a lack of experience in alignment and taking measurements.

That the shape of the curve can be recovered indicates that the refractive indices inputted into the theory are close to those in reality. This is pleasing given that working so close to the critical angle, if the refractive indices of any of the materials were different then very different results could be obtained. As multiples

hemispheres were used during experiments it is possible that small differences in refractive indices could lead to some of the variation in angular shifts required for agreement with theory. This was considered as the refractive index used above is higher than is typically suggested by manufacturers.[122] If $n_i = 1.458$ (rather than $n_i = 1.461$) then the theoretical curves would be shifted approximately 0.7° to higher angles of incidence. As this would shift the curves away from the unshifted results it seems unlikely that hemisphere inconsistencies are the cause of the different shifts required instead of hemisphere positioning.

3.5.2 Vary Composition - Fixed Angle

Once the angular dependence of reflectance was determined the dependence on composition (from n_t) at a fixed angle could be verified. This approach was much closer to how an experiment would normally run except that rather than looking at time-resolved compositions, I would look at µL droplets of known composition. To look for a residue of ethanol we wanted greater sensitivity at low concentrations of ethanol so I chose an angle of incidence close to the critical angle for water. By the same logic if instead there was some interesting phase transition at 10 wt% ethanol a greater sensitivity at that composition could be obtained by working at the critical angle for that mixture. However this would come with a trade off of losing most of the sensitivity for lower mass fractions of ethanol. This can be observed in Figure 3.13 where in the right plot as the angle of incidence is increased the point at which the reflectance changes most quickly with ethanol mass fraction also shifts while the gradient rapidly decreases for lower mass fractions of ethanol.

Due to the divergence of the laser beam there was a distribution of angles hitting the interface which lead to $R_p^* < R_p^{\text{theory}}$ where R_p^* is the measured reflectance. Given the angles of incidence $n_i = 1.461$, $n_{\text{H}_2\text{O}} = 1.333$, from Snell's Law the critical angle for water is $\theta_c^{\text{H}_20} = 65.84$. At this angle the reflectance

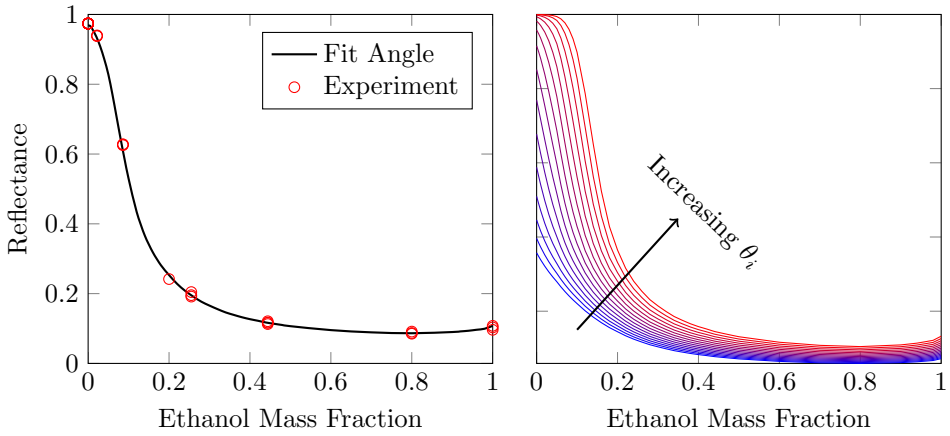

Figure 3.13: Experimental reflectances (red circles) versus calculated R_p^* (black line) where $n_i = 1.461$ and $\theta_i = 66.16°$ is varied to give the best fit to the data. For this n_i, the right plot demonstrates how R_p^* changes when going through the critical angle with the set of theoretical curves for $65.2° \leq \theta_i \leq 66.6°$ at $0.1°$ intervals with lower angles of incidence appearing blue, transitioning to red at $\theta_i = 66.6°$.

$R_p^*(\theta \equiv \theta_c^{H_20}) = 0.78$ rather than $R_p(\theta \equiv \theta_c^{H_20}) = 1$. Therefore angles of incidence above the critical angle of water were chosen to maximise the difference in signal between pure ethanol and water while still keeping the reflectance for water below a value of 1. This effectively traded off sensitivity at the lowest ethanol mass fractions for better sensitivity in general.

3.5.3 Uncertainties

The dependence of reflectance on the angle of incidence in Figure 3.12 demonstrated that my measured angles of incidence needed a shift to allow comparison with theory. This was problematic as the required shift in the analysis was not consistent between sets. The right hand plot in Figure 3.13 demonstrates that small changes to the angle of incidence could change the reflectance curves used to extract composition data where these small changes are of the same order of magnitude as the analytical shifts of the angle of incidence.

Therefore in experiments I took the approach of not paying much attention to the measured angles of incidence and instead calculating them by fitting to

calibration curves as in Figure 3.13.

An uncertainty in the angle of incidence could then be estimated from how well the calibration fitted the theory. This estimation could be further refined by taking calibration measurements in between inkjet printing ethanol-water mixtures to judge whether the effective angle of incidence shifted over time. However care had to be taken when using tissues to dry and wipe the surface after pipetting µL drops so as to not press on the hemisphere and change the angle of incidence. This was actually the main source of uncertainties in the angle of incidence.

These uncertainties in the angle of incidence could then be propagated[83] through my calculations to give an uncertainty in the ethanol mass fraction.

$$\delta(R_p^*(\theta_i)) \approx \frac{1}{2}\left(R_p^*(\theta_i + \delta\theta_i) - R_p^*(\theta_i - \delta\theta_i)\right) \tag{3.20}$$

i.e. the uncertainty in the reflectance (as a function of the refractive index and hence composition) from the uncertainty in the angle was the mean of the change in reflectance if the angle of incidence was higher or lower than desired.

There was then an additional uncertainty arising from the noise in the measurements. This was quantified by taking the standard error of voltage measurements in each time-averaging bin. Every bin would contain N voltage elements (this was chosen to be an odd number) separated by the time difference dt determined by the oscilloscope timebase

$$V_{\text{circuit}}(t) = \frac{1}{N}\sum_{i=0}^{N-1} V_{\text{circuit}}\left(t - \frac{dt(N-1)}{2} + dt\ i\right) \tag{3.21}$$

$$\delta V_{\text{circuit}}(t) = \frac{1}{\sqrt{N}}\ SD_{V_{\text{circuit}}(t)} \tag{3.22}$$

where $SD_{V_{\text{circuit}}(t)}$ is the standard deviation of measurements over the time bin. Given Equation 3.19, this lead to an uncertainty in the experimental reflectances of

$$\delta R_{\text{exp}}(t) = R_{\text{exp}}(t)\sqrt{\frac{\delta V_{\text{exp}}(t)^2 + \delta V_{\text{off}}^2}{(V_{\text{exp}}(t) - V_{\text{off}})^2} + \frac{\delta V_{\text{on}}^2 + \delta V_{\text{off}}^2}{(V_{\text{on}} - V_{\text{off}})^2}} \tag{3.23}$$

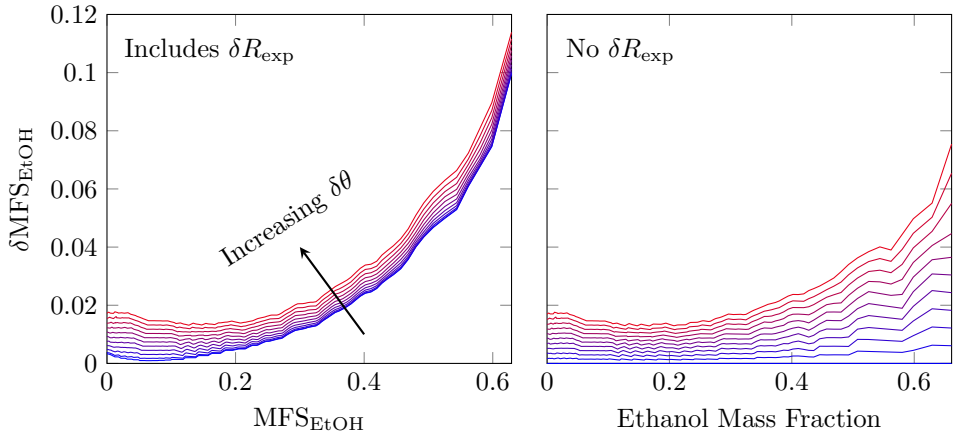

Figure 3.14: Uncertainty in Ethanol Mass Fraction as a function of Ethanol Mass Fraction for $\theta_i = 66.12°$ as the uncertainty in the angle of incidence is increased from 0 (blue) to 0.1° (red) in 0.01° increments with characteristic experimental uncertainty $\delta R_{\text{exp}} = 0.006$. In the right hand plot this noise contribution to the uncertainty from the signal has been removed.

The overall uncertainty in the reflectance was then

$$\delta R_p^* = \sqrt{\delta(R_p^*(\theta_i))^2 + \delta R_{\text{exp}}(t)^2} \tag{3.24}$$

For real measurements $\delta R_{\text{exp}}(t) < 0.01$ because in each time bin I would average over upwards of 20 data points. As a result at low ethanol mass fractions where the reflectance was approaching 1 the uncertainty was dominated by the uncertainity in the angle of incidence. However at high ethanol mass fractions, where the reflectance and change in reflectance with composition were lower, both uncertainties were important. This occurred because at higher concentrations the smaller changes in refractive index meant that changing the angle of incidence had little impact. However as the overall reflectances were lower due to the higher refractive indices then the uncertainty from the noise, whose magnitude was fairly constant over the composition range, became relevant.

In my analysis of the results I have been conservative in my estimating the quality of the calibration. When microlitre calibration droplets showed changes I took a mean of the different fitted θ_i for a set of experiments such that $0.05 \leq$

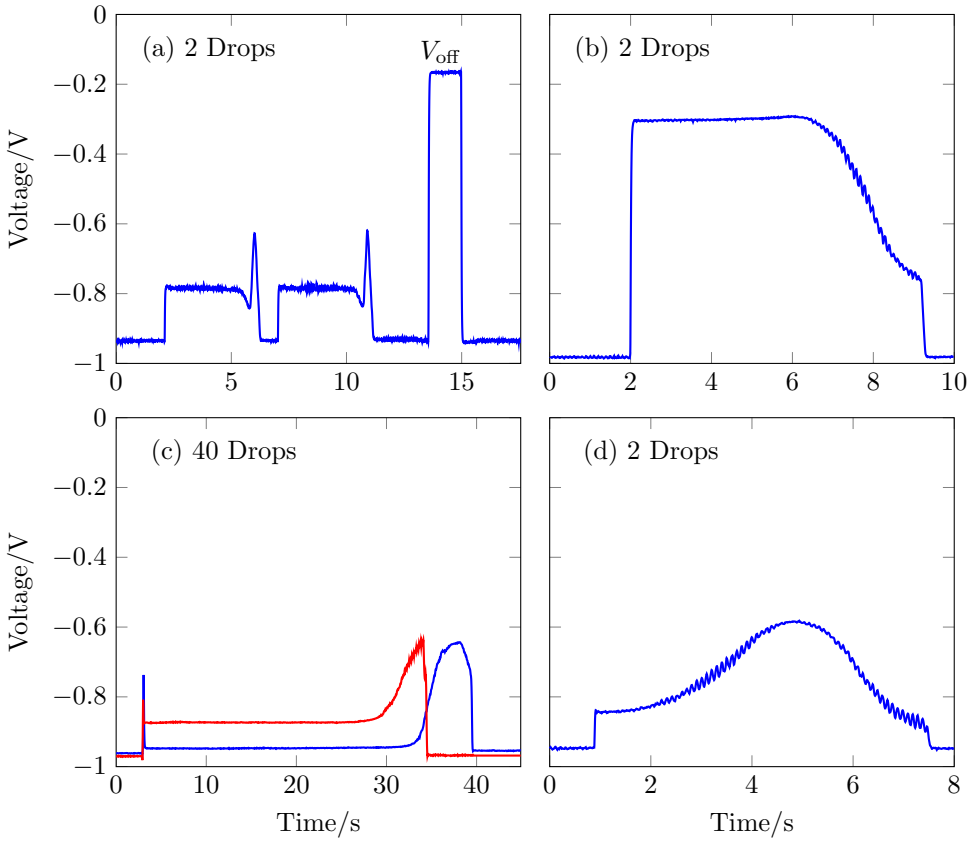

Figure 3.15: Time-averaged PMT voltages over time for a selection of inkjet-printed water droplets of different volumes and at different angles of incidence to display unusual signal features.

$\delta\theta_i \leq 0.08°$. It is feasible to reduce this uncertainty with more regular calibration throughout a set of experiments and greater experience handling the hemisphere.

3.6 Results

The calibration curves in Figure 3.12 showed that results from large µL drops and inkjet-printed droplets of pure fluid could both be fitted by Fresnel's Equations. However inkjet-printed droplets would be much smaller, evaporating more quickly so the raw signals could change over the course of a few seconds. Figure 3.15 gives some examples of the raw signals from the PMT for such inkjet-printed water droplets where in addition to steady voltage readings, that could be used for calibration, there were additional features. Plot (a) shows two droplets with

volumes equivalent to '2 Drops' (recall the printing frequency was > 100 Hz so time between pulses at the nozzle was much shorter than the drying time) where the laser shutter was also closed for a few seconds. The two droplets had very similar profiles, starting with a steady value as predicted. However this was followed by the measured voltage becoming more negative and then a sharp 'peak', or decrease in voltage. By watching how the droplets dried with the alignment camera I learned that such peaks indicate that the droplet fully dried while over the laser spot. In the other three plots the droplet moved off the laser spot as it evaporated and the contact line depinned. As a result plot (b) has a similar shape to (a) except it lacks the peak. Plots (c) and (d) give examples of where the measured voltage became less negative at later times, perhaps as a result of flattening of the drop leading to upper interface reflections to the detector. These features may have also been present in microlitre drop calibration experiments had those drops been allowed to fully evaporate. Plots (b) and (d) also show that there were some interference effects (can zoom-in on fringes in electronic version).

The causes of these anomalies are discussed later in Section 3.7.2. At this stage it is only important to consider that the signals were more complicated than predicted and that any region where such anomalies occurred were not included when converting voltages to reflectances to determine compositions. In mixtures the cut-off was less clear as there would naturally be changes in reflectance as the composition of a droplet changed. Given the dependence on refractive index on ethanol composition and that evaporation would drive the droplets to become more water rich over time the refractive index would decrease over time. A decrease in refractive index would lead to larger reflactances and so more negative voltages. As a result the anomaly shapes in Figure 3.15(c) and (d) (as well as the peak in (a)) would lead to unphysical increases in the amount of ethanol in the drop if they had been taken at face value while a shape like (b) was possible if unlikely.

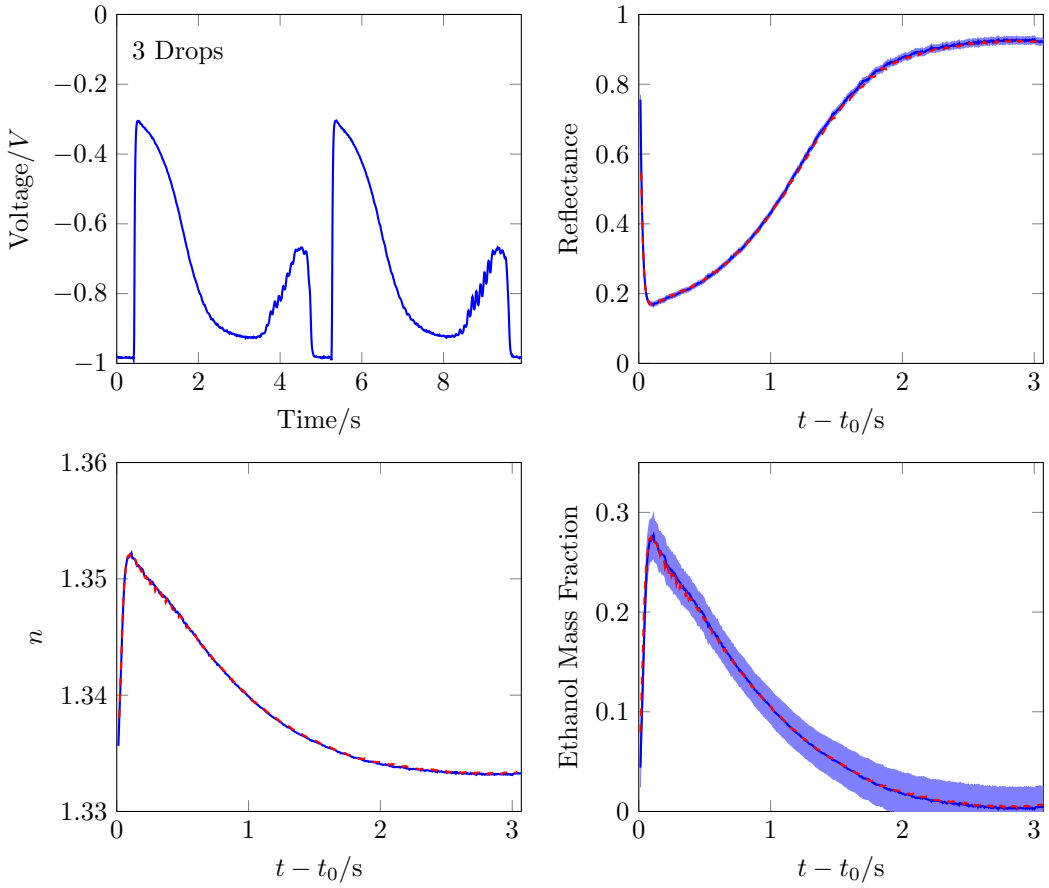

Figure 3.16: PMT voltages over time for droplets with volumes equivalent to 3 Drops of nominally 35 wt% ethanol with conversion to reflectance (with uncertainties from noise), refractive index and ethanol mass fraction (noise and angle uncertainties).

In the figures to come in this chapter the ethanol mass fractions will be presented using the following convention:

- A black line if there was a delay before printing,
- the next droplet is displayed with a blue line,
- further droplets are displayed with purple-coloured lines, becoming increasingly red with subsequent droplets,
- uncertainties are represented with a light blue area above and below the curves. They are only shown for one set per figure to reduce clutter,
- 'X Drops' refers to the number pulses per print action. Therefore the volume

of a droplet investigated is $V \approx 400 \cdot X$ pL.

Figure 3.16 shows the raw signal for two droplets of intermediate ethanol concentration, each generated by three pulses, printed one after the other. The jumps to less negative voltages were taken as the time at which a drop impacted on the surface, t_0, accounting for this offset droplets from the same oscilloscope trace could be compared directly. The reflectances were calculated, converted into refractive indices and thus into ethanol compositions. The uncertainties in the reflectance and ethanol composition were calculated as described in Section 3.5.3. When the limits of the time axis of the figures are reduced it becomes clear that the jumps in voltage are not vertical, information is lost at early times due to the response time of the PMT (Section 3.4.1).

3.6.1 High Ethanol Concentrations

It has been mentioned previously that it was frequently difficult to obtain nice signals for low surface tension fluids due to light transmitted into the drop getting reflected back at the droplet's liquid-vapour interface. Some good results were obtained on fresher low-energy substrates which were still reasonably hydrophobic, however the associated uncertainties were large.

Figure 3.17 shows some results for 80 wt% droplets of different sizes. While the measured composition traces are reproducible the shallow gradient of dn/dc close to the maximum at an ethanol concentration of 80 wt% means that the uncertainties (see blue area in bottom right plot) are large. In the second row, the first droplet (black) was waiting in the nozzle for significantly longer so lost more volatile ethanol while the fluid was waiting to be printed; a higher water content would have also increased the surface tension and so contact angle, further extending the drying time and so changing the overall shape of the composition curve. At 80 wt% ethanol the system starts at the maximum in the refractive index or the minimum in reflectance as a function of ethanol concentration. As a

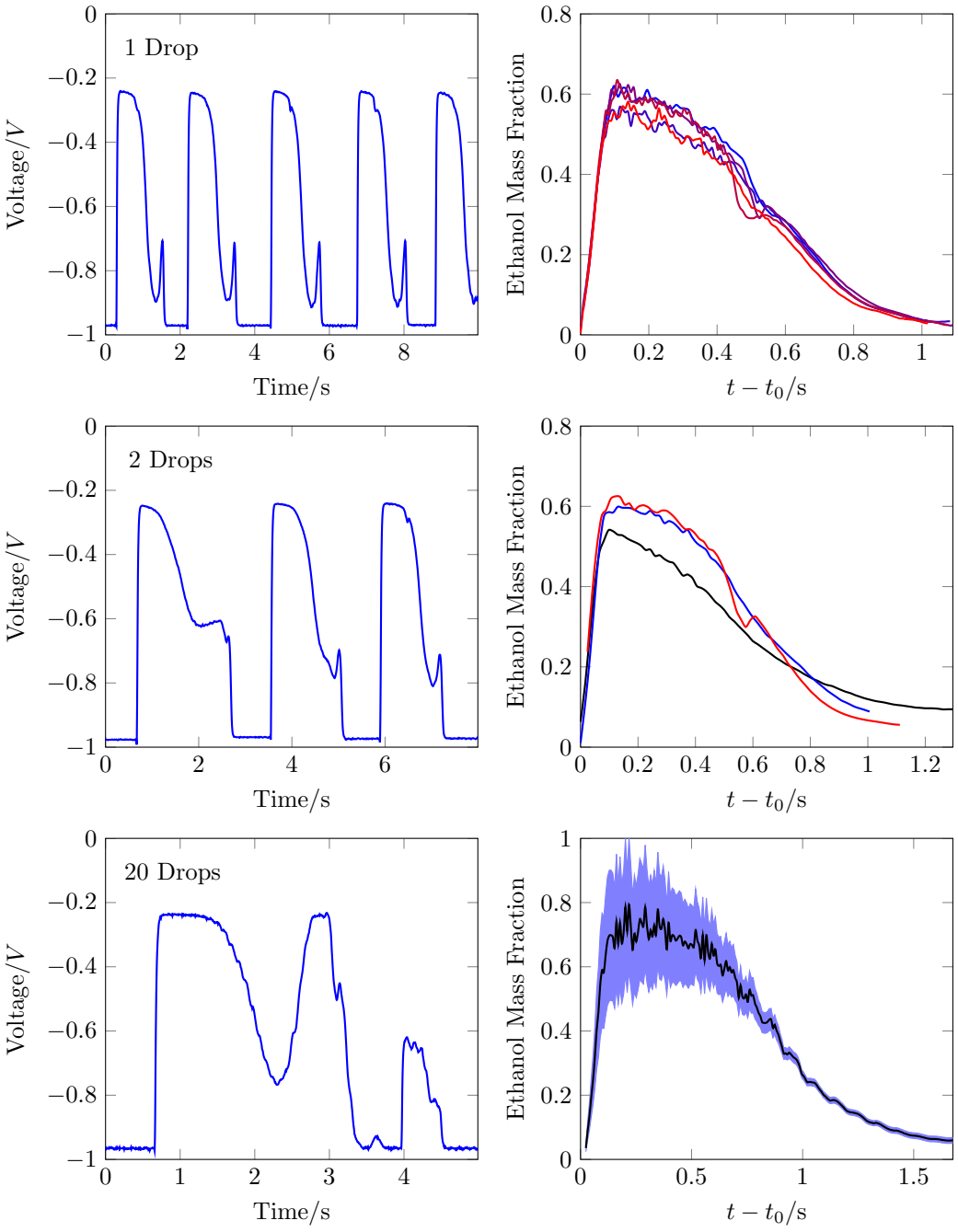

Figure 3.17: Raw signals and time evolution of ethanol mass fraction for nominally 80.4 wt% ethanol droplets of different sizes.

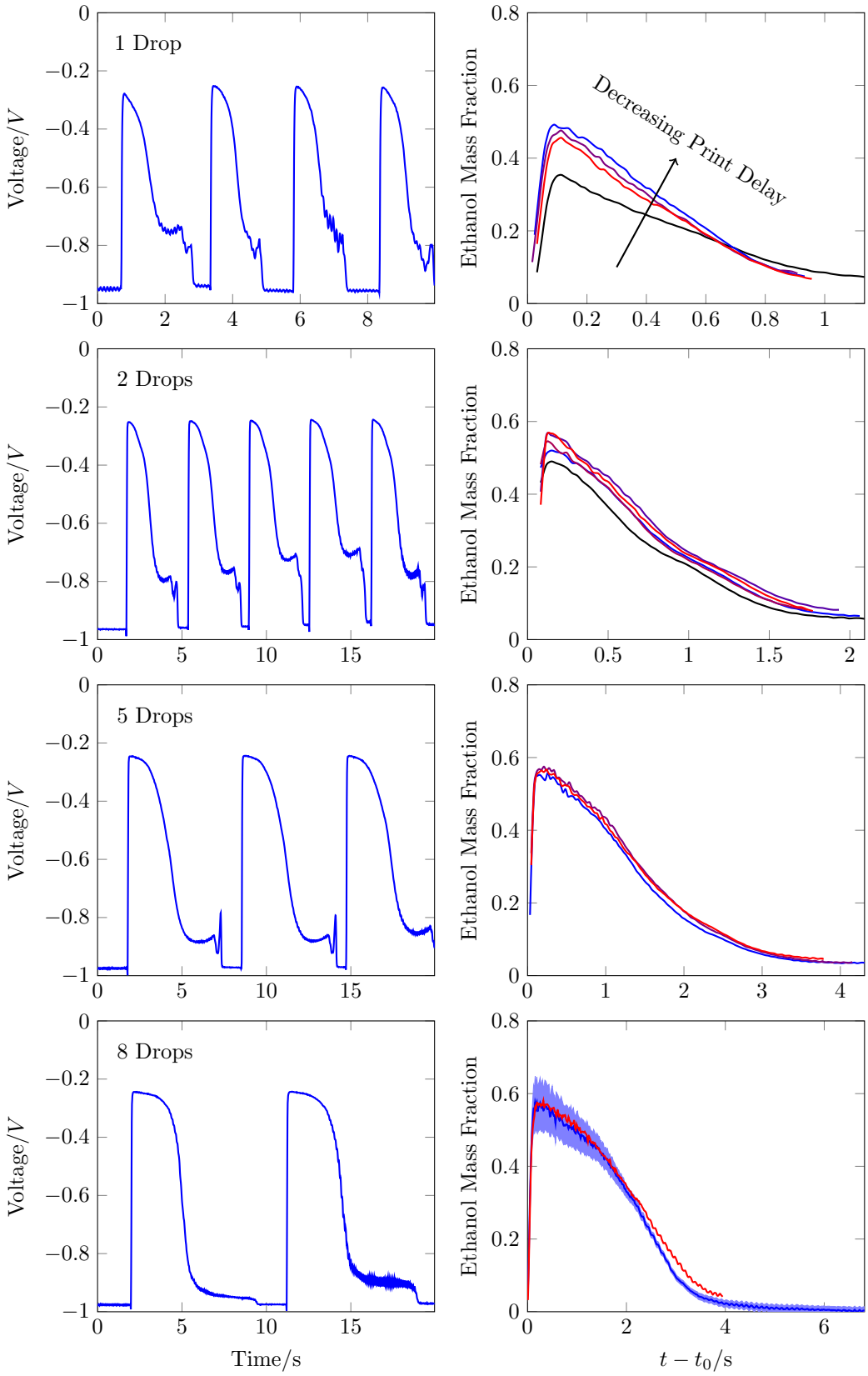

Figure 3.18: Raw signals and time evolution of ethanol mass fraction for nominally 65.4 wt% ethanol droplets.

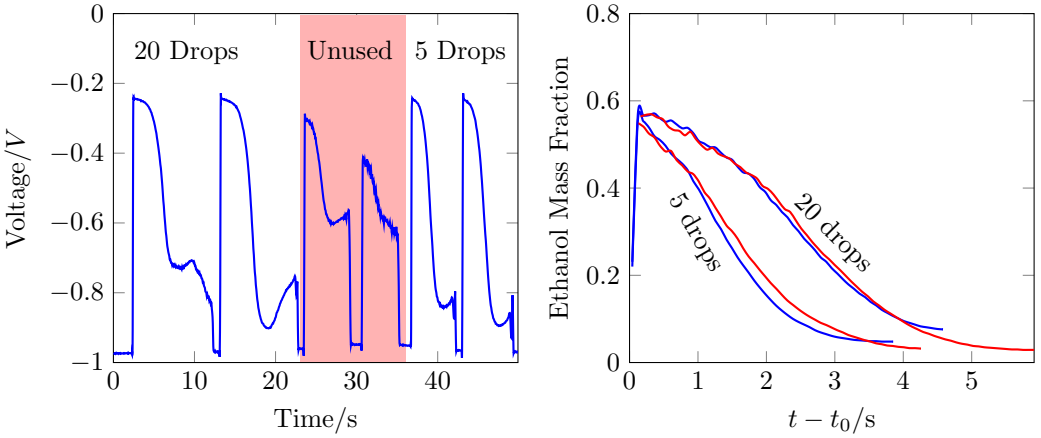

Figure 3.19: Raw signals and time evolution of ethanol mass fraction for larger nominally 65.4 wt% ethanol droplets. The "Unused" droplets were partially off the laser spot.

result the PMT signals appear very flat at early times as it takes a much larger change in composition to provide the same change in reflectance/voltage as at lower ethanol concentrations.

Nominal ethanol concentrations of 65 wt% were much easier to print and had smaller uncertainties as the concentration away from the maximum in the mixture's refractive index. Some results are given above in Figure 3.18 for droplets made from 1-8 pulses while larger droplets are presented in Figure 3.19. Compared to the 80 wt% droplets the PMT signals are less rounded at early times. Even as the droplets get larger the mass fraction curves appear similar, this is not surprising given that the evaporation of droplets is often described in non-dimensional terms and then scaled appropriately.

As the ethanol fraction is still large, the droplets evaporate quickly and small differences in the initial conditions have a greater impact. In the top left plot of Figure 3.18 the lengths of the time periods between droplets approximately doubled between the first and second to the third and forth. This resulted in measurable differences in the composition evolution although such changes are not larger than the uncertainties presented in the bottom right plot.

3.6.2 Intermediate Ethanol Concentrations

Of particular interest were droplets of intermediate ethanol concentrations which were well studied on the main printing rig (see Chapter 4) and for which well-defined solutal Marangoni flows could be observed. Two specific concentrations examined were 50 wt% ethanol mixtures commonly found in the literature and 35 wt% (30%v) ethanol mixtures which were found to have the fastest Marangoni flow speeds in similar inkjet-printed droplets.[88]

Figure 3.20 below presents some results for 50 wt% ethanol droplets. In the first row the first droplet printed reached lower reflectances than the later droplets. It is unclear why the signal is different as while it is possible to decrease the print delay, by printing onto a removable barrier between the nozzle and hemisphere between measurements, that approach was not attempted for these fast-drying droplets. Going down the rows as the droplet size increases it is very clear that the initial ethanol concentration also increases, this is a result of the overall concentration of larger droplets being less susceptible to evaporation at the nozzle.

Figure 3.21 below presents some results for 30%v ethanol droplets of different sizes. In the first row the analysis was extended into the region where the signal is unreliable due to anomalies which leads to slight increases in ethanol concentration at late times. This is unlikely as the only sources of ethanol that could condense on the droplet are the nozzle and remainders from previous droplets (or the droplet itself). As the y-axis limits are reduced compared to the high-ethanol figures, periodic fluctuations in some of the signals can be seen. In between experiments it was sometimes noted that the laser spot appeared to be moving slightly in the view of the alignment camera. These oscillations are likely a result of low frequency vibrations. While the hemisphere itself was on an optical table the large board supporting the laser and PMT was on a heavy steel frame directly on the floor so it would not isolate the equipment from local vibrations.

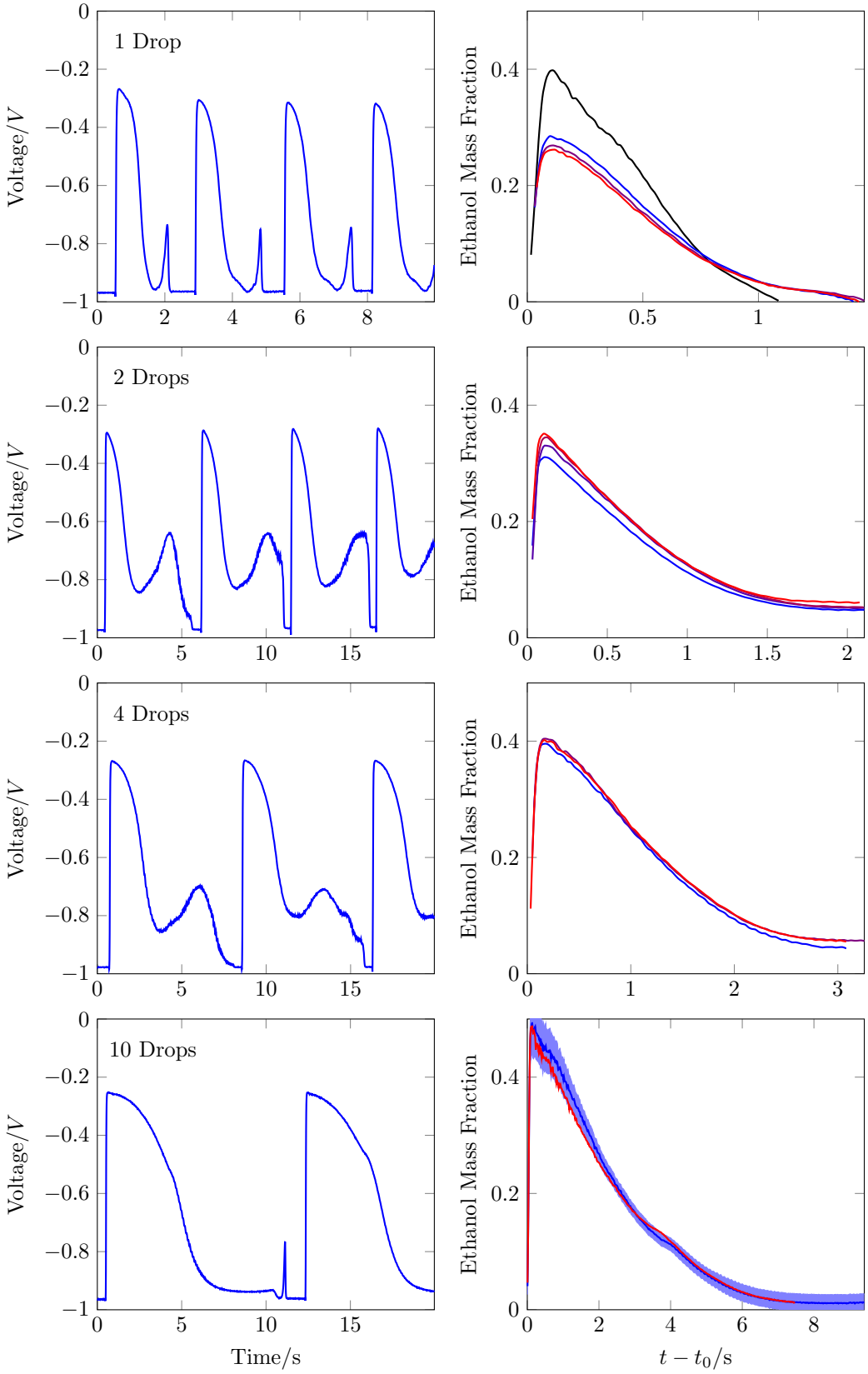

Figure 3.20: Raw signals and time evolution of ethanol mass fraction for nominally 50.2 wt% ethanol droplets.

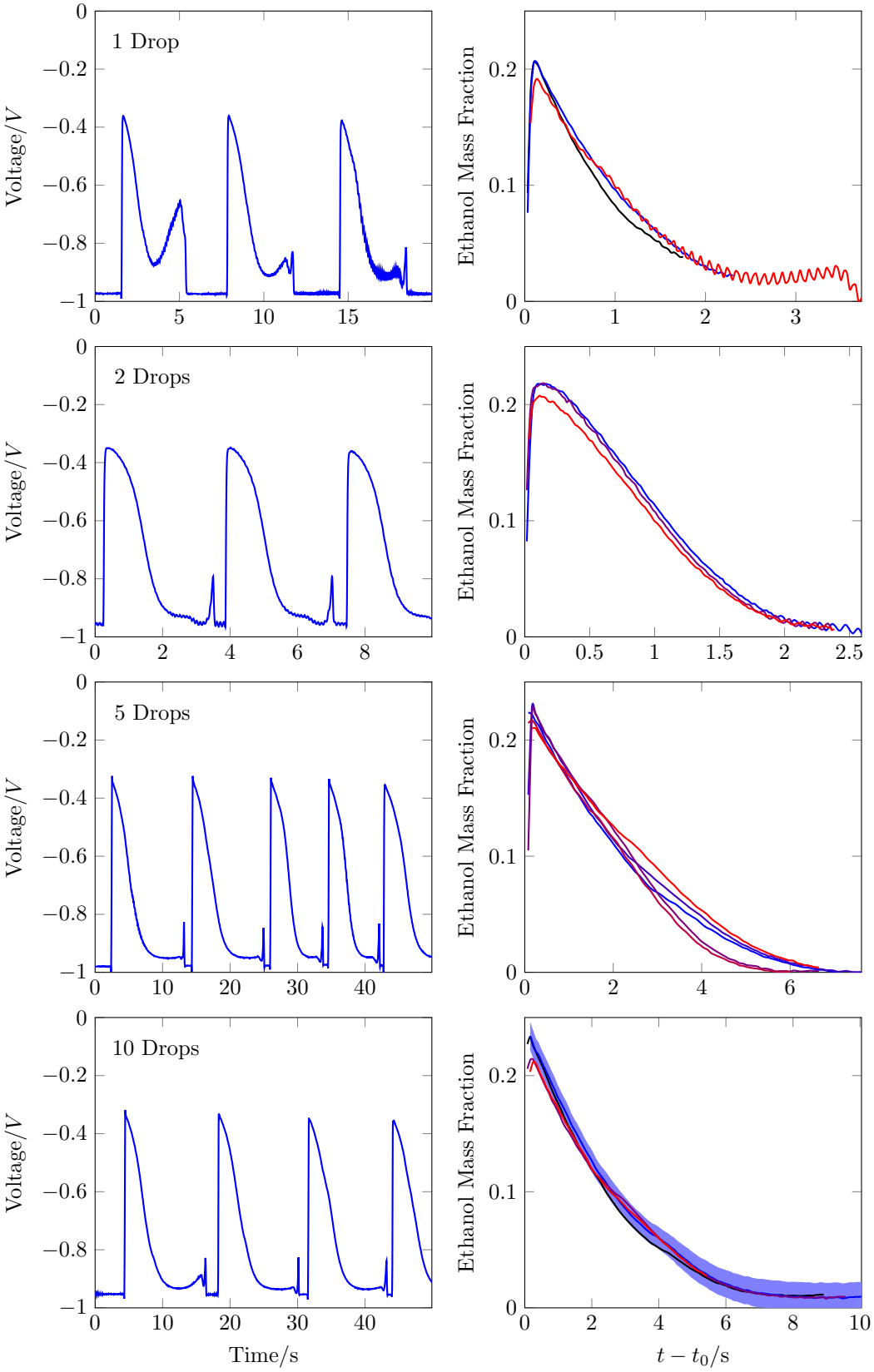

Figure 3.21: Raw signals and time evolution of ethanol mass fraction for nominally 25.5 wt% (30%v) ethanol droplets.

3.6.3 Low Ethanol Concentrations

Low ethanol concentrations were also investigated using this experimental setup. Figure 3.22 shows results for 8 wt% ethanol while Figure 3.23 shows results for 2 wt%. For these mixtures the refractive index change with ethanol mass fraction is approximately linear. As a result there are no 'humps' in the raw signal at early times as were found at intermediate and high ethanol concentrations and the mass fractions curves closely follow the PMT outputs. The initial concentrations measured by our technique also show that larger droplets were much less susceptible to evaporation at the nozzle.

The low concentration in these experiments limited the possible total changes in refractive index, so that changes in reflectance were also small. Therefore for 2 wt% droplets I changed the voltage divisions on the PMT to zoom-in on the region where the signal appears. As a result when the anomalies towards the end of drying appeared and the recorded voltage from the PMT became less negative then the trace went out of the recording window of the oscilloscope. As the refractive index and so voltage changes are small the uncertainty arising from electrical noise becomes significant (see bottom left plot of Figure 3.23). Despite this the calculated compositions still are able to show the same trend of slowing change of ethanol mass fraction.

That I was able to measure such small changes in composition demonstrates that this experimental approach has a great deal of potential in being able to be applied to other chemical systems where refractive index changes are even smaller than those between ethanol and water.

3.7 Discussion

Using this technique the solid-liquid interface is investigated although how far into the droplet is actually probed is not well defined. It seems reasonable to

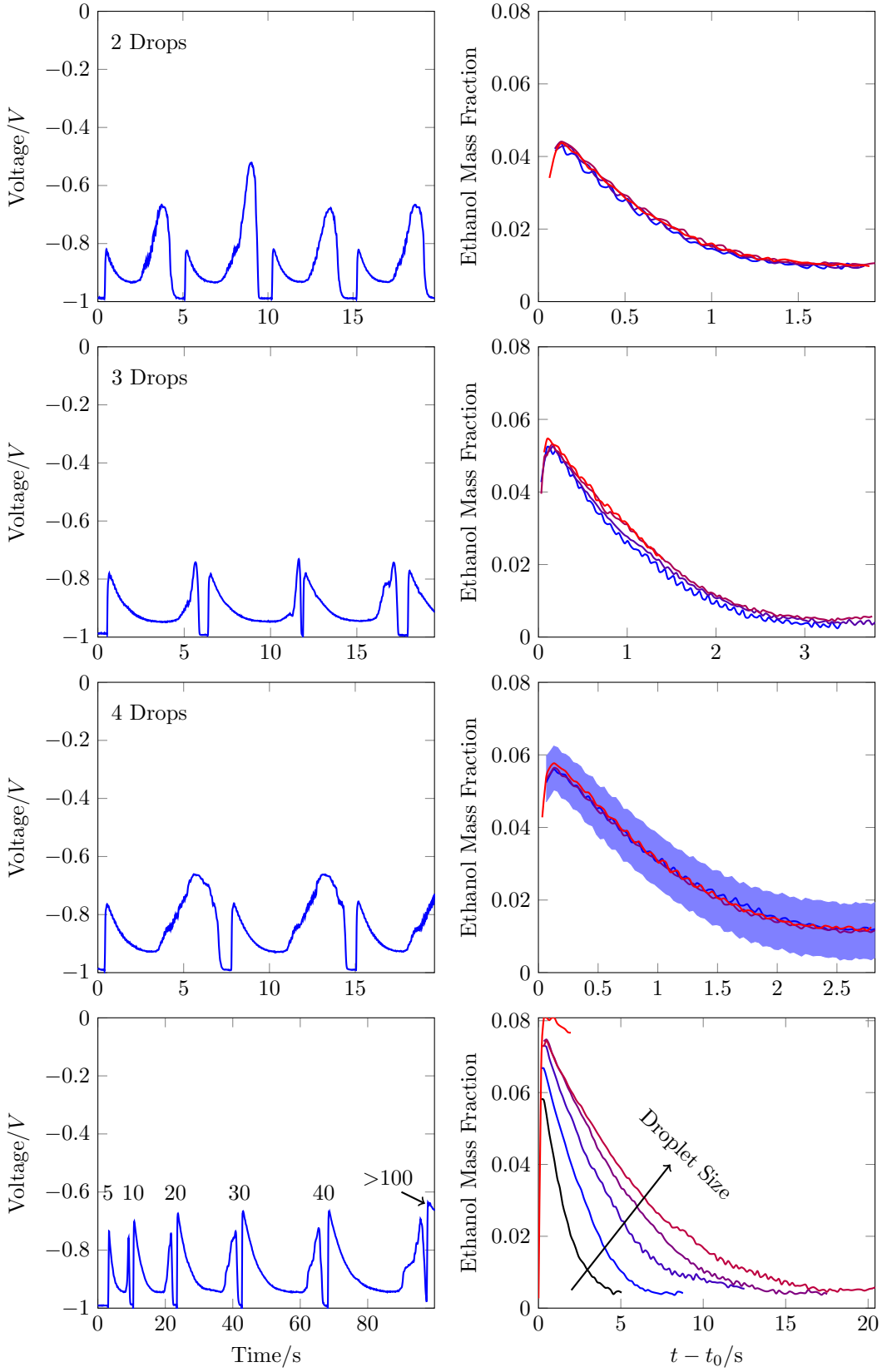

Figure 3.22: Raw signals and time evolution of ethanol mass fraction for nominally 8.0 wt% ethanol droplets.

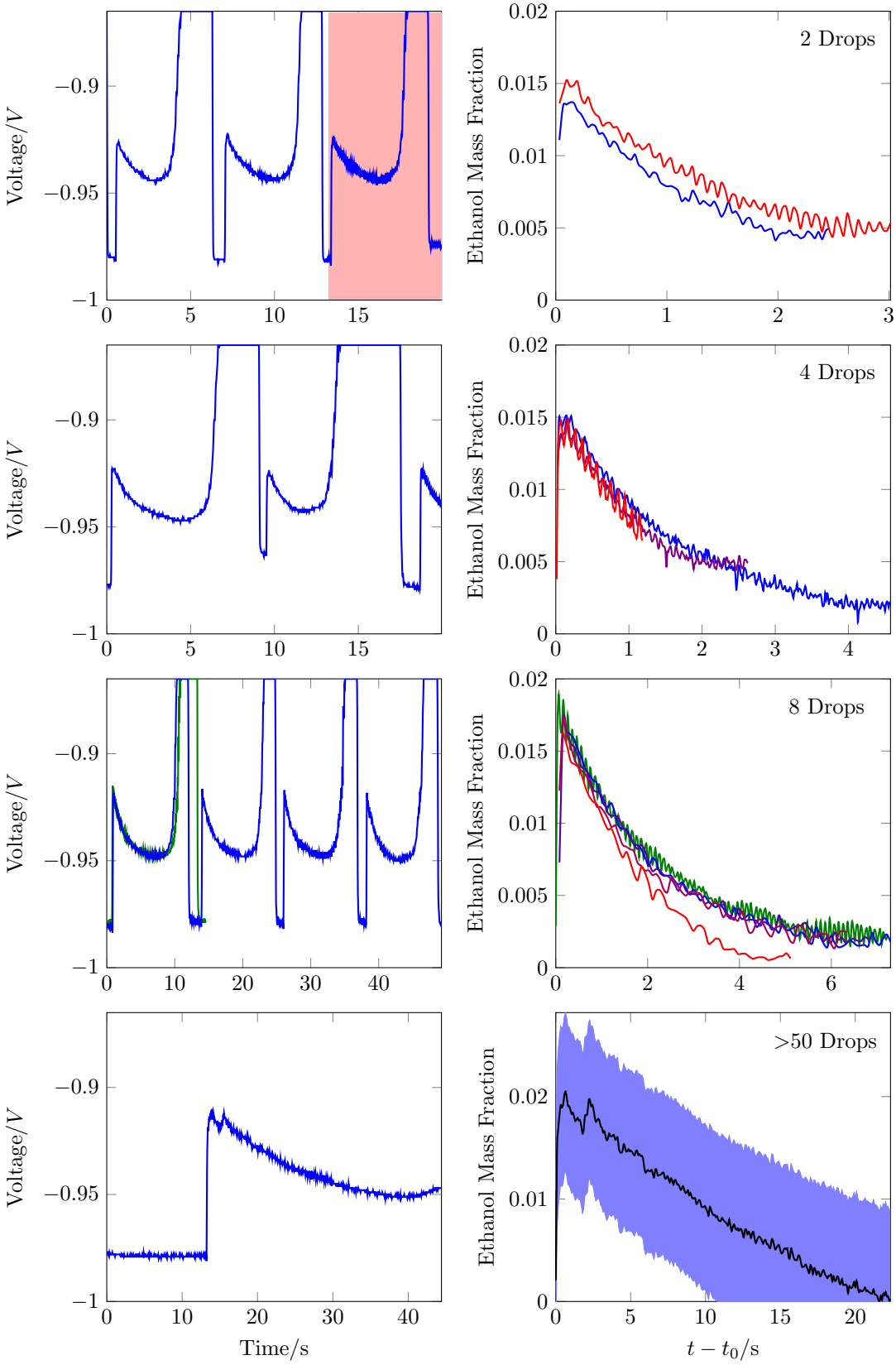

Figure 3.23: Raw signals and time evolution of ethanol mass fraction for nominally 2.1 wt% ethanol droplets.

assume that the depth is on the order of the wavelength of the laser. Evanescent waves are generated at angles of incidence above the critical angle in order to fulfil the electromagnetic boundary conditions, however the intensities decay exponentially with the lengthscale β.

$$\beta = \frac{2\pi n_i}{\lambda}\sqrt{\left(\frac{n_i}{n_t}\right)^2 \sin^2\theta - 1} \tag{3.25}$$

The penetration depth is then defined as

$$d = \frac{\beta^{-1}}{2} \tag{3.26}$$

which for a fused silica-water interface at a typical angle of incidence of 66° gives a depth of 540 nm. In their UV-Vis reflectometry experiments on the growth of a lignin film Soetedjo and Räty[119] only considered a region 600 nm from their prism surface. Campbell *et al.*[123] modelled the reflectivity of an aqueous solution containing a single Lorentz oscillator covered by a pure water film. From this they found that the (exponential) decay length of reflectivity into the sample went as approximately 2λ. In our experiment this would correspond to approximately 1 micron so both these examples suggest that only the fluid layer close to the interface is under scrutiny rather than the bulk.

This is important as the droplet does not have a homogeneous composition. The liquid-vapour interface will be ethanol-deficient so the solid-liquid surface would also be ethanol-deficient relative to the bulk as Marangoni flows from the apex to the contact line pull the ethanol-deficient fluid into the region probed by reflectometry. This is illustrated by Figure 3.24 which shows a snapshot of some FEM simulations of ethanol-water droplets by Diddens *et al.*[38]. Such simulations explicitly include diffusion but diffusive mixing is slow compared to the lifetime of the droplet.

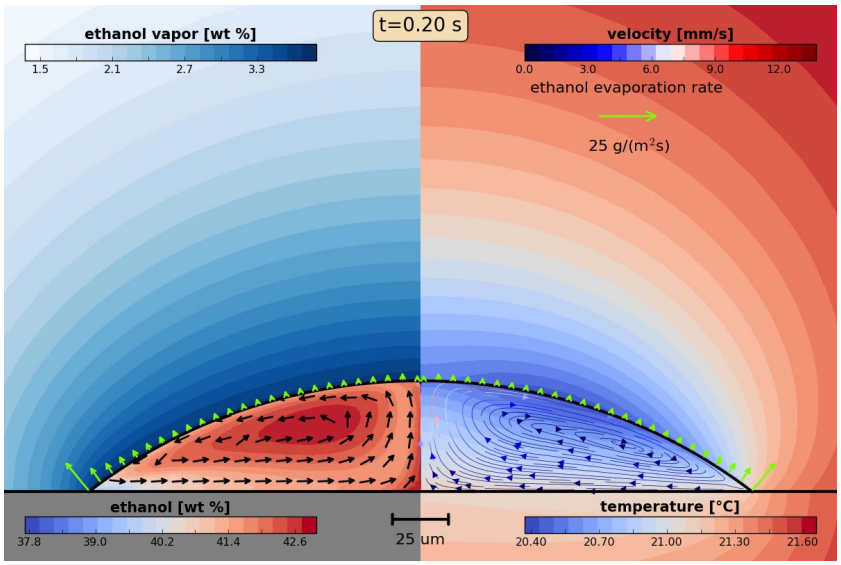

Figure 3.24: Snapshot from a simulation by Christian Diddens of one of my "4 Drop" droplets from Figure 3.20 with parameters $V_0 = 1900$ pL, $c_0 = 44$ wt% ethanol, silica hemisphere substrate giving $\theta_0 = 35°$ at 35% *RH*. Taken with permission from a personal communication.[124]

3.7.1 Comparison to Model

Using Popov's Equations[31] a straightforward model was developed (Section 2.9) in which the ethanol and water components evaporated with an unpinned contact line according to their own sets of equations, with modified activities (using the mean droplet composition) to account for their being a mixture. Figure 3.25 shows the comparison between this model and the experimental mass fraction data in the previous section for a range of compositions and droplet sizes. The inputs for the model were estimated based off the measurements collected in Section 3.4 that $RH \approx 30\%$, the volume of a droplet was some multiple of that of a single Drop (approximately 400 pL) and the initial contact angle was between 30° and 50° depending on the starting ethanol concentration. The length of the simulation was then determined based upon the duration of the non-baseline signal in the raw voltage outputs (see Figure 3.26), these could potentially have been underestimates if the evaporating droplet had moved off the laser spot area so the signal returned to the baseline too early. The starting mass fractions were approximated by back extrapolation from the reflectometry results while the

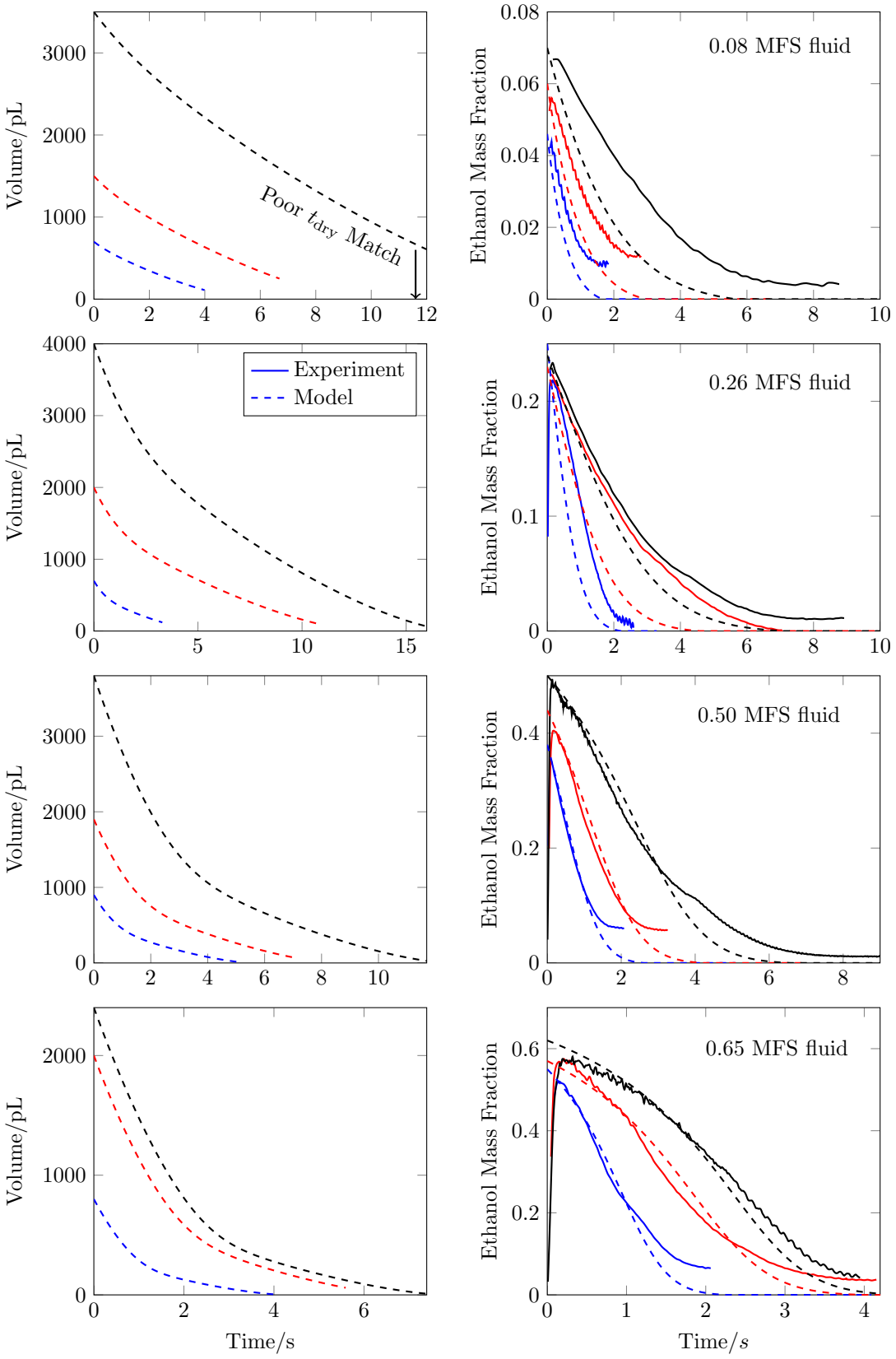

Figure 3.25: Comparison between experimental (solid) ethanol MFS results and output from volume-averaged model (dashed) alongside model volume evolution. Subplots in the same row correspond to the same nominal starting concentration of ethanol. Within each set there are a range of volumes: 2 Drops (blue), 4/5 Drops (red) and 10 Drops (black).

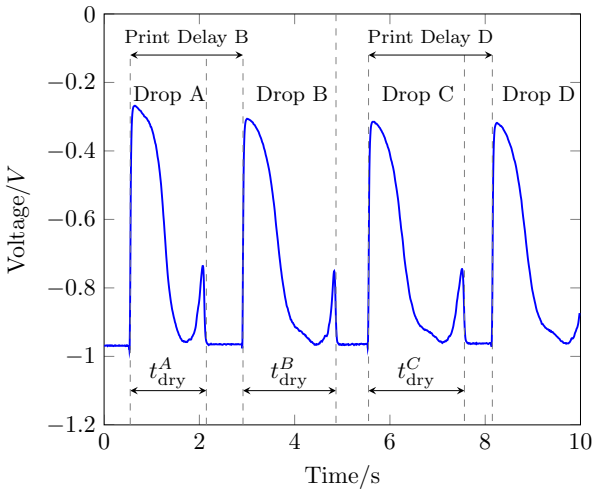

Figure 3.26: The drying time of a droplet can be found from the period that the signal deviates from the V_{on} baseline, therefore a complete signal is required (such as for t^D_{dry}). The difference between printing times gives how long the fluid of a droplet waits at the nozzle before printing. Data from 50 wt% 1 Drop set in Figure 3.20.

relative humidity and starting volume and contact angle were tuned to within ±10% of their estimated values in order to achieve better matches between the measured and modelled drying times. A good match was achieved in most cases, excluding the larger droplet in the 0.08 MFS set of measurements.

The match between my simple model and the experimental data is pleasing (note the model gives the average ethanol concentration and the experiment the concentration near the substrate). It fits qualitatively, accounting for the MFS decreasing more slowly as the droplet evaporates as well as capturing the shallow backwards S-shape found at high starting ethanol concentrations. A very good match is found above intermediate concentrations of about 0.4 MFS. At lower concentrations the model breaks down, predicting significantly faster ethanol evaporation than is observed. This suggests that at higher ethanol concentrations the Marangoni flows effectively mix the droplet so the volume-averaged assumption in the model is useful while the absence of strong Marangoni flows at lower concentrations means the droplets are not well mixed so less ethanol reaches the surface leading to slower evaporation. The model is volume-averaged so it

necessarily fails to account for the presence of the ethanol residue measured as there is no mechanism to prevent the ethanol from evaporating to completion. As in the above sections it is possible that anomalies are present throughout so the slow down in the reduction of ethanol concentration and so the presence of a residue is artificial. However following Sefiane *et al.*'s approach[101], the diffusion coefficient of ethanol in water is about $1 \cdot 10^{-9}$ m s^{-1} (Figure 3.29) so for a lengthscale of 100 µm the diffusion timescale is

$$\tau \approx \frac{L^2}{D} = 10 \text{ s} \tag{3.27}$$

which is greater than the drying time for droplets of less than 10 Drops. Therefore the diffusion of ethanol to the interface is slower than evaporation so it is possible for a residue to indeed remain.

3.7.2 Anomalies

The cause of the smaller than expected reflectances towards the end of evaporation is not obvious. The main difficulty is in determining a mechanism which might cause the amount of light reaching the detector to decrease.

If light is reflected back at the top interface the reflectance would increase, rather than decrease as happens during the anomalies. I have already discussed that the curvature of the droplets means that any reflected light would be very diffuse unless the droplet was close to being flat; therefore flat droplets could lead to increases in reflectance as in the ethanol droplet in Figure 3.10. The different increase in reflectance in the bottom left plot of Figure 3.15 was caused by the droplet depinning and moving off the laser spot so the more negative voltage a result of total internal reflection at the silica-air interface across part of the laser spot. Another signal feature observed were the sharp peaks in PMT signal at the end of drying preceded by a small dip in signal (to more negative voltages equivalent to a small increase in reflectance) such as in Figure 3.21. Given that

these increases in reflectance are so close to the end of drying it is possible that they are a result of droplet surface reflections.

In these results the larger droplets were more likely to exhibit sharper changes in voltage which obscure less of the drying time. However there were examples of single droplets having 'cleaner' signals than larger ones such as in the 50 and 80 wt% sets. Aside from the difference in size, having a larger footprint meant that the location of the laser spot within the droplet footprint could be either towards the centre or the edge. It will be seen in the Chapter 4 (Figure 4.6) that different locations changed the signal anomaly shapes at late times, meaning that the positioning of the droplet is relevant even though the cause of the change is unclear.

Another interesting point is when the anomalies appear. Apart from in thin, pure ethanol droplets they are only present at late times, suggesting that the cause is suppressed when ethanol and/or solutal Marangoni flows are present. When I included particles, anomalies prevented measurement of the reflectance at the time at which Marangoni flows ended in more than half of the experiments (but not always, meaning they started around the end of Marangoni flow).

One possible cause of anomalies could be heating of the droplet as a result of laser light being absorbed. This light getting absorbed must be transmitted into the drop so as it would not reach the detector anyway, absorption in itself would not change the signal. However if the droplets heated up then that would result in a change in the refractive index which could lead to a measurable change. The refractive indices of fluids typically decrease at higher temperatures, in this reflectometry setup that would increase the difference in refractive index relative to the hemisphere which would increase the reflectance measured. As the anomalies decreased the reflectance then laser heating does not appear to be the cause.

3.7.3 Laser Heating

While laser heating would not lead to an increase in refractive index to explain the anomalies it is still useful to determine whether droplets might heat up which could prevent compatibility with some chemical systems and make comparisons with picolitre droplet results in the next chapter less reliable.

The absorption or attenuation coefficient is defined as the lengthscale over which light travelling through a medium is reduced to $1/e$ of its intensity before entering the medium. At a wavelength of 633 nm the absorption coefficient of water is approximately 10 times larger than for ethanol.[125] Therefore for this estimation I will consider a droplet of pure water as a case of maximal laser absorption which might occur towards the end of drying for one of the binary mixture droplets. The laser has an intensity of 2 mW although a neutral density filter cut that down to 0.2 mW. The fraction of light entering the droplet is $1 - R_p^*$, or about 10% of the total incident power, i.e. 20 µW. From Pope and Fry[126] the absorption coefficient of water at the wavelength used here is 0.3 m^{-1}. At the onset of anomalies even the largest droplets would be expected to have heights of less than 50 µm so only approximately one and a half ten thousandths of that energy would be lost while passing through the droplet so the absorbed power in one second would be $Q = 3$ nJ. If the remaining volume of the droplet was about 200 pL then $M = 200$ ng. Given the specific heat capacity of water is $C_p = 4.2$ J/g then in a single second the droplet would raise in temperature by $\Delta T = Q/MC_p = 0.004$ °C. The timescale for thermal diffusion is

$$\tau_{\text{thermal}} = \frac{L^2}{\alpha} \tag{3.28}$$

if the characteristic lengthscale L is a droplet diameter of 400 µm then using the thermal diffusivity of fused silica[127] $k_{\text{silica}} = 8.8 \times 10^{-5}$ m^2 s^{-1} we get a timescale of 2 ms. Based on this timescale it appears that fused silica is good enough at conducting heat away from the laser spot for the droplet to not heat

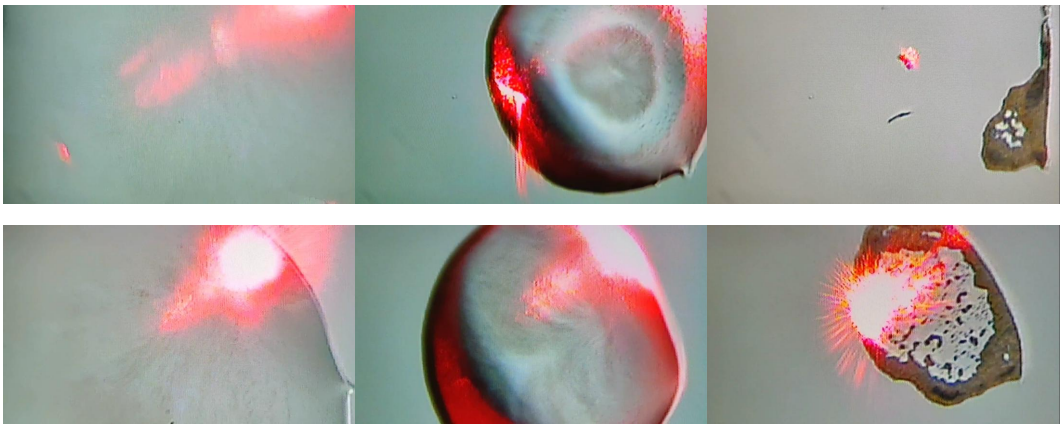

Figure 3.27: Central and off-centre solutal Marangoni vortices in 20 Drop droplets of 50%v ethanol with high particle concentration.

up significantly over the course of experiments lasting multiple seconds.

Temperature gradients from laser heating had the potential to induce thermal Marangoni flows. The temperature change calculated above is small so such flows were not observed in experiments with droplets containing particles. However there was evidence of the laser changing the flow structure by shifting the centre of the vortices in the direction of the laser spot so they were no longer axisymmetric. In Figure 3.27 (where the field of view and laser spot location are unchanged between rows) the first row shows a droplet placed over the laser spot. In the second row the laser spot is much closer to the edge of the droplet and the centre of the vortices is shifted. In this latter case there was little particle migration. As a result there were more particles near the contact line leading to pinning and a more ring-like deposit.

3.7.4 Nozzle Evaporation

An obvious feature of the above results is that the measured concentrations of ethanol are always lower than in the prepared fluid. Furthermore, the larger the droplet the smaller the concentration difference to the prepared fluid, while this can be noticed when moving down rows in each of the above figures, there is a

particularly clear example in Figure 3.22 in which the droplet sizes was increased from 5 Drop equivalents to 10, 20, 30, 40 and a droplet generated by printing continuously at 500 Hz with a volume of hundreds of nanolitres. As has been noted it is not strictly correct to extrapolate back to $t-t_0 = 0$ s as the evaporation rate of ethanol is not constant over the time when signal is lost to the circuitry's response. However with the time not being too long compared to the overall drying time then it is possible to do a linear extrapolation to get a reasonable estimate. Therefore in Figure 3.22 and other cases rough initial concentrations at the start of drying are extracted for comparison with theory.

Larger droplets necessarily require more fluid so while there is evaporation from the nozzle before a droplet is dispensed the larger droplets will include fluid further from the tip of the nozzle whose composition will be closer to that of the reservoir. However experiments with this equipment with a stationary substrate meant that the previous droplet printed needed to fully evaporate before the next could be printed. Therefore a trade-off existed where increasing the droplet size made the ethanol depleted fluid at the nozzle a smaller fraction of the printed droplet but also increased the delay between measurements, allowing for more ethanol to evaporate from the nozzle.

With the above composition data it was possible to build a one dimensional steady-state model if we simplified the conical fluid feed of the nozzle as a cylinder where evaporation could only occur from one surface. The results could then be compared against experimental snapshots of the starting concentration of droplets printed after certain delays with the reflectometry apparatus to help understand the speed at which fluid waiting at the nozzle before printing became ethanol-depleted.

In the literature the calculation of evaporative flux from a surface often uses

the Hertz-Knudsen equation

$$J = \frac{p}{2\pi M_p k_B T} \tag{3.29}$$

which takes a ballistic, molecular approach where M_p is the mass of the particle/-molecule and k_B is Boltzmann's constant. In practice this significantly overestimates the evaporation rate so evaporation coefficients are introduced. These coefficients are derived from fitting to experimental data so I instead decided to use Popov's equations[31] for the rate of mass loss given that the nozzle orifice had circular symmetry and evaporation might still be expected to be diffusion limited. Using Equation 2.4 simply involved taking the radius of the orifice instead of a droplet and taking the limit of the contact angle going to zero. This approach ignored any wetting of the nozzle (which would increase the effective radius) and the presence of the nozzle guards which would reduce air flow around the nozzle, leading to a higher effective relative humidity. This method could be used to estimate the uniform evaporation rate (required by using a 1D model) of fluid across the nozzle.

For the fluid at the nozzle to have a steady composition the concentration of ethanol in the fluid lost to evaporation would need to be the same as that of the bulk, which would be drawn into the cylinder to keep the meniscus at the end of the nozzle. Therefore I could apply Popov's equations[31] to calculate the mass loss of fluid over an arbitrary small (1 ms) timestep at different relative humidities. At $RH = 30\%$ the evaporated fluid from fluid with an ethanol MFS 0.09 would have a mass fraction of 0.44 ethanol while the evaporated fluid from a mixture with 0.23 MFS ethanol would have an ethanol mass fraction of 0.65. Therefore, at $RH = 30\%$, fluid with bulk concentrations of 0.44 or 0.65 MFS ethanol would have a steady-state ethanol concentration of 0.09 or 0.23 MFS respectively at the liquid-vapour interface.

With an assumption of plug flow so the radial position in our cylinder was not

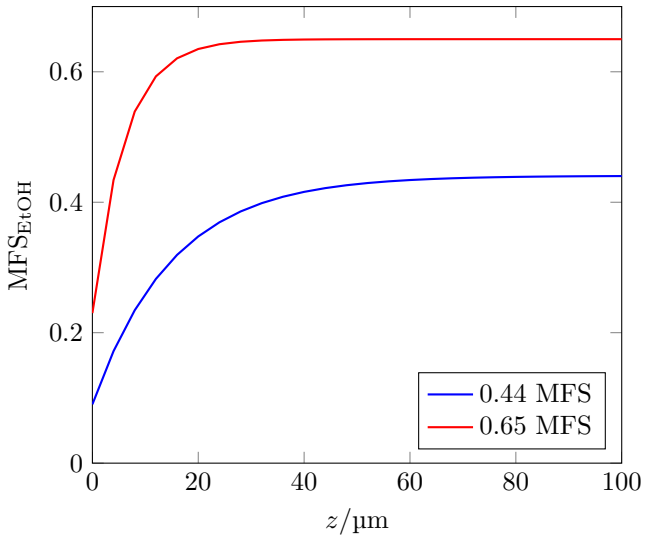

Figure 3.28: Blue and red lines for 0.44 and 0.65 ethanol MFS fluids respectively. Length L is zero at the surface, increasing going into the bulk.

important (as in reality the fluid elements would not move at a constant speed but have a parabolic profile across the nozzle cross-section due to a non-slip boundary at the chamber walls), the volume of fluid lost will correspond to a reduction in cylinder length as a result of evaporation (E in units of m s^{-1}). To maintain a steady-state system this loss of fluid must be matched by an incoming flow from the nozzle reservoir with speed $v = -E$.[128] For simplicity we will assume that the excess volume of mixing is zero and we will neglect the concentration dependence of D within the nozzle in order to get an analytical solution. At steady-state, $c(z)$ is independent of time, where z is the depth into the nozzle from the liquid-vapour interface. The convective-diffusion equation for the ethanol therefore reads

$$\frac{dc}{dt} = -v\frac{dc}{dz} + D\frac{dc^2}{d^2z} = 0 \tag{3.30}$$

which can be integrated once, to equal some constant W

$$-vc + D\frac{dc}{dz} = W. \tag{3.31}$$

The boundary conditions $\frac{dc_{\text{bulk}}}{dz} = 0$ and $c(z_{\text{bulk}}) = c_{\text{bulk}}$ fix the constant $W =$

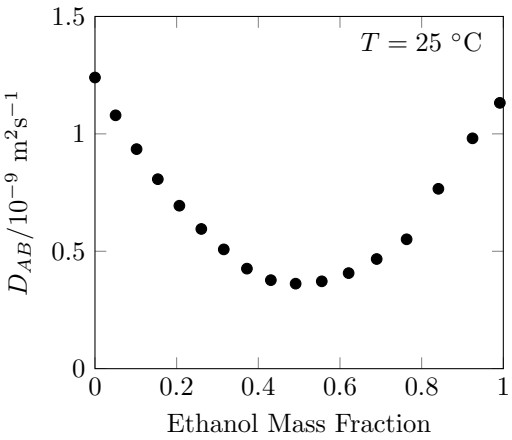

Figure 3.29: Mutual Diffusion Coefficients of ethanol-water in a binary ethanol-water mixture, data from Ref. 129.

$-vc_{\text{bulk}}$.

Therefore Equation 3.31 can be solved to find

$$c = A \exp^{\frac{v}{D}z} + c_{\text{bulk}} \tag{3.32}$$

where the constant A is determined from the bulk and surface concentrations such that

$$c = (c_{\text{surf}} - c_{\text{bulk}}) \exp^{\frac{-E}{D}z} + c_{\text{bulk}}. \tag{3.33}$$

In this equation the ratio $\frac{D}{E}$ describes the lengthscale of the exponential while the ratio $\frac{D}{E^2}$ gives the timescale for the steady-state to be reached. The diffusion coefficient of ethanol in water was assumed to take its value at the steady-state surface concentration.[129] From the calculated evaporation rates for fluid from the nozzle, the evaporation velocity is approximately $30\,\mu\text{m}\,\text{s}^{-1}$; for diffusion constants on the order of 10^{-9} m^2 s^{-1} this results in a timescale on the order of 1 second. Therefore considering the drying times of droplets in the previous section of multiple seconds we would expect to be close to the nozzle steady-state for the reflectometry experiments. As a result the mean composition of a droplet can be estimated by taking the mean concentration across the depth into the nozzle from the interface which would need to be ejected to generate a droplet of

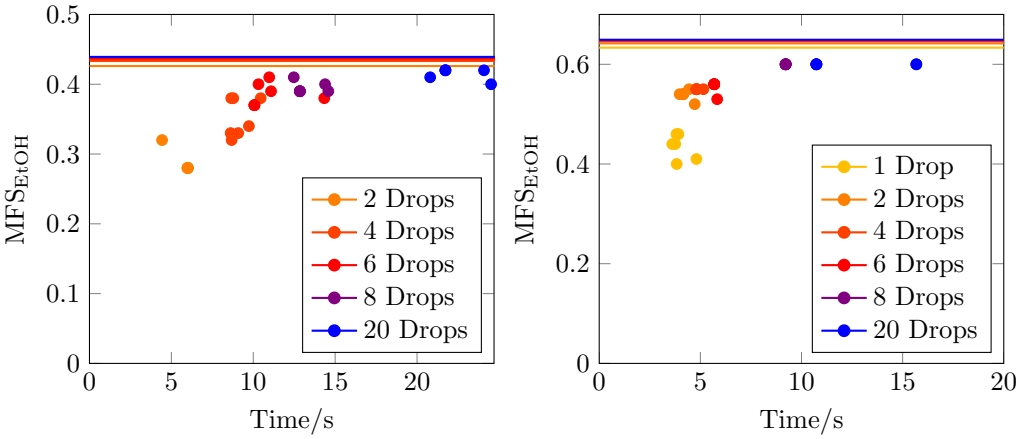

Figure 3.30: Evolution of concentration profile near the end of the nozzle in 0.5 s intervals going from blue to red and comparison between theoretical and experimental compositions of printing droplets of different volumes (X Drop Equivalent) after some delay. Theoretical compositions come from taking the average composition over the equivalent volume within the nozzle nearest to the interface. $RH_{\text{model}} = 30\%$.

predetermined volume. The composition profiles for the two test cases are given in Figure 3.28. The short lengthscale over which the fluid is depleted of ethanol means that the fraction of fluid which is ethanol-depleted only makes up a small portion of a droplet's total volume (for droplets with volumes of the order of nL's).

Figure 3.30 shows the predicted steady-state concentrations of droplets of different size for two different starting compositions of 44 and 65 wt% with the experimental composition data (circular markers). The experimental delay times could be found from PMT signals where droplets were printed consecutively within one trace and the initial compositions of the droplets approximated by a linear backward extrapolation from reflectometry results. Figures 3.20 and 3.18 previously show that the uncertainties on these extrapolated compositions are on the order of ±3 to 4% and ±6 to 7% for 0.44 and 0.65 MFS droplets.

Figure 3.30 shows that all the experimental droplets had lower mass fractions than the predicted steady-state results, meaning either the model severely underestimated the amount of evaporation at the nozzle or there was another

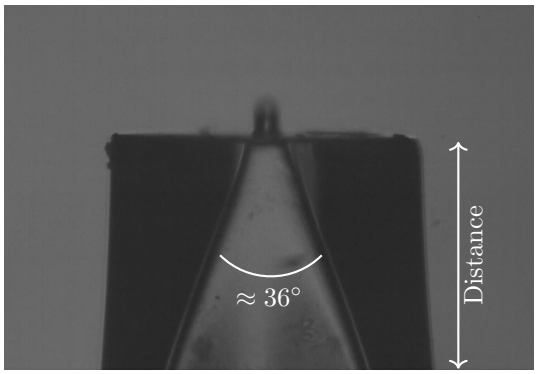

Figure 3.31: Snapshot of a 50 µm diameter orifice Microfab nozzle (with a cone-shaped internal fluid chamber) jetting a droplet vertically upwards.

mechanism for loss of ethanol which was unaccounted for.

There are multiple possible causes for this mismatch with experiment as this model is relatively simple. Firstly the internal chamber of the nozzle is actually a cone (see Figure 3.31) so the ethanol-depleted fluid is in contact with more bulk fluid which might increase diffusion of ethanol to the nozzle. However this only leads to minor changes in lengthscale and would also lead to less, rather than more ethanol-depleted droplets. The conical shape also means the nozzle tip is narrower, therefore the fraction of fluid closest to the nozzle would make up a smaller portion of the total volume ejected when a droplet is printed. However as the fluid nearest the interface is likely to be the most ethanol-depleted, then by mixing it with more fluid of composition closer to the bulk the ejected droplet would be less ethanol-depleted. Therefore this mechanism does not help in explaining the limitations of the model.

Additional losses of ethanol are also possible (relative to the bulk concentration) as a result of evaporation during flight after a droplet is ejected from the nozzle but before it lands on the substrate. Inkjet-printed droplets are typically ejected with velocities of metres per second and the distance between the nozzle and substrate is on the order of a few millimetres, therefore the time-in-flight will

be on the order of a millisecond. For a pure fluid the diffusion-limited evaporation rate of a spherical droplet can be described in terms of a linear equation in the droplet radius squared

$$R^2 = R_0^2 - \frac{2MrDt}{\rho R'T}\left(p_v - p_v^{\infty}\right) \tag{3.34}$$

where all terms have been previously defined but we clarify R is the droplet radius R' is the ideal gas constant. A "5 Drop" droplet of volume 2 nL would have an in-flight radius of 78 µm, if we assume the droplet is pure ethanol to deliberately overestimate the evaporation rate then using Equation 3.34 the droplet radius would only shrink by 0.03 µm in 1 ms. Therefore in-flight evaporation can easily be neglected in this instance.

There are limitations from my description of the evaporation at the nozzle. It is not actually clear that we can apply Popov's equations and whether my choice of angle (equation not particularly sensitive) or radius is appropriate; typically there is a layer of fluid at the nozzle plate which can also evaporate, and so increase the loss of ethanol.[130,131] Capillary action causing fluid to wet the nozzle plate could increase the effective radius and so is a likely a contributor to the degree to which real evaporation from the nozzle differed from our model.

The large difference between the steady-state model and the experimental results suggests that the 1D model is missing crucial physics. In a 2D system the fluid flowing to the nozzle would have a parabolic flow profile so the fluid arriving at the surface would come from deeper within the nozzle than the 1D model predicted. This could enhance the evaporation of ethanol at the surface and so explain some of the difference between model and experiment; however without further modelling it could also be argued that as the incoming fluid was more ethanol-rich then the printed fluid could be less ethanol-depleted. Therefore it is unclear whether such a detail would be helpful in explaining the disagreement between model and experiment.

A 2D system would also allow the presence of mixing flows in the nozzle surface region[132] (as the fluid does not all have to travel towards the interface) which could refresh the nozzle region; this could mean that ethanol could continually evaporate at a high rate while still maintaining the steady-state surface concentration. As a result the region of fluid nearest the nozzle surface could become more ethanol-depleted, in line with the experimental data. Of the candidates for mixing flows, a buoyancy-driven mechanism does not make sense as the ethanol-depleted interface in a nozzle is at the bottom of the system and has a higher density than the bulk so is stable with respect to gravity. Alternative mixing flows might be a result of the acoustic pulses from the piezoelectric actuators that cause jetting. Meinhart and Zhang[133], and Castrejón-Pita *et al.*[134] have shown that the jetting-related flows essentially coincide with the driving voltage pulse, which makes sense as otherwise nozzles would have difficulties at high print frequencies if there were remnant flows from previous pulses. This means that such flows must die out almost immediately and so do not keep the nozzle fluid mixed during a delay, as required to explain the extent of the model's deviation. Therefore solutal Marangoni flow due to evaporative flux differences across the nozzle orifice, inducing composition and surface tension gradients, is the most likely candidate for mixing in the nozzle. This is especially true in light of experiments, which did not make it into this thesis, of the evaporation of ethanol-water mixtures in a capillary (i.e. a 1D system excluding meniscus effects) where there were strong solutal Marangoni flows near the interface.

3.8 Conclusions and Future Developments

In summary we developed a novel experimental setup, demonstrating that it is possible to apply Fresnel's Equations to measure changes in refractive index and so the evolving composition of an evaporating droplet (or other geometry

of fluid against a hemisphere). Compared to existing methods in the literature the same droplet is measured throughout its lifetime, rather than attempting to compare reproducibly printed droplets while the droplets involved are also orders of magnitude smaller. However there are limits to when good signals can be obtained, we have been able to rule out a few potential mechanisms for such anomalies but the cause is still uncertain.

To advance the method a side view camera is required to accurately measure the droplet volumes and a PMT with a faster response time would reduce the loss of signal at early times. Another useful improvement would be designing a shutter system which would avoid any chance of the laser heating the optics components which could introduce inconsistencies. This would also be an important development were smaller droplets to be printed as when they were experimented with the thermal gradient across the droplet footprint as a result of the laser lead to the small droplets being repelled from the laser spot. Finally a useful advancement would be to have the reflected laser light fall on a charge-coupled device rather than a PMT to allow for the mapping of concentrations across a droplet.

Reflectometry experiments on ethanol-water binary droplets quantified the residue of ethanol remaining at the end of solutal Marangoni flows and into late stages of drying. This residue was near the substrate as the technique measured the concentration in this region rather than the bulk concentration. Measurements of the composition at early times allowed estimation of the extent of evaporation at the nozzle and the impact on the actual compositions of printed droplets. A steady-state diffusive model was presented and its underestimation of evaporation at the nozzle demonstrates the presence of mixing at the nozzle tip.

It would be useful to apply this technique to study droplets containing different components. However the other systems described in this thesis contain involatile components which would be left on the hemisphere after the droplet finished

evaporating. Therefore there would have to be very frequent cleaning of the hemisphere, which would make the method of printing a series of droplets with a known delay unfeasible. To allow these kinds of droplets to be studied more effectively there are two approaches which could allow the printing substrate to be moved without impacting on the laser alignment. The first of these would to use a triangular prism with angles set to the system in use. The prism could then be moved along its length perpendicularly to the incoming beam to uncover fresh substrate. Alternatively the hemisphere could have some cover slip with the same refractive index placed on top with refractive index matching fluid between it and the substrate. Then the challenge would be to adjust this cover slip to move a fresh section over the laser spot.

That I was able to measure such small changes in composition demonstrates that this experimental approach has a great deal of potential in being able to be applied to other chemical systems where refractive index changes are even smaller than those between ethanol and water.

Chapter 4

Solvent Mixtures

4.1 Introduction

In droplet technologies utilising drying droplets, such as inkjet printing, the bulk of the volume/mass of the formulation will be made up of (often multiple) solvents. Therefore studying model solvent mixture droplets is useful to gain a better understanding of the evaporative dynamics and internal flows and how they relate to the droplet deposits. Such mixtures have a much greater degree of complexity than single solvent systems as the existence of multiple components can lead to non-uniform compositions, different wetting behaviour and different evaporative dynamics with multiple stages.

In this chapter I discuss many aspects of droplet evaporation by simultaneously studying the droplet profile, internal flows and deposits. The chapter starts with examples of various solvent mixtures in the literature to grasp the breadth of possible behaviour before describing each of my model systems in turn. Firstly ethanol-water mixtures as they are well studied at microlitre volumes and so could be used to test the applicability of results from the literature to small droplets. I then discuss the impact of ethanol vapour on drying droplets before introducing ethylene glycol as a model humectant for different binary and tertiary solvent

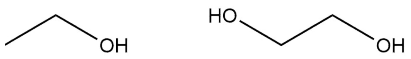

Ethanol Ethylene Glycol

Figure 4.1: Skeletal formulae of ethanol and ethylene glycol.

mixture combinations.

Studies of the evaporation of aqueous binary mixture sessile drops began with Rowan *et al.*[135] who studied water and propan-1-ol systems. They found that mixtures containing less alcohol than the azeotrope showed a period of instabilities as a result of preferential adsorption of propan-1-ol at the surface. Once the system became stable the residual drop was inferred to be water as a result of a much increased contact angle.

Other experiments from Sefiane *et al.*[101] studied methanol-water drops. The methanol-rich drops evaporated more quickly, leading to contact angle maxima at different points through drying that were consistent with most of the methanol having evaporated. Considering the timescale for diffusion compared to evaporation led to them introducing the idea of a methanol residue persisting at late times.

Guéna *et al.*[136] investigated the spreading and drying times of binary alkane mixtures. Despite small surface tension differences (1.3 mN m^{-1} between pure heptane and octane) they found Marangoni enhanced spreading such that the mixtures dried much faster than the pure fluids, while also seeing the formation of bulges near the contact line.

Park and Moon[137] obtained well-ordered colloidal crystals of silica spheres from inkjet-printed droplets of water with either of the (low volatility) drying agents diethylene glycol or formamide; Marangoni flows prevented particle segregation as a result of the Coffee-ring effect and so were the driving force behind the deposit structure.

However not all binary solvent mixtures have solutal Marangoni flows, Kim

and Stone[42] set up an experiment to view a radial front of critical 1-Methyl 2-Pyrrolidinone concentration moving inwards from the contact line where it was enriched due to the water component being more volatile.

From our research group Talbot *et al.*[138] studied methoxypropanol-water mixtures where the identity of the more volatile component switched above a relative humidity of 50%. At lower RH they found circulating eddies towards the contact line while particles away from the contact line migrated inwards. In contrast at high RH when methoxypropanol would evaporate more quickly than water, there was recirculation in the inner part of the droplet, with outward radial flow in the outer section. These outer sections bore resemblence to recent work on competing Marangoni and Rayleigh convection[139], however considering the scaling of Rayleigh convection with size, buoyancy-driven flows would not be expected at inkjet-printed droplet lengthscales.

Isopropanol (IPA) and 2-butanol binary mixtures have received interest because they allow printing of uniform desposits for 2D materials.[7] PIV and surface tracking experiments (utilising the presence of diffraction fringes) with IPA and 2-butanol droplets showed that this uniformity in the deposit was a result of Marangoni enhanced spreading, coupled with the droplet forming a flat pancake which suppressed the coffee ring effect. Pahlavan *et al.*[140] built a model to explain the non-spherical cap profiles, finding that the spatial concentration gradients that developed required the vapour fields to be explicitly modelled over time in a quasisteady analysis (rather than a static vapour field described by Laplace's Equation, Equation 1.11[24,30,31,44]). This model better fitted the change in profile shape from experiments and showed that there was a critical volume fraction of IPA needed for the droplet to form a pancake-shape.

The most general modelling capabilities of solvent mixtures comes from Diddens *et al.*[38] whose FEM approach can handle evolving concentration and temperature fields in the liquid and vapour phases. For glycerol-water droplets they

assumed the glycerol component was involatile, and modelled the evaporation and Marangoni flow velocities. They found that the evaporation rate decreased very quickly with RH and that the increasing viscosity at late times turned off the flows and trapped a residual amount of water within a glycerol shell. In this paper they also investigated ethanol-water droplets. After multiple, transient flow vortices merged at early times their modelled behaviour roughly converged on the experimental data of Christy *et al.*[141] who found a peak in vorticity when the ethanol has mostly evaporated. The vorticity is defined as the curl of the velocity field and so is a measure of the rotation rate of fluid elements. In the model the simulated Marangoni velocities likewise reached their maxima when the volume fraction of ethanol went to zero.

4.2 Physical Properties

In this chapter I investigate (fully miscible) binary and tertiary solvent mixtures containing water, ethanol and ethylene glycol (EG). Of these the physical properties of ethanol-water and ethylene glycol-water mixtures have been reported in the literature and are displayed in Figures 4.2 and 4.3.

An increasing mass fraction of the organic component in a binary aqueous mixture lowers the surface tension, although ethanol leads to much larger reductions. Ethanol-water mixtures show a maximum in the dynamic viscosity although unlike with EG-water mixtures the change is not significant enough to lead to trouble in jetting droplets reliably. Therefore according to Equation 1.20 the flow velocities in ethanol-water mixtures tend to be higher as for the same concentration gradient the surface tension difference will be larger, while the viscosity is lower.

The other major difference between the fluids is that the vapour pressure of EG is very low, approximately $1/300^{\text{th}}$ that of water at 25 °C, so in many cases

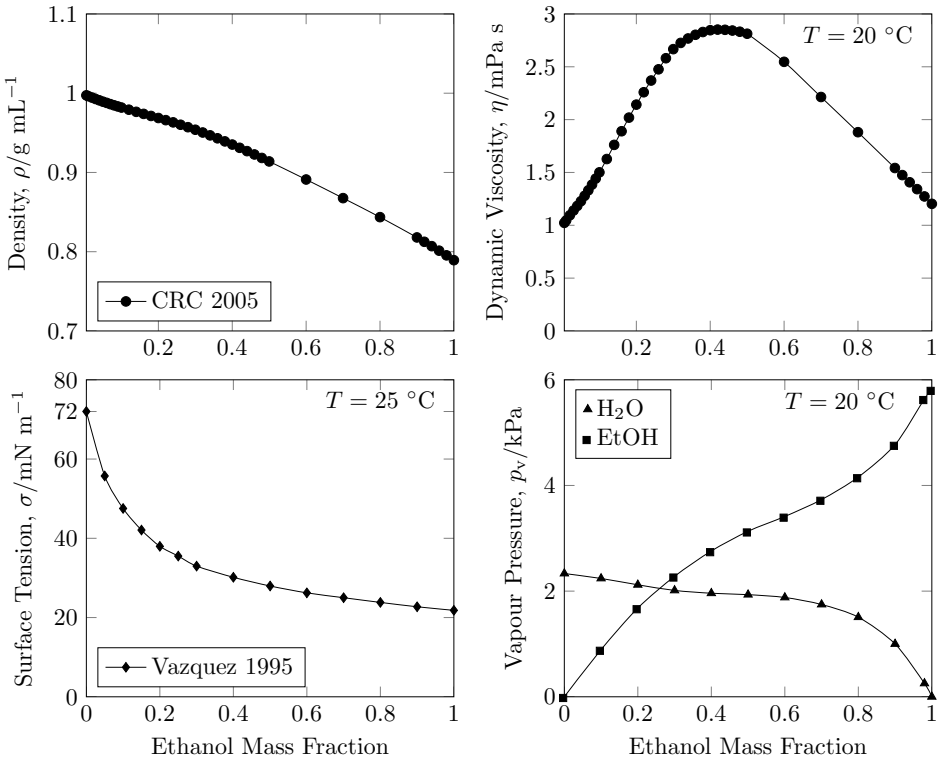

Figure 4.2: Properties of ethanol-water mixtures from Refs 91 (CRC 2005 circles), 94 (Washburn 1926 - vapour pressures), 142 (Vazquez 1995 diamonds).

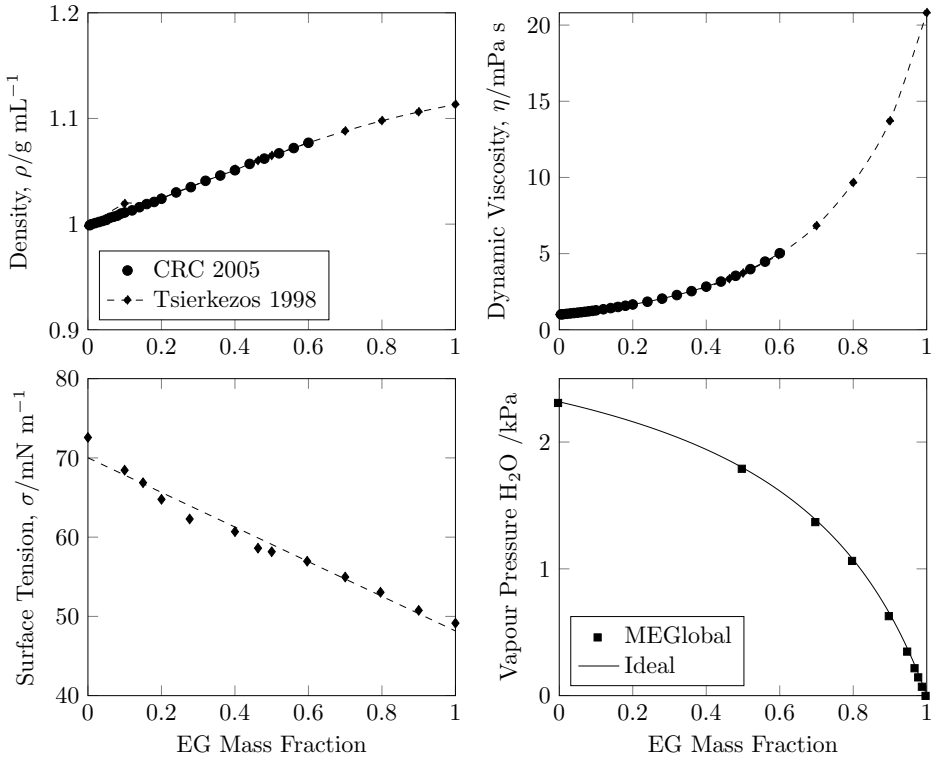

Figure 4.3: Properties of ethylene glycol-water mixtures from Refs 91 (CRC 2005 circles), 143 (Tsierkezos 1998 diamond), 144 (MEGlobal squares). Ideal vapour pressure (solid line) modulated by mole fraction of water in binary mixture.

it can be assumed to be involatile. It can also be shown that the vapour pressure of water closely follows ideal behaviour. In contrast ethanol-water mixtures are non-ideal and both components are volatile, with an azeotropic composition at a mass fraction of 0.955 ethanol at 1 atm and 78 °C.[91]

4.3 Ethanol - Water

4.3.1 Literature

Previous work in the literature regarding the existence of a residual of ethanol at the end of drying in binary ethanol-water mixtures has already been discussed in Section 3.1, therefore to avoid duplication this section will report other findings regarding evaporative dynamics, internal flows, deposits, etc.

Sefiane *et al.*[97] investigated the evaporation of microlitre drops on a rough PTFE substrate, dividing the evolution of the drop profile into three distinct stages. In the first stage the contact angle and radius both decreased and the evaporation rate was close to that of pure ethanol, lasting longer longer if the initial ethanol concentration was higher. For the second stage onwards the contact angle increased and the contact radius decreased so the evaporation rate also decreased. This behaviour was explained as a result of the ethanol component evaporating, leaving the higher surface tension, and so less wetting, water component to dominate. The third stage then appeared similar to the evaporation of water, thus Sefiane *et al.* suggested the ethanol had fully evaporated. However in later work with methanol-water drops they came to the conclusion that alcohol was still present at late times as the late-time contact angles differed from those of pure water on the same surface. In the following years other groups also reported on the evaporation of microlitre ethanol-water drops of various concentrations on self assembled gold-monolayers,[98] PMMA,[145] fluoropolymer coated substrates[100] and on heated substrates,[146] bolstering the evidence for these different stages of

evaporation.

Liu *et al.*'s work on ethanol-water mixtures[99] placed greater focus on the relative humidity and the drop's ethanol concentration. As a result they could observe increases in contact angle as a result of the changing composition and hence surface tension of the droplet, with large changes at high relative humidity (93%) when condensation resulted in the contact angle nearly reaching that of pure water regardless of the initial ethanol composition.

The other side of the literature focuses primarily on the internal flows in ethanol-water drops.

Kang *et al.*[147] developed a ray tracing method to track particle motion in ethanol-water drops on fluoropolymer-coated glass. The high contact angle meant that they viewed the drops from the side, reconstructing their particle positions (with fidelity issues towards the edges). They were able to demonstrate the presence of axisymmetric Marangoni flows of velocities on the order of tens of micrometres per second at low ethanol concentrations (1, 5%) and unsteady flows with velocities on the order of a millimetre per second at 20% ethanol. As predicted the circulatory flows went in the direction of the apex to the contact line along the liquid-vapour interface.

Sefiane and collaborators observed particle flows in ethanol-water drops of different composition: azeotropic mixtures[148] and 5% ethanol.[141] In these they related the three stages of evaporation (in terms of evolving volume) to the vorticity. In the ethanol-dominated stage there was high, constant, vorticity (in a single plane parallel to the substrate), as they found multiple recirculation cells of random orientation and number throughout the drop with particle speeds of 100's of microns per second, in the second stage the vorticity exponentially decayed so that it was low throughout the third stage. Separate to the vorticity, the second stage was associated with a spike in the radial velocity, while the third stage showed the typical increase in radial velocities for the CRE at late times.

Bennacer and Sefiane[149] examined the relative importance of solutal Marangoni and Reynolds numbers. Their approach was able to give a good fit to experimental PIV data if they rescaled the initial particle velocities by their experimental values; however their calculations of the solutal Marangoni number included a number of assumptions which was why the mentioned scaling was necessary. They used drop profile measurements to get experimental changes in volume and then estimated the maximum possible concentration gradient given a bulk concentration at the apex but pure water at the contact line. These assumptions meant they were unable to determine what composition would lead to a subcritical solutal Marangoni flow (below which there would be no solutal Marangoni flows) and change in drying stage.

One of the few works relating the flows in ethanol-water mixtures to the actual end deposits came from Zhong and Duan[150] who studied mixtures up to 50%v ethanol with aluminium nanoparticles that increased pinning and aggregated in the presence of ethanol. Increasing the ethanol content led to more aggregates, breaking up the well-formed ring deposits at low ethanol concentrations. From particle tracking they observed the aggregates forming at the drop interface, ending up around the interior region of the drop as they started moving inwards along the substrate under the influence of Marangoni flows.

All the above authors working with binary solvent mixtures did so with microlitre drops. More relevant to this work is that from previous members of our research group who did experiments with inkjet-printed droplets. Talbot *et al.*[138] tracked the internal flows of micron diameter polystyrene particles within ethanol-water droplets evaporating on glass coverslips fluorinated by a plasma process. They found that in addition to recirculatory solutal Marangoni flows, there was particle motion across the flow streamlines so that despite starting uniformly distributed throughout the droplet, these particles collected into the droplet's centre around a quiescent "hole" with a well-defined radius R_g, leaving the ex-

terior region depleted of particles. After reaching a minimum size this collected group was pulled apart by radial flows, leaving a ring stain. In follow-up work[73] they developed ways to fix this collected group to deposit a concentrated mass of particles. Firstly they could cause a sol-gel transition to coincide with $R_{g,\min}$ by adding laponite (the suspension was shear thinning so that it could pass through the nozzle) which would form a network through the droplet once concentrated. Secondly a non-adsorbing polymer (polystyrenesulfonate) could induce depletion flocculation. To achieve a uniform deposit Shi *et al.*[151] added a low-loading of hydrophobic fumed silica nanoparticles. These nanoparticles gelled as they increased in concentration at the interface. From ellipsometry the authors were able to show that it was a sol-gel transition suppressing the Marangoni flow, and not particle adsorption to the droplet surface as in Yunker *et al.*'s work with anisotropic particles.[65]

4.3.2 Evaporation

In this section I first present some profile data for evaporating ethanol-water droplets to see how they behave and compare against the results in the literature while validating the model set out in Section 2.9.

Figure 4.4 presents the evaporation of ethanol-water droplets at different ethanol starting concentrations. A number of droplets of similar initial volume have been displayed: the 18%v, 28%v and 58%v curves came from data collected on the same day, at the same RH and on substrates prepared at the same time.

In line with expectations the evaporation rate is fastest just after the droplet is deposited, when it has the highest ethanol concentration as well as the greatest radius. The vast majority of droplets experimented with had a starting concentration of 50%v, therefore an example of one these more typical droplets has been included. This other droplet has contact angle behaviour more typical of my ethanol-water experiments as a collection. After a period of pinned evaporation

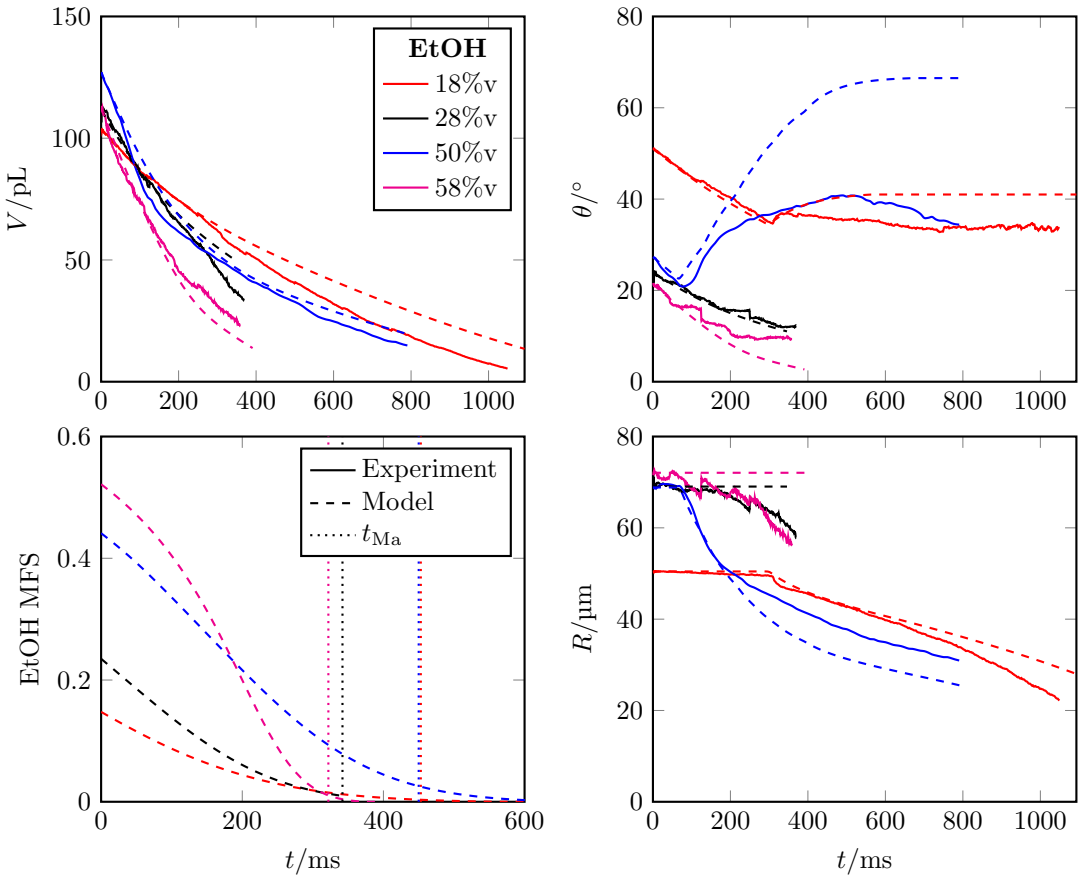

Figure 4.4: Evaporation of ethanol-water droplets of different starting ethanol concentration: 18%v (red), 28%v (black), 50%v (blue), 58%v (magenta). Droplets all contained particles and evaporated on Decon-cleaned substrates at $RH \approx 35 \pm 4\%$. Experimental data (solid lines), model results with experiment starting conditions (dashed lines), time at end of Marangoni flows, t_{Ma} (vertical dotted lines). The 50%v droplet came from experiments at an earlier time while the others were on the exact same substrate.

at early times the contact line becomes unpinned; as ethanol has evaporated from the 50%v ethanol-water droplet the surface tension increases, which leads to an increase in the contact angle so that this example droplet ends up evaporating more slowly than the 28%v ethanol droplet. The contact angle behaviour at the other concentrations where both radius and contact angle decreased after the pinning period is atypical of my general results (perhaps a result of less effective cleaning of the substrates that week) and is poorly handled by the model (in that if the contact radius was not forcibly fixed the resulting curve was a very poor

match to experiment) although some general trends are still captured.

The model used to generate the dashed lines in Figure 4.4 is described in Section 2.9. To summarise there are two sets of mass loss equations for each of the volatile components with physical properties derived from the mean droplet composition. The model's inputs are taken from experiment while the contact line is forced to pin for the same duration as in the experiments. Once unpinned the contact angle adjusts to take into account the change in droplet composition over the model's timestep.

While the droplets were pinned the model performed well, matching the experimental changes in volume and contact angle/radius closely. However the red and blue lines in Figure 4.4 show that while the model handles the beginning of the contact angle adjustment following depinning effectively, it overestimates the contact angle at long times meaning that the modelled droplets evaporate more slowly than in reality.

The good match for pinned droplets suggests that the volume averaged model performs well, meaning that mixing as a result of solutal Marangoni flows is sufficient to prevent the formation of large concentration gradients. Given that there is solutal Marangoni flow there must be a surface tension, and so composition gradient, in which the contact line region is depleted of ethanol compared to the bulk. This goes some way to explaining why the model overestimates the increase in contact angle after depinning. My adjustments are based on calculating the surface tension from the mean ethanol composition. However when discussing wetting, the contact line region is of importance rather than the rest of the contact area;[152] therefore if the ethanol composition in this region is much lower than the mean composition, then the surface tension leading to the measured initial contact angle is larger. As a result the difference in surface tension between the start and the final states, where the droplet ends up as pure water in the model, is smaller so the adjusting contact angle will tend to lower values which would

better fit reality.

Another important piece of information that the model provides is the mean ethanol concentration. Despite working in volume percentages when preparing fluids, concentrations are reported as mass fractions as that is more common in the literature and so was previously used in Chapter 3. From Figure 4.4 I can estimate the remaining concentration of ethanol with the model at the experimental time at which the Marangoni flows ended, t_{Ma}. For the 18%v set the ethanol has fully evaporated while at 28%v and 58%v ethanol, the droplets still contain about 1% ethanol. For the 50%v data set the remaining ethanol concentration is above 1%. Assessing the volume fits more closely: the modelled 18%v set is much slower than experiment, therefore given that the model already suggests total ethanol evaporation then it seems reasonable to assume that the ethanol really has fully evaporated. For the 28%v set the modelled volume is also higher than the experimental droplet. Therefore the model has underestimated the evaporation, so more ethanol should have evaporated than the model predicts meaning that the predicted residue of 1% ethanol at t_{Ma} for 28%v ethanol is not reliable. For the higher ethanol concentrations (blue and magenta dotted lines) the model either still fits well (50%v), or has overestimated the evaporation rate (58%v). As the 50%v set gave a good fit then the presence of an ethanol residue is believable. At 58%v the model predicted a residue and overestimated the evaporation rate, this overestimate means that more ethanol should be present than predicted, which reinforces the idea of there being an ethanol residue.

One question arising from the match between the model and experiment is that the model used the bulk ethanol concentration of the prepared fluid. In the previous chapter Figure 3.30 showed that small droplets were susceptible to becoming depleted in ethanol from a delay at the nozzle before printing, therefore the real starting ethanol concentrations would be lower than inputted into the model. Seeing as there is still a good match then my model appears to

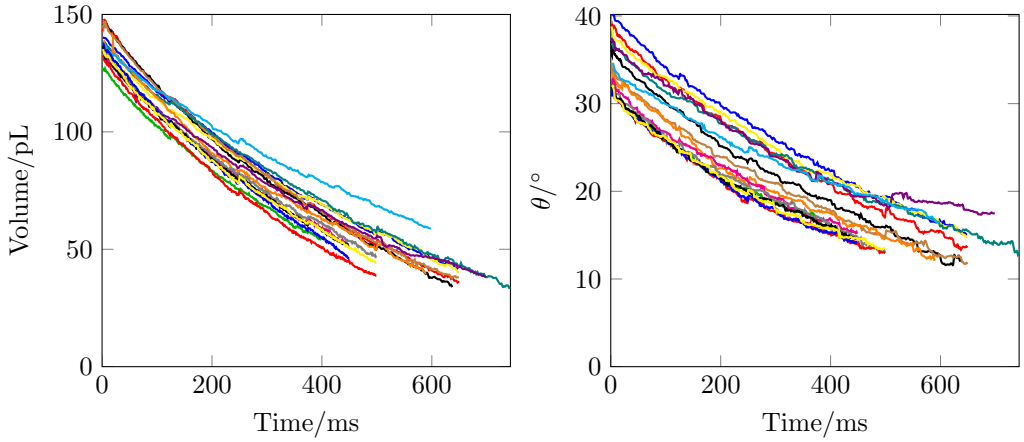

Figure 4.5: Volume and contact angles over time for 15 consecutive experiments with 50%v ethanol-water pinned droplets generated by identical voltage pulses on the same Decon-cleaned substrate, $RH \approx 35\%$, contained particles, means $\overline{V_0} = 137 \pm 1$ pL and $\overline{\theta_0} = 34.5 \pm 0.8°$.

underestimate the real evaporation rate.

In Chapter 3, consecutively printed droplets on the hemisphere gave very similar MFS evolution results, showing the reproducibility of the droplet generation method. However these examples used droplets each generated by depositing multiple droplets one after the other at a high frequency. Figure 4.5 shows how reproducible the initial volumes of single droplets were where there was no averaging of volume fluctuations by printing "> 1 Drop" droplets as in the reflectometry work. While the droplet profiles were very similar, due to slight variations in the delay between printing the actual droplet and the pre-droplet to refresh the nozzle, it is clear the starting volumes were not identical. The mean and standard error for this set of droplets were 137 ± 1 pL and $34.5 \pm 0.8°$, meaning that the percentage variation in contact angle was more than twice that of the droplet volume.

4.3.3 Reflectometry with Particles

In this section I use the Reflectometry method developed in Chapter 3 to add to the evidence for the existence of an ethanol residue persisting at the end of

Marangoni flows. Given that 50%v ethanol systems were mainly studied on the main printing rig this was the concentration tested. The moment the Marangoni flows ended was determined by looking frame by frame for the time at which particles were distinguishable. As the frame rate of the alignment camera is not high, only 30 fps, then when solutal Marangoni flows were ongoing the particles moved too fast to be captured, instead appearing as a mass of streaks. Therefore the time at which the flows ended could be found to within 60 ms.

The reliability of the results presented in Figure 4.6 appears good as the composition curves appear similar to those of mixtures without particles. The results with higher particle concentration also appeared fine at early times although the end reflectances, when the change in signal slowed, seemed too high. This was possibly a result of particle scattering as when droplets dried it was very obvious that higher particle concentrations lead to drops in the measured V_{on} (the baseline signal with no droplet present) of up to 20%.

The results presented in Figure 4.6 support the conclusion that there is a residue of ethanol present at the end of Marangoni flows and quantifies it to be in the range of $3 - 5$ wt%, about the same as experiments without particles.

In the smaller droplets the flows end as the change in ethanol mass fraction levels out, this is not unexpected as if flows were still ongoing then the fluid layer at the interface being measured would get mixed with the ethanol-deficient surface so the ethanol concentration would decrease further. In the larger droplets there are still changes in composition after the end of Marangoni flows. From the recordings of the alignment camera I know that these particular droplets were deposited off-centre, with the droplet only just covering the laser spot (while the smaller droplets needed to be directly over the laser spot to collect a usable signal). Therefore that the ethanol concentration continues to evolve after the end of Marangoni flows is potentially a result of where in the droplet is being measured. When measuring the composition near the centre of the droplet's

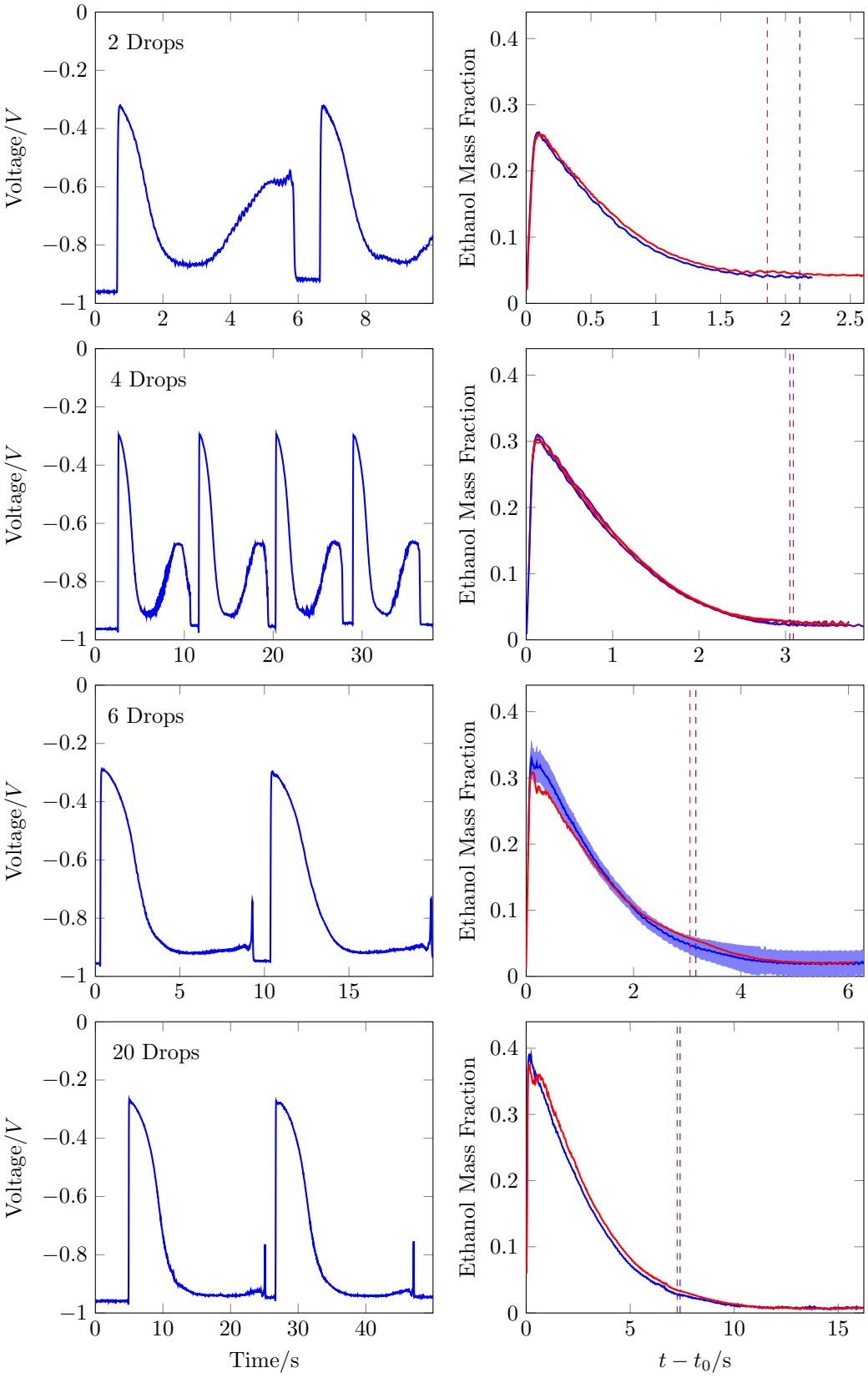

Figure 4.6: Raw signals and time evolution of ethanol mass fraction for nominally 44 wt% (50%v) ethanol droplets containing PS particles. Vertical dashed lines for end of solutal Marangoni flows. From Chapter 3: the first droplet is blue while later droplets are increasingly red.

footprint, once the flows end then ethanol-depleted fluid near the contact line will not get transported across the investigated region. However when investigating the region near the contact line the remaining ethanol residue can still diffuse/convect to the liquid-vapour interface and evaporate.

That the mass fraction of ethanol decreases more slowly with time agrees with the results of Chen *et al.*[105]. They also found that it took a long time for the ethanol to disappear entirely from the substrate region although with the presence of the reflectance anomalies those results cannot be corroborated by this work. However in their study they used IR measurements and when they were unable to detect vortices with an IR camera they suggested the Marangoni flows had finished, given those times and their presented ethanol composition curves they expected much larger fractions of ethanol at the substrate to still be present, upwards of 20% for 50 wt% drops which is much higher than in these results. This discrepancy could be a result of their thermal vortices not being the same as the Marangoni flows that reported here; the strong solutal-driven flow might have evened out temperature differences across the surface before extinguishing.

4.3.4 Model Comparison to Reflectometry Results

Following the same approach as in Section 3.7.1, the ethanol mass fraction data can be compared against outputs from the volume-averaged evaporation model with estimated inputs based on calibration measurements. Figure 4.7 shows that the model could generate a good match to the data for droplet volumes equivalent to 2, 4 or 6 Drops. It is interesting to note that for the 2 and 4 Drops droplets the model MFS was close to zero at the experimental end of Marangoni flows while the larger 6 and 20 Drops droplets still had some residue. This reflects how there are likely to be larger ethanol residues at the end of Marangoni flows in larger droplets as the same surface tension difference is spread out over a larger physical distance, making it harder to achieve any critical gradient to maintain

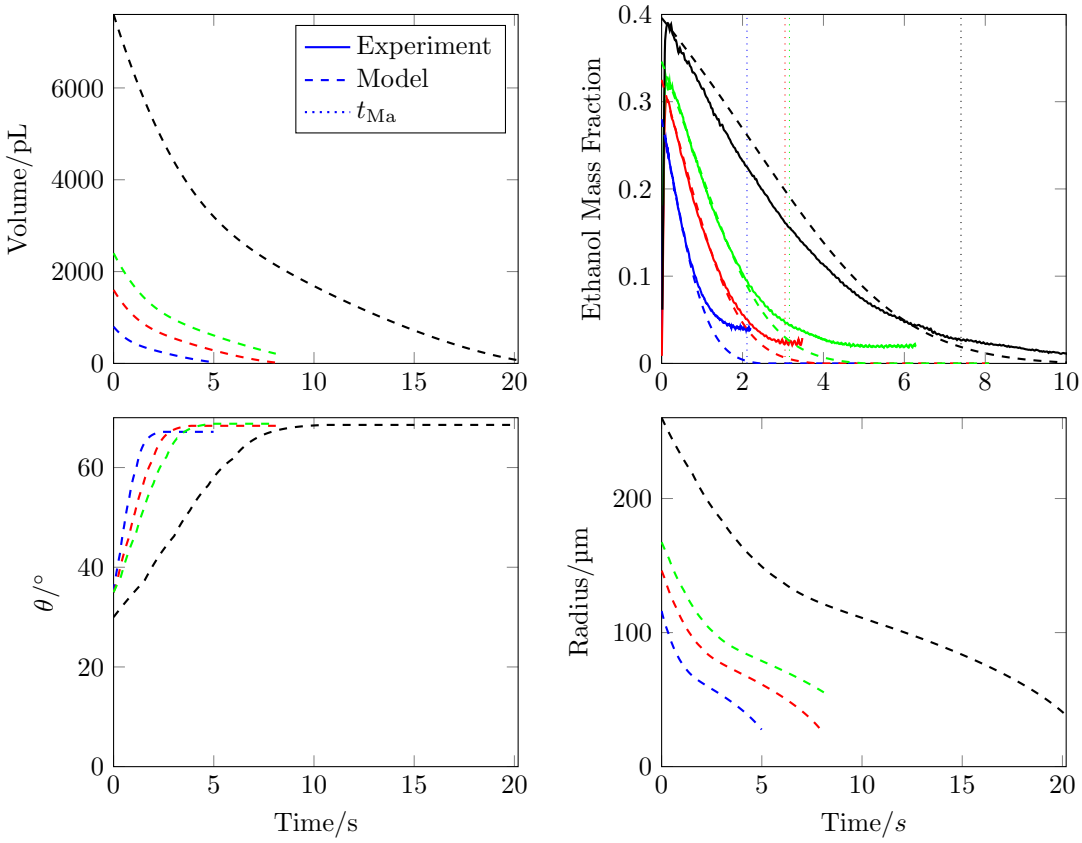

Figure 4.7: Comparison between experimental (solid) ethanol MFS results for droplets containing particles and output from volume-averaged model (dashed). Dotted lines show the time at which solutal Marangoni flows were observed to cease. Subplots in the same row correspond to the same nominal starting concentration of ethanol. Within each set there are a range of volumes: 2 Drops (blue), 4 Drops (red), 6 Drops (green) and 20 Drops (black). Prepared fluid was 0.44 MFS ethanol.

recirculatory flow, so flows die out sooner.

4.3.5 End of Marangoni Flows

Critical Composition - Reflectometry

The above reflectometry results provide real composition measurements to use as a basis for estimating the surface tension gradient and solutal Marangoni number at the time when the Marangoni flows ended. At this time the Marangoni number would have dropped below what I describe as some critical value for

continuing flow. The following calculation uses data from the "20 Drops" set (i.e. black line in Figure 4.7) where the flows end 36% through the droplet's drying time. For results for 50%v ethanol pL droplets on HMDS-treated glass coverslips I can estimate a contact angle of 30°. As the droplet is not towards the end of its drying time then the volume decreases approximately linearly, thus $V_{\mathrm{Ma}} \approx 0.36\ V_0$. Given $RH \approx 30\%$ I could apply the volume-averaged model so that I would expect an ethanol concentration of 3 wt% as the flows ended. For a further timestep at this point $\Delta m_{\mathrm{H_2O}} \approx -12$ ng, $\Delta m_{\mathrm{EtOH}} \approx -2$ ng over 31 ms (time interval in 20 drop measurement; compared to a total droplet mass on the order of 2900 ng). While the model used Popov's equations,[31] in the following I use the more direct equations from Hu and Larson[30] to avoid considering integrals over toroidal coordinates. Thus

$$J = J_0(1 - \widetilde{R}^2)^{-\lambda} \tag{4.1}$$

where the exponent $\lambda = (\pi - 2\theta)/(2\pi - 2\theta)$ and $\widetilde{R} = R/R_0$

$$\frac{dm}{dt} = \int_S \mathbf{J} \cdot \mathbf{n}\ dS = \int_0^1 2\pi \widetilde{R} J \sqrt{1 + \left(\frac{\partial h}{\partial \widetilde{R}}\right)^2} \tag{4.2}$$

From Equation 4.1 the evaporative flux near the contact line ($\widetilde{R} = 0.99$) is over three times higher than at the apex ($\widetilde{R} = 0$). Using the mass changes of the water and ethanol components I can do a numerical integration of Equation 4.2 to approximate the mass loss of each component at the contact line compared to the apex. In the integration I only went up to $\widetilde{R} = 0.995$ to avoid the divergence in the evaporative flux; the flux equation diverges in an integrable way meaning that I can truncate the radius without introducing significant errors.

As the droplet is thickest at the apex I use the approximation that the composition is unchanged over the timestep considered so the composition at the apex is still 3 wt%.

The region $\widetilde{R} > 0.95$ in the right hand plot of Figure 4.8 corresponds to

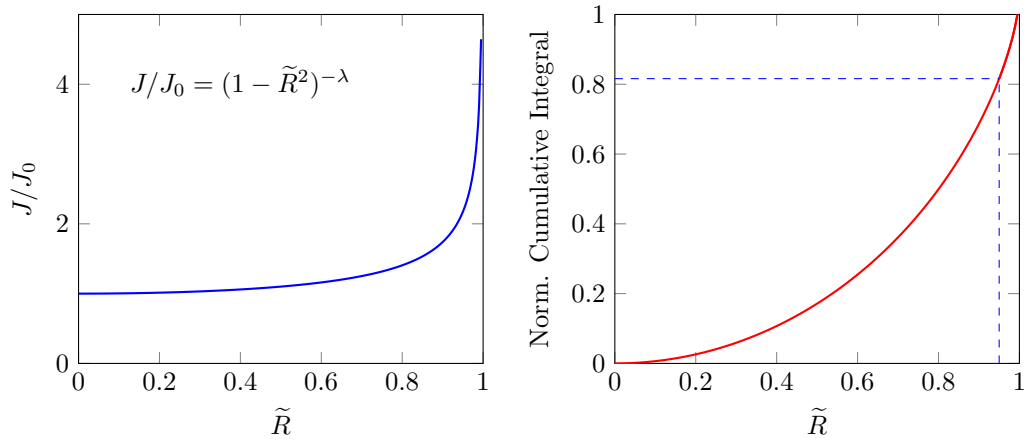

Figure 4.8: Spatial variation of theoretical evaporative flux ($\theta_{\text{drop}} = 30°$) following Equation 4.2. In the right hand plot the function in the left hand plot was numerically integrated from 0 to $\widetilde{R}$ and normalised by the value of the integral with limits $0 \leq \widetilde{R} \leq 0.99$. This shows that while the flux is highest at the contact line, the total evaporative flux mostly comes from the rest of the droplet.

approximately 20% of the mass loss calculated by Equation 4.2. Therefore over this region the mass change would be $\Delta m_{\text{H}_2\text{O}} \approx -12/5$ ng, $\Delta m_{\text{EtOH}} \approx -2/5$ ng. From a similar integration of the height profile I find that this same region of the drop holds 4% of the total volume of the droplet so given the density of a 3 wt% the total mass of this region of the droplet is 11 ng. For the above mass loss of ethanol all the ethanol would be lost from the contact line region within 25 ms. As a result this calculation leads to Bennacer and Sefiane's assumption[149] in calculating Marangoni numbers as the calculated surface composition difference is between a bulk composition at the apex and water (fully ethanol-depleted fluid) at the contact line.

Bennacer and Sefiane[149] argued that the relevant critical control parameter to describe whether solutal Marangoni flows dominated over convective flow was the ratio of the Marangoni and Reynolds numbers. We instead formulate a different Marangoni number (to Equation 1.22) which relates the Marangoni flows

to evaporation-driven convective flows in a single parameter:

$$Ma_S = \frac{d\sigma}{dc}\frac{h\Delta c}{R\eta}\frac{h}{RE}, \tag{4.3}$$

where the aspect ratio $\frac{h}{R}$ comes from the fact that the surface tension gradient is in radial direction while the height is required to determine the flow speed (see Appendex B), while the $\frac{R}{D}$ factor in Equation 1.22 is replaced by a dimensionally consistent factor of $\frac{1}{u} = \frac{h}{RE}$ where E is the evaporation rate in a vertical capillary and the aspect ratio h/R converts to a horizontal (radial) direction. Using typical droplet dimensions and a value for E of $30\,\mu m\,s^{-1}$ (estimated in Section 3.7.4) then the Marangoni number is very large, approximately 10^5, for a form of the Marangoni number where a value of 1 is expected at the end of Marangoni flows. This suggests that the inputted surface tension gradient is too large as otherwise further solutal Marangoni flows would be expected. The whole concept of a 'critical' value is also a little problematic for ethanol-water mixtures as at low ethanol concentrations a concentration difference of fixed magnitude (for example 2 wt%) would give a larger surface tension gradient while the other physical properties such as viscosity hardly changed (see Figure 4.2). This would result in the Marangoni number at the time the flows ended being larger than earlier times during the droplet's evaporation. Combined with the lack of agreement between experiment and the magnitude of modelled Marangoni flow in the literature[35,43] I do not find the current Marangoni number useful. This work should act as motivation for theoreticians to rework the Marangoni number for evaporating droplets as the idea that the concentration gradient is destroyed by diffusion does not seem effective, the destruction of the concentration gradient arises from the motion of the surface as a result of the flows compared to how quickly the concentration gradient is generated by evaporation.

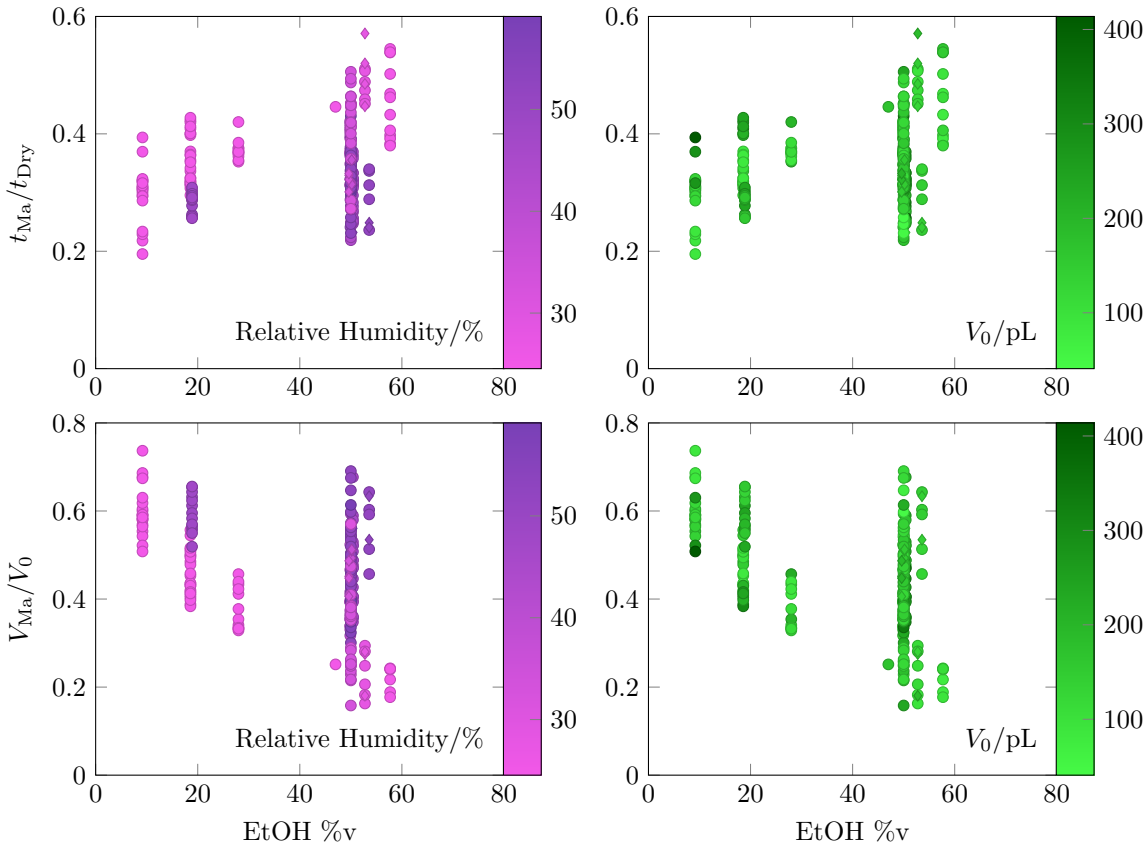

Figure 4.9: Normalised times (top row) and volumes (bottom row) at which solutal Marangoni flows were observed to end in ethanol-water droplets on Decon-cleaned (circle markers) or HMDS-treated (diamond markers) substrates. Two colourmaps are used to show the relative humidity (purple) at which experiments took place and the starting volumes (green).

Printing Rig Experiments

For this section I measured when the turnoff in Marangoni flows occurred and the state of the droplet at that time during experiments on the main printing rig with picolitre ethanol-water droplets.

Figure 4.9 shows the fraction of the drying time at which solutal Marangoni flows ended and remaining fraction of the droplet volume at that time. The two colourmaps allow for trends in volume and relative humidity on these parameters to be observed. As the end of Marangoni flows is related to the near complete evaporation of ethanol within a droplet these parameters are necessarily

dependent on the ethanol concentration. Droplets with a higher starting ethanol concentration have longer lasting Marangoni flows, and as a result the fraction of the droplets' volumes remaining at that point will decrease as the longer time means more evaporation can occur. Aside from these points the scatter in the figure makes more quantitative analysis pointless.

In the commonly reported stages of drying of ethanol-water drops, the evaporation of ethanol dominates in the first stage. However the water component also evaporates at the same time so the droplet volume remaining after the end of the Marangoni flow is lower than the starting volume of water in the droplet. The ethanol component evaporates into an environment devoid of ethanol at long distances, however water vapour is present in the air so the remaining volume is strongly dependent on the relative humidity. The bottom left plot of Figure 4.9 shows that for droplets around 50%v ethanol the volume remaining at the end of solutal Marangoni flows, V_{Ma}, is noticeably larger when high relative humidity suppresses the evaporation of water (darker purple markers).

4.3.6 Flows, Migration and Deposits

In this section I discuss the direction and velocities of Marangoni flows during evaporation and relate the flow behaviour to the actual deposits of suspended particles found after drying.

During a droplet's evaporation both ethanol and water are evaporating, with the ethanol evaporating more quickly. As a result the contact line, where there is the greatest evaporative flux, becomes deficient in (lower surface tension) ethanol relative to the rest of the droplet interface. Consequently the solutal Marangoni flows travel from the more ethanol-rich apex to the contact line along the liquid-vapour interface (see Figure 1.6B). In these videos the drying droplets are viewed through the substrate; the substrate can be moved up and down through the focal plane of the objective lens to focus on either the apex or the substrate (the

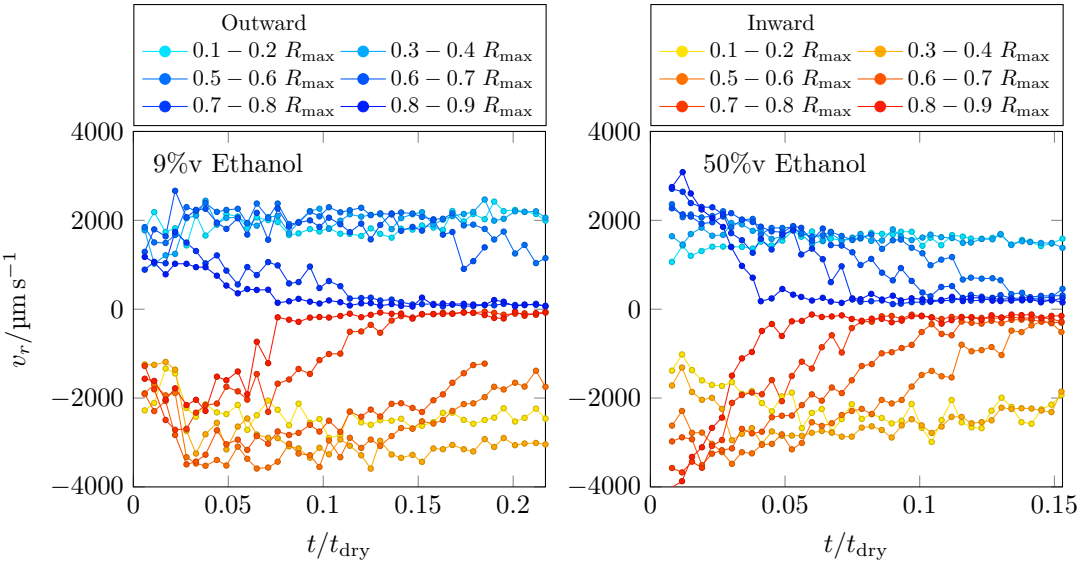

Figure 4.10: Particle velocities over time within radial bins (see legend) for droplets of different ethanol concentrations (left 9%v, right 50%v) on Decon-cleaned substrates, $RH \approx 40\%$.

droplets are too thin for mid-droplet focusing) to verify that the observed flows acted in the same direction as predicted.

Figure 4.10 displays some PIV results for two droplets with different ethanol concentrations. The droplets chosen had pinned contact lines as well as axisymmetric internal flows, making them good candidates for tracking. A comparison of the two plots shows that the overall average binned velocities at early times of drying are similar (individual particles were also be measured travelling at up to $8\,mm\,s^{-1}$ in both directions), this suggests that the magnitude of the surface tension difference that is established during evaporation is not strongly dependent on the starting concentration for this low viscosity fluid. The particles began circulating almost instantaneously with velocities on the order of millimetres per second; these velocities are in line with the results of Talbot[88] but higher than the velocities presented in microlitre droplets in the work of Kang *et al.*[147] and Christy *et al.*.[141] Compared to these other works, here the particles settle into a single toroidal axisymmetric vortex (i.e. without the multiple vortices in the contact line regions of Christy *et al.*[141]) near instantaneously (although its centre

is not stable immediately) .

The measured inward (red, negative) velocities in Figure 4.10 are larger than the outward (blue, positive) flows. From a lubrication model the outward average particles speeds would be expected to move twice as fast (as the sum of velocities at a point is zero and the inward motion occurs over two thirds of the droplet height, i.e. twice the height accorded to outward flow so the inward flow speed would need to be half that of the outward flow; see Appendix B), with the fastest particles moving outwards along the liquid-vapour interface and the slowest inwardly moving particles subject to the no-slip boundary condition at the substrate. A contributing factor to the inward particles instead being found to move more quickly is that the droplets are viewed through the substrate: the outwardly moving particles follow curved streamlines along the liquid-vapour interface, so that in a projection from below the particles appear to cover less distance; however this would not account for the divergence with the lubrication result as it would only reduce the velocities by $\cos\theta$. The best explanation is that the flow streamlines nearest the substrate and liquid-vapour interface are not occupied by particles as a result of particle migration. Our research group[88] observed in particle migration in inkjet-printed ethanol-water in which particles migrate to the centre of the droplets, leading to a concentrated collected group. As a result, averages taken over outward particles are missing the fastest particles while averages taken over the inward particles are not decreased in magnitude by including near stationary particles close to the substrate. Figure 4.10 only shows about half of the period of Marangoni flows (as particle migration generated particle densities are too high for the particle correlation algorithms applied to be effective so the tracking for Figure 4.10 needed to end early) so the Marangoni flows are still ongoing. As Marangoni flows are surface-driven then the surface must therefore still be moving, which is inconsistent with the algorithm output of near-zero velocities, but understandable in the context of a lack of tracer particles

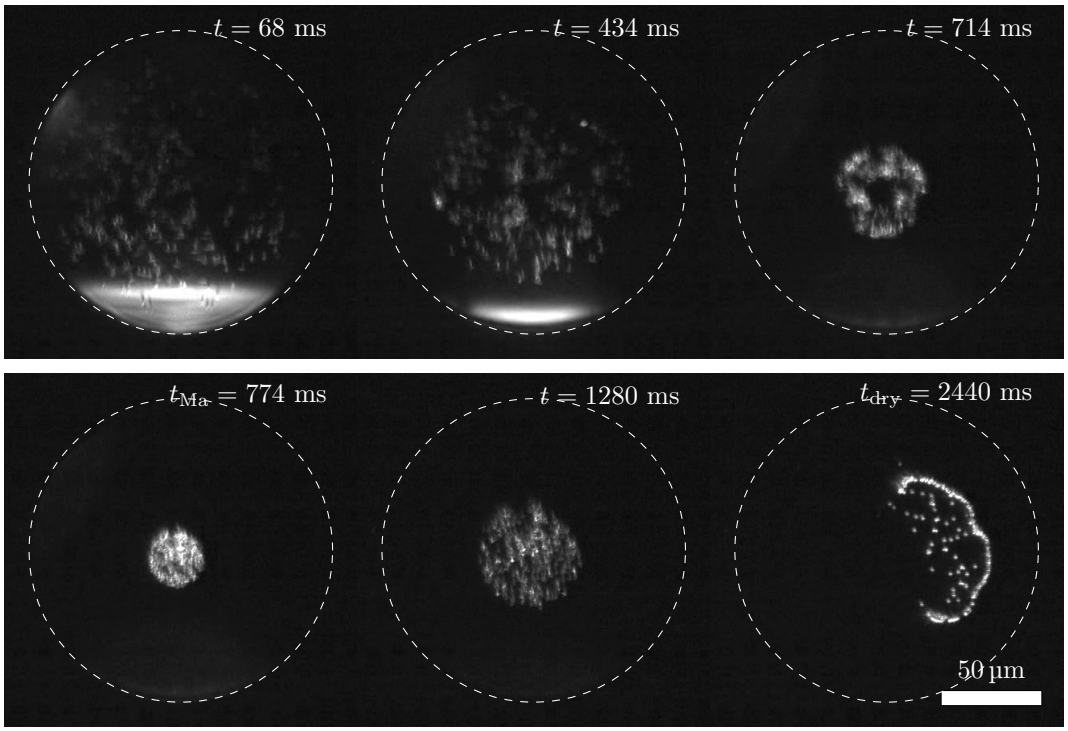

Figure 4.11: Darkfield video frames for the evaporation of a 50%v ethanol-water droplet on a Decon-cleaned substrate, $RH \approx 60\%$. Dashed white circles show position of contact line until depinning after the Marangoni flows end. Particles migrate towards the centre of the droplet, becoming most concentrated towards the end of Marangoni flows. The particles are then pulled apart by convective flow.

towards the contact line, leading to the code only taking the mean over "fake" particles where noise was incorrectly registered as a particle. Another positive for the argument that the low velocities are a function of taking the mean over fake particles is that in the right plot of Figure 4.10 the radial bin velocities approach zero over time, with further out bins approaching zero earlier. This result is consistent with particles vacating those regions over time as a result of particle migration, so that the number of true velocity measurements in a bin decreases over time until only fake transient particle measurements remain.

Frames from a bottom-view recording of an ethanol-water droplet are given in Figure 4.11 to illustrate the migration of particles towards the centre of the droplet. The particles are initially distributed throughout the droplet although over time they become more concentrated towards the centre of the droplet; however the

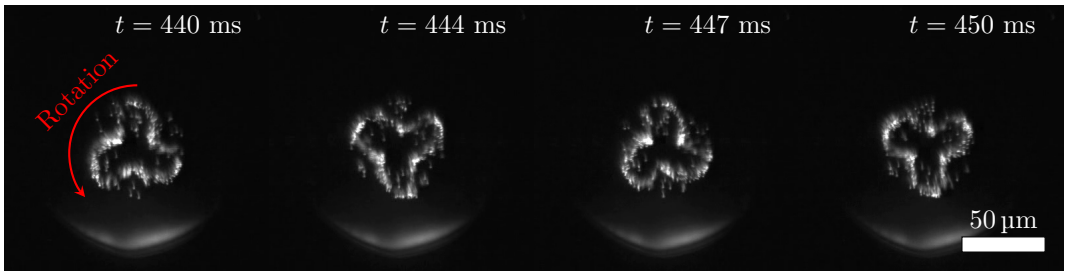

Figure 4.12: Darkfield video frames for the evaporation of a 50%v ethanol-water droplet on a Decon-cleaned substrate, $RH \approx 40\%$. The appearance of a rotating 3-arm propeller of particles developed as the particles migrated to the centre of the drop. Red arrow gives direction of rotation, half a rotation of the propeller is shown.

minimum size of the collected group is not found to coincide perfectly with the end of Marangoni flows. At high frame rates the particles at the very centre of the collected group are still circulating while the defined edge of the collected group has already begun to relax; as a result the true minimum group radius is reached a few milliseconds before the end of Marangoni flows and the group radius can be 1 or 2 microns (i.e. about 10%) smaller than at the end of Marangoni flows.

The non-uniform distribution of particles in the droplet after the Marangoni flows ended meant that convective flow was unable to lead to complete ring deposits (i.e. particles distributed along the entire circumference). A lack of particles near the contact line meant droplets did not simultaneously pin at multiple sites along the contact line so the contact line retreated unevenly, leading to partial ring deposits such as in Figure 4.11.[153] On HMDS-treated rather than Decon-cleaned substrates there was still particle migration and the collected group was of a similar size; however the end deposit was different as the retracting contact line swept particles to the centre of the droplet.

Before ending this section I recount an interesting unexplained phenomenon. For the 50%v ethanol-water experiments I collected upwards of ten examples across multiple days in which there were "propellers" as the particles migrated to the centre of the droplet. Figure 4.12 and the supplementary videos for Figures

and 4.11 4.12 show how while individual particles appeared to still move purely radially, there was the appearance of a rotating three-arm propeller. As useful analogy is a "Mexican wave" where individuals only stand up and down but a wave can propagate through a group; in the droplet the particles only give the impression of rotating as the rotation is transverse to their actual radial motion.

4.4 Ethanol Vapour

In this section I describe experiments with water and ethanol-water droplets evaporating in an ethanol-rich environment generated according to Section 2.8. I first discuss experiments in the literature on the interaction of droplets with ethanol vapour before presenting my own data including droplet profiles during evaporation, deposits and flows.

4.4.1 Literature

Liu *et al.*[99] used controlled gas flows to add ethanol to the environment of evaporating water or ethanol-water drops. Small amounts of ethanol vapour introduced deviations from CCA evaporation which became more pronounced with higher ethanol vapour concentration such that the volume increased at early times as a result of condensation. The presence of ethanol decreased drying times by causing the drops to spread more. By the same mechanism others found that a methanol vapour also accelerated the evaporation of water drops.[154] For ethanol-water mixtures in ethanol vapour the results were similar, to water drops in ethanol vapour, except any volume increases and surface tension changes were accordingly smaller as the drops already contained some ethanol.[99]

Majumder *et al.*[155] divided a petri dish, depositing microlitre volume drops in one quadrant on various treated substrates and filling the remaining quadrants with ethanol, methanol or isopropanol. As a result while their alloy nanoparticles

would simply settle in standard experiments with water, the presence of alcohol vapour lead to strong internal recirculating flows which kept the particles suspended, resulting in wider (from spreading), uniform deposits. This outcome relied on the vapour being present until the end of drying, if the vapour was removed once the drop finished spreading or the other quadrants were instead filled with water (to test if slowing the evaporation was enough to achieve uniform deposits) then ring deposits returned.

More recently Malinowski *et al.*[156] used a suspended needle to act as a localised ethanol vapour source to control particle deposits. The needle's positioning led to there being a lower surface tension at the apex, and so solutal Marangoni flows from the apex to the contact line along the liquid-vapour interface. Within a certain distance of the apex they reported that the induced recirculation totally disrupted the development of a ring deposit, instead concentrating particles at the apex. The particles attraction to the needle's location could be used to pattern the deposit if the needle was moved during evaporation, or if there were multiple needles. Kabi *et al.*[157] instead lowered a pendant ethanol drop from a needle over an elongated water drop, leading to a "Moses Effect" as the induced Marangoni flows split the drop as fluid vacated the region nearest the ethanol source.

Hegde *et al.*[158] created a non-uniform ethanol environment by printing a second ethanol drop at fixed distances from a water drop on a superhydrophobic substrate. During the ethanol adsorption stage, a Marangoni flow away from the ethanol source along the liquid-vapour interface developed. Once the ethanol drop evaporated the ethanol in the water drop desorbed, leading to flow reversal, then chaotic flows, before finally reverting to buoyancy-driven flow in the total absence of ethanol. The process was explicitly desorption rather than condensation as they expected very little ethanol to be present in the water drop.

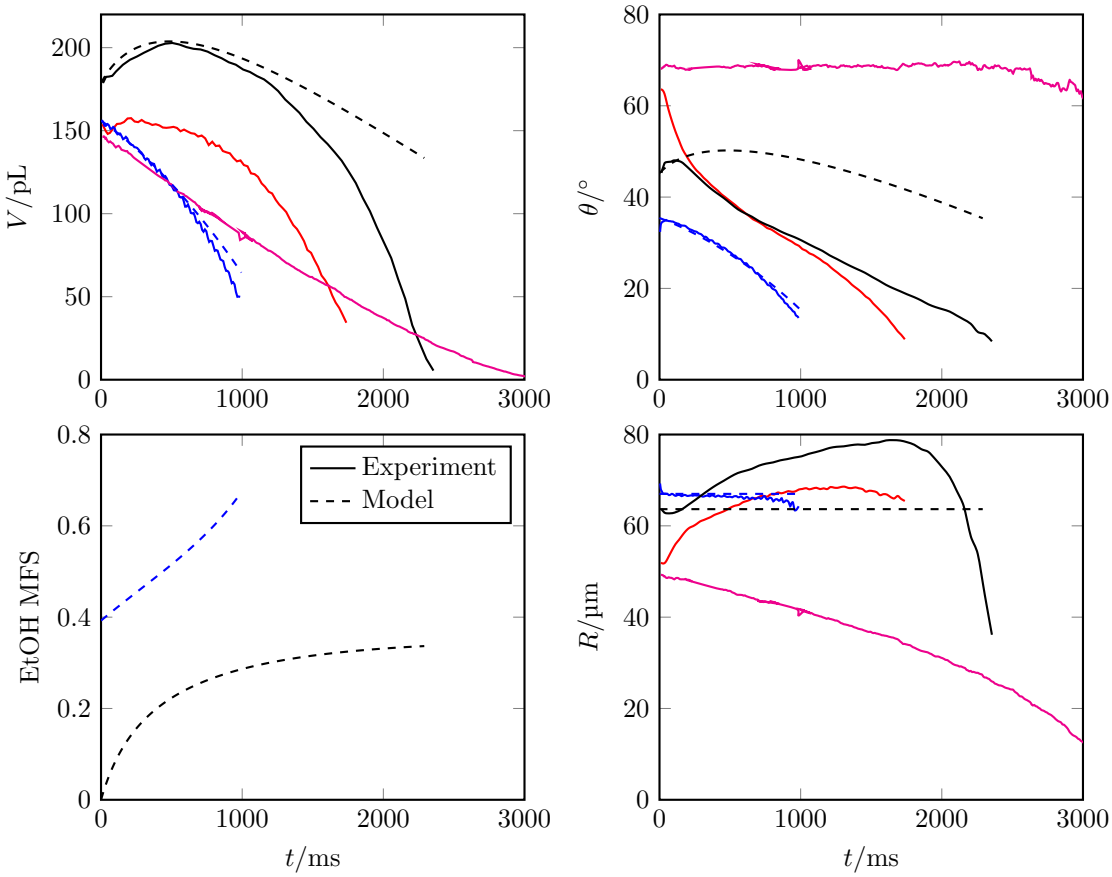

Figure 4.13: Comparison of droplets evaporating in the presence of ethanol vapour on HMDS-treated substrates. Experimental data are given by solid lines, modelled results by dashed lines. In order of ascending drying time the drops refer to: blue - 50%v $RH = 35\%$ (ethanol content) $a_{\mathrm{EtOH}} = 0.4$, red - water $RH = 35\%$ $a_{\mathrm{EtOH}} = 0.4$, black - water $RH = 60\%$ $a_{\mathrm{EtOH}} = 0.4$, magenta - water $RH = 60\%$ $a_{\mathrm{EtOH}} = 0$ (no ethanol vapour).

4.4.2 Evaporation

In this section I present the first experiments to our knowledge of inkjet-printed droplets evaporating in a vapour field of solvents other than water, and the impact of the resulting condensation of ethanol onto the picolitre droplets.

Figure 4.13 shows some typical droplet profiles for water or ethanol-water droplets evaporating in an ethanol environment. To generate the dotted lines I use the same model as introduced in Section 2.9 where $a_{\mathrm{envir}}^{\mathrm{EtOH}}$ in Equation 2.8 is no longer zero so the mass of ethanol has the potential to increase due to

condensation. The ethanol-water droplet (blue) still evaporates more quickly than a water droplet (red) when both are in similar ethanol enriched environments. This difference arises because there is less condensation onto the mixture droplet as it already contains ethanol, while the ethanol component of the binary droplet still evaporates more quickly than water in these experiments. Comparing the red and magenta lines, for water droplets with and without ethanol vapour, there are obvious changes to the evaporation profiles; at early times the pure water droplet evaporates more quickly while one in an ethanol environment increases in volume as a result of condensation. However at late times the increase in volume is offset by much faster evaporation as the lower surface tension leads to spreading. This spreading behaviour is difficult to capture within the current model as the change in contact angle is a result of changes in liquid-vapour surface tension without knowledge of how the liquid-solid surface tension would change with ethanol concentration. Therefore to avoid unphysical superspreading, as a small addition of ethanol to pure water leads to large decreases in the liquid-vapour surface tension so that the droplet artificially becomes completely flat within a second, I forced the droplet to evaporate in an unrepresentative CCR evaporation mode (for a better fit the solid-liquid surface tension must also need to be considered). Despite this the model is able to achieve a qualitative match, capturing the different evaporation profiles of droplets where the volume change is not monotonic as a result of condensation.

The red and black curves are both of water evaporating in an ethanol environment except with different water relative humidities of 35 and 60% respectively. The impact of this increase in RH is that the ratio of maximum volume to initial volume increases. This is a consequence of the evaporation of water slowing down while the condensation of ethanol onto the droplet is unchanged, meaning that the total increase in volume at early times is greater. The final feature of Figure 4.13 is that when ethanol is present in the environment the mass fraction of ethanol

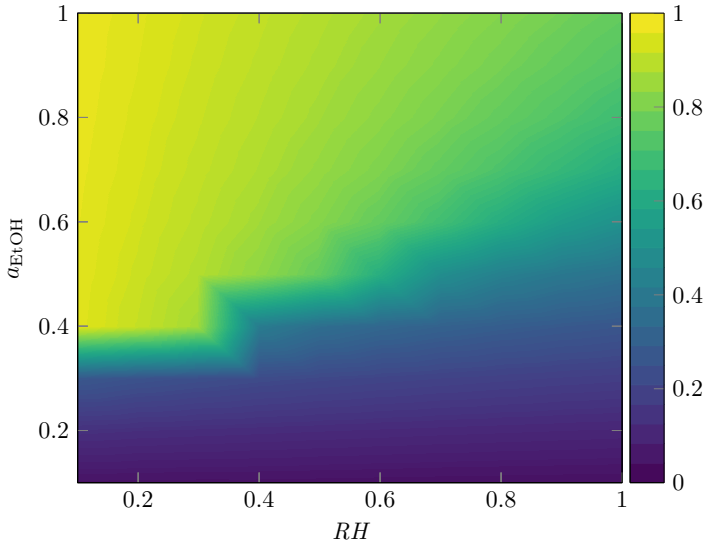

Figure 4.14: The ethanol mass fractions of ethanol-water droplets evaporating in an ethanol-rich atmosphere once the droplets equilibriate with the environment. The relative humidity RH and the ethanol equivalent to relative humidity for ethanol, a_{EtOH}, were both inputted into the model in steps of 0.1.

is always monotonically increasing.

Figure 4.14 shows the surface of calculated ethanol mass fractions at which mass fraction of evaporated fluid equals the mass fraction of the evaporating droplet so the composition of an evaporating droplet no longer changes over time. This is the origin of the result in the bottom-left MFS plot in Figure 4.13 where the increasing ethanol mass fraction black set at $RH = 60\%$ bends back towards the x-axis while the blue set at $RH = 35\%$ ($a_{\mathrm{EtOH}} = 0.4$ for both) has an ethanol mass fraction increasing more rapidly over time. The surface in Figure 4.14 shows that at low RH and $a_{\mathrm{EtOH}} = 0.4$ all the water will evaporate until the droplet is essentially pure ethanol (yellow) while at higher RH there is the possibility of reaching some equilibrium ethanol mass fraction.

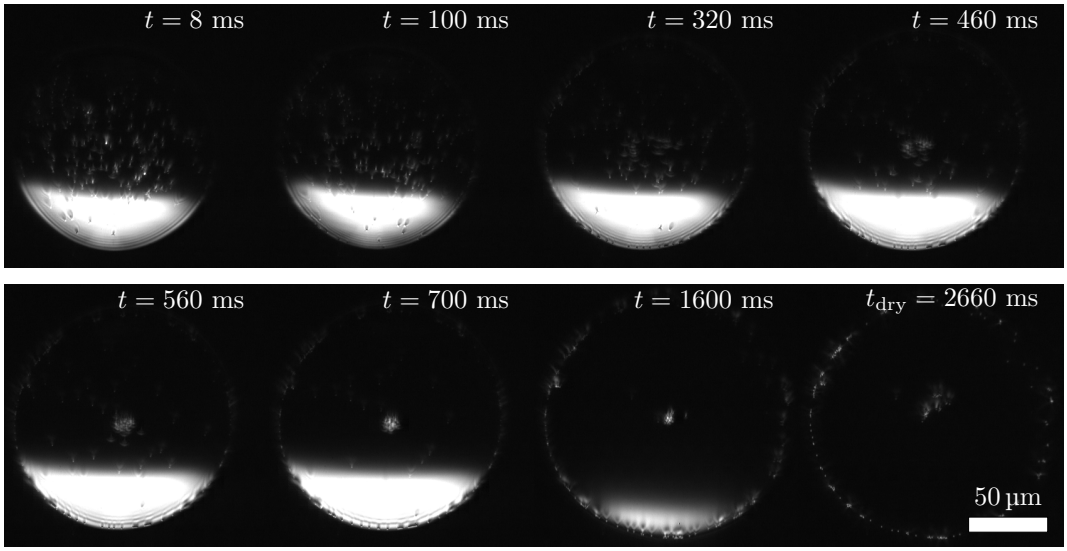

Figure 4.15: Water droplet evaporating on a HMDS-treated substrate in an ethanol-rich vapour, RH= 48%. Particles collect at the contact line and as a raft at apex of the drop, leading to a ring deposit with a central mass of particles.

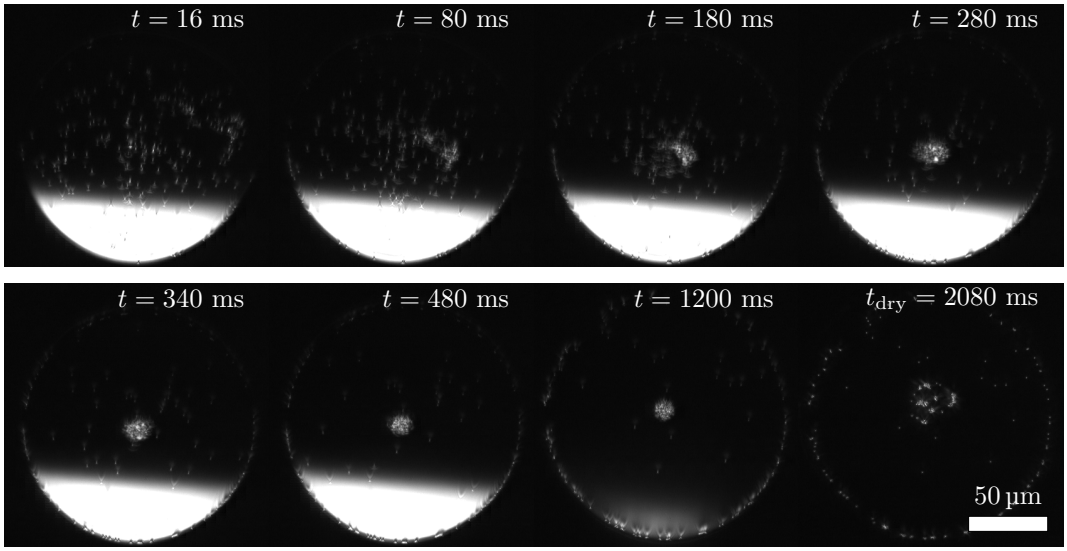

Figure 4.16: 50%v Ethanol-water droplet evaporating on a HMDS-treated substrate in an ethanol-rich vapour, RH= 62%. Particles collect at the contact line and apex of the drop, leading to a ring deposit with a central mass of particles.

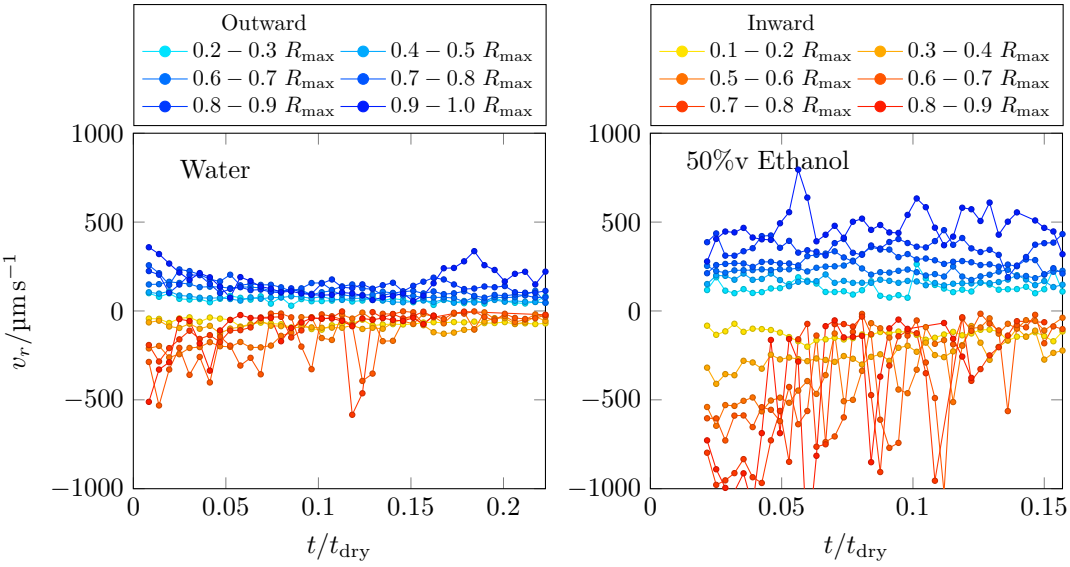

Figure 4.17: Particle velocities over time within radial bins (see legend) for water (left, same droplet as in Figure 4.15) or ethanol-water droplets (right 50%v) evaporating in an ethanol-rich environment on HMDS-treated substrates.

4.4.3 Flows, Migration and Deposits

Water droplets evaporating in air can have thermal Marangoni flows but no solutal Marangoni flows.[51,53] The addition of ethanol vapour leads to condensation of ethanol onto the water droplets. The droplet is thinnest towards the contact line so the condensation of ethanol changes the composition of the contact line region the most resulting in the contact line having a lower surface tension than the more water-rich apex. This causes solutal Marangoni flows to develop which flow from the contact line to the apex along the liquid-vapour interface. The flows in ethanol-water droplets evaporating in an ethanol-rich vapour also follow the same direction from the contact line to the apex (in these experiments where the combination of low relative humidity and high ethanol vapour density is such that the ethanol component of the droplet evaporates more slowly than the water component), the reverse of the case where no ethanol vapour is present.

Figures 4.15 and 4.16 show examples of the standard behaviour found in bottom-view recordings of the evaporation of water and ethanol-water droplets

respectively. Qualitatively the flows are the same although the Marangoni flow speeds are higher in the ethanol-water droplets as shown in Figure 4.17. This goes against expectations as larger surface tension gradients across the interface were predicted for water in ethanol vapour systems which would experience greater condensation of ethanol. From Figure 4.17 the particle velocities are on the order of 100's of microns per second, with the spikes showing the difficulties in applying PIV methods to such droplets as most of the particle motion occurs at the beginning of evaporation, with only the occasional particle acting as a useful tracer (i.e. the peaks are the only reliable measurements and the near zero measurements are the result of the code averaging over fake particles of noise). Increasing the particle concentration just made the raft lager. The highest measured outward and inward are from the radial droplet bins closest to the contact line. This is especially clear in the right plot for the 50%v ethanol droplet in ethanol vapour, which also illustrates how the fastest particle motion was inwards at the beginning of evaporation. It it worth pointing out that as the flow-directions are reversed, compared to ethanol-water droplets without an ethanol vapour environment, our previous argument about the projection through the bottom of the droplet introducing a $\cos\theta$ factor reducing the velocities would instead lower the inward velocities rather than the outward velocities from before. Combined with the fact that there are actually particles travelling along the liquid-vapour interface (where the flows are fastest according to Appendix B, bumping up the measured inward mean velocity) this results in a better match to the expected lubrication result: that the (here inward) surface-direction flows are on average twice as fast as the (here outward) substrate-direction flows.

The particles begin a little unevenly distributed when the droplets hit the substrate but quickly become uniformly distributed after a few milliseconds (note the first frames in Figures 4.15 or 4.16 are 8 and 16 ms respectively rather than the first frame recorded, i.e. 1 ms for a 1000 fps recording) as a result of mixing from

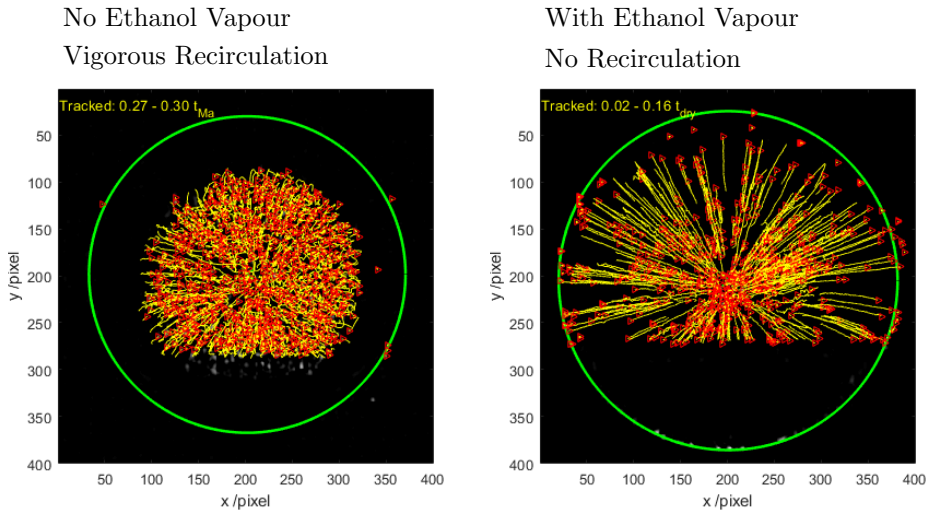

Figure 4.18: Comparison of the particle tracks from 50%v ethanol-water droplets evaporating without and with an ethanol-rich environment. A normal ethanol-water droplet shows vigorous particle recirculation even in very short time frames while the tracks when evaporating in an ethanol-rich environment as disconnected.

impact and the onset of Marangoni flows. Particles towards the liquid-vapour interface migrate to the apex, becoming increasing concentrated into a compact raft. In contrast those particles towards the substrate are carried out to the contact line where they get stuck. This is very different to the behaviour in drying ethanol-water droplets without ethanol vapour where the particle recirculate; with ethanol vapour present the particles either move to the apex or contact line, shown in Figure 4.18; after the raft forms particles are occasionally detached and are carried towards the contact line close to the substrate and sometimes back along the liquid-vapour interface, leading to the measured spikes in velocity in Figure 4.17. It is unclear from the videos whether the particles are pulled off the raft by inward flow at the surface or outward flow near the substrate. At higher particle concentrations (such that the radius of the particle raft is more than twice that of those in Figures 4.15 or 4.16) this detachment process can lead to the deposition of radial spokes outward from the central thick deposit, in addition to the ring deposit.

4.5 Ethylene Glycol Mixtures

Following the work with ethanol-water based mixtures I looked into combinations with low volatility solvents. In the literature glycerol is the most common option, however I decided upon ethylene glycol as it is directly relevant for inkjet applications as a humectant.[70] Experiments used mixtures that were mostly water so that the viscosity was lower (see Figure 4.3) to aid printing reproducibility.

4.5.1 Literature

Karpitschka *et al.*[23] studied drops of binary mixtures of fluids which individually wet a high-energy surface but when combined had an apparent contact angle. These mixtures were of water and various diols including ethylene glycol (1,2-ethanediol) which exhibited Marangoni contraction. The apparent contact angle could be modelled as a function of the relative humidity by utilising the near ideal behaviour of the diol mixtures.

Talbot *et al.*[88,159] looked into the flows of inkjet-printed binary mixtures of ethylene glycol with water or ethanol. With 10%v EG in water at early times there was relatively fast outward particle motion towards the contact line; above 50%v EG there was no evidence of any solutal Marangoni flow. For EG-ethanol droplets they found that the larger surface tension difference between ethanol and EG was sufficient to lead to some Marangoni flow.

4.5.2 Evaporation

In this section I describe the evaporation of ethylene glycol mixture inkjet-printed droplets, presenting how the droplet profiles evolve rather than only their flow directions.[88,159]

Ethylene Glycol - Water

Compared to water, ethylene glycol has a very low volatility. Therefore Figure 4.19 shows that after the water component of a droplet evaporated over a few seconds a very slowly drying residual droplet was left (see Figure 4.20 which was mostly ethylene glycol. Compared to a pure water droplet, the initial evaporation rate is slightly slower as a result of the water activity of the droplet dropping as the concentration of EG increases. That the droplet is a mixture also means that rather than evaporating in a CCA mode on a HMDS-treated substrate, the contact angle decreases over time as the droplet becomes richer in the lower surface tension EG.

To model the evaporation I apply the model from Section 2.9, making the assumption that EG is fully involatile. As a result a modelled droplet reaches an equilibrium where the concentration of EG is high enough for the water activity of the droplet to be suppressed to equal the relative humidity. In Figure 4.19 the model qualitatively captures the slow down in evaporation although the fit needs improvement; the initial evaporation rate in the model is much faster than in experiments for droplets with more than 5%v EG.

Another problem with my model is that the predicted final volumes are much lower than my experimental values; these issues suggest that the assumption of a homogeneous droplet is not fulfilled. Larger amounts of EG at the interface could suppress the local water activity and the formation of a layer, reduce transport of water molecules to the interface and so hinder evaporation as a result of the higher viscosity of EG slowing diffusive transport. Such trapping of water by an involatile component has been described in the literature, for example with glycerol,[38] which like EG is fully miscible with water, or the surfactant 1,2-hexanediol which phase separates at high concentration.[41] The formation of such a layer is feasible, assuming EG is involatile then for the changes in volume of EG-water droplets shown in Figure 4.19 the Péclet number can be calculated to assess

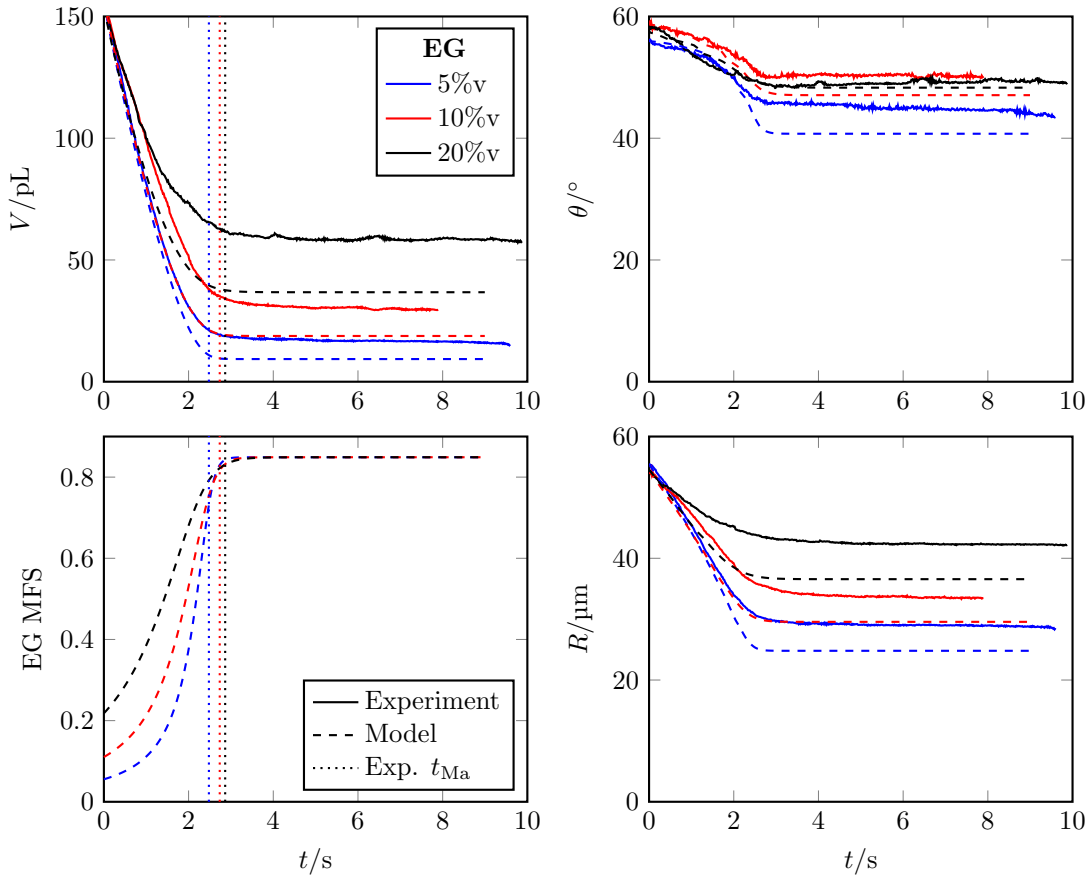

Figure 4.19: Evaporation of ethylene glycol-water droplets of different starting EG concentration: 5%v (blue), 10%v (red), 20%v (black). Droplets all contained particles and evaporated on HMDS-treated substrates at $RH \approx 38 \pm 2\%$ (no humidity chamber). Experimental data (solid lines), model results with experiment starting conditions (dashed lines), experimental time of end of Marangoni flows (dotted vertical lines).

whether diffusion occurs quickly enough to prevent the build-up of concentration gradients. The Péclet number is defined by

$$Pe = \frac{uL}{D} \tag{4.4}$$

where u and L are the characteristic velocity and lengthscale. Therefore if $Pe > 1$ then the diffusion of solute away from the interface is slower than the rate at which solute accumulates at the interface so the formation of a EG-rich layer is possible. I consider two ways of defining u and L for the Péclet number; knowing the evolution of the droplet profile the velocity can be taken as the

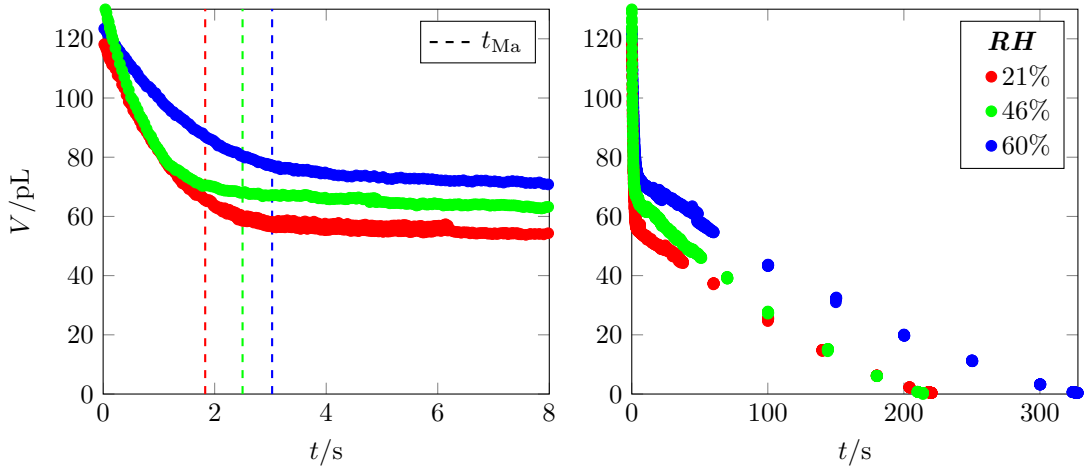

Figure 4.20: Evaporation of 27%v ethylene glycol-water droplets on HMDS-treated substrates at different relative humidities: 21% (red), 46% (green) and 60% (blue). Dashed vertical lines show the experimental end times of the solutal Marangoni flows.

rate of change of height of the droplet, in such a case the characteristic length is the height. Alternatively, for a pinned droplet the convective flow can be approximated from the rate of change of volume and the contact area of the droplet while the characteristic lengthscale is the droplet radius (this version is more commonly used to assess whether a concentration gradient can develop and generate Marangoni flow).[160]

$$Pe_h = \frac{\frac{dh}{dt}h}{D} \tag{4.5}$$

$$Pe_R = \frac{\frac{1}{\pi R^2}\frac{dV}{dt}R}{D} \tag{4.6}$$

Figure 4.21 shows that the vertical Péclet numbers were below 1 while the radial Péclet numbers were greater than 1 before the slowdown in evaporation (see corresponding volume curves in Figure 4.19). A Péclet number greater than one suggests that diffusion is not fast enough to prevent the buildup of an EG layer in our experiments, it is also worth noting that the calculation used a diffusion coefficient dependent on the mean-concentration viscosity, local EG concentrations could be higher, reducing the diffusion coefficient and so leading to larger Péclet numbers that would more strongly suggest the appearance of an involatile layer.

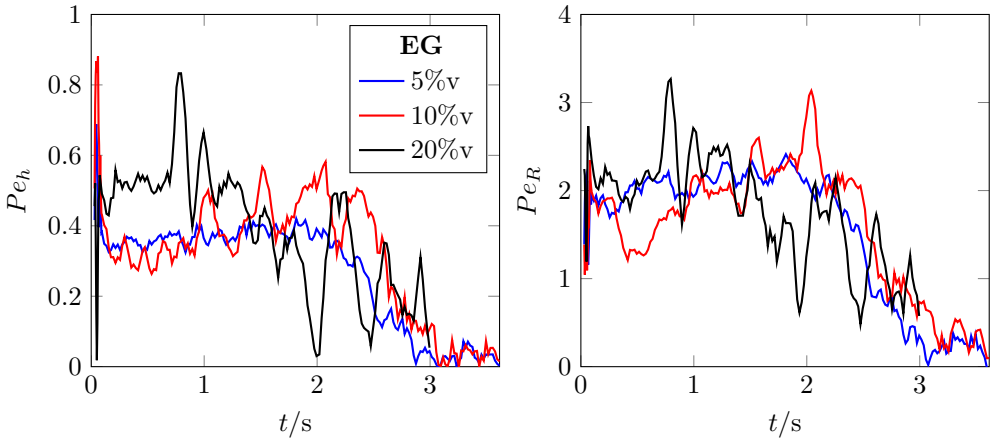

Figure 4.21: Calculated Péclet numbers for evaporating ethylene glycol-water droplets of different starting EG concentration: 5%v (blue), 10%v (red), 20%v (black), same droplets as Figure 4.19. Droplets all contained particles and evaporated on HMDS-treated substrates at $RH \approx 38 \pm 2\%$ (no humidity chamber).

This effect would also be self-reinforcing so it is still possible for a layer to develop despite $Pe_h < 1$ since the value is still close to 1. Estimations using Einstein's equation for the distance travelled in three dimensions in a random walk

$$\langle z^2 \rangle = 6Dt. \tag{4.7}$$

do not provide conclusive evidence supporting the formation of an EG-rich layer. In one second the distance travelled at the estimated diffusion coefficient is roughly equivalent to the droplet radius so some equilibriation of the concentration gradient should occur which would oppose the formation of an EG-rich layer.

If I define the "final" volume which appears constant over a 10 s timescale as V_∞ then comparing the ratio V_∞/V_0 quantifies the divergence between model and experiment in Figure 4.22 as a result of this trapped water. The modelled remaining fluid is not simply the volume percentage of ethylene glycol in the "ink". It will be slightly larger as a result of the evaporation of water from the nozzle meaning the real EG concentration is higher, but also because EG suppresses the evaporation of water. This latter cause is more important at higher EG concentrations when Figure 4.3 shows the water activity drops increasingly

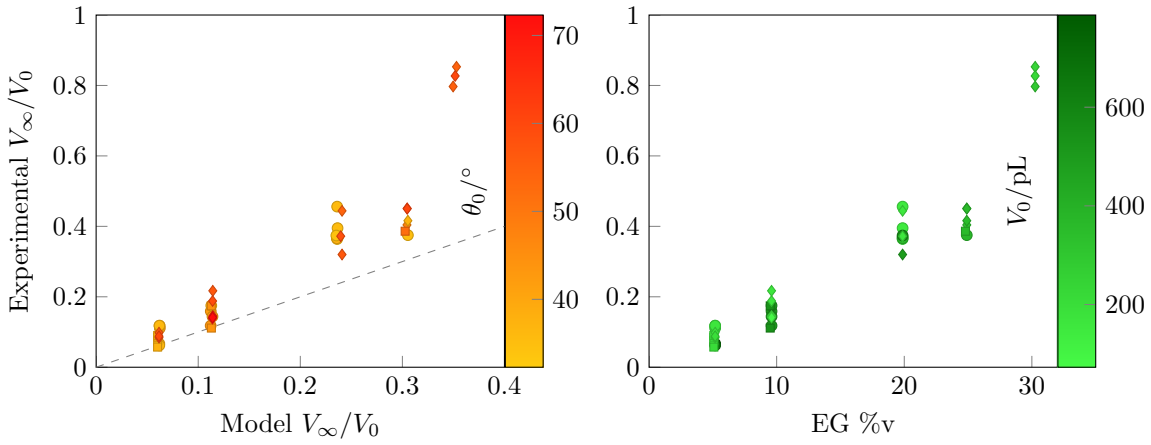

Figure 4.22: Difference between the experimental and calculated residual volumes when the evaporation rate plateaued after a few seconds of evaporation for initial concentrations between 5 and 30%v EG. The calculated residual volume were determined by considering the droplets as a homogeneous ideal mixture at the same relative humidity as the experiments, the model is seen to consistently underestimate the remaining volume. The dotted grey line is for a perfect match between experiment and my model. The marker shapes represent different substrate preparation methods: Decon-cleaned (circles), HMDS-treated (diamonds), or plasma-cleaned (squares).

quickly at greater EG concentrations.

The dashed line in Figure 4.22 acts as a baseline, showing when model and experiment would match. The amount of additional water trapped within the droplets at long times beyond that expected within the model can be large, for instance the 20%v set already has a remaining volume approximately 60% larger than predicted while the 30%v set's remaining volume was more than double that predicted. Outside the range of the Figure, at high EG concentrations (70%v) the droplet volume only decreased by 5% in the first second and a further 2% in the following 30 seconds of drying. That the experimental "final" volume increases so quickly at high EG concentrations suggests that a higher amount of EG in the droplets means it takes less time to reach a state in which an involatile layer at the interface has formed, suppressing further evaporation of volatile water.

Ethylene Glycol - Ethanol

A natural extension of the experiments with ethanol-water and ethylene glycol-water droplets was to study ethylene glycol-ethanol droplets to test for particle migration in additional systems. Here I describe the evaporation behaviour of such mixtures.

At low EG concentrations the droplets followed the same type of behaviour as EG-water droplets. There were two stages of evaporation: in the first the more volatile ethanol evaporated, in the second the droplet appeared to stop evaporating on a timescale of 10's of seconds. As ethanol is more volatile than water the first stage lasted for 100's of microseconds rather than the 1 to 2 seconds for EG-water droplets of comparable volume. The "steady" volume in the second stage was again a function of EG concentration, at high EG concentrations the droplet only decreased in volume by a few percent or even increased as evaporation of ethanol was offset by condensation of water. Overall, at low EG concentrations, the fraction of volume left after the first stage was much greater in EG-ethanol droplets than EG-water droplets. For example in the left plot of Figure 4.23 approximately two thirds of the droplet's volume remained into the second stage for a 20%v EG EG-ethanol droplet; meanwhile in Figure 4.20 depicting EG-water droplets, at a 20%v EG concentration only about 40% of the droplet remained and to match two thirds of the droplet remaining an EG-water droplet needed a higher EG concentration of 27%v (also 60% RH).

Between 30 and 40%v EG the droplets would not evaporate on a pL droplet timescale; Figure 4.23 shows that the volume actually increased over time as a result of condensation of water onto the hygroscopic droplets. As a result the droplets would contain ethylene glycol, ethanol as well as appreciable amounts of water; however I place the discussion outside of Section 4.6 on tertiary solvent systems as the condensation did not lead to significant changes to the particle flow behaviour.

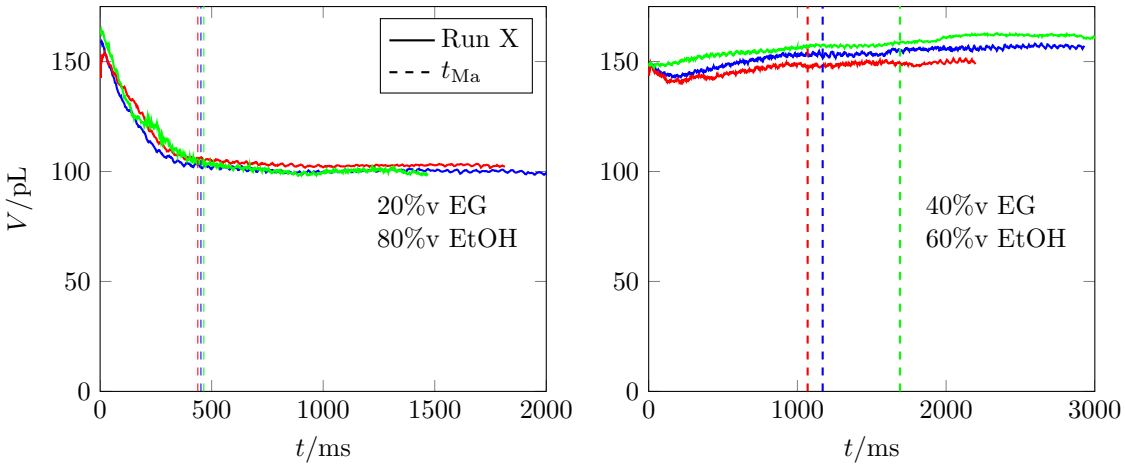

Figure 4.23: Change in volume with time for three ethylene glycol-ethanol droplets printed in the same session. EG concentrations in the plots are 20%v EG (left) and 40%v EG (right). Droplets evaporated on HMDS-treated substrates at 60% *RH*. Dashed lines for experimental end of Marangoni flows.

4.5.3 Flows, Migration and Deposits

Ethylene Glycol - Water

For an EG-water droplet, evaporation causes the contact line to become richer in EG, which is less volatile than water and has a lower surface tension. Solutal Marangoni flows go from the contact line to the apex along the liquid-vapour interface. This flow is the same direction as water droplets evaporating in an ethanol-rich vapour, although the particle velocities were approximately half the magnitude, in the range of $100 - 300\ \mu m\,s^{-1}$ (see Figure 4.27). As before the lowest velocity measurements around $\pm 50\ \mu m\,s^{-1}$ are not real and are a result of the algorithm incorrectly assigning noise as particles.

The end of Marangoni flows (shown by vertical dashed lines in Figure 4.23) preceded the transition to the slow stage of evaporation. Snapshots of the particle distribution during evaporation of ethylene glycol-water droplets are given in Figures 4.24 and 4.25. Particles initially migrated to the apex of the droplets with the raft of particles then breaking apart after the Marangoni flows finished. The collected group itself did not last in the deposit as the lack of pinning on HMDS-

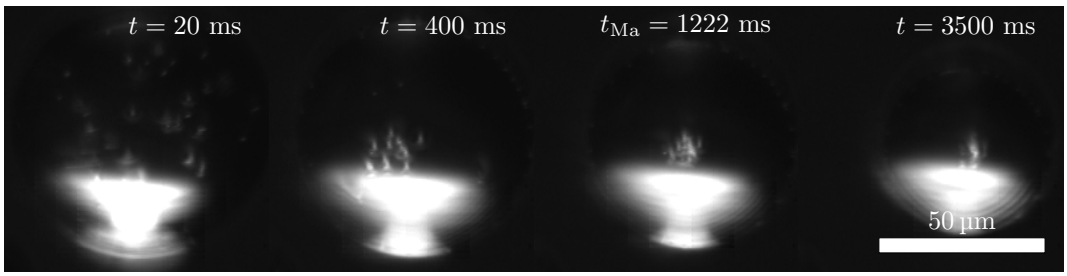

Figure 4.24: Darkfield video frames for the evaporation of a 10%v EG-water droplet on a HMDS-treated substrate, $RH = 36\%$. Particles migrate towards the apex of the droplet, becoming most concentrated towards the end of Marangoni flows. The particles are then pulled apart by convective flow.

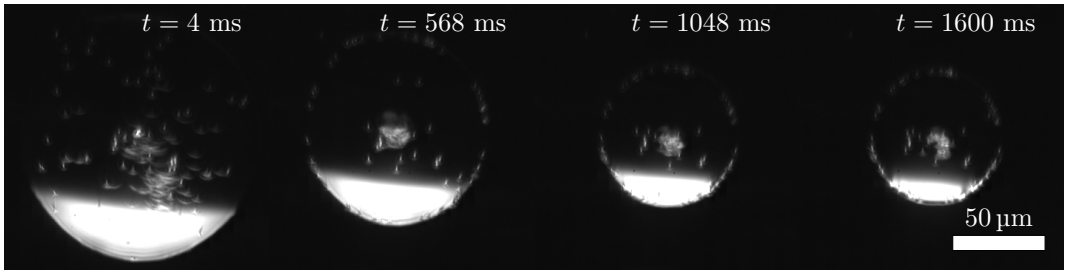

Figure 4.25: Darkfield video frames for the evaporation of a 5%v EG-water droplet on a plasma-cleaned substrate, $RH = 36\%$. Particles migrate towards the apex of the droplet and the contact line, becoming most concentrated towards the end of Marangoni flows. The particles at the apex are then pulled apart by convective flow.

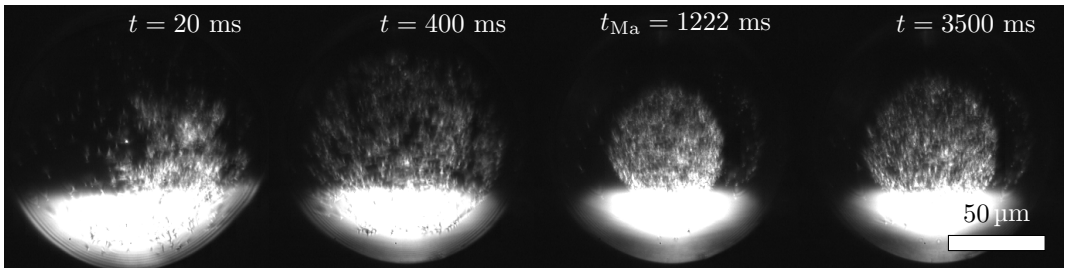

Figure 4.26: Darkfield video frames for the evaporation of a 40%v EG-ethanol droplet on a HMDS-treated substrate, $RH = 60\%$. Particles migrate towards the centre of the droplet, becoming most concentrated towards the end of Marangoni flows. The particles are then pulled apart by convective flow.

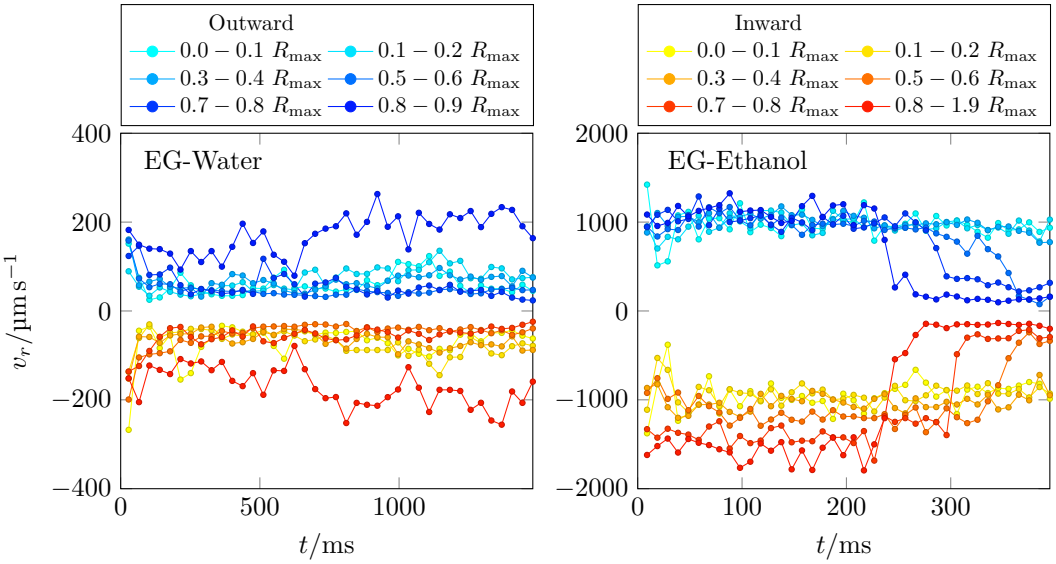

Figure 4.27: Particle velocities over time within radial bins (see legend) for a 30%v EG-water droplet (left, $RH = 35\%$, $V_0 \approx 220$ pL) and a 20%v EG-ethanol droplet (right, $RH = 60\%$, $V_0 \approx 160$ pL) evaporating on a HMDS-treated substrate.

treated substrates meant particles were swept up by the retracting contact line. On a plasma-cleaned substrate particles also accumulated at the contact line (see Figure 4.25) leading to deposits with a ring structure and broken particle rafts. At higher EG concentrations (30%v compared to 5%v in Figure 4.25) there was some spreading on plasma-cleaned substrates as a result of the droplets becoming enriched in lower surface tension EG. However this only occurred after the end of Marangoni flows, suggesting that the tendency to spread was opposed in the first stage of drying by the Marangoni contraction described by Karpitschka *et al.*[23].

Ethylene Glycol - Ethanol

For an EG-ethanol droplet the contact line becomes richer in EG as the much more volatile ethanol evaporates faster. The greater evaporative flux towards the contact line results in the contact line region having a higher local surface tension than at the apex so the resulting solutal Marangoni flows go from the apex to the contact line along the liquid-vapour interface (same direction as ethanol-water

droplets and the opposite of EG-water droplets). Figure 4.26 also shows particle migration to the centre of the droplets towards higher ethanol concentrations. As in EG-water droplets, the end of these solutal Marangoni flows is associated with the transition in evaporation rate; however Figure 4.23 shows that the picture was complicated at higher EG concentration and relative humidity by the condensation of water, in such cases it makes more sense to consider the droplets as having three components. Another difference to ethanol-water droplets is the lower particle velocities (see Figure 4.27) as a result of increased fluid viscosity and that pure EG is much closer in surface tension to ethanol than water so it was harder for large surface tension differences to develop.

The fast solutal Marangoni flows have little impact on the end deposit. The ethylene glycol evaporates very slowly, meaning that there is enough time for the collected group to be fully dispersed by Brownian motion before the droplet fully dries. Therefore the morphology of the deposit depends on whether or not the contact line pinned due to particles: a lack of pinning on HMDS-treated substrates led to particles getting swept up by the contact line.

4.6 Tertiary Mixtures

There is little in the literature on multicomponent, complex droplets; some of the few examples already mentioned include model ouzo drops of water, ethanol and anise oil[40] or model whiskey drops of water, ethanol, surface-active surfactant and surface adsorbed polymer.[61] Finally Matavž *et al.*[8] developed a ink of ethanol, 2-methoxyethanol and 1,3-propanediol (and/or glycerol) and used solutal Marangoni flows and a sol-gel transition to produce uniform deposits of tantalum particles across indium oxide arrays for inkjet-printed electronics.

In this section I relate the results from a limited number of experiments with tertiary inkjet-printed droplets of water, ethanol and ethylene glycol generated in

two ways: by a direct mixture, and the addition of ethanol vapour to evaporating binary EG-water droplets.

4.6.1 Tertiary Mixture

In investigating droplets of tertiary mixtures I only looked at a small section of the possible formulation space: to allow comparison with my standard model system of 50%v ethanol-water I took such mixtures and added different amounts of EG (so the EG fraction came to 10, 20, 34%v).

Without detailed thermodynamic data on tertiary mixtures, I approximate the system as an ethanol-water one with the activities equally scaled down by the mole fraction of EG For example EG-water is close to ideal so a mole fraction of 30%v EG in an EG-water mixture reduces the water vapour pressure by 30%, I then assume that 30%v EG added to an ethanol-water mixture reduces the vapour pressures of both water and ethanol by 30% in this example so that the ethanol remains more volatile than water, i.e. I assume the EG-ethanol intermolecular interactions are not so strong that the volatility order switches so the water component becomes most volatile. Within this framework it is straightforward to discuss the different stages of evaporation. At early times both water and ethanol evaporate until the droplet is essentially a binary mixture of EG and water. At intermediate times the water evaporates until the remaining tens of picolitres of EG-rich are in equilibrium with the water vapour. The final composition takes minutes to evaporate.

Figure 4.28 shows that the volume evolution of a tertiary droplet is qualitatively similar to a binary EG-water or EG-ethanol (low RH) droplet as the evaporation rate continually decreases then approximately plateaus. The dotted blue line shows the final dissipation of all types of solutal Marangoni flow in the droplet; compared to binary droplets this moment occurs much later so that the evaporation rate is already near zero. One feature of Figure 4.28 is that the

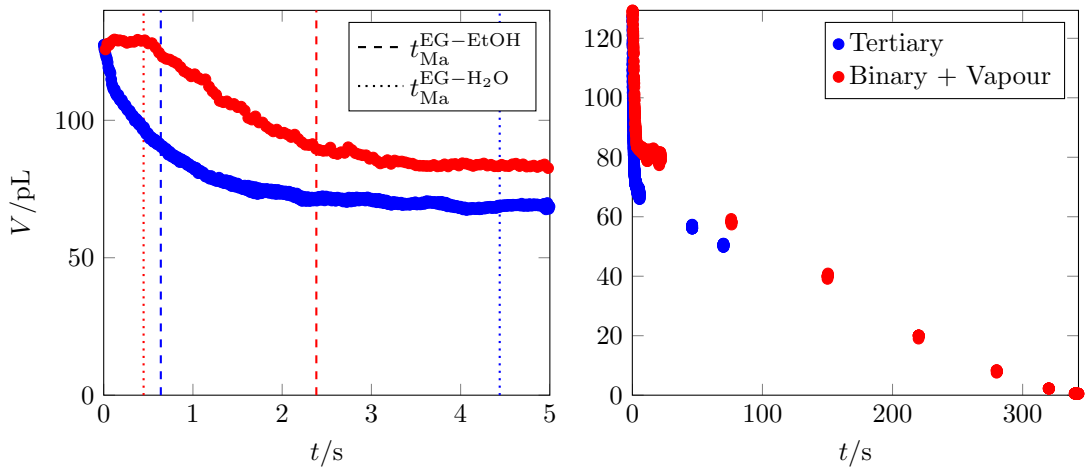

Figure 4.28: Evaporation of different three component EG-ethanol-water droplets on HMDS-treated substrates. The blue markers are for a 34-33-33%v EG-ethanol-water tertiary droplet, $RH = 47\%$. The red markers are for a 27%v EG-water droplet evaporating in an ethanol-rich vapour (no gas flow), $RH = 34\%$, $a_{EtOH} \approx 0.5$. The dashed vertical lines show the experimental end of the EG-ethanol type Marangoni flows from the apex to the contact line; the dotted vertical lines show the experimental end of the EG-water type Marangoni flows from the contact line to the apex.

evaporation rate seems much faster immediately after printing. The slowdown after a few 100's of milliseconds is not related to the ethanol having finished evaporating, shown by the end of the fast drying period not coinciding with the dashed vertical blue line but instead the end of a contact line retraction phase.

In the first stage of evaporation both water and ethanol are evaporating, but the ethanol more so. Therefore the flows are like those in an ethanol-water droplet from the apex to the ethanol-depleted contact line with higher surface tension, except slowed by EG which suppresses evaporation and increases viscosity. At some point the amount of ethanol at the interface is insufficient to generate a surface tension gradient so these flows terminate. After this stage the concentration gradient in the remaining EG-water droplet becomes relevant so that there are flows from the contact line to the apex like in a binary EG-water droplet. This interpretation is supported by the particle velocities in Figure 4.29; in the first flow stage the velocities are lower than those in an ethanol-water mixture,

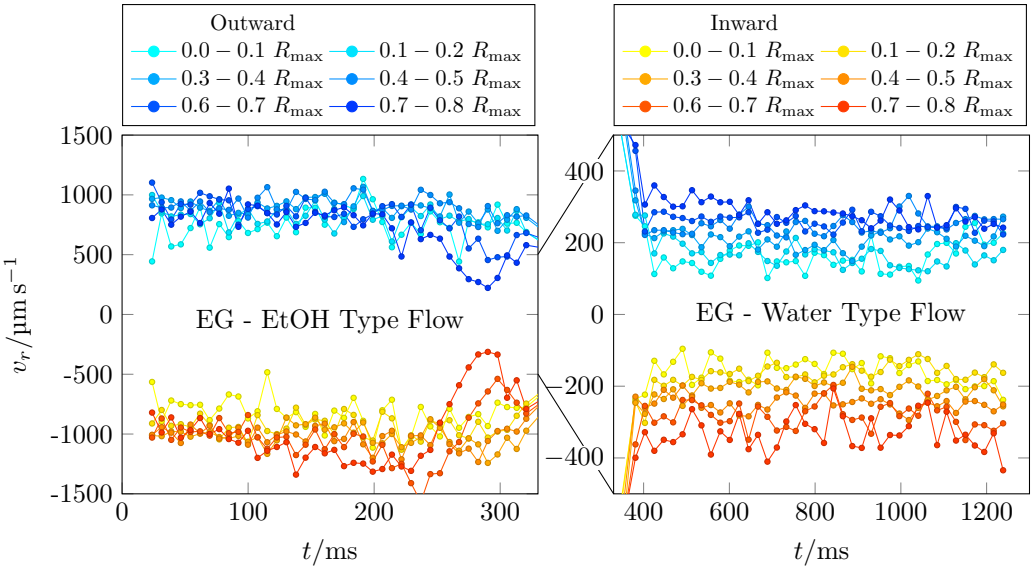

Figure 4.29: Particle velocities over time within radial bins (see legend) for a 34-33-32%v EG-ethanol-water droplet evaporating on a HMDS-treated substrate, $V_0 \approx 150$ pL, $RH = 42\%$. The right plot is a continuation of the first after 330 ms with an expanded y-axis due to the much lower particle velocities following the very fast flow transition at $t_{Ma} = 372$ ms.

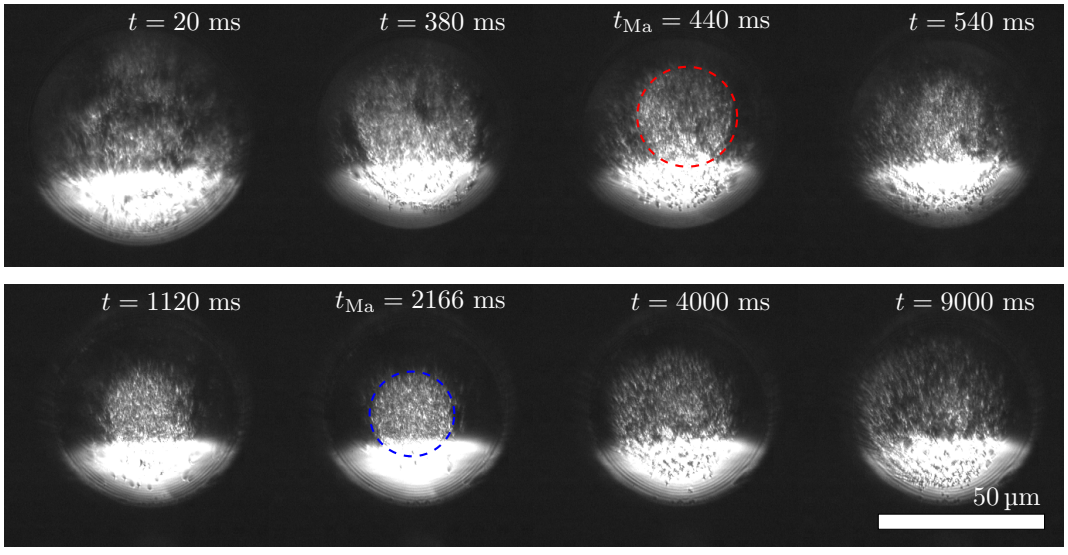

Figure 4.30: Darkfield video frames for the evaporation of a 34-33-32%v EG-ethanol-water droplet on a HMDS-treated substrate, $RH = 42\%$, $V_0 \approx 130$ pL. During solutal Marangoni flows from the apex to the contact line particles migrate towards the centre of the droplet with the smallest radius of the collected group given by the dashed, red circle. The direction of the solutal Marangoni flows then reverses to go from the contact line to the apex, leading to a raft forming at the apex with minimum radius given by the dashed, blue circle. After the end of Marangoni flows the particles are pulled apart by capillary flow.

due to the higher viscosity and the opposing surface tension gradient from the concentration profile of EG within the droplet, while in the second flow stage the velocities are very close to the binary EG-water results in Section 4.5.3. In the third flow stage there are no solutal Marangoni flows so the raft assembled in the second flow stage is pulled apart by convective flow (see Figure 4.30). At the same time it is possible to see that some of the collected group at the centre of the drop from the first flow stage remained in place throughout the second stage. Over the many minutes required for the droplet to fully evaporate this interesting particle distribution is broken up and does not persist into the deposit.

4.6.2 Binary Mixture + Ethanol Vapour

The evaporation of binary EG-water droplets in ethanol vapour showed evidence of condensation (see red markers in Figure 4.28) as the volume change was not monotonic, however the degree of condensation was much lower than for water droplet in ethanol vapour (comparing against Figure 4.13). The presence of EG also changed the contact line behaviour: water or ethanol-water droplets in ethanol vapour would spread for longer than a second until the droplet had less than a third of its volume remaining, however the EG-containing droplets only spread during the first few 100's of milliseconds (longer on plasma-treated substrates which also exhibited significant spreading after the first flow stage). The low volatility EG also meant that at late times a very slow drying residual droplet remained.

When running these experiments with ethanol vapour and EG mixtures I found that the flow of gas into the humidity chamber became a factor when the dominant early-time solutal Marangoni flows died out. In order to achieve axisymmetric tracks like in Figure 4.31 I needed to turn off the gas flow as droplets evaporated, otherwise I would observe a single vortex aligned towards the vapour inlet (see Figure C.1 in Appendix C.1).

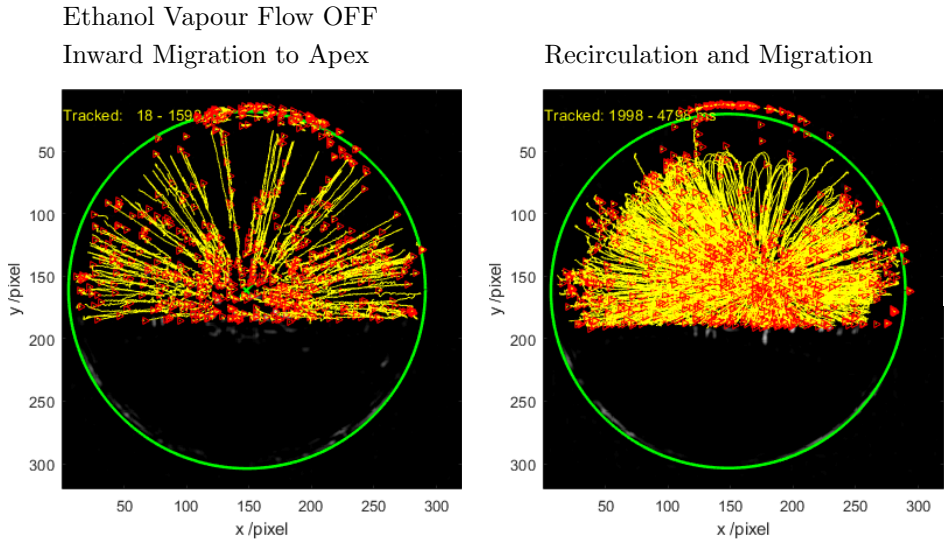

Figure 4.31: Particle tracks from 70%v EG-water droplets evaporating in an ethanol-rich environment with ethanol flow into the chamber shut off immediately prior to printing. At first there is migration towards the apex of the droplet, as the water evaporates the flows reverse and particles recirculate, accumulating at the centre of the droplet.

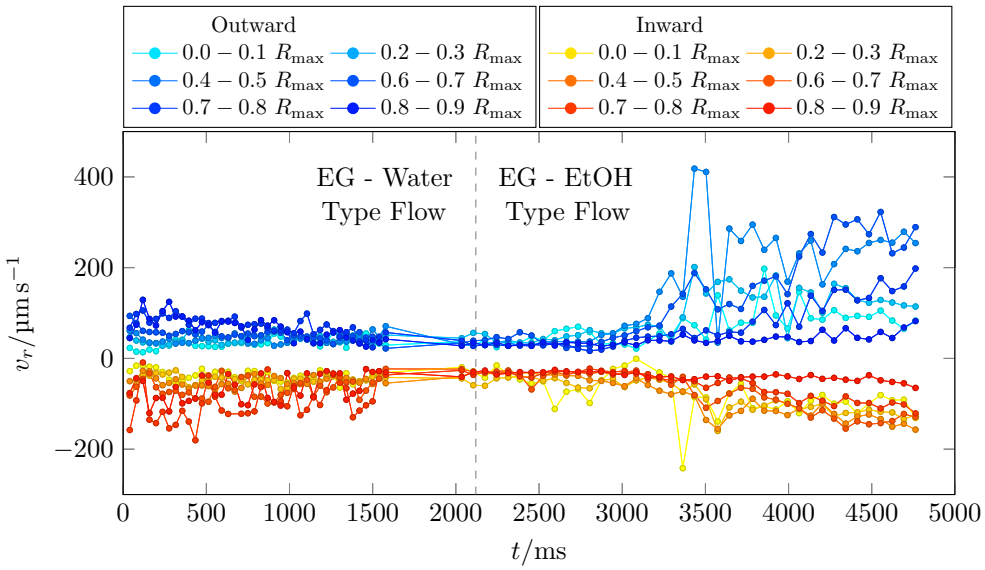

Figure 4.32: Particle velocities over time within radial bins (see legend) for the 70%v EG-water droplet in ethanol vapour whose tracks are provided in Figure 4.31. The droplet evaporated on a HMDS-treated substrate, $V_0 \approx 120$ pL, $RH = 65\%$. The vertical dotted line marks the approximate boundary between the flow stages.

At the start of evaporation the droplet is a binary EG-water droplet so the contact line region becomes deficient in higher surface tension water as it evaporates due to its higher volatility. At the same time ethanol condenses onto the droplet, preferentially at the contact line, reinforcing the lower surface tension so that there is Marangoni flow from the contact line to the apex ("EG-water type"). In less than a second the direction of flow reverses. This is puzzling as if ethanol is still condensing then there should be no change in the direction of the surface tension gradient over time. This suggests that this flow transition is a result of the ethanol vapour flow being turned off (to maintain axisymmetry of flows) as the droplet is printed. This means that it is possible for the nearby ethanol in the vapour to disperse and ethanol condensed onto the EG-water droplet to then evaporate. This would lead to the contact line region becoming ethanol-deficient relative to the apex, increasing the local surface tension, and so create a surface tension gradient to oppose that of the EG-water concentration gradient. In the second stage the flows are like that of a binary EG-ethanol droplet although the flows are more long-lived, dying out around when the evaporation rate plateaus as in the binary EG droplet experiments.

In the first stage of evaporation the particles would migrate, forming a raft at the apex. In the second stage the particles travelled in the opposite direction along the interface and there was particle migration towards the centre of the droplet (see Figure 4.31). On a plasma-cleaned substrate no second flow stage was observed, and the droplets spread significantly after the end of the flows of this first stage. This spreading is likely due to the end of Marangoni contraction as in the first stage the flows are from the contact line to the apex along the liquid-vapour interface and so would oppose the spreading of the contact line.

Figure 4.32 shows the PIV outputs from tracking the flows in an EG-water droplet in an ethanol vapour. The existence of two stages in the flow is clear: at the beginning the flows are on the order of several $100\,\mu m\,s^{-1}$ like EG-water

droplets evaporating without an ethanol-rich surrounding vapour. This is then followed by nearly a second of very little flow as the EG-ethanol concentration gradient is established, after which there are faster, reversed flows relative to the first stage.

4.7 Conclusions and Future Directions

To summarise, I printed and collected profile and flow data for: ethanol-water, ethylene glycol-water and ethylene glycol-ethanol droplets; water, ethanol-water or ethylene gylcol-water droplets in an ethanol vapour; and ethylene glycol-ethanol-water droplets. Due to each solvent having differing volatilities and surface tensions there were multiple stages in the evaporation of each droplet which were often associated with changes in flow behaviour, leading to flows terminating in binary mixtures or reversing in three-component droplets.

Of these mixtures only ethanol-water, ethylene glycol-water, and water and ethanol-water in ethanol-rich vapour droplets were modelled with my volume-averaged composition model as other systems had little data on their physical properties in the literature. My model was able to qualitatively capture the slow-down of evaporation of ethanol-water droplets as the higher volatility ethanol component evaporated preferentially at the start of drying. The good quality of the match meant that the Marangoni flows sufficiently mixed the droplet for the volume-average assumption of the model to be effective. For water, or ethanol-water, droplets in ethanol vapour the model could capture the condensation of ethanol onto the droplet, or slow-down of evaporation of the ethanol component, due to the presence of ethanol in the environment. However further refinements to the model are required to better handle the changes in contact angle with droplet composition and obtain a quantitative match with experiment. Work towards this goal would require more information on the solid-liquid surface tension term

and could be extracted from contact angle data of droplets of known composition on well characterised substrates. The evaporation profiles of real ethylene glycol-water droplets were well matched by model data at early times however once the evaporation rate appeared to plateau as they became more concentrated in low volatility EG the modelled droplets evaporated more. This lack of agreement suggests that the droplet composition was non-uniform in a way that suppressed evaporation, for instance surface enrichment of EG at the liquid-vapour interface would decrease evaporation rates due to lowering the water activity. The current state of the model assumes that EG is fully involatile, which is effective over timescales of tens of seconds. However the real droplets were seen to evaporate so there is scope for future work to study the evaporation rates of EG-water mixtures over longer timescales of a few minutes until the droplets fully evaporate in order to input that data into the model and generate high quality data on the properties of EG-water mixtures at high EG mass fractions. This is a current limitation in the literature as Diddens's simulations with glycerol-water mixtures also assumed the glycerol to be totally involatile.[38]

For ethanol-water mixtures the model was also validated by reflectometry experiments. While the reflectometry data suggests the presence of a residue of ethanol at the end of solutal Marangoni flows the predicted ethanol composition at the experimental flow end times were not consistently non-zero. However this is not too surprising as the residue would not be expected to be large. Trying to calculate the Marangoni number at the end of solutal Marangoni flow to determine if there was some critical value for turn-off was not successful. From this I suggest that the Marangoni number used for describing flow in droplets should be reworked by theoreticians as it consistently overestimates experimental flow velocities. In my opinion the idea that the concentration gradient is destroyed by diffusion (i.e. D is in the denominator in Equation 1.22) does not seem effective, the destruction of the concentration gradient arises from the motion of the surface as a result

Table 4.1: Summary of solutal Marangoni flow directions and approximate range of the magnitude of flow velocities in solvent mixtures, directions of Marangoni flow along the liquid-vapour interface: AC - apex to contact line, CA - contact line to apex. The three component droplets have two flow stages: S1 and S2. EG-Water S2 has "N?" for for whether there is ethanol vapour as we suggested that there should only be one stage if the ethanol vapour did not dissipate.

Droplet Fluid	EtOH Vapour?	Direction	$\lvert v_r \rvert$ /µm s^{-1}	Migration to
Ethanol-Water	-	AC	1000-3000	Centre
Water	Y	CA	150-300	Apex
Ethanol-Water	Y	CA	200-600	Apex
EG-Water	-	CA	150-300	Apex
EG-Ethanol	-	AC	600-2000	Centre
EG-Water S1	Y	AC	100-300	Centre
EG-Water S2	N?	CA	200-500	Apex
EG-EtOH - H_2O S1	-	CA	600-1200	Apex
EG-EtOH - H_2O S2	-	AC	300-500	Centre

of the flows compared to how quickly the concentration gradient is generated by evaporation.

From Table 4.1 when the surface tension at the contact line was greater than at the apex (as a result of preferential evaporation of the lower surface tension component) flows went from the apex to the contact line and there was vigorous recirculation and particle migration to the centre of the droplet. On plasma-cleaned substrates flows were less axisymmetric as the toroidal vortex broke up after 100's of milliseconds. In ethylene glycol-ethanol and ethanol vapour droplets the surface tension gradient was reversed and particles collected into a raft at the droplet apex, with a ring of particles at the contact line if the contact angle was low. In terms of flow velocities the raft forming flows were all slower, being only 100's of µm s^{-1} rather than on the order of a mm s^{-1}.

The observed particle migration meant the flows had less of an impact on the deposition of particles than expected. In the literature researchers have frequently designed solutal Marangoni flows to keep particles distributed throughout the droplet to prevent a ring stain forming; however the migration towards the centre

of the droplet in our experiments meant that the deposits were mostly controlled by the substrate dependent depinning behaviour of the contact line in the absence of particles near the contact line to act as pinning sites. This was the case for ethanol-water or ethylene glycol-water systems. Ring stains were still found for EG-ethanol droplets, perhaps because there was a longer time for Brownian motion to disrupt the collected group and redistribute particles which could then pin the contact line. The deposition from droplet systems in ethanol vapour was in a pattern with a ring stain, with most the particles in a central raft which typically fractured and moved off-centre in the final milliseconds before complete evaporation of the droplet. The rafts found bear some resemblance to those of Malinowski *et al.*[156] in response to a local ethanol vapour source or possible intermediates in octane droplets with thermal Marangoni flows that had central deposits;[51] therefore this work can be used to help explain why those systems did not exhibit the typical behaviour of recirculation leading to more uniform deposits. Our analysis of the migration behaviour will be further discussed in Chapter 7.

In terms of experimental improvements the spread of the end fractional time and volumes at which Marangoni flows ended during the evaporation of ethanol-water droplets indicates the importance of better standardising delays between printing experiments. Other improvements could involve introducing a second nozzle for experiments involving ethanol vapour to cover for the lack of an equivalent sensor to measure the amount of ethanol in the environment like the relative humidity. The second nozzle could print ethanol droplets in between other experiments to check for consistency in drying time without changing the fluid in the primary nozzle.

Quantitative work to fill in gaps in the literature on the properties of EG-ethanol mixtures and tertiary mixtures of EG, water and ethanol would allow further testing of my model and show whether my approach would work for three

component systems. The deposits from droplets containing EG could also receive more attention as in most cases it was not recorded to maximise the time in the lab recording the dynamic period of evaporation.

Other experiments that could be imagined under the banner of "solvent systems" could involve more focus on complex mixtures, these could differ from the above set by not being fully miscible so that phase separation could be observed. Solvent systems are also particularly interesting for coalescence studies because surface tension differences between coalescing droplets can be generated by printing droplets of the same fluid with a delay so that the first droplet can evaporate and change composition. This is of direct practical application in coating applications where many droplets are deposited on a substrate but are not all generated simultaneously. With this motivation our research group has investigated droplet vapour interactions between droplets, finding similar chasing and repelling behaviour as Cira *et al.*[78]. Our research group has also been experimenting with the impact of humid environments on low surface tension organic solvents such as IPA where enhanced spreading can lead to more uniform particle deposition.

Chapter 5

Sugars

5.1 Introduction

In Chapter 4 I studied solvent mixtures, sometimes with ethylene glycol as a cosolvent; while ethylene glycol has a low volatility it would evaporate within the a few minutes. To look at systems with truly involatile components it is useful to study solutions where the droplets contain a miscible, involatile solute. Therefore in this chapter I discuss solutions where crystallisation does not occur to avoid additional complexity, before discussing systems where crystallisation did occur in the next chapter. It was also useful to study a wider range of chemical systems to investigate the universality of the migration behaviour observed in Chapter 4.

Sucrose and lactose are water-soluble sugars which are frequently used in food formulations. The sugars reduce the water activity of the sample and so can be used to extend shelf-life, act as bulking agents, or change mouth-feel or sweetness. They are also key excipients in the pharmaceutical industry for the production of pills as they are biologically safe but can prevent degradation of the active pharmaceuticals.[161] Sucrose has received a lot of attention from drinks companies so its physical properties are very well defined such that sugar solutions can be used as references to determine the impurities in processed sugar.[162]

Lactose is also known as milk sugar as it is the most prominent carbohydrate of milk and almost exclusively found in mammalian milk (about 4.8% in bovine milk)[163] and so is a key constituent of the 1.4 million tonnes of milk powder produced in the EU last year.[164] In such processes a feed solution goes into a spray drier where the system can be described as a collection of free-drying droplets in a heated chamber.[165] One of the key practical problems in this industry is an understanding of the process by which droplets stick to walls. This leads to a loss of product and requires the chambers to be frequently cleaned and thus factory downtime. Therefore the drying of droplets on surfaces is of interest, in addition to free-drying droplets.

These sugars are also interesting chemical systems to study as they have some uncommon properties. In contrast to salt solutions, sugar solutions are not expected to crystallise near room temperature and pressure, instead they form highly viscous glasses.[166] A glass is a disordered, amorphous material that lacks the periodicity of a crystal but has the mechanical properties of a solid. On a molecular level it resembles a liquid for which time has slowed down to the extent that it has lost the ability to flow. The transition from liquid to glass is often a result of supercooling[167] although in this case it is a result of diffusive slowdown[168] as the concentrated sugar droplets can reach very high viscosities.

Power *et al.*[169] used an electrodynamic balance to dry single sucrose aerosol particles in environments with different relative humidities. Partially dried droplets could then by manipulated to coalesce and the damped oscillations used to measure a 12-order magnitude increase in dynamic viscosity as the sucrose mass fraction was driven up to 0.9. From the temperature dependence of the glass transition temperature sucrose is expected to crystallise at room temperature at a mass fraction of 0.95.[170] Crystal growth would then be kinetically limited due to the high viscosity of the surrounding solution hindering the release of the hydrating water molecules previously bound to sucrose.[171]

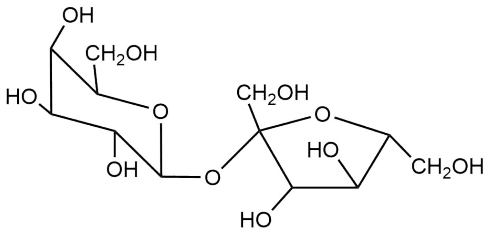

Sucrose

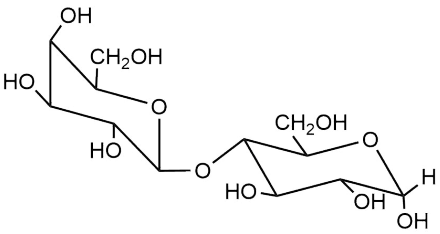

$\alpha-$Lactose

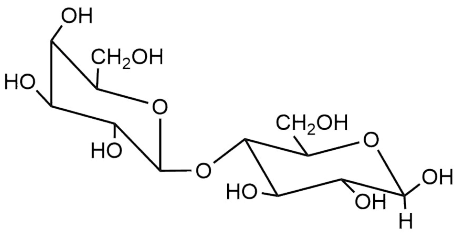

$\beta-$Lactose

Figure 5.1: Chemical structures of sucrose and the α and β anomers of lactose.

While these chemical systems have not been studied as sessile droplets previously there are a number of similarities to free-drying aerosol experiments such as there being a droplet remaining even at the end of evaporation. However as the droplets are no longer spherical, it is possible for there to be surface tension gradients and so Marangoni flows within sessile droplets.

In this chapter I first look into the evaporation behaviour of sugar solutions of different concentrations and at evaporating under different relative humidities. From this I determine the supersaturation ratio, S, to describe the final concentration state of the droplet. This ratio is simply defined as the mean concentration relative to the concentration at saturation; its value varies depending on the units of the 'concentration' such as molarities, molalities or mass fractions. To maintain consistency all supersaturations will involve concentrations in terms of g L^{-1}, the amount of solute is better described as a mass rather than in terms of moles as the molecular weights of sugars are high so concentrations in terms of mol L^{-1} appear very small when compared to other solutes discussed in this thesis. Initial

concentrations are typically presented in terms of mass fractions, or equivalently wt% as such percentages tend to be more intuitive. Measuring the supersaturation ratio here defines a baseline to make comparisons against in Chapter 6 in which crystallising solutes are discussed and where the supersaturation influences the nucleation behaviour. Finally I describe the flow behaviour within sugar droplets, relating it to the evaporation dynamics.

5.2 Physical Properties

Sucrose and lactose are both dissacharides, each built from two covalently bonded carbohydrate molecules where sucrose is built from glucose and fructose while lactose is built from glucose and galactose (see Figure 5.1). Lactose comes in two isomeric forms due to different possible configurations of an $-$OH group in the glucose part of the molecule.

In solution at $T = 20$ °C the α and β forms of lactose mutarotate (flip between sterioisomeric forms) until they reach an equilibrium with $37.3\alpha : 62.7\beta$.[163] In the solid state there are a number of forms, the most common being the crystalline $\alpha-$lactose monohydrate and $\beta-$lactose (anhydrous). The beta form is produced by crystallising lactose at higher temperatures and its crystals are less hard and brittle.[176]

To prepare lactose solutions I used the cheaper $\alpha-$monohydrate form of lactose. In a saturated solution, the total concentration of lactose is determined by the

Table 5.1: Solubilities of sucrose and the enantiomers of lactose at $T = 20$°C from Refs. 91 and 163.

Sugar	Solubility/ g/100 g H_2O	Solubility/ g L^{-1}	Solubility/MFS
Sucrose	204	892	0.671
$\alpha-$Lactose	7	67	0.07
$\beta-$Lactose	50	407	0.33
$\text{Lactose}_{\text{eqm}}$	18.8	168	0.16

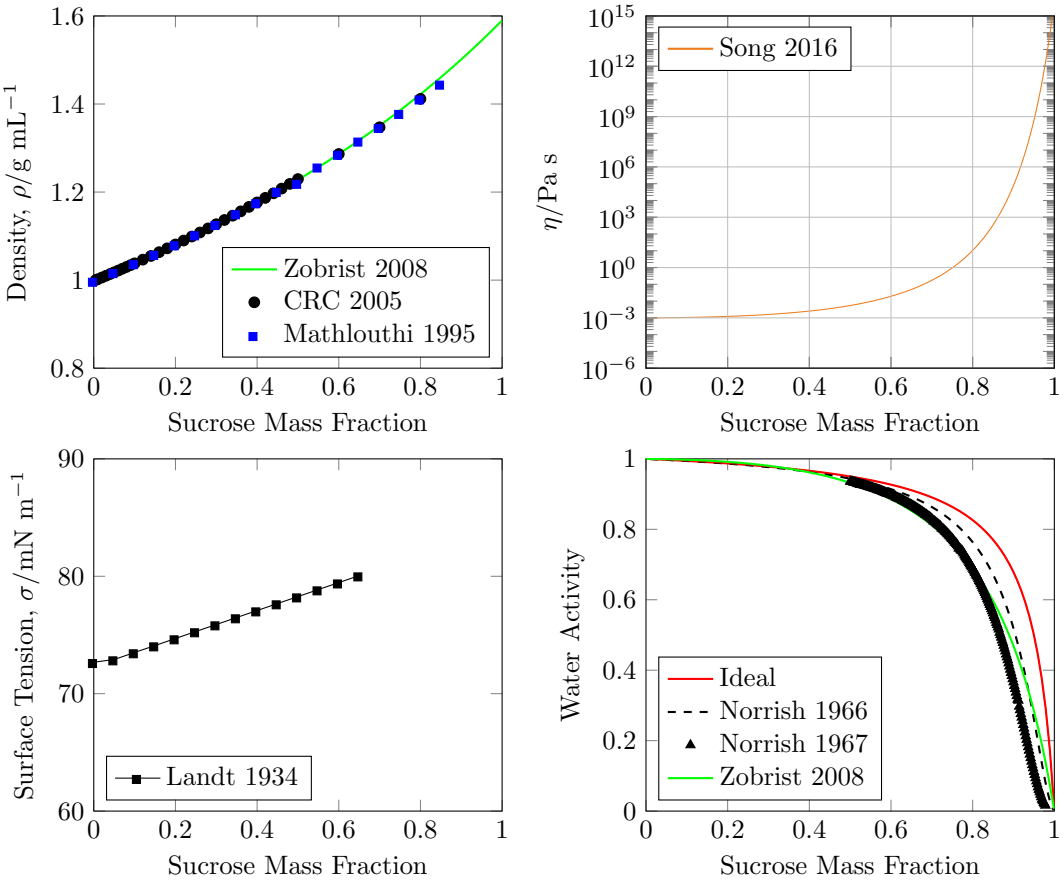

Figure 5.2: Properties of sucrose solutions from Refs. 91 (CRC 2005 black circles), 162 (Mathlouthi 1995 blue squares), 166 (Zobrist 2008 Model green line), 172 (Song 2016 Model), 173 (Landt 1934 black squares), 174 (Norrish 1966 Model dashed black line) and 175 (Norrish 1967 black triangles). Ideal water activity (red line) from mole fraction of water.

Table 5.2: Water activity at sugar solubility limit.

Sugar	Water Activity ($c = c_{\text{sat}}$)
Sucrose	0.827
Lactose$_{\text{eqm}}$	0.991

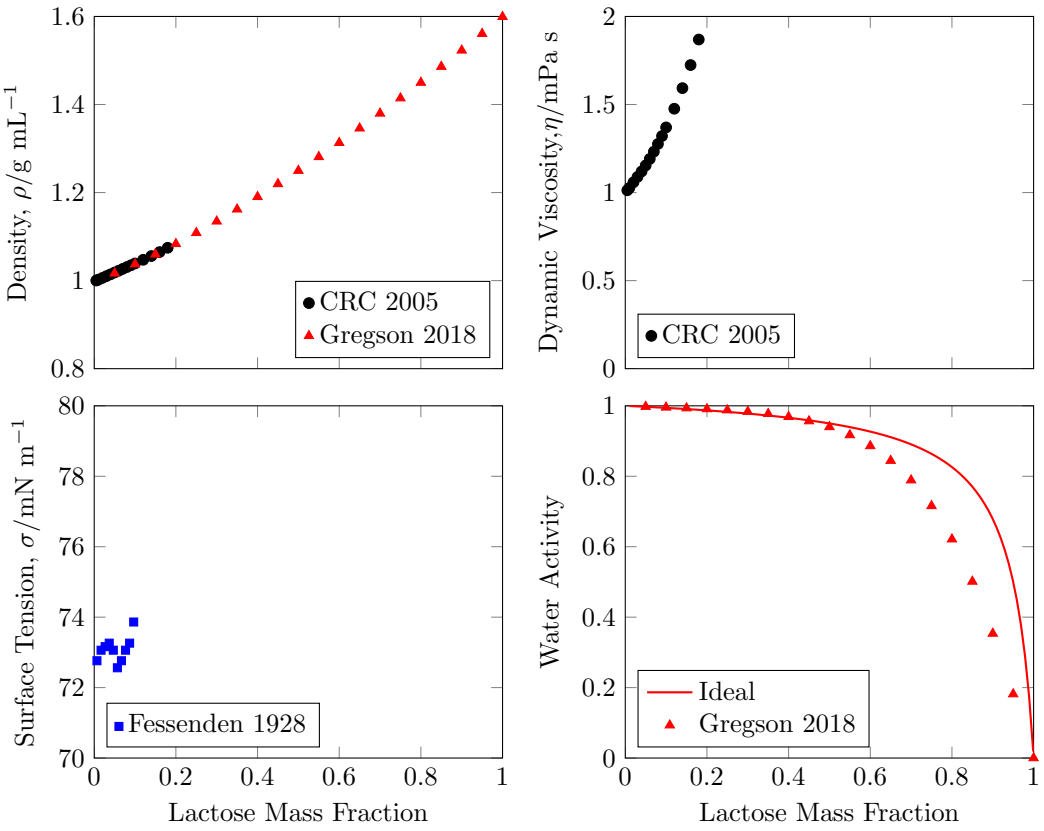

Figure 5.3: Properties of lactose solutions from Refs. 91 (CRC 2005 black circles), 177 (Fessenden 1928 blue squares) and 178 (Gregson 2018 red triangles). Ideal water activity (red line) from mole fraction of water.

solubility of the α form (see Table 5.1). The total amount of lactose dissolved is $7/0.373 = 18.8$ g/100 g H_2O giving an equilibrium concentration of 168 g L^{-1}. Lactose solutions up to 12 wt% were investigated. For the more concentrated samples the solutions were left for at least an hour after mixing to allow the α form to mutarotate. Sucrose solutions up to 40 wt% were investigated although the majority of the work was for concentrations below 20 wt% where lower viscosities made it significantly easier to print droplets.

Figure 5.3 shows that lactose was similar to sucrose in that the surface tension only varied weakly with concentration while the density and water activity also behaved similarly despite the much lower solubility. An additional plot of lactose viscosity is given in Appendix D.1, showing how the viscosity increased dramat-

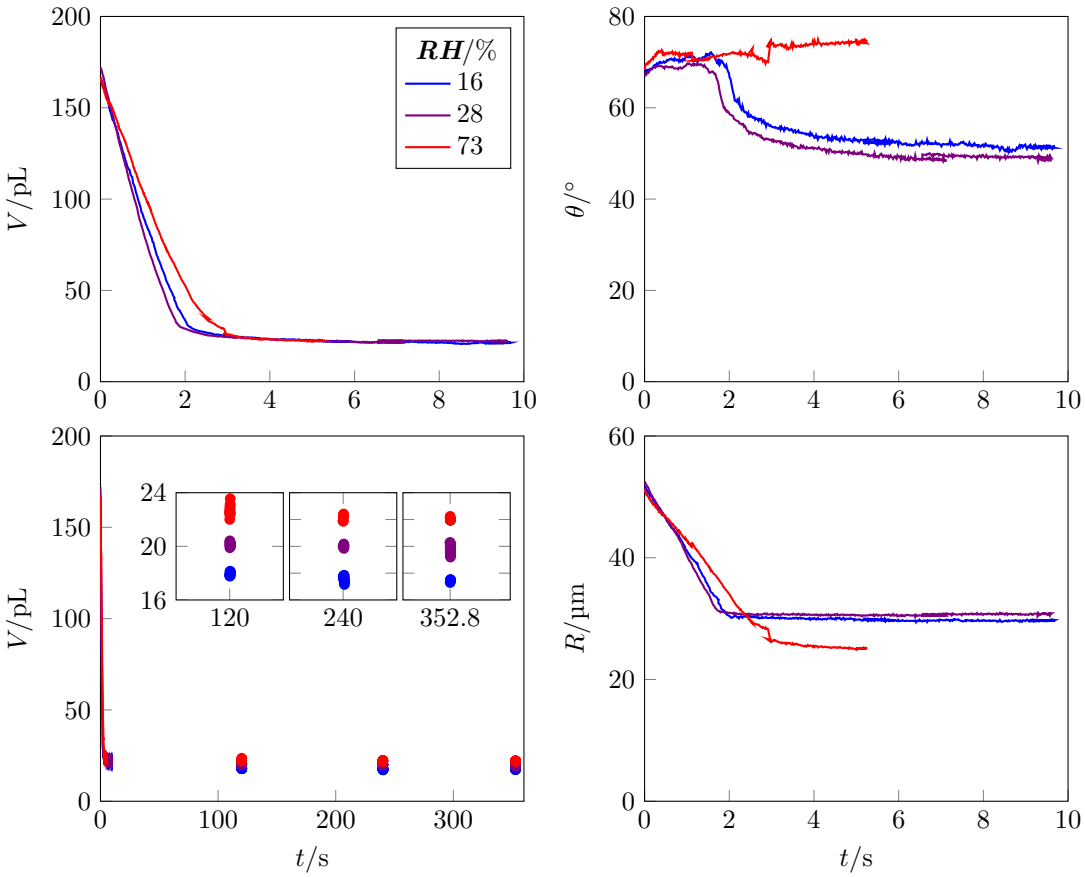

Figure 5.4: Evaporation of 10 wt% sucrose droplets with similar volumes at different relative humidities: RH =16 (blue), 28 (purple) or 73% (red). No particles, HMDS-treated substrate. The left hand plots show the change in droplet volume, with the lower plot showing additional volumes at longer time with insets that have restricted y-axis limits.

ically, by about 9 orders of magnitude as the mass fraction reached 0.8.[172,178]

5.3 Evaporation

To begin with it is beneficial to draw attention to the differences in evaporation behaviour for sugar droplets compared to the solvent systems studied.

5.3.1 Sucrose

Figure 5.4 displays some droplet profile data for sucrose droplets evaporating in the humidity chamber. At early times the evaporation rate was still linear, although over time the droplet became enriched in sucrose decreasing the water activity (see Figure 5.2) so the the difference in water activity between the droplet and environment reduced over time. However in order for this difference to go to zero, leading to the total suppression of evaporation, high sucrose mass fractions greater than 0.6 were needed. As the initial sucrose concentration was below this, the droplets behave similarly to pure water droplets as they begin evaporating in a near CCA mode. This continued at high relative humidities but at lower *RH* it appears that sucrose could build up at the contact line faster than it could diffuse away, leading to the contact line becoming pinned. After a few seconds of drying the evaporation rate was suppressed enough that the droplets appeared to stop evaporating, the top left plot of Figure 5.4 shows that the remaining volume was marginally lower for lower *RH*. Based on the water activity data in Figure 5.2 the lower *RH* droplet was expected to evaporate to a more concentrated final state based upon an averaged concentration approach; compared to the numerically expected end volumes of 11.6, 12.5 and 16.0 pL for the 16, 28 and 73% *RH* droplets the measured end volumes were more than 30% higher at 17, 20 and 22 pL (see Table 5.3). These higher than predicted end volumes suggest the presence of something inhibiting further evaporation such as a solute-rich shell developing. The higher sucrose content of the shell would lead to an increased local viscosity

Table 5.3: Comparison of normalised "final" droplet volumes for the experiments at different relative humidity given in Figure 5.2 for 10 wt% sucrose droplets.

$RH/\%$	$V_{\mathrm{End}}^{\mathrm{Exp}}/V_0$	$V_{\mathrm{End}}^{\mathrm{Model}}/V_0$
16	0.105	0.070
28	0.116	0.072
73	0.132	0.097

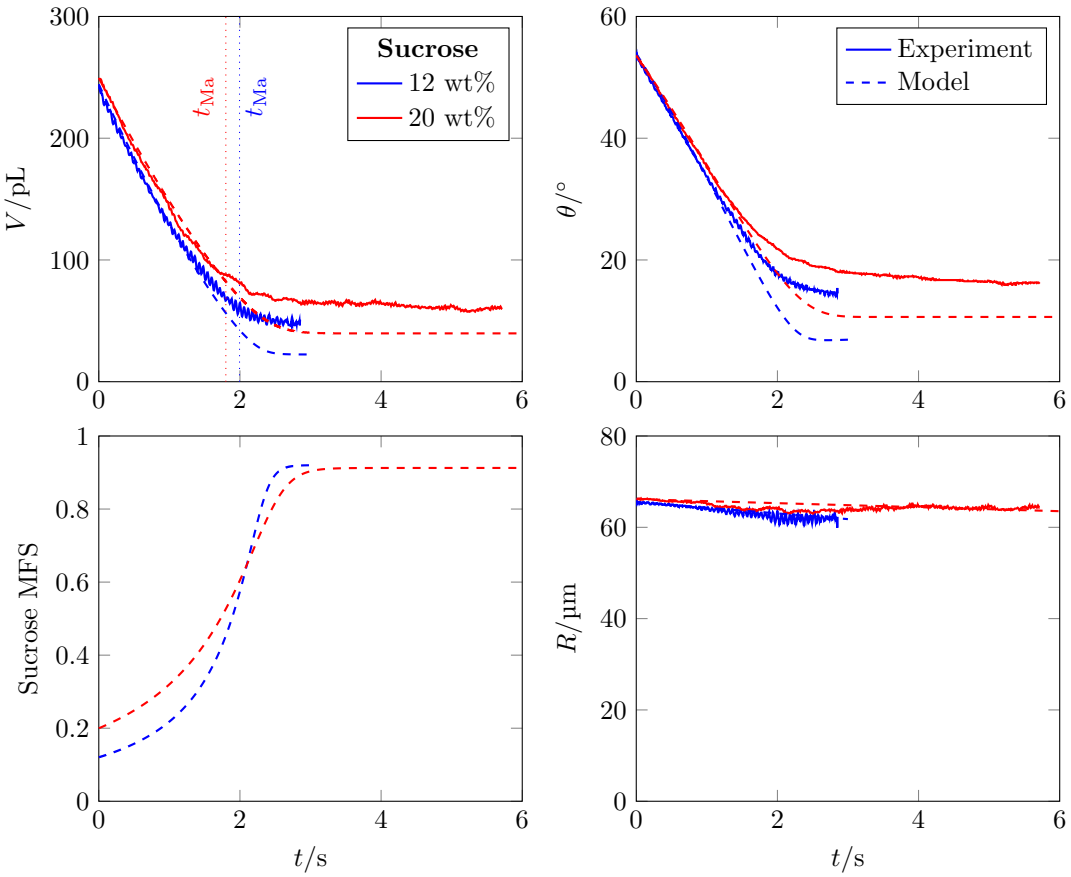

Figure 5.5: Evaporation of sucrose droplets of similar volume and different concentrations: 12 wt% (blue) and 20 wt% (red). No humidity cell, $RH = 40 \pm 2\%$, Decon-cleaned substrate, droplets included particles. Solid lines for experimental data, dashed lines for pinned droplet modified Popov model and dashed lines for experimental time of end of Marangoni flows.

so the evaporation of water would be hindered by slow diffusion of water through the shell to the interface. It would also reduce the water activity at the droplet interface, and so reduce the water activity difference with the environment so that it would not be as favourable for water molecules to escape.

In the bottom left plot of Figure 5.4 it appears that there is a very small amount of further evaporation over the course of a number of minutes, with slightly greater decreases in volume for lower RH. While this may indeed be occurring, at such small volumes the uncertainty in the measurement is of the same size as the slight decrease so this decrease cannot be definitively corroborated.

Even if the slow evaporation at late times was definitely measured the volume would not approach zero as sucrose is involatile. Figure 5.5 shows that the remaining volume, after the slow-down in evaporation, increased with the starting concentration of sucrose in the droplets. I modelled the evaporation of droplets by taking Popov's Equations[31] and modifying the water activity of the droplet, a_{H_2O} according to the mean mass fraction of solute within the droplet. To make implementation easier I printed onto decon-cleaned substrates upon which the droplets pinned allowing the use of the $d\theta/dt$ form of the equations

$$\frac{d\theta}{dt} = -\frac{D^{air}_{H_2O}\, c_v}{\rho\, R^2}\, (1+\cos\theta)^2\, (a_{\text{fluid}} - RH)\, F_{\text{Popov}}(\theta) \tag{5.1}$$

to determine the evolving droplet dimensions where $F_{\text{Popov}}(\theta)$ was defined by Equation 2.5. From the bottom left plot of Figure 5.5, the modelled final mean mass fraction of sucrose was the same across different starting concentrations (at same RH). This arises from the $(a_{\text{fluid}} - RH)$ term which results in continuous evaporation and solute enrichment until the droplet's water activity matches that of the environment. However comparisons with experiment show that the droplets did not evaporate as much as predicted by this model. This is likely because my model assumed a homogeneous distribution of sucrose throughout the droplet. This is unrealistic, instead the droplet's liquid-vapour interface would be enriched in sucrose as the volatile water evaporated, although this effect could be partly balanced by mixing from solutal Marangoni flows. Over this range of concentrations there is a 6-order of magnitude increase in the viscosity (see Figure 5.2) so it is plausible that the fluid can behave like a glass and form a sucrose-rich shell that hinders the diffusion of water to the droplet's surface.

5.3.2 Lactose

Figure 5.6 displays some droplet profile data for lactose droplets. The behaviour of such droplets was very similar to that of sucrose droplets although there

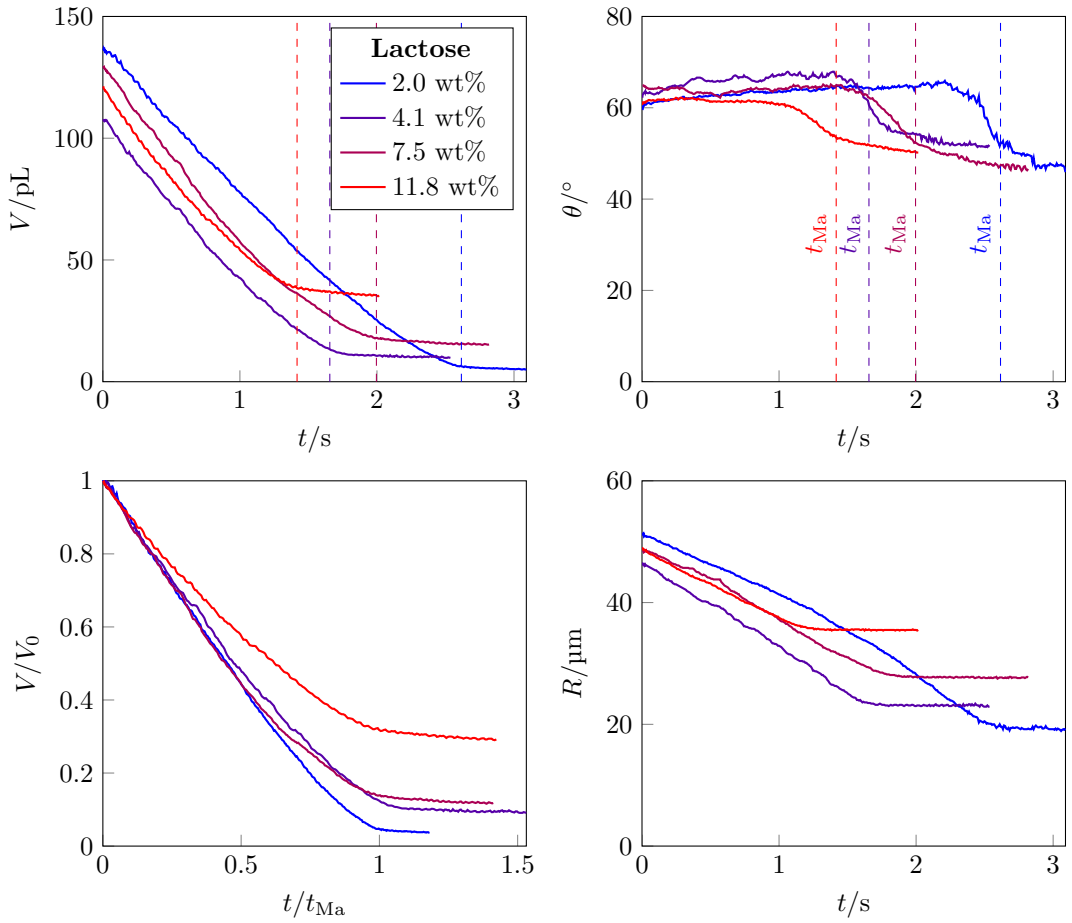

Figure 5.6: Evaporation of lactose droplets of different concentrations: 2.0 wt% (blue), 4.1 wt% (purple), 7.5 wt% (magenta), 11.8 wt% (red). No humidity cell, $RH = 45 \pm 2\%$, HMDS-treated substrate, droplets included particles. Solid lines for experimental data, dashed lines at end of Marangoni flows.

were some differences as a result of the lower starting concentrations because of the much lower solubility limit of lactose. The droplet volumes still evaporated linearly at early times before the evaporation rate plateaued when some volume was approached which depended on the starting solute mass fraction.

In these lactose results it is very clear that the end of the solutal Marangoni flows appeared to coincide with the point at which the evaporation rate began to plateau, as shown in the bottom left plot of Figure 5.6 where the volumes were normalised by their starting volumes and the time was normalised by the end of Marangoni flows (with the solute being involatile it does not make sense

to discuss a 'drying time' in such systems). Two possible explanations for this behaviour are that: one, as the evaporation slows down (as a result of a sugar-rich shell developing) the driving force of the Marangoni flow stops; or two, that the recirculating Marangoni flows prevent the formation of a sugar-rich shell and that once the flows end the shell can quickly develop to then hinder diffusion of water through the droplet, slowing evaporation. Of course it is also possible that these effects are coupled.

Figure 5.6 also shows the contact angle behaviour of lactose droplets as they dried. At the start the contact angle slowly increases as the surface tension increases with increasing solute concentration. After some time, but preceding the end of Marangoni flows, the contact angle switches to start decreasing along with the contact radius with time. This suggests that as the droplet became more concentrated in solute, and thus viscous, it became more difficult for the contact line to retract and rearrange fluid away from the contact line as required for an increasing contact angle. However in other examples of lactose droplet evaporation, on the same substrate, the droplets initially started in a CCR evaporation mode before switching into the CCA mode (like in Figure 5.5 for sucrose), in line with the substrate exhibiting some contact angle hysteresis.

5.4 Supersaturation

The above results showed there is a plateau in the evaporation rate leading to the droplets approaching a final maximal concentration. In this section I will calculate this final concentration, assuming a mean concentration throughout the droplet.

Assuming the initial droplet concentration was the same as the bulk prepared fluid, the mass of solute dissolved in the droplet was known, using literature values for the density. Therefore the mean concentration of the droplet when

the evaporation effectively finished could be found by dividing by the measured volume. This concentration can then be compared to that at saturation to find the supersaturation ratio. In addition to considering the supersaturation at the end of experiments it can also be interesting to look at the supersaturation when the Marangoni flows ended. In this section I present a number of plots containing supersaturation data. These figures are useful as they collate many experimental results to attempt to collapse the data and allow different variables to be simultaneously considered when searching for trends. The best way to view these figures is to focus on an individual plot and see whether there is a trend in the supersaturation reached (y-axis) by considering the colouring and shape of the markers. I have developed the convention for markers that (reoccurs and extended in Chapter 6):

- Filled markers are for droplets containing tracer particles,
- Half-filled markers are for droplets without tracer particles,
- Circle markers are for droplets on Decon-treated substrates,
- Diamond markers are for droplets on HMDS-treated substrates,
- Blue colourmaps are for different starting concentrations,
- Purple colourmaps are for different relative humidities,
- Red colourmaps are for different starting contact angles.

5.4.1 Sucrose

Figure 5.9 presents the entirety of the lactose results for droplets which had circular contact lines. Supersaturations were calculated after the evaporation rate appeared to plateau or at the end of Marangoni flows.

In the majority of experiments the relative humidity was uncontrolled with $RH = 42 \pm 2\%$ or $62 \pm 2\%$. The 10 wt% data set without particles took place in the humidity cell, despite large changes in relative humidity from 17 to 73%

the droplet supersaturations at the end of drying are clustered. Of these measurements the majority of the higher relative humidity droplets reached lower supersaturations (although the spread is still large). This is expected as in the averaged concentration model a higher relative humidity would limit the degree of evaporation and hence the maximum possible concentration reached. However Figure 5.9 shows this trend was not always obeyed, therefore it appears that the relative humidity was not the primary factor in determining the end concentration.

The top left plot suggests that there was a trend in supersaturation as a function of the starting composition. It is clear that the lowest concentration droplets did not even evaporate enough to reach a mean concentration equivalent to the solubility limit of 892 g L^{-1} or 67.1 wt% sucrose. The supersaturations then increased with initial concentration, reaching a maximum for droplets starting at around $16 - 18$ wt% before dropping again so that more concentrated droplets approximately ended at the saturation composition.

This result strongly supports the development of a sucrose-rich shell at the interface which hinders evaporation. That the lower initial concentration droplets only reach low mean supersaturations suggests that the droplets have less uniform solute distributions. This can be explained by referring to Péclet numbers (see Equation 4.4); for lower concentration droplets more water has to evaporate for a sufficiently high concentration to be reached that will suppress the water activity. If $Pe > 1$ then the diffusion of solute away from the interface is slower than the rate at which solute accumulates at the interface so the formation of a solute-rich shell is plausible. As in Section 4.5.2 I consider two ways of defining the characteristic velocity and lengthscales for the Péclet number given by Equations 4.5 and 4.6.

Figure 5.7 shows the calculated Péclet numbers for the droplet profiles in Figure 5.5 alongside a 370 pL, 4 wt% droplet evaporating at $RH = 60\%$. From Ref. 179 the diffusion coefficient of sucrose in water is $5.6 \cdot 10^{-10}$ m^2 s^{-1}. It has

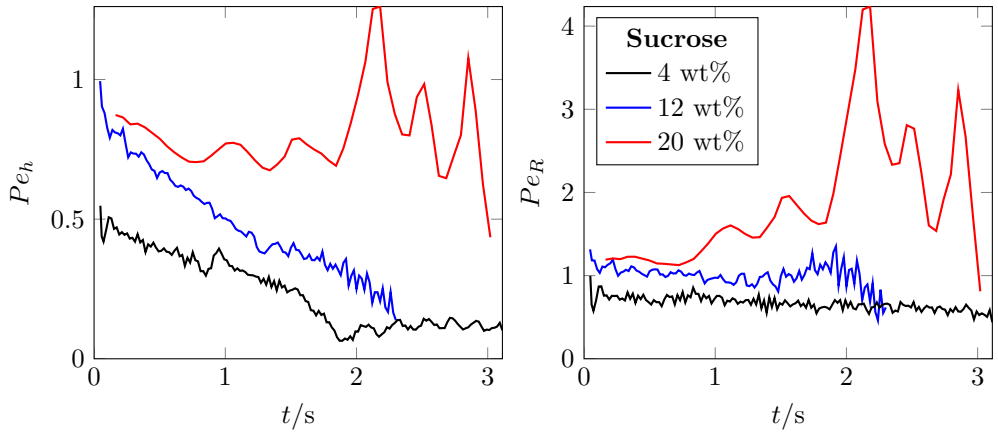

Figure 5.7: Calculated Péclet numbers for evaporating sucrose droplets of different concentrations: 4 wt% (black), 12 wt% (blue) and 20 wt% (red). No humidity cell, $RH = 40 \pm 2\%$, Decon cleaned substrate, droplets included particles.

been found that the inverse relationship between the Diffusion coefficient and the viscosity in the Stokes-Einstein equation gives a good fit to experimental results for sucrose.[180]

$$D = \frac{k_B T}{6\pi\eta r} \tag{5.2}$$

Therefore the mean mass fraction of sucrose in the droplets were calculated to estimate the change in dynamic viscosity η during evaporation. This resulted in 6 and 40-fold increases in the viscosity for the 12 and 20 wt% droplets respectively, accounting for why the Péclet numbers did not vary too much over time as the reduction in characteristic velocity in the numerator as the evaporation slowed was offset by a decrease in diffusion coefficient in the denominator. The fluctuations in Pe were caused by the volume fitting (with a fixed substrate location) being affected by vibrations moving the position of the droplet in the field of view of the camera. Strictly the Péclet numbers in themselves are not so large as to clearly indicate a non-uniform concentration of sugar developing, especially at low concentrations. However the diffusion coefficients were calculated using a mean concentration. If there was a non-uniform concentration distribution then the effective diffusion coefficient near the interface would be much lower so the real

Péclet numbers would be larger. This would promote the enrichment of sucrose molecules towards the liquid-vapour interface and so create a self-reinforcing loop promoting the formation of a sucrose-rich shell at higher Péclet numbers. The formation of a shell is important from a formulation standpoint as it means the droplet's history becomes important in determining the end state, not just the environmental conditions.

5.4.2 Lactose

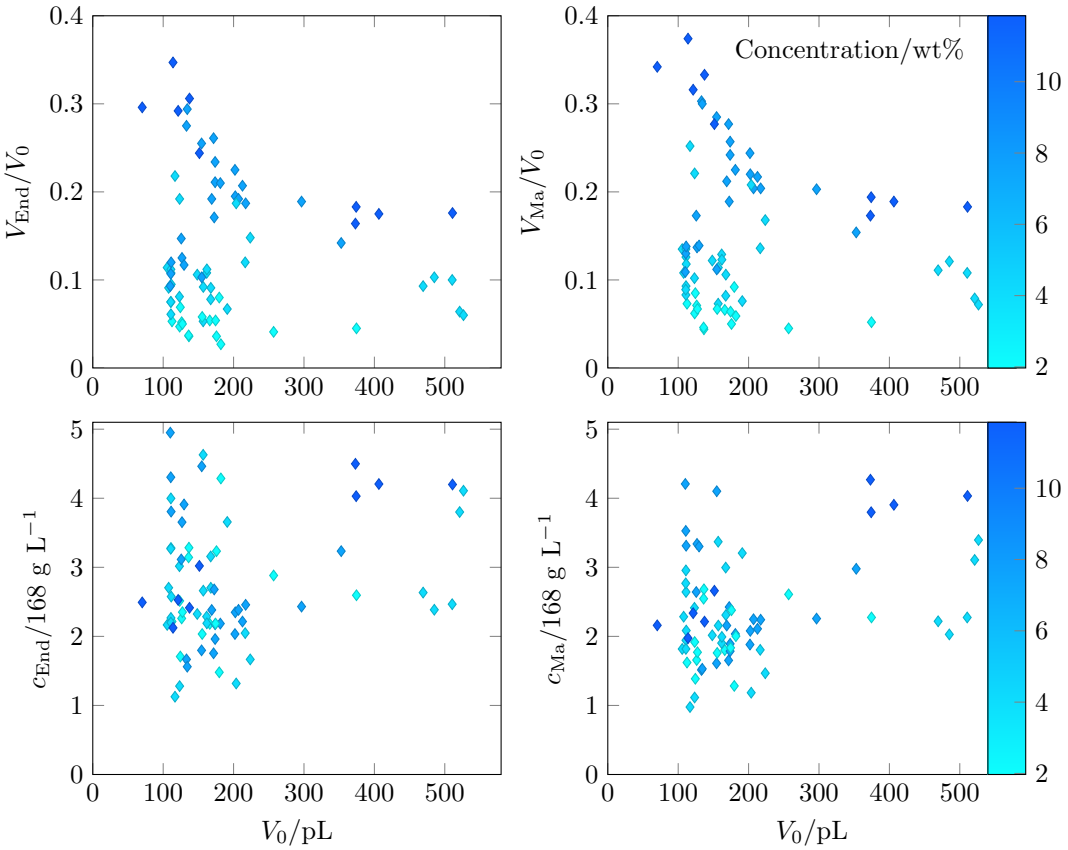

Figure 5.8: Top row: ratios of end volume or volume at end of Marangoni flows to starting volume. Bottom row: mean supersaturations for lactose droplets as a function of volume and starting composition. Colour-map for starting concentration in wt%. No humidity cell, $RH = 45 \pm 2\%$, HMDS-treated substrate.

Figure 5.8 presents the entirety of the lactose results for droplets which had circular contact lines, where there were fewer experiments compared to with

sucrose. There are a few cases included where Marangoni flows were present but the droplets were not recorded long enough to capture the plateau in evaporation rate, such droplets would appear in the right plots but not the left ones. One obvious trend is that V_{End}/V_0 was smaller for the droplets containing less lactose. The end of solutal Marangoni flows occurred close to the end of the droplet profile recordings, as a result the top right plot of V_{Ma}/V_0 is very similar in the distribution of points, except the volumes ratios are slightly larger. The bottom plots present the supersaturation ratio, from these it is clear that the droplets had already reached saturation by the end of Marangoni flows. However there do not appear to be any obvious trends in the supersaturations reached as a function of starting composition.

One difficulty in the analysis came from the low lactose concentrations. While this made the experiments themselves easier as the fluid had a lower viscosity, the viscous droplets left after the plateau in evaporation rates were very small, reducing the precision (typically a few picolitres, see Section 2.4) with which the volumes to determine the supersaturation could be measured. This is partially reflected in the larger amount of scatter in the plots for the lower starting composition droplets. By the same logic only HMDS-treated substrates have been included in Figure 5.8 as on more wetting substrates the residual droplet could have a height of only a few microns/pixels of the camera so end volumes could not be measured without huge uncertainties.

Compared to the sucrose results, the supersaturation ratios for lactose are potentially misleading. As the solubility limit of lactose is much lower, then a concentration of $c_{\mathrm{End}} = 892$ g L^{-1}, at which the mean sucrose supersaturation would be 1, would be equivalent to a lactose supersaturation of 5.3. In terms of the actual concentrations the sucrose droplets reached higher mean concentrations, up to 1000 g L^{-1} rather than 800 g L^{-1} for lactose.

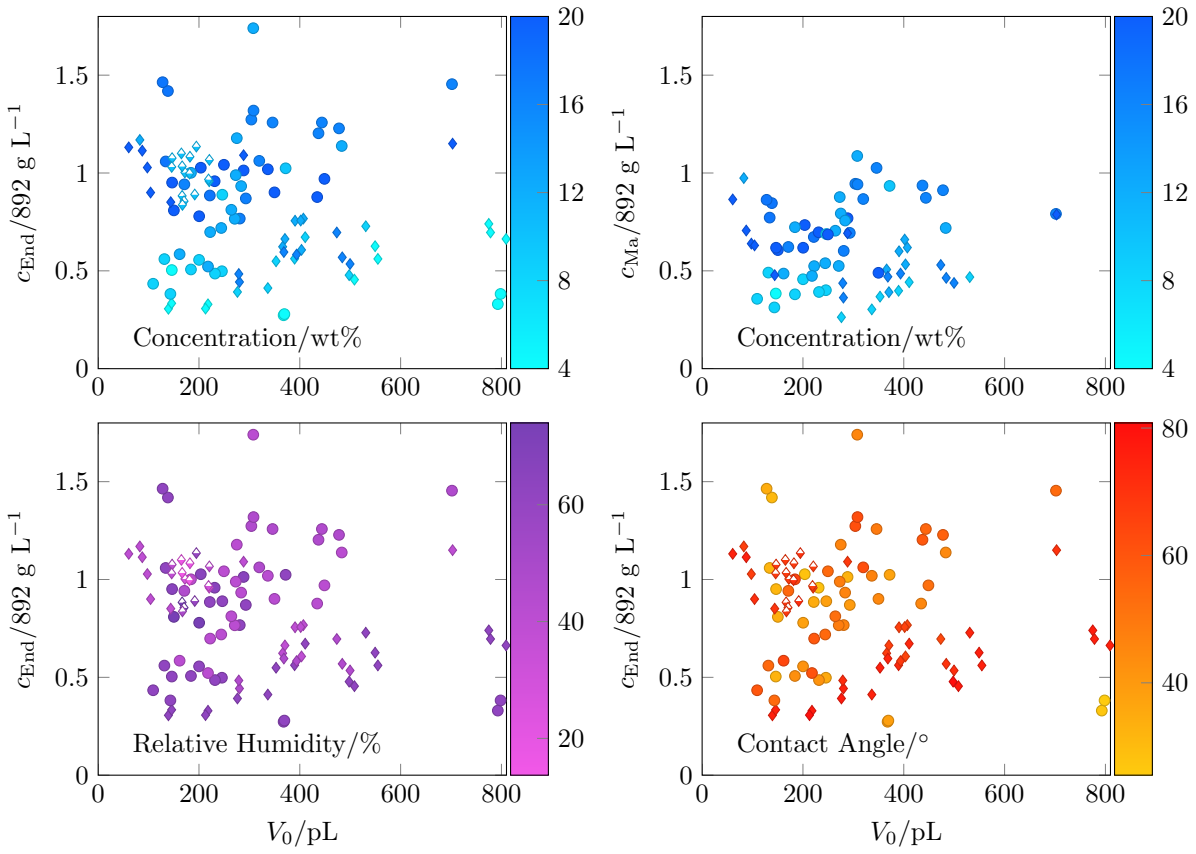

Figure 5.9: Supersaturations for sucrose droplets as a function of volume with colormap dependence on starting concentration in wt%, relative humidity, or initial contact angle. Half-filled markers without particles were from humidity cell measurements, others were in an open lab. Circles and diamonds for Decon-cleaned or HMDS-treated substrates respectively.

5.5 Flows

As in Chapter 4, the non-uniform evaporation of a multicomponent sessile droplet can lead to solutal Marangoni flows which Figure 5.6 suggested were important to the plateauing of the evaporation rate. In this section I describe those Marangoni flows in more detail.

During a droplet's evaporation the sugars are involatile and water can evaporate. As a result the contact line, where there is the greatest evaporative flux, becomes enriched in sugar relative to the rest of the droplet interface. This means that the fluid towards the contact line has a greater surface tension than the less

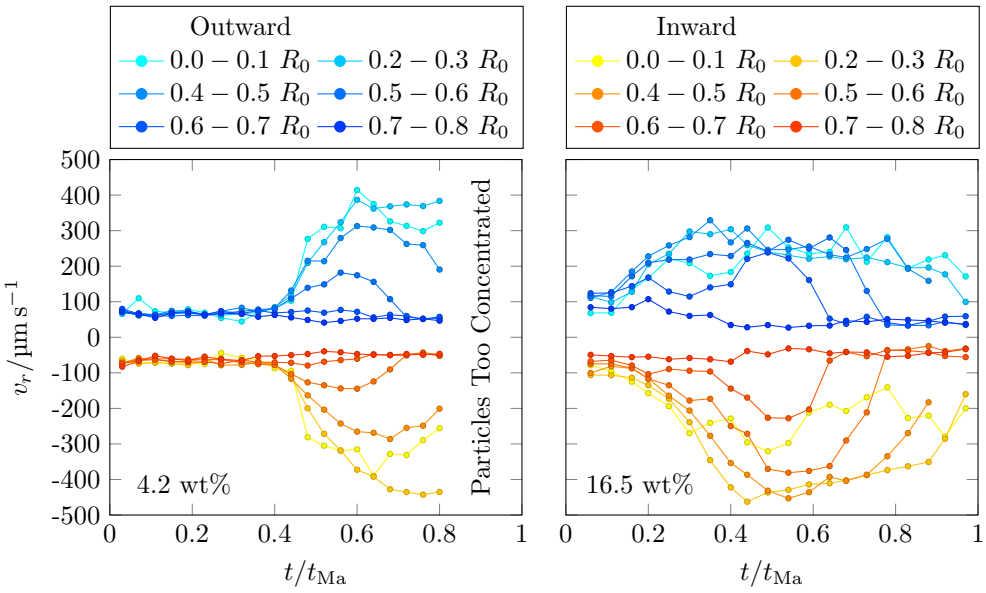

Figure 5.10: Particle tracking velocimetry outputs for 4.2 and 16.5 wt% sucrose droplets. No humidity cell, $RH = 62 \pm 2\%$, Decon-cleaned substrate.

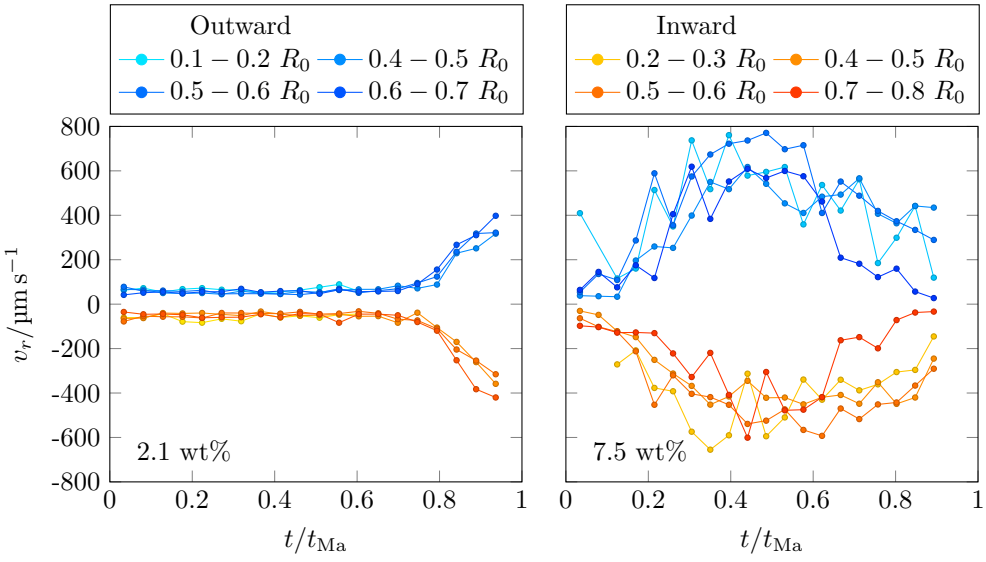

Figure 5.11: Particle tracking velocimetry outputs for 2.1 and 7.5 wt% lactose droplets. The Outward legend gives the radial bins in the left plot while the Inward legend gives the radial bins for the right plot. No humidity cell, $RH = 45 \pm 2\%$, HMDS-treated substrate.

sugar enriched apex of the droplet. Consequently the solutal Marangoni flows travel from the apex to the contact line along the liquid-vapour interface (see Figure 1.6B).

Figures 5.10 and 5.11 show some particle velocities for different radial bins over time for low and higher sucrose and lactose concentration droplets. As discussed in the previous chapter, the measured particle velocities less than $100\,\mu m\,s^{-1}$ where the curves are near horizontal over time are a result of the PIV tracking script incorrectly recognising noise as real particles and so should be ignored.

Given the small change in surface tension with concentration it is surprising that Marangoni flows were observed on hydrophobic substrates for lactose droplets (Figure 5.11) where the difference between the evaporative flux near the contact line and at the apex would be smaller than for thin droplets. This suggests that there was little mixing within the droplet, allowing for large concentration gradients to build up across the liquid-vapour interface.

For both sucrose and lactose droplets at low concentrations there were sometimes no Marangoni flows, or if they did develop they only did so later, and for a short period of time (see Figure 5.11). This is likely a consequence of the surface tension only changing slowly with composition. Therefore significant evaporation was required before there was a sufficient surface tension gradient to drive fluid flow. At intermediate concentrations Marangoni flows developed within the first 100 ms, with the velocity magnitudes increasing and then decreasing towards the end of the flows. As in binary mixture experiments it was hard to track velocities towards the end of drying when there was particle migration towards the centre of the droplet. This resulted in a non-uniform particle distribution (see Figure 5.12) where at the centre, the particles overlapped too much for the PIV algorithm to efficiently determine the particle trajectories. This behaviour impacted Figure 5.10 where the particle velocities in outer radial bins dropped earlier than the more central bins as the particle migrated towards the centre of the droplet,

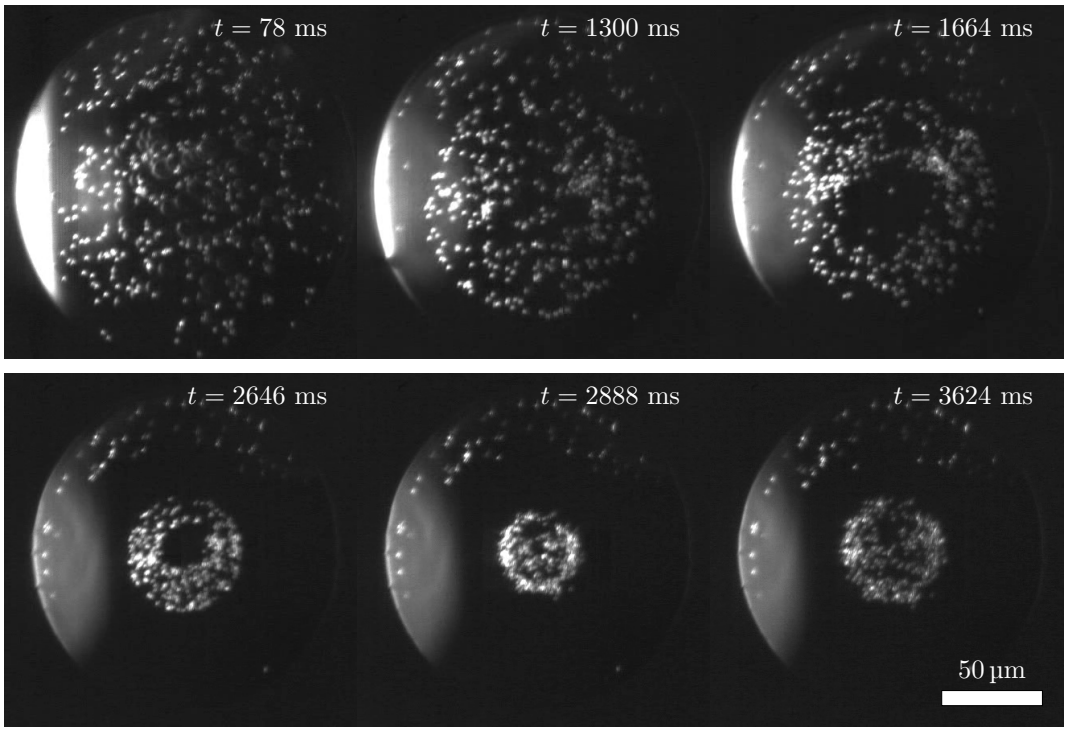

Figure 5.12: Darkfield video frames for the evaporation of a 16 wt% sucrose droplet. $t_{\mathrm{Ma}} = 2.94\,\mathrm{s}$, Decon-cleaned substrate, $RH = 62 \pm 2\%$. While Marangoni flows are present the particles migrate towards the centre to a minimum collected group before relaxing slightly.

leaving those bins empty.

Figure 5.12 gives an example of Marangoni flows in a sucrose droplet. The flows were qualitatively similar to those in ethanol-water mixtures as the higher concentration of sucrose at the contact line compared to the apex resulted in inward Marangoni flows along the substrate. While the flows themselves were slower, the structure was also a little different as the hole in centre of the flows corresponding to the quiescent point was larger. After the end of solutal Marangoni flows in binary solvent mixtures the droplet would continue evaporating, in these sugar droplets further evaporation was very slow. The higher viscosities in sugar droplets also meant that following the initial relaxation of the edge of the collected group after the end of Marangoni flows (such as between the fifth and final pictures in Figure 5.12), the particles would remain fixed in position over the course of multiple minutes.

In high sucrose concentration experiments with starting concentrations of 29 or 40 wt% solutal Marangoni flows were less likely. At 29 wt% the droplets behaved much like the low concentration droplets where Marangoni flows appeared late into drying, however due to the much higher viscosities the particle velocities were slower than those in the intermediate concentration solutal Marangoni flows. Then at the highest concentration no Marangoni flows were observed at all, from the droplet profiles there was very little evaporation so it was not possible for enough of a surface tension gradient to develop to drive flow.

5.6 Conclusions and Further Work

To summarise, I studied the evaporation behaviour, internal flows and deposition of particles from droplets of sucrose or lactose solutions. At early times the evaporation rate of sucrose droplets could be well described with a volume-averaged concentration evaporation model, however at late times when the evaporation rate was observed to plateau the model overestimated how much the droplet would evaporate before the plateau was reached. This lack of agreement between the model and experiment led us to postulate the existence of large concentration non-uniformities where a highly viscous sugar shell would form during drying, preventing further evaporation by lowering the water activity at the surface and slowing the diffusion of water to the surface. To achieve a better fit more complex modelling is required that is able to take into account the non-uniformity of the sugar concentration in the droplet reducing the water activity at the liquid-vapour interface.

Adding tracer particles to track the internal flows showed that the increase in surface tension with solute concentration could lead to solutal Marangoni flows from the apex to the contact line as a result of solute enrichment near the contact line. The weak surface tension dependence on sugar concentration and higher

viscosities (than the solvent mixtures in the previous chapter) resulted in flows with velocities comparable to EG-water mixtures and much lower than ethanol-water mixtures. Compared to solvent mixtures the flows started later into drying as it took time for the contact line to become enriched enough that the surface tension gradient was sufficient to drive solutal Marangoni flow. Solute enrichment reduced the evaporation rate and increased the viscosity, leading to the solutal Marangoni flows dying out. The times that these flows ended drying the droplets evaporation appeared coupled to the slow down in evaporation rate, explained as the absence of flows allowing the formation of a viscous shell. Like ethanol-water mixture droplets there was particle migration towards the centre of the drop, to be discussed in Chapter 7. I see three avenues to learn more about the mechanism causing the droplet to become glassy, with the first two requiring information about particle motion perpendicular to the substrate so that the source of the slowdown can be observed (i.e. from the contact line or from the liquid-vapour interface). Firstly there are holography techniques which would allow particle tracking in three dimensions. This would be challenging for inkjet-printed droplets as the spatial resolution is on the order of a few microns and low particle densities are required. A more simple method would be to print much larger droplets and view particle motion from the side using Optical Coherance Tomography, in such experiments the moving front of cessation of particle motion could hopefully be observed (similar to the cessation of Brownian motion in Jalaal *et al.*'s work on gelling drops[112]). A final approach could involve printing a large enough droplet that a needle could be accurately inserted into the droplet at different times and at different locations along the liquid-vapour interface and the force to enter the droplet measured to learn more about the shell formation.

Particle migration coupled with the viscosity of the droplets increasing dramatically meant that the collected group of particles towards the centre of the droplet was effectively "set" in that position. Therefore the addition of sugars

is a new mechanism to allow for the control of particle deposits, where sugar concentrations can be tuned to fix particles in a certain distribution similar to the work of Talbot[88] using laponite to fix the collected group in ethanol-water inkjet printed droplets.

Compared to solvent mixtures, one of the advantages of having an involatile solute is that it is straightforward to calculate a mean concentration for the drop. Therefore once the reflectometry equipment is equipped with a side view camera it would be possible to run experiments where the mean bulk concentration and sugar concentration at the liquid-solid interface could be determined in parallel for evaporating droplets. Compared to ethanol-water mixtures the refractive index changes measured would be larger and more linear. This would lead to much higher sensitivity although a different hemisphere with higher refractive index would be required as at saturation concentration a sucrose droplet would have a refractive index at 1.458 compared to the hemisphere's 1.461. As a result with the current setup if the droplets were supersaturated then the light would entirely transmit through the droplet so there would not be any reflection at the solid-liquid interface to be measured.

Chapter 6

Salts

6.1 Introduction

Salts are inorganic compounds which dissociate in solution into their constituent anions and cations and are abundant in nature and industrial contexts.[181] Therefore it is useful to gain an understanding of whether there are commonalities in how different salts alter the evaporation of sessile droplets either through suppressing evaporation, or accelerating it through internal flows. Experiments with crystallising solutes also allowed comparisons to be made to the experiments with non-crystallising solutes (sugars) described in Chapter 5 where the maximum supersaturations reached, flow behaviour and deposits were examined.

At concentrations above the solubility limit the solution is said to be supersaturated and it is thermodynamically favourable for phase separation to occur in which solutes crystallise out of solution into a solid phase. However this process is kinetically limited; in Classical Nucleation Theory[182,183] there is a free energy cost for ions to come together for the solid phase until it is of a sufficient size, which is called the critical nucleus. At high concentrations there are more ions in solution so the likelihood of enough ions coming together in a critically large nucleus to cause a nucleation event increases. This means that there is scope for different

crystals to form depending on the concentration at which nucleation occurs so different environmental conditions could lead to different crystallisation behaviour from drying droplets,[184] possibly leading to different crystal polymorphs and biological activity.[185,186] Knowledge of different crystal forms is still important for possible applications even if the biological use is the same. An amorphous[187] or high surface area[188] crystal will have a higher dissolution rate than the most stable crystal form so crystal shape is relevant to drug delivery and food science. Certain applications (such as in OLED displays) can also require amorphous crystalline films over more localised, ordered crystals. In particular salty drops are important in fields such as corrosion[189–191] as sea salt sprays contain sodium chloride (NaCl), while sodium nitrate ($NaNO_3$) is a common component of atmospheric aerosols[192] and fertilisers, and ammonium sulfate (AMS:$(NH_4)_2SO_4$) is a component of agrichemical formulations that are sprayed onto fields as droplets.[1]

In this chapter I describe the evaporation behaviour of salt solutions of different concentrations and at different relative humidities. I then move onto crystallisation topics, introducing classical nucleation behaviour and discussing how the crystallisation behaviour is dependent on the relative humidity and initial concentration, as well as the supersaturations at which nucleation occurs. The actual crystal deposits themselves are then discussed before I finish with an analysis of the flows generated (or not) during the evaporation process, and how crystals changed the internal flows.

6.2 Physical Properties

When added to solution the salts will dissolve until a solubility limit, given in Table 6.1, is reached. The addition of a salt will change the physical properties of a solution, increasing density, viscosity and surface tension while reducing the water activity. Some literature data for these relationships can be seen in Figure

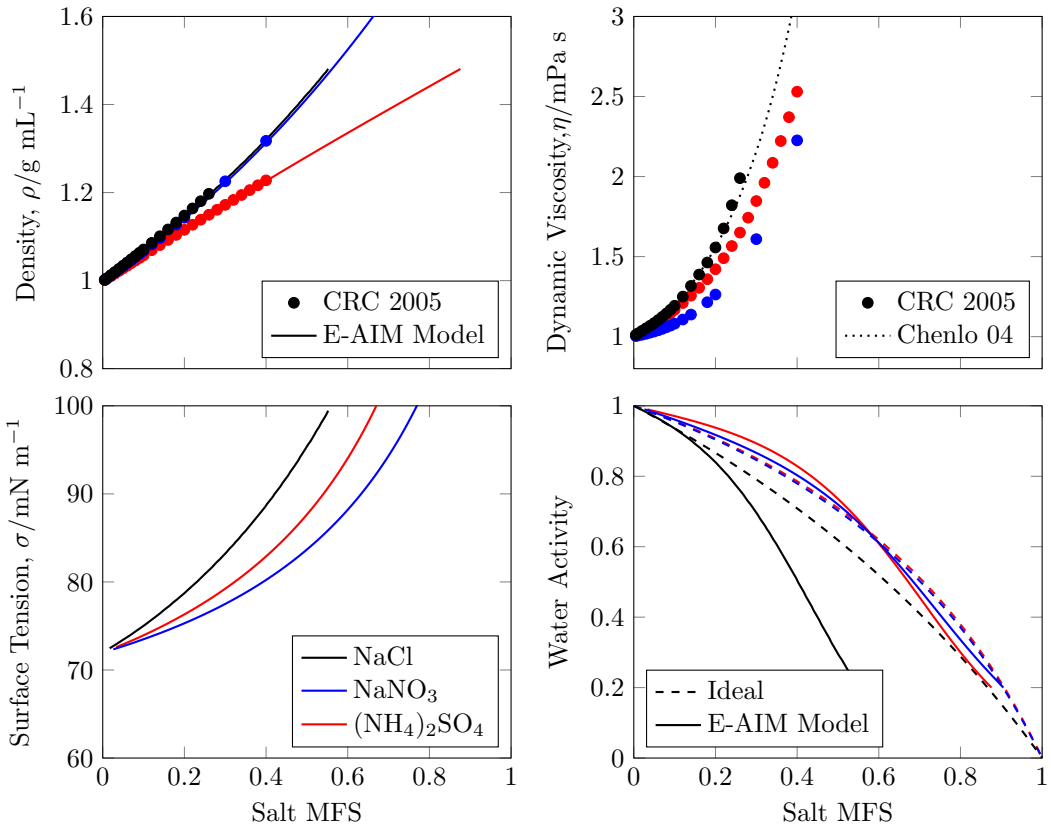

Figure 6.1: Properties of different salt solutions, NaCl (black), $NaNO_3$ (blue) and $(NH_4)_2SO_4$ (red) taken from Ref. 91 (CRC 2005 circles) or calculated using Refs. 193, 194 (E-AIM Model solid lines) and 195 (Chenlo 2004 Model dotted line for NaCl viscosity). Ideal water activity (dashed line) from mole fraction of water.

6.1 for the three salts studied. Surface tension (and water activity) data are uncommon in the literature, and is normally given in terms of a gradient as in Table 6.2 because it changes linearly with concentration below the solubility limit. Reported water activities for salt solutions are often limited to low concentrations on the order of a few weight percent, however concentrations in my experiments often reach above the solubility limit. Therefore much of the following analysis relies on the Extended AIM Aerosol Thermodynamic Model (E-AIM) developed by Clegg *et al.*[193,194] for aerosols. In this model the partitioning of the liquid into a liquid and solid phase (i.e. crystallisation) can be turned off, allowing properties well above the solubility limit to be calculated for aerosol models.

Sodium chloride experiments took place with droplets with initial concentra-

Table 6.1: Solubilities (in terms of g Solute/L Solution, wt%) of different salts at $T = 25$ °C from Refs. 91, 193 and 194.

Salt	Solubility/ g L^{-1}	Solubility/ wt%
Sodium Chloride, NaCl	318	26.5
Sodium Nitrate, $NaNO_3$	663	47.7
Ammonium Sulfate, $(NH_4)_2SO_4$	537	43.3

Table 6.2: Change in surface tension for salts in terms of molarities or molalities from the literature.

Salt	Gradient mN m^{-1}	Range	Authors
NaCl	1.63 M^{-1}	0 – 5 M	Adamson and Gast [196]
NaCl	1.76 M^{-1}	0.5 – 3 M	Henry *et al.* [197]
$NaNO_3$	1.35 M^{-1}	0.5 – 3 M	Henry *et al.* [197]
NaCl	1.69 M^{-1}	0 – 7.6 M	Bzdek *et al.* [198]
NaCl	1.46 M^{-1}	0 – 5 M	Tuckermann [199]
$NaNO_3$	1.01 M^{-1}	0 – 4 M	Tuckermann [199]
$(NH_4)_2SO_4$	1.96 M^{-1}	0 – 5 M	Tuckermann [199]
NaCl	2.08 M^{-1}	0 – 1 M	Weissenborn and Pugh [200]
NaCl	1.62 kg mol^{-1}	0 – 1 mol kg^{-1}	Matubayasi *et al.* [201]
$NaNO_3$	1.13 kg mol^{-1}	0 – 1 mol kg^{-1}	Matubayasi and Yoshikawa [202]
NaCl	1.62 kg mol^{-1}	0 – 6 mol kg^{-1}	Svenningsson *et al.* [203]
$(NH_4)_2SO_4$	2.362 kg mol^{-1}		Svenningsson *et al.* [203]
NaCl	1.62 kg mol^{-1}	Model	Dutcher *et al.* [204]
$NaNO_3$	1.19 kg mol^{-1}	Model	Dutcher *et al.* [204]
$(NH_4)_2SO_4$	2.38 kg mol^{-1}	Model	Dutcher *et al.* [204]

tions up to 20 wt%. Sodium nitrate has a higher solubility limit, therefore those experiments took place for concentrations between 5 and 30 wt% $NaNO_3$ while ammonium sulfate experiments were only conducted at 1 or 10 wt%. It was much easier to print lower concentration salt solutions to avoid crystals nucleating at the nozzle. Once crystals appeared at the nozzle plate they would grow over time and reduce the reproducibility of where a droplet would land on the substrate and eventually completely block the nozzle (see Figure 6.2), as a result most NaCl experiments were done with 10 wt% solutions.

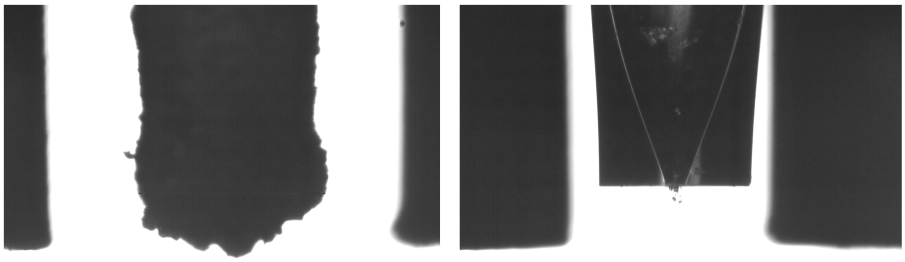

Figure 6.2: Picture of 50 µm diameter orifice Microfab nozzle (with nozzle shields) after a set of 20 wt% NaCl experiments followed by a rinsing procedure.

6.3 Evaporation

To begin this discussion of the evaporation of salt droplets it is beneficial to draw attention to the differences in evaporation dynamics compared to the solvent and sugar systems studied. The following figures show a few sets of droplet profiles where the initial dimensions were similar but the droplets had different compositions or evaporated into different relative humidities.

The salts dissolved in solution are involatile, therefore as a droplet evaporates the solute will become more concentrated, reducing the water activity, slowing the evaporation. Figure 6.3 illustrates how as the concentration of sodium nitrate in a droplet is increased to 30 wt% (at a fixed relative humidity), the evaporation rate decreases. In the previous section Figure 6.1 showed that the water activity does not significantly decrease at low salt concentrations, as a result the early evaporation rates were similar for the 5 and 15 wt% droplets in Figure 6.3.

In contrast to the sugar droplets in the previous chapter, the salts crystallise out of solution. This leads to kinks in the curves displaying the evolution of droplet profiles taken from the side-view camera as a spherical cap shape is fitted to something asymmetric. Droplets were simultaneously recorded from the side and from below and in these bottom-view videos any crystals could be observed when they were still on the order of a micron in size. This allowed the true crystallisation times to be found, which were tens of milliseconds earlier than the kinks in the droplet profiles. This discrepancy arose from the crystals needing to

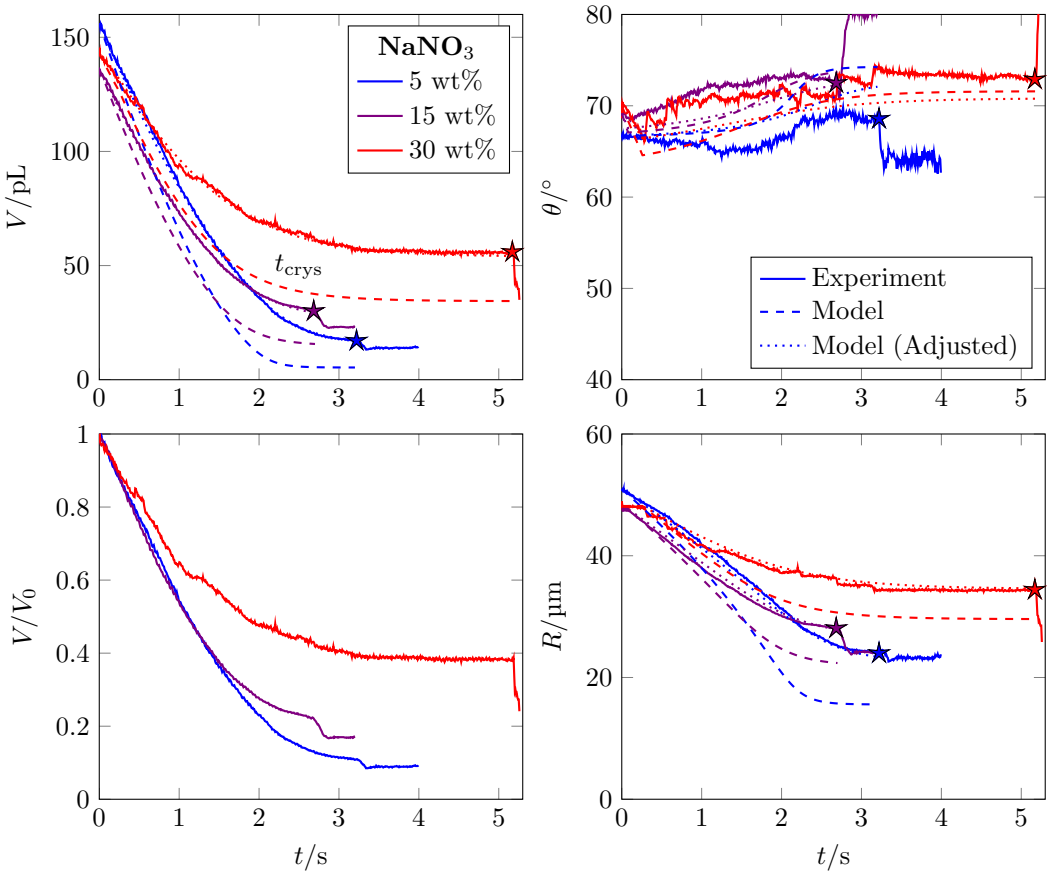

Figure 6.3: Evaporation of sodium nitrate droplets of different concentrations: 5 wt% (purple), 15 wt% (blue) and 30 wt% (red). No humidity cell, $RH = 30 \pm 2\%$, HMDS-treated substrate, no particles. Stars mark measured time of crystallisation. Experimental data shown with solid lines. Dashed lines for my composition averaged model with the same RH and nominal initial concentration as the experimental droplet. Dotted lines for the composition averaged model where RH and c_0 have been adjusted to give the best fit to the experimental data.

grow to a sufficient size to distort the droplet profile.

Figure 6.4 reflects the expected behaviour that the evaporation of water from the salt droplets slows as the relative humidity is increased. High relative humidity delayed or prevented the salts from actually crystallising, in the figure the red line for a droplet at 65% RH had not crystallised after 350 s (shown by the insert in lower left plot) despite the lower concentration droplets crystallising in under 4 seconds when $RH \leq 33\%$. This lack of crystallisation at high RH shall be elaborated on in Section 6.5 on efflorescence.

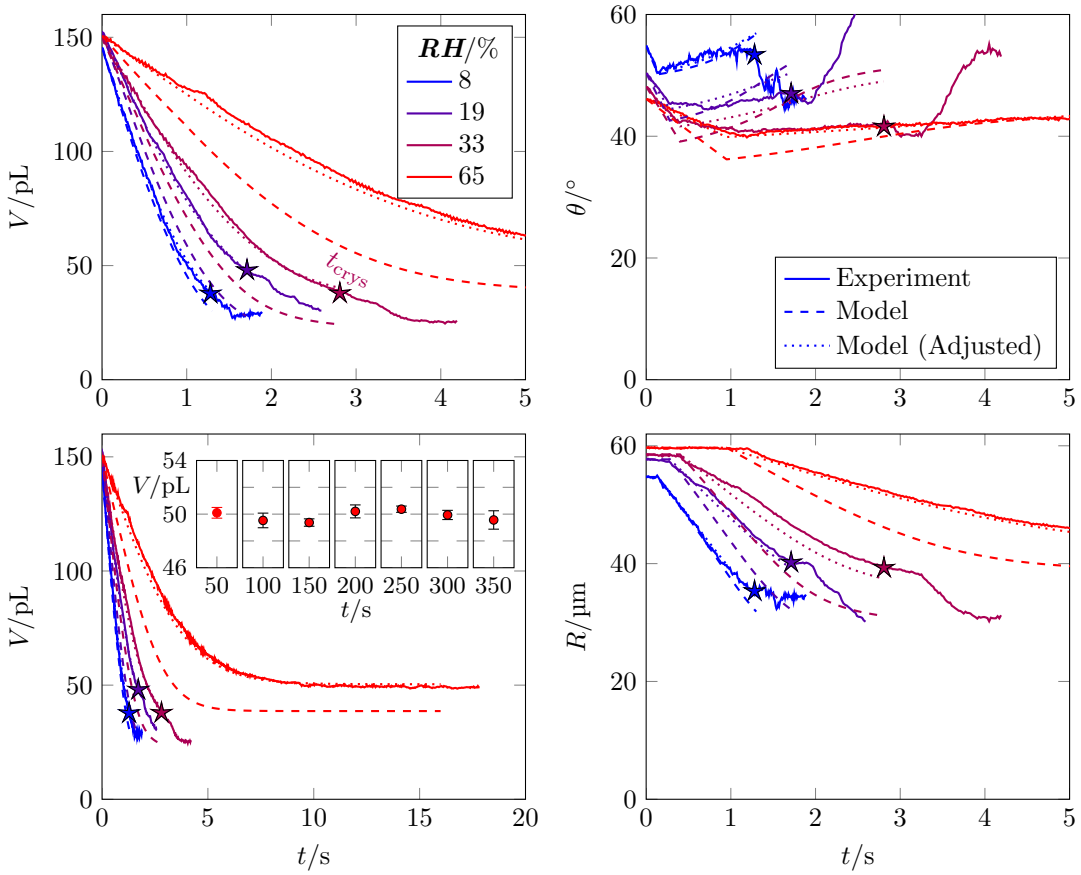

Figure 6.4: Evaporation of sodium chloride droplets of concentration 10 wt% NaCl droplets evaporating in a humidity chamber on HMDS-treated substrates, no particles in the droplets. Different RHs were 8 (blue), 19 (purple), 33 (magenta) and 65% (red). Stars mark measured time of crystallisation, t_{crys}. Experimental data shown with solid lines. Dashed lines for my composition averaged model with the same RH and nominal initial concentration as the experimental droplet. Dotted lines for the composition averaged model where RH and c_0 have been adjusted to give the best fit to the experimental data. Insert in bottom left plot shows droplet volume for the 65% system at long times, error bars come from standard error of droplet volume extracted from a set of droplet profiles about each time point.

6.3.1 Evaporation Model

In Figures 6.3 and 6.4 the experimental data (solid lines) are compared against modelled droplets with matching initial conditions (dashed lines). There is also a second set of modelled results where the inputted initial salt concentration and relative humidity were adjusted (increased) to give a better match to experiment as the unadjusted modelled droplets evaporated much more quickly than their experimental counterparts.

The evaporation model used was introduced in Section 2.9 and applied Popov's mass loss equation[31] (Equation 2.4) with a modified water activity term depending on the mean concentration of salt.[205] The majority of experiments took place on HMDS-treated substrates, this increased the contact angle so the volumes at the moment of crystallisation could be determined more precisely. On such substrates the droplets might only be pinned for a small portion of the droplets lifetime. Therefore at the measured time when experimental droplets depinned I would force modelled droplets to stop evaporating with constant contact radius. After the CCR evaporation stage there was a mixed mode of evaporation in which the contact angle changed slowly. During this stage the instantaneous mass change (water lost) would be computed, then the contact angle would be adjusted to reflect the surface tension at the new (mean) composition relative to the previous timestep.[206]

When this model was applied to sucrose droplets (in Section 5.3) the evaporation rate using the experimental relative humidity was close to that measured experimentally. However at late times the effective mass fraction of sucrose needed to be higher to match the final volume. In contrast when experimental data was plugged in as initial conditions for the salt model, the evaporation rates did not agree even at early times, except for low humidities, in addition to the final volume being a poor match.

6.3.2 Evaporation Model Adjustments

To achieve better agreement between modelled salty droplets and experiment, both the starting salt concentration (c_0) and the relative humidity needed to be increased when inputted into the model. Increasing these variables slowed the evaporation, which was necessary as the real droplets always took longer to dry than droplets modelled with the same experimental conditions. The results of these changes are given by the dotted lines in Figures 6.3 and 6.4 which much more closely align with experimental changes in volume than the unadjusted model (dashed lines), although the contact angle behaviour was only a qualitative match.

In order to derive the necessary adjustments the starting droplet dimensions would be unchanged and I would simultaneously vary the starting concentration and the relative humidity to best fulfill two constraints: the end volume ratio V_{end}/V_0 and the evaporation rate at early times. In this model where the droplet composition is fully averaged across the drop, the ratio V_{end}/V_0 is a function of c_0 and RH as the model droplets evaporate until the mean mass fraction leads to a water activity equal to the relative humidity. The evaporation rate is also modified by c_0 and RH, although as it was the "early time" evaporation rate being fitted, the salt concentrations were still low (so the water activity would not have yet deviated strongly from 1) meaning the evaporation rate was dominated by the relative humidity term, allowing the variables to be fixed for the fit.

The changes required to achieve a better fit were significant, Figure 6.5 shows that the concentration typically needed to be increased by a few wt% while the relative humidity needed an increase of more than 10% RH. To understand Figure 6.5 it is best to imagine the change required to the model inputs so that a marker's fill colour (from an experimental droplet evaporating under those conditions) would be given by the model, as shown by the background colour. As an example in the right hand plot the adjustments needed for the 33 and 65%

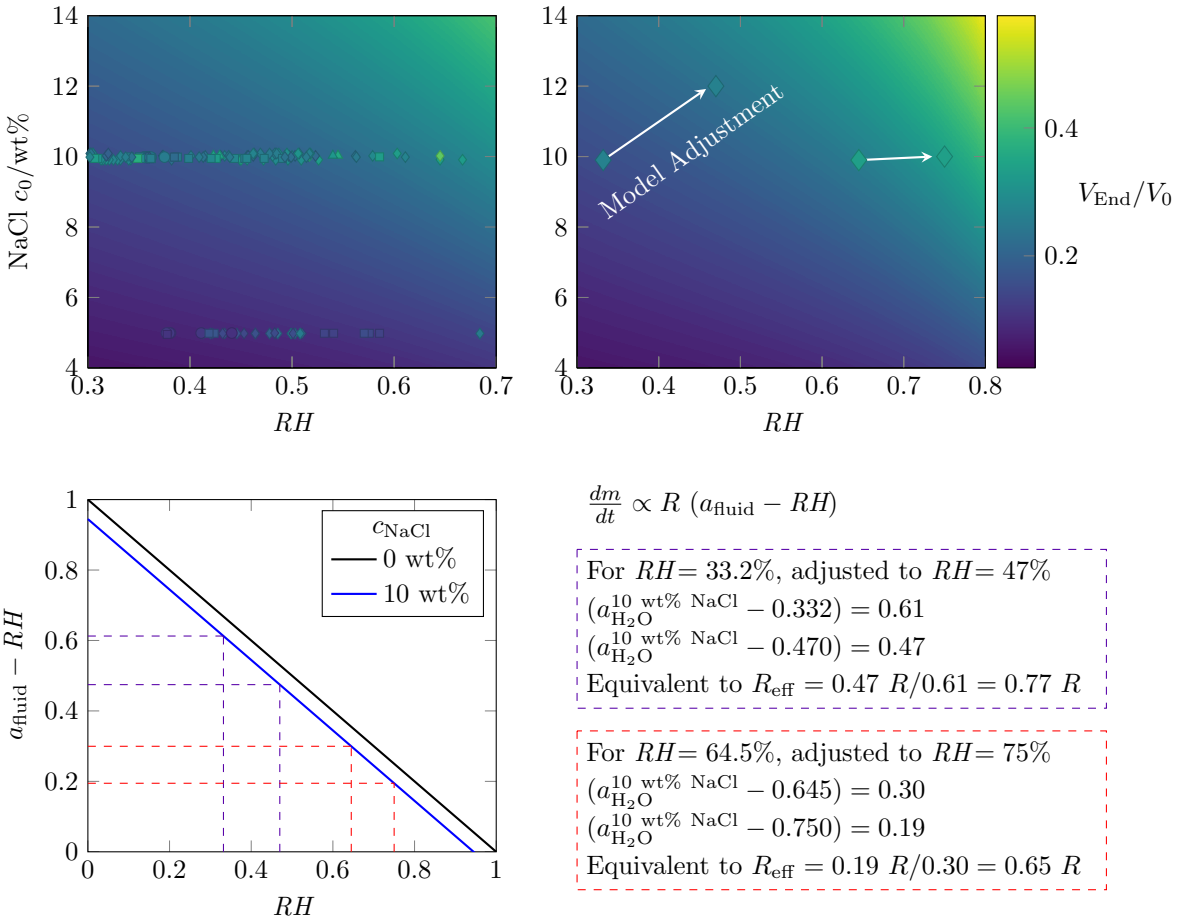

Figure 6.5: Comparison between surface of expected equilibrium end volumes for initial salt concentration-RH combinations and experiment. The fill of the markers gives the experimental V_{end}/V_0 which do not match the surface calculated using the composition-averaged model. In order for droplets modelled on the experimental data to agree with the background colourmap, c_0 and RH must be increased, with the right hand plot giving an example for the adjustments required for the higher RH NaCl droplets in Figure 6.4 where the marker fill is kept constant so agreement following adjustment can be observed. The lower half of the figure shows how the modelled evaporation rate could be reduced by instead adjusting the effective droplet radius. For a 10 wt% NaCl droplet the activity of water $a_{fluid} = 0.94$, then to give an an equivalent reduction in the evaporation rate (proportional to $a_{fluid} - RH$ to the two RH adjustments given by the magenta and red dotted lines (to match the colours in their time dependent droplet profiles in Figure 6.4) the effective radius would need to be 23 or 35% smaller.

RH NaCl droplets in Figure 6.4 are shown. The surface plot shows that there were many ways to achieve a given end volume ratio, as there are effectively lines of constant end volume to initial volume ratio running approximately diagonally from high c_0 and low RH to low c_0 and high RH.

It is easy to rationalise the increases in the initial concentration used for adjustments. The reflectometry experiments with ethanol-water droplets in Section 3.7.4 showed that a printed droplet can deviate from the prepared fluid concentration after a short time as a result of evaporation at the nozzle. Therefore after a 1 to 2 second delay in printing a droplet (time taken to replenish the nozzle fluid by printing out-of-view and moving the nozzle back into position) it is certainly feasible for the actual starting concentration of salt to be higher than assumed.

However there is little evidence to suggest that the real relative humidity is so much higher than measured. The sensor was calibrated (see Section 2.7) and the efflorescence results to be presented in Section 6.5 showed RH dependent transitions in good agreement with literature values. Therefore the adjustments to RH are merely a proxy to account for other things going wrong in the model. As the rate of loss of mass is directly proportional to the droplet radius then an effective droplet radius can be used instead of RH to adjust the evaporation rate. This different approach is shown in the lower part of Figure 6.5. For a 10 wt% NaCl droplet the change in evaporation rate from a RH adjustment from 33.2% to 47% is equivalent to a reduction in the effective radius by 23% while the adjustment from 64.5% to 75% would be equivalent to a reduction of 35% in the effective radius. In this scenario the contact line region of the droplet can be imagined as so enriched with salt that the droplet effectively evaporates as if it is smaller. However given the disagreement in the evaporation rates of upwards of 20% this is unlikely to be the sole contributor to the disagreement.

A similar surface plot to Figure 6.5 plot for sucrose is provided in Appendix D.2. The difference between the degree of agreement between experiment and

theory for sugars and salts is likely a result of the water activity dependence. A high salt concentration causes a larger decrease in the water activity than a concentrated sucrose solution as the salts dissociate into ions which increase the degree of ordering in the molecular structure of the fluid. As a result droplet evaporation is more sensitive to salt enrichment (than sugar enrichment) at the surface.

6.4 Classical Nucleation Theory

In order to understand the significance of the shift in the efflorescence relative humidity described later this chapter it is necessary to discuss Classical Nucleation Theory in more detail.

In Classical Nucleation Theory[182] (CNT) processes with a single nucleation barrier have a rate of nucleation per unit volume, J_{CNT}, described by an Arrhenius type equation

$$J_{\mathrm{CNT}} = \kappa \exp\left(\frac{-\Delta G^*}{k_B T}\right) \tag{6.1}$$

where ΔG^* is the free energy barrier to nucleation and κ is a kinetic prefactor that describes the nucleation attempt frequency, often approximated as

$$\kappa = n_I j Z \tag{6.2}$$

where n_I is the number density of possible nucleation sites and j is the rate at which molecules reach those possible sites. This rate goes as

$$j \sim n_s D R_c^* \tag{6.3}$$

where n_s is the number density of molecules, D is the diffusion coefficient of the ions and R_c^* is the size of the critical nucleus. The Zeldovich factor, Z, has the meaning of the probability that a molecule will cross the nucleation barrier from

the top of the barrier and is given as

$$Z \sim (N^*)^{-2/3} \tag{6.4}$$

where N^* is the number of excess molecules in the critical nucleus.

For homogeneous nucleation the molecules themselves are the sites of nucleation (so $n_s = n_I$), therefore if a spherical nucleus is considered then it will have a free energy barrier to forming of

$$\Delta G = 4\pi r^2 \sigma - \frac{4\pi}{3} r^3 \Delta\mu \; n_c \tag{6.5}$$

where n_c is the number density of molecules in the crystal, σ is the surface energy of the liquid-crystal interface and $\Delta\mu$ is the difference in chemical potentials between the crystal and liquid phases. Equation 6.5 can be understood as the sum of a free energy for the formation of a new spherical crystal with and a free energy penalty for the interface, and so is dependent on the geometry of the critical nucleus. As the radius of the cluster increases, ΔG increases until it reaches its maximum value ΔG^* when $r = R_c$. Beyond this critical radius ΔG decreases monotonically with r as the surface energy penalty term becomes less significant for a larger crystal. Therefore the maximum free energy barrier is

$$\Delta G^* = \frac{4\pi}{3} \sigma R_c^2. \tag{6.6}$$

The critical radius is calculated from the change in chemical potential relative to that at the saturation concentration. Given that the chemical potential, μ, defined relative to some standard state, is

$$\mu = \mu^0 + R'T \ln a \tag{6.7}$$

where we recall R' is the ideal gas constant, then

$$\Delta\mu = k_\mathrm{B} T \nu \ln \left(\frac{\gamma_\pm}{\gamma_\pm^\mathrm{sat}} \frac{m}{m^\mathrm{sat}} \right) \tag{6.8}$$

where $\nu = 2$ for NaCl due to the dissociation into ions and $\gamma_{\pm}$ is the mean activity coefficient at molality m.[207] From this chemical potential difference the critical radius can then be determined

$$R_c = \frac{2\gamma}{n_c|\Delta\mu|} \tag{6.9}$$

Heterogeneous CNT

For heterogeneous nucleation on an infinite, smooth, flat surface the critical nucleus can instead be described by a spherical cap with some contact angle ϕ depending on the interaction between the solid and the substrate which decreases the free energy barrier ΔG^*. Using Volmer's early work[208] there is Sear derived[182]

$$\Delta G^*_{\text{SESSILE}} = \Delta G^*_{\text{HOMO}}\ F(\phi) \tag{6.10}$$

where $F(\phi)$ is the purely geometric factor

$$F(\phi) = (1/2) - (3/4)\cos\phi + (1/4)\cos^3\phi \tag{6.11}$$

The impact of heterogeneous nucleation is that the critical cluster can be smaller, making it more likely for a growing crystal to reach the critical size. In addition the surface can lead to ordering in the fluid, promoting the formation of the critical cluster so the rate of nucleation can be many orders of magnitude faster than for homogeneous nucleation.

6.5 Efflorescence

In this section I discuss the conditions under which salt droplets actually crystallise. In the Evaporation section, Section 6.3, Figure 6.4 showed that at high relative humidity the 10 wt% sodium chloride droplet did not crystallise during the typical experimental time frame of a few seconds. Extending the

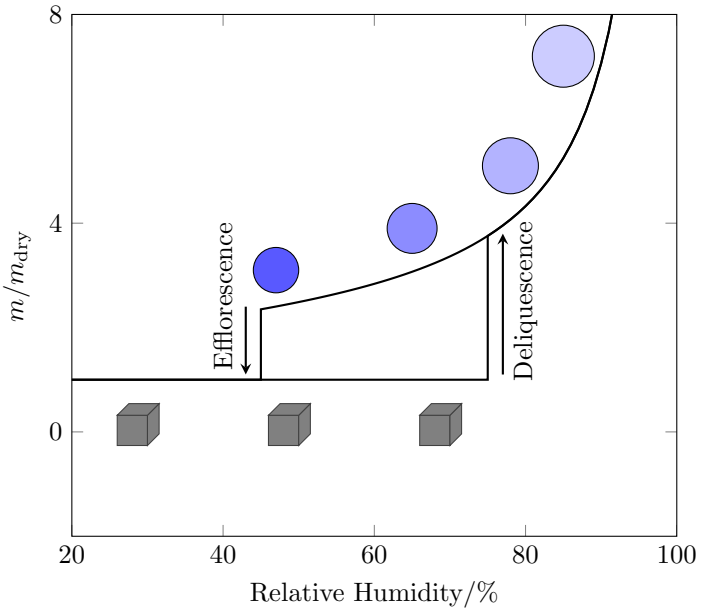

Figure 6.6: Particle mass relative to dry mass for sodium chloride aerosols undergoing a humidity cycle using the E-AIM model.[193] Starting at low relative humidities the particle is dry until the deliquenscence relative humidity. Starting at high relative humidities the droplet will shrink, become more concentrated (represented by the darker blue colour), and effloresce. Droplet radii along the top edge are proportional to the change in RH.

period over which droplets were viewed to a few minutes (but only taking a few short videos at different times to save memory: the high speed camera had a minimum frame rate of 50 fps so a 6 minute video would have an impractical 180,000 frames and a file size of hundreds of gigabytes) showed that droplets could display behaviour similar to sugar droplets in that a steady end volume would be reached. This was not expected as the droplets were supersaturated so crystallisation was thermodynamically possible.

This behaviour has not been previously reported in the literature for sessile droplets; however it is not entirely novel as it is a well known phenomenon in aerosol science.[209,210] In single-droplet evaporation studies, an aerosol droplet (containing some involatile solute) can be suspended in an electromagnetic trap where it will come to equilibrium with its surroundings. If the droplet starts off in a environment with a high relative humidity the droplet will contain a lot

of water, if the relative humidity is lowered the droplet will re-equilibriate and lose some of that water. It is possible to keep drying the droplet by lowering the relative humidity so the droplets can become highly concentrated with the solute.[169] If that solute is an inorganic salt then there comes a point at which the droplet is so supersaturated that the salt will crystallise out into a solid phase. The relative humidity at which the droplet has been sufficiently dried out to lead to this behaviour is called the efflorescence relative humidity (*ERH*). At relative humidities below the *ERH* the particle will always become dry. If a dry particle undergoes an experiment in which the relative humidity is increased, then as the crystal is exposed to the *ERH* it will not imbibe water and revert to a droplet; instead the relative humidity has to be increased to the higher deliquescence relative humidity (*DRH*), which appears around the water activity of the salt at its solubility limit, before it will imbibe water. This behaviour is displayed in Figure 6.6 for sodium chloride, the figure shows that there is hysteretic behaviour where at the same humidity a particle can be solid or liquid depending on the starting conditions of the particle (low or high *RH* respectively). Therefore droplets equilibriated to a relative humidity between the *ERH* and *DRH* are metastable, existing at supersaturated concentrations.

In my experiments the droplets evaporate at fixed *RH* rather than equilibriating with a gradually lowered relative humidity. The transition between when the inkjet-printed sessile droplets crystallised or not with increasing relative humidity show the first results of efflorescence in sessile droplets. Deliquescence in sessile droplets is not new, Desarnaud and Shahidzadeh-Bonn[226] used humidity cycles to get a NaCl sessile droplet to expel impurities in which after crystallisation the relative humidity was repeatedly brought above the *DRH* around 75% (see Table 6.3).

To prevent any confusion arising from terminology is worth pointing out that outside of aerosol science "efflorescence" can have other definitions. In discussions

Table 6.3: Literature deliquescence relative humidities for different salts at $T = 25°C$.

Salt	$DRH/\%$	Authors
NaCl	75.3	Tang *et al.*[211]
NaCl	75.7	Tang[212]
NaCl	75.3	Richardson and Snyder[213]
$NaNO_3$	74.3	Richardson and Snyder[213]
$NaNO_3$	74.5	Tang and Munkelwitz[192]
$(NH_4)_2SO_4$	79.5	Tang[212]

Table 6.4: Literature efflorescence relative humidities for different salts at different temperatures.

Salt	$ERH/\%$	$T/°C$	Authors
$(NH_4)_2SO_4$	37	25	Tang and Munkelwitz[192]
$(NH_4)_2SO_4$	35	20	Cohen *et al.*[214]
NaCl	44	20	Cohen *et al.*[215]
NaCl	45	25	Tang *et al.*[211]
NaCl	45.1	24.8	Gao *et al.*[216]
NaCl	47.4		Li *et al.*[217]
NaCl	47	21.8	Lee and Hsu[218]
$NaNO_3$	N/A	21.8	Lee and Hsu[218]
NaCl	$45-48$	23	Liu *et al.*[219]
$NaNO_3$	N/A	23	Liu *et al.*[219]
$(NH_4)_2SO_4$	$32-35$	23	Liu *et al.*[219]
NaCl	$46-51$	$23-26$	Ma *et al.*[220]
$(NH_4)_2SO_4$	$36-46$	23-26	Ma *et al.*[220]
NaCl	45.5	25	Richardson and Snyder[213]
$NaNO_3$	N/A	25	Richardson and Snyder[213]
$NaNO_3$	< 40	Room	Lamb *et al.*[221]
$NaNO_3$	20	25	Tang and Munkelwitz[222]
$NaNO_3$	< 6	20	Gysel *et al.*[223]
$NaNO_3$	< 15	5	Hoffman *et al.*[224]
$NaNO_3$	< 53	5	Lu *et al.*[225]
$NaNO_3$	$0.5-30$	25	Tang and Munkelwitz[192]

of weathering such as in the construction industry the term is used to describe the growth of salt crystals on the outside of buildings where crystals may grow on the surface of a porous material (such as brick or rock) rather than subflorescing where crystallisation occurs within pores.[227,228] On porous materials there is a creeping mechanism[229] as fluid from inside the pores can partially redissolve the crystal and spread across a solid before crystallising again.

6.5.1 Sodium Chloride

In Section 6.3 on the evaporation dynamics of salt droplets Figure 6.4 showed that at high relative humidities the sodium chloride droplet did not crystallise after a number of minutes. This was not a one-off result, Figure 6.7 shows the experimental crystallisation times for all the NaCl droplets measured which had circular contact lines after impact on the substrate. It is clear that there is a discontinuity in the crystallisation time around the literature ERH where the lower plots demonstrate that the jump was not a result of just printing much larger droplets. The red curve in the lower left plot is described by the equation $t = A/(1 - RH)$ where A is an expected crystallisation time (purely a empirical fitting constant) for a droplet in a totally dry environment. While this functional form could successfully describe the drying time of water droplets of similar sizes at different RH it is not effective for describing the crystallisation time for salt droplets as the 1 in the denominator should really be a_w which would vary over time and with the initial droplet composition. Therefore the denominator is smaller than this simple calculation would predict, leading to longer crystallisation times, as are observed.

For the following figures in this chapter I have extended the convention given in Section 5.4 so that

- Filled markers are for droplets containing tracer particles,
- Half-filled markers are for droplets without tracer particles,

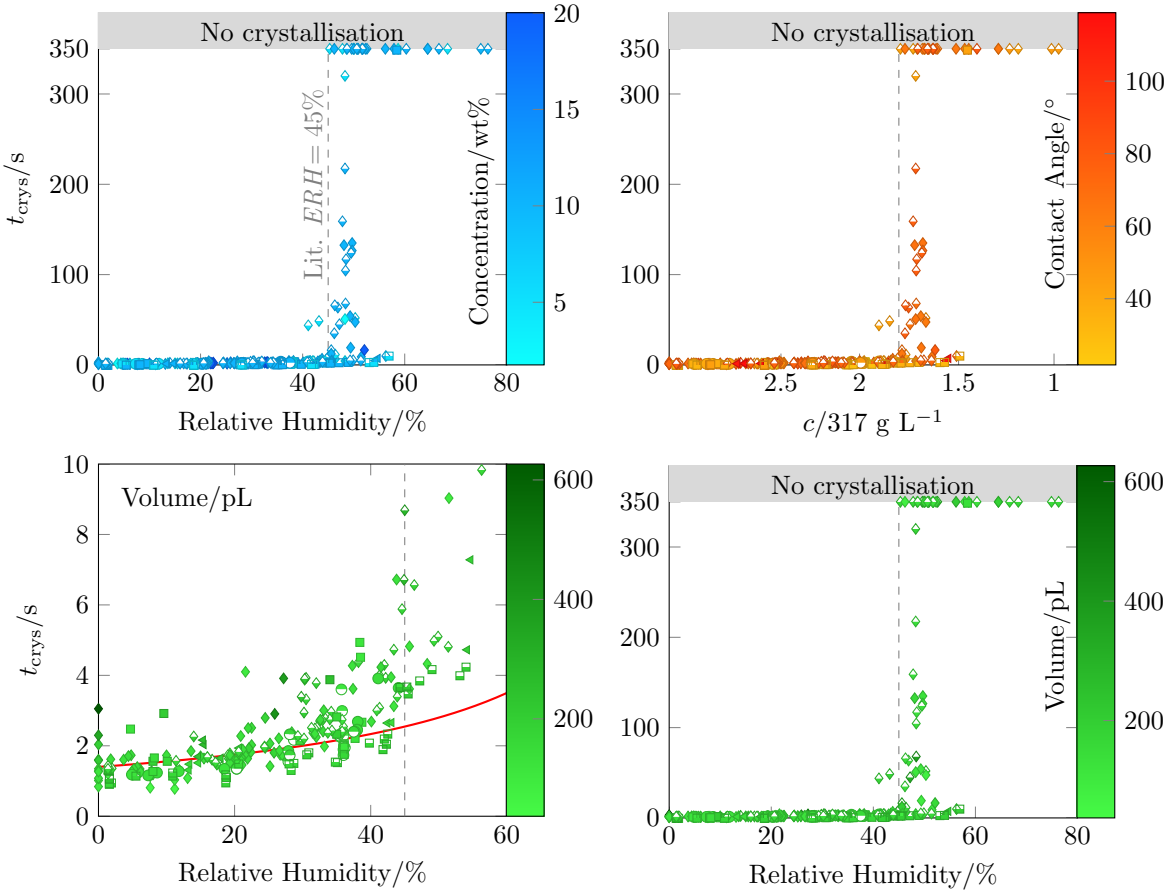

Figure 6.7: Experimental crystallisation times for evaporating sodium chloride droplets of different concentrations and volumes on different substrates and at different relative humidities. The red curve is for a $t = A/(1 - RH)$ fit which would approximate the drying time of a pure fluid.

- Circle markers are for droplets on Decon-treated substrates,
- Diamond markers are for droplets on HMDS-treated substrates,
- Square markers are for droplets on plasma-cleaned substrates,
- Triangle markers are for droplets on OTS-treated substrates,
- Blue colourmaps are for different starting concentrations,
- Red colourmaps are for different starting contact angles,
- Green colourmaps are for different starting volumes,
- Purple colourmaps are for different relative humidities,

- Greyscale colourmaps are for different crystallisation times.

Therefore in the top right plot of Figure 6.7 describing the contact angle dependence (plasma-cleaned) square markers are yellow/orange, (HMDS-treated) diamond markers are dark orange and (OTS-treated) triangles markers are dark red. This shows that there was not a substrate dependence on the efflorescence behaviour. Of the measurements on OTS-treated substrates the few at relative humidities above the literature *ERH* did still crystallise after a few seconds so it is possible that there was different crystallisation behaviour when $\theta_0 > 90°$ although not enough experiments took place on OTS-treated substrates to verify this. In the majority of experiments salt droplets above the efflorescence relative humidity did not crystallise (within of a few minutes). Then there were a number of cases where the droplet did not crystallise on the typical timescale of an experiment (< 10 s) but did crystallise as I watched after the bottom-view recording finished. This occurred at relative humidities only a few percent greater than the literature *ERH* so it is possible these shifts could be a result of the *RH* in the humidity chamber not being perfectly constant over longer times. The gas flow tended to slowly decrease over time as the room relative humidity was below the *ERH*, as a result the humidity in the chamber would slowly tend towards lower values to match the lab *RH*. Where droplets crystallised after a delay of a few minutes but not the full 350 s the *RH* at that moment was recorded instead of the relative humidity at the start of the experiment.

My experiments with NaCl put its *ERH* at around 48%. The majority of the reported studies on the evaporation of sessile sodium chloride droplets in the literature are at lower relative humidities than this in which crystallisation would therefore be expected. However there have been experiments at relative humidities above the *ERH* in which crystallisation was still seen. In Shahidzadeh *et al.*[160] and Desarnaud and Shahidzadeh-Bonn's work[226] a chamber with $RH = 50\%$ was used, while in Zhong *et al.*'s[230] experiments the droplets dried in an open

environment with $RH = 55 \pm 5\%$. Rodriguez-Navarro and Doehne[227] investigated sodium chloride droplets on glass at relative humidities of 20, 35, 50 and 65% with crystallisation in all cases. In these examples the substrates were not heated so droplets were also around room temperature but could be up to 2°C colder than my experiments, however Cziczo and Abbatt[231] showed that the *ERH* of sodium chloride decreases slowly with temperature, meaning that the *ERH* would not have changed appreciably. The main difference between the literature and my results is that their experiments all used larger microlitre drops, therefore this aerosol-like behaviour might require droplets approaching aerosol dimensions (as nucleation is stochastic so is more likely to occur in a larger volume) , requiring inkjet-printing technology.

The NaCl *ERH* of 48% is larger than the most precise aerosol measurements which report it as 45%. This shift is on the order of the precision of the Sensiron thermohygrometer (±2%) used. Furthermore when the sensor was calibrated, the measurements for potassium carbonate ($a_w = 0.431$), the salt with the closest water activity to NaCl's *ERH*, were slightly above the literature value. Therefore it is certainly possible that there is no real shift in the efflorescence relative humidity for sessile droplets. However if the shift is indeed real then these experiments would fit in with a little discussed trend in the literature.

The reported values for the efflorescence relative humidity of sodium chloride are in the range $44-51\%$, of these all the higher values were for aerosols which were on some sort of substrate which could act as a surface for heterogeneous nucleation. Li *et al.*'s aerosol particles[217] ($ERH = 47.4\%$) were generated by an atomizer and deposited as dry particles on transmission electron microscopy grids. Likewise Lee and Hsu[218] ($ERH = 47\%$) collected their aerosols on a filter before the relative humidity was varied while Liu *et al.*'s experiments[219] ($ERH = 45 - 48\%$) also required the use of a substrate for Fourier-transform infrared spectroscopy (FT-IR) measurements of the amount of water in the droplets. However only Ma

et al.[220] ($ERH = 46 - 51\%$) explicitly acknowledged how the FT-IR substrate could lead to heterogeneous crystallisation.

6.5.2 CNT for Sodium Chloride

In Figure 6.8 CNT is applied to calculate the nucleation rate for sodium chloride using Equations 6.1 to 6.11 and literature values combined with outputs from the E-AIM model.[194] The crystal surface tension was taken as $\sigma = 0.08$ Nm^{-1},[207,232] the diffusion coefficient treated as I will discuss in Section 6.6.2 where the increase in viscosity[195] is accounted for through the Stokes-Einstein Equation (Equation 5.2). Chemical potentials, number densities and an approximate Zeldovich factor (0.05, as Z goes into the prefactor only the order of magnitude is significant) were then taken from Zimmermann *et al.*'s work.[233] The work of Desarnaud *et al.*[207] and Robinson *et al.*[232] demonstrated that the nucleation rate is a very strong function of supersaturation, changing by tens of orders of magnitude between the saturation concentration and the supersaturations they were calculated to reach in Section 6.6.

In typical aerosol efflorescence experiments the humidity is varied slowly so the particle stays in equilibrium with the environment. Therefore the relative humidity of the environment is equivalent to the water activity of the particle which is a function of solute concentration (see the x-axis label in the top right plot in Figure 6.7). Therefore an increase in the *ERH* is equivalent to the phase transition occurring at lower (supersaturated) concentrations. An increase from the literature *ERH* from 45% to the 48% here is equivalent to the critical supersaturation ratio of the droplet decreasing from 1.80 to 1.72 for NaCl. Figure 6.8 shows that such a change of about 0.1 supersaturation leads to a dramatic change in J_{CNT} from the blue to the red curve. I chose to have the shift occur for nucleation rates of 10^{17} m^{-3} s^{-1}. This order of magnitude was calculated by

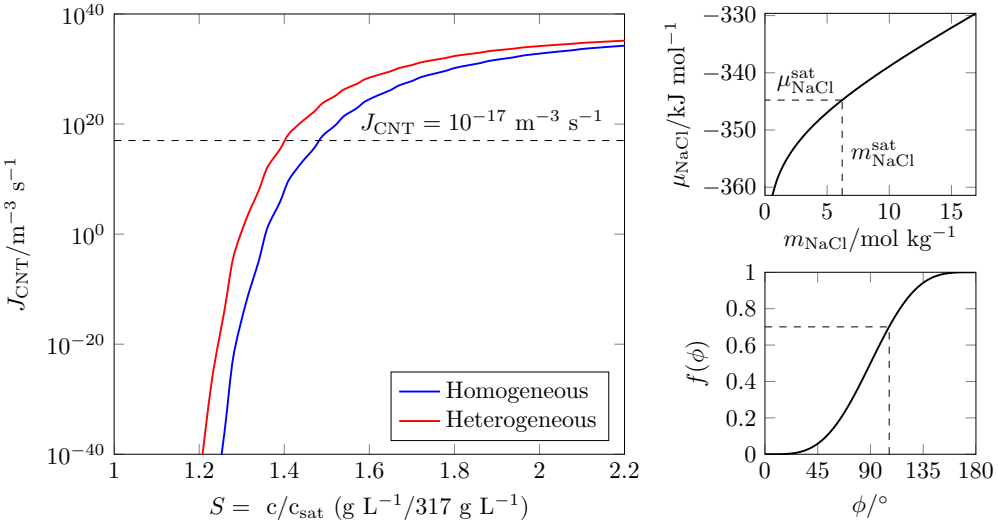

Figure 6.8: Main Plot: Nucleation rates from CNT for NaCl as a function of the supersaturation, blue line for homogeneous nucleation, red line for heterogeneous nucleation where the free energy barrier has been reduced by multiplication with a factor of 0.7 so the intercept through the dashed line reduces by 0.1 supersaturation, approximately equivalent to my 3% *RH* shift to higher *ERH*. The horizontal dashed line for a nucleation rate of 10^{17} m^{-3} s^{-1} comes from assuming nucleation within 1 ms for a micron hemispherical shell with a radius equal to the droplets in these experiments. Top Right Plot: chemical potentials of NaCl as a function of molality from Ref 233 used in calculation of R_c (Equation 6.9). Bottom Right Plot: Heterogeneous nucleation geometric factor as a function of crystal contact angle on the substrate (ϕ) with dashed lines for the factor 0.7 applied to the free energy barrier to give the red curve in the main plot.

rearranging the induction time for nucleation[215]

$$t_{ind} = \frac{1}{V\ J_{CNT}} \tag{6.12}$$

assuming $t_{ind} = 1$ ms while the volume was approximated as a 1 micron thick hemispherical shell (dR, as the droplets nucleate at the contact line) of typical droplet radius of 40 µm, thus $V = 2\pi R^2 dR$.

In this framework where the shift in *ERH* is a result of a heterogeneous nucleation pathway, what decrease in the free energy barrier that would lead to the shift of 0.1 supersaturation can be calculated. This is heterogeneous nucleation at the substrate rather than the surfaces of particles; in Figure 6.7 the

filled markers for droplets containing particles did not show different efflorescence behaviour to droplets which did not contain particles.

In order to achieve a 0.1 supersaturation shift a 30% decrease in ΔG^* was required, which from Equation 6.11 would mean a crystal contact angle $\phi \approx 106°$. The crystal deposits to come in Section 6.7 were not strongly "wetting" (NaCl crystals tended to be blocky rather than thin and flat crystals along the substrate) so this is a plausible contact angle.

However there are issues with this approach. The next section shows that there was a similar shift of about 3% *RH* between literature values and measured *ERH* of ammonium sulfate (AMS) droplets. However the AMS deposits were very different and would completely cover the substrate within the droplet contact line area, so a lower critical nucleation cluster contact angle is expected which the 3% *RH* shift does not show. Another problem is that for heterogeneous nucleation then different *ERH*'s would be expected for different substrate wettabilities, however no difference between plasma-cleaned and HMDS-treated substrates was found in this regard.

Finally there are general issues with how valid these calculations are. For instance one limitation of CNT is that it includes the assumption that the cluster has properties similar to the bulk crystal and that the surface free energy is for an infinitely flat planar surface rather than a realistic one with high curvature.[234] Therefore while it is useful to discuss CNT and how a heterogeneous nucleation pathway is a plausible reason for a shift in the *ERH*, the crystal contact angles calculated here are of limited use.

6.5.3 Ammonium Sulfate

The shift in the measured efflorescence relative humidity was also measured in evaporating ammonium sulfate droplets. While Tang and Munkelwitz[192] gave the *ERH* as 37%, Figure 6.9 shows that my measurements were better fit by an

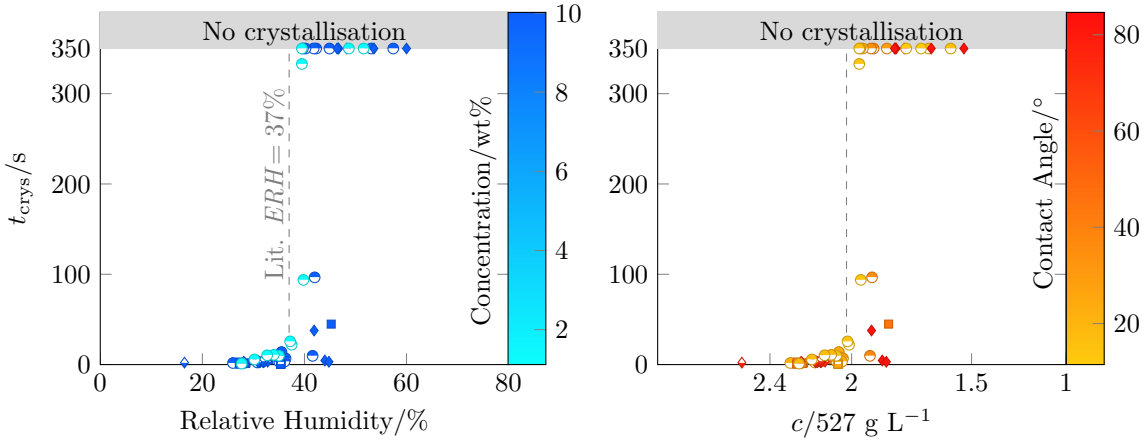

Figure 6.9: Experimental crystallisation times for evaporating ammonium sulfate droplets of 1 or 10 wt% on different substrates and at different relative humidities.

efflorescence relative humidity of around 40%, which is supportive of the above interpretation that these salts are crystallising via a heterogeneous nucleation pathway.[220] As for sodium chloride droplets, the discontinuity in the crystallisation times was not affected by changing the concentration or substrate and the measured volumes of the droplets did not change by an order of magnitude, being almost entirely in the range of $130 \leq V_0 \leq 210$ pL.

That ammonium sulfate sessile droplets demonstrate the same type of efflorescence behaviour as aerosols is important as this salt is commonly included in agricultural formulations, although at much lower concentrations than have been used in this study. These agricultural formulations are designed to be used outdoors so the droplets are generated as a spray out in a field which will then land over the leaves of a plant as sessile droplets with a typical volume on the order of tens of nanolitres.[235] As the droplets are outside, the relative humidity can vary greatly depending on the weather. There can also be local variations due to plant cover where sheltered regions trapping water vapour lead to higher relative humidities for some droplets. This means that the efflorescence of sessile AMS droplets can be very relevant to a plant's uptake of chemicals in the formulation as if the relative humidity is above the *ERH* then the droplet will not crystallise,

leaving the active ingredients in solution rather than locked away in a solid phase. Obviously such an effect would be highly dependent on the formulation; in studies of the efflorescence behaviour of mixed salt aerosols, as the droplet dries the salt with the higher *ERH* will crystallise first, then the more stable second salt nucleate on that solid phase via a heterogeneous mechanism.[213]

6.5.4 Sodium Nitrate

As an inorganic salt, sodium nitrate will also crystallise from evaporating droplets. However unlike sodium chloride and ammonium sulfate the efflorescence behaviour is not well behaved. In Table 6.4 it is clear that the recorded *ERH*s for NaCl and AMS are reasonably reproducible but there is a wide range of reported values for sodium nitrate. This unpredictibility has also been shown earlier in this chapter, Figure 6.3 showed the droplet profiles for evaporating sodium nitrate droplets of different initial concentrations but at the same relative humidity. If Figure 6.3 was for NaCl then as the initial concentration increased then the more concentrated droplets would crystallise sooner as they would reach higher supersaturations earlier. Instead the highest $NaNO_3$ concentration droplet of 30 wt% (chosen to demonstrate this unexpected crystallisation behaviour) in the figure crystallised much later.

Past studies have shown that during the nucleation of sodium nitrate droplets there is some probability that droplets will persist without crystallising, unlike what would be expected based on the single-nucleation step CNT that can be effective at describing NaCl and AMS systems.[232] Zhang *et al.*[236] used FT-IR spectroscopy coupled with attenuated total internal reflectance spectroscopy to follow the crystallisation of sodium nitrate aerosol droplets on a ZnSe substrate. The humidity was kept constant for an hour at certain relative humidities and the fraction of the droplets which evaporated tracked. When *RH* was in the range $75.7 - 62.5\%$, 4% of the starting number of droplets had crystallised; in

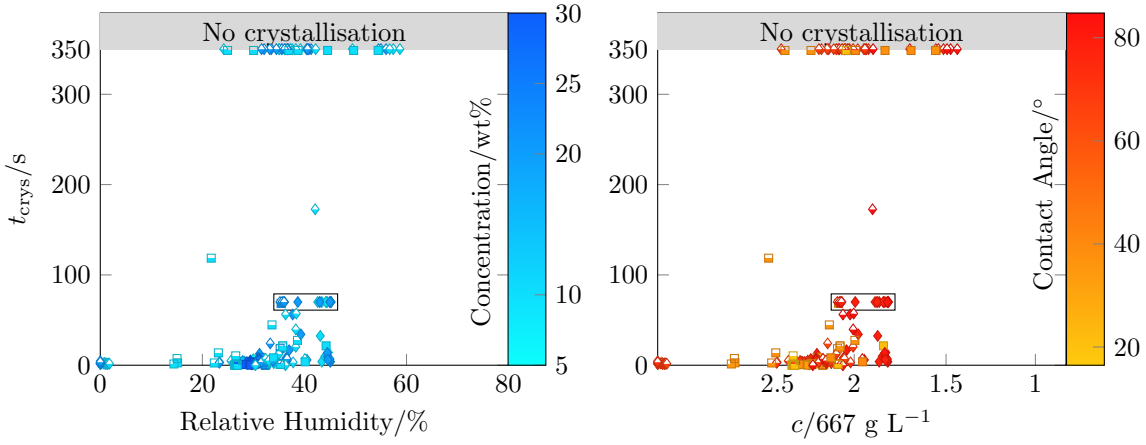

Figure 6.10: Experimental crystallisation times for evaporating sodium nitrate droplets of different concentrations and volumes on different substrates and at different relative humidities. Droplets in the black box had their droplet profiles recorded at a higher fps so the experiment duration was only 70 seconds.

the range 62.5 – 51.9%, an additional 79% of the total had crystallised; 51.9 – 43.1%, another 16% of the total had crystallised; 43.1 – 27.9%, another 1% of the total had crystallised; by a relative humidity of 4.5% all the droplets had crystallised. Similarly Gregson *et al.*[237] found stochastic behaviour where different percentages of droplets would have crystallised depending on the relative humidity, with even 2.5% of 20 wt% $NaNO_3$ droplets not crystallising during the 10 s timeframe of their experiment despite evaporating in pure nitrogen, i.e. 0% relative humidity. Such extreme resistance to crystallising has been noted before, Tang and Munkelwitz[192] measured sodium nitrate droplets persisting at 0.5% *RH* at which point they calculated each solvent molecule would be expected to be shared between 5 – 6 solute molecules. Gregson *et al.*[237] ruled out heterogeneous nucleation of the droplets which did crystallise by trapping a single particle and exposing it to multiple humidity cycles. For aerosol droplets heterogeneous nucleation would require a dust-particle or the like but their experiments showed that the same particle (i.e. particle had a fixed level of impurities if any were present) undergoing *RH* cycling would crystallise at different times or not at all.

This was different to Lee *et al.*[238] who found that they could classify their sodium nitrate particles differently after humidity cycles depending on the reproducibility of their efflorescence. Their fraction of particles that reproducbily effloresced was then found to increase as a less pure sodium nitrate was used in experiments and they argued that without impurities the induction time for homogeneous nucleation was too long for crystallisation to be observed. Kim *et al.*[239] used SEM experiments so their particles may have experienced heterogeneous nucleation on the substrate and also grouped their sodium nitrate particles into different classes. Over 90% of their droplets did not crystallise at 15% *RH* but of those that did there was a class which had a well defined *ERH* and *DRH* such as in one of the earlier studies by Tang and Munkelwitz[222].

The difference between the behaviour of sodium nitrate compared to sodium chloride or ammonium sulfate is contested. Robinson *et al.*[232] argue that because of the exponential form of J_{CNT} only factors that influence ΔG^* are important, therefore they suggest that the disagreement with CNT is a result of sodium nitrate following a more complicated nucleation pathway, possibly involving multiple steps. However Gregson *et al.*[237] were able to validate an Arrhenius form for the nucleation rate (Equation 6.1) by getting a linear result in a logarithmic plot of a crystallisation timescale vs $1/T$ to estimate the free energy barrier to nucleation. They then argued that the lack of crystallisation could be a result of the viscosity of sodium nitrate droplets increasing by orders of magnitude as the mass fraction of solute rises.[240] An increase in viscosity would reduce the diffusion coefficient and so prevent enough solute molecules reaching a growing pre-critical nucleus. This behaviour would not be observed for sodium chloride where the viscosity does not change so significantly but they suggest that for sodium nitrate the change would be important enough for the kinetic prefactor term to be affected.

In experiments with sodium nitrate droplets I collected a broad range of efflorescence behaviour rather than an obviously stochastic system where there

was some percentage of droplets that did not crystallise as a function of relative humidity. Figure 6.10 shows that droplets were found which did not crystallise at relative humdities as low as 22% while other droplets did crystallise at relative humidities as high as 45%. That my sodium nitrate droplets did not persist in very dry environments like in some of the above studies has three possible causes. The least significant would be that these inkjet-printed droplets were a little larger than typical aerosol sizes, therefore given relatively long experiment durations of 350 s it was more likely to observe droplets crystallising than small aerosols that might be a fifth of the sessile droplet volumes. Secondly sessile droplets would be expected to reach higher surface supersaturations as electromagnetically trapped aerosols evaporate uniformly in all directions whereas sessile droplet evaporation is enhanced towards the contact line making it easier to reach high local supersaturations under the same relative humidity. Most importantly given the likely presence of heterogeneous nucleation in sodium chloride and ammonium sulfate droplets is that sodium nitrate could also follow a heterogeneous nucleation pathway. As a result crystallisation would occur more quickly for all supersaturations but especially at the high supersaturations which droplets at low relative humidity reach. Another point of interest was that compared to the other salts studied any efflorescence was more sensitive to the substrate: in one set of experiments at fixed RH all the droplets on plasma-cleaned substrates crystallised while those on HMDS-treated substrates did not. This can be explained by how the thin droplets on plasma-cleaned surfaces could reach high supersaturations near the contact line, increasing the local nucleation rate.

6.6 Supersaturation

Section 6.3 (Evaporation) showed the volume evolution of different salt droplets until they crystallised or the evaporation rate plateaued. In this section those

volumes are used to calculate maximum mean supersaturations and I attempt to relate them to nucleation behaviour and the crystalline forms observed.

Like for sugar droplets, it was possible to determine the mean supersaturation of droplets by measuring the change in volume and assuming the droplet concentration at the start of drying was the same as the bulk fluid. At high RH when there was no crystallisation the final (minimum) droplet volume was used in calculations. When droplets did crystallise then the maximum mean supersaturation would occur at the moment of crystallisation as beyond this time the growth of the crystal would reduce the salt concentration in the fluid. In addition any calculations could no longer be accurate as the density was only applicable for a single phase droplet.

Figure 6.11 shows the maximum mean supersaturations of approximately 400 sodium chloride droplets, with different colourmaps for the initial concentration and contact angle as well as the time of crystallisation and the relative humidity at crystallisation. The majority of measurements used droplets from a bulk concentration of 10 wt% but the highest mean supersaturations were reached for those droplets with larger initial concentrations of 20 wt%. The lowest starting concentration included in the Figure is 1.8 wt%, however on high energy substrates in most cases at the moment of crystallisation the droplet had too low a contact angle for the end volume to be found so a supersaturation could not be determined. Surprisingly the lowest measurable supersaturations were found for 5 wt% droplets on plasma-cleaned substrates rather than 1.8 wt% droplets on a HMDS-treated substrate. There is no obvious trend in volume over the admittedly small range sampled and most droplets reached mean supersaturations greater than 1.

It did not appear that changing the substrate, and so wetting behaviour and contact angle, was as important for the supersaturation as was expected before measurements were collected. Plasma-cleaned substrates were predicted to give lower mean supersaturations as if there was some threshold supersaturation

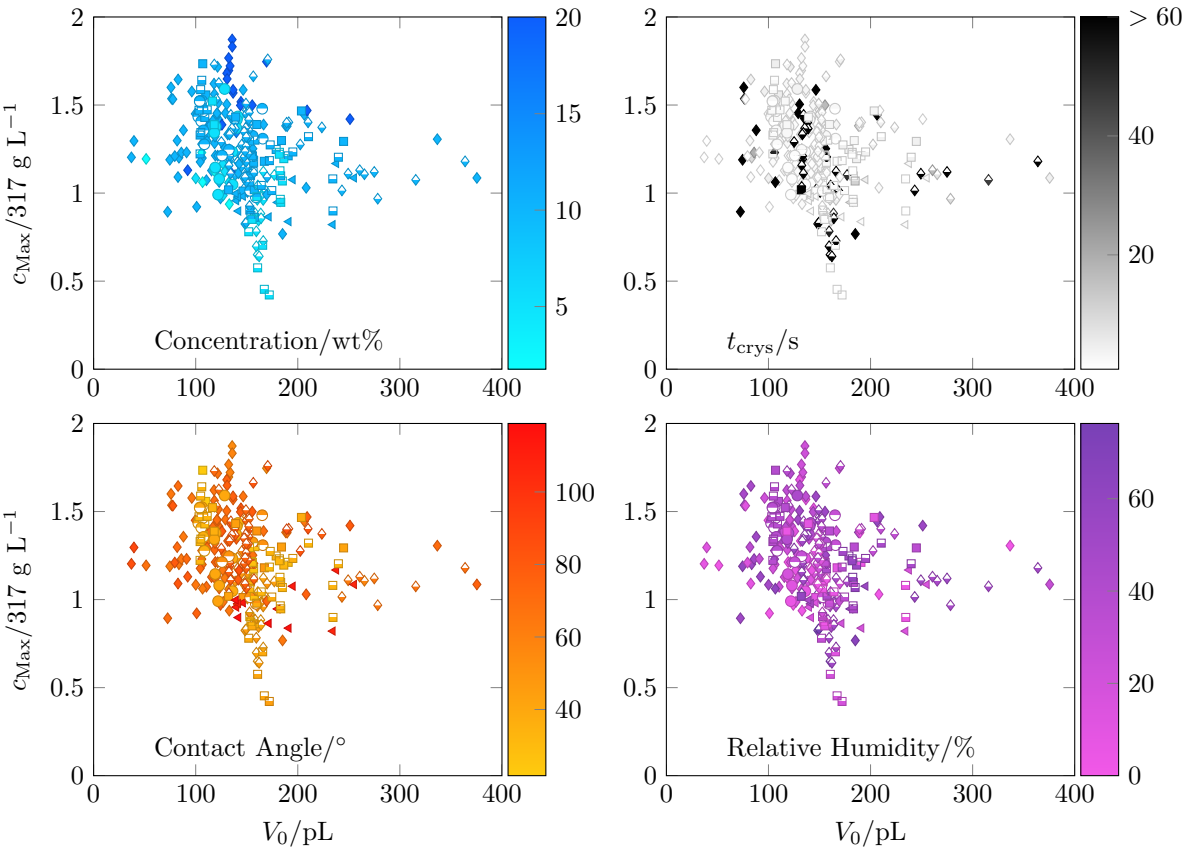

Figure 6.11: Maximum mean supersaturations for NaCl droplets as a function of volume with colourmap dependence on starting concentration in wt%, measured crystallisation time, initial contact angle or relative humidity.

that would lead to nucleation at some locale, then droplets with more uneven evaporative flux might have been expected to reach that threshold sooner. While the lowest measured values were on plasma-cleaned substrates, in most cases the range of supersaturations found for each substrate overlapped greatly. One possible cause for this behaviour could be that solutal Marangoni flows were not a consistent feature in experiments, therefore for thinner droplets where Marangoni flows were common then that mixing could lead to a more homogeneous droplet, meaning that higher contact angle droplets could potentially end up with more inhomogeneous concentration profiles. More likely given the analysis in Section 6.3, that modelled droplets better fitted experimental data if the starting concentration was increased, is that the scatter in the figure is a result

Table 6.5: Literature Supersaturations converted in terms of concentration units $M = \text{mol/dm}^3$ or g/L for NaCl from different sources in order of date published. Underlined results have been converted into concentration supersaturations. * denotes critical supersaturation (S_c) rather than mean supersaturation.

S	Authors	System
1.84	Tang *et al.*[241]	Aerosol
1.9	Cohen *et al.*[214]	Aerosol
1.98	Na *et al.*[242]	Aerosol
> 1.97	Grossier *et al.*[243]	Microfluidics
$\underline{1.49 \pm 0.15}$	Desarnaud *et al.*[207]	Capillary
$\underline{1.49 \pm 0.15}$	Shahidzadeh *et al.*[160]	Sessile
$\underline{1.4}$	Naillon *et al.*[244]	Capillary
$\underline{1.45^*}$	Naillon *et al.*[244]	Capillary
$\underline{1.11 - 1.65}$	Zhong *et al.*[230]	Sessile
$\underline{1.9}$	Utoft *et al.*[245]	Micropipettes
2.04^*	Gregson *et al.*[246]	Aerosol

of inconsistent salt enrichment due to evaporation at the nozzle.

6.6.1 Literature NaCl Supersaturations

Figure 6.11 shows that the largest maximum mean supersaturation measured were around 1.9 while the lowest were around 0.4. As discussed as this is a mean supersaturation, derived from assuming a homogeneous density profile then the actual supersaturation at the moment of crystallisation is expected to be higher due to surface enrichment of the salt. In order to determine how close these mean supersaturations were to the concentration required for immediate crystallisation the values need to be contextualised with literature results (summarised in Table 6.5).

Grossier *et al.*[243] investigated crystallisation in sodium chloride microdroplets generated by microfluidics, therefore the droplets evaporated into an oil phase rather than air and the concentrations were determined by refractive index matching to the oil. As a result they found that crystallisation occurred when the supersaturation ratio was greater than 1.97. In a follow-up paper they used

microfluidics to generate a large population of droplets and showed evidence of cooperative effects.[247] If a crystal nucleated in one drop then it would expel its water into the surrounding oil, which would diffuse into neighbouring droplets, decreasing the salt concentration and so delaying nucleation relative to a droplet without neighbours. This particular effect would not be important in my experiments; their droplets "evaporated" into oil, mine evaporated into air which already contained water vapour as a typical relative humidity might be in the range of 30 to 40%. While the main droplet volume would not increase because of condensation, satellite droplets could suppress evaporation on one side of the main droplet and lead to asymmetric concentration profiles and potentially off-centre Marangoni flows. Therefore one side of the droplet could reach a higher local supersaturation than a droplet with an axisymmetric concentration profile of the same volume and so lead to crystallisation at lower mean supersaturations. However despite this being plausible, satellite droplets were simply not common enough to lead to the degree of scatter in the supersaturation results so it cannot be the only relevant factor.

Utoft *et al.*[245] experimented with single sodium chloride droplets diffusing into a continuous oil phase. They measured a maximum supersaturation ratio of 1.9 which was not dependent on the sodium chloride concentration in their droplet but was lower when decane was used instead of octanol for the continuous oil phase.

Work in Shahidzadeh's group on crystallisation of sodium chloride in micro-capillaries and[207] microlitre sessile drops[160] found a mean supersaturation at the moment of crystallisation of 1.6 ± 0.2 for concentrations in terms of molalities. As molalities are defined in terms of moles of solute per kilogram of water while concentrations are amount per volume of fluid then supersaturations using different descriptions of concentration will differ. As the density of the solution increases then the molality (m) will increase more quickly than the molarity/concentration.

Therefore for consistency I will use the E-AIM model (for solutions at 25°C) to convert literature supersaturations into molalities or units of g L^{-1} so their values can be directly compared to the results in this section. Following this approach Shahidzadeh *et al.*'s result of $S_m = 1.6 \pm 0.2$ would instead be given as $S_{g/L} = 1.49 \pm 0.15$. That both capillary and sessile droplet systems investigated by Shahidzadeh's group reached this same supersaturation is unexpected as in the capillary the crystallisation was homogeneous although in the sessile droplet experiments there was a substrate which could be involved in a heterogeneous mechanism. If nucleation followed a heterogeneous pathway the lower free energy barrier would have resulted in lower supersaturations being reached. In their earlier work they reported a supersaturation of 3 in microlitre salt drops as a result of humidity cycling but this appears anomalous.[226] Aside from this group Zhong *et al.*[230] also conducted experiments with sodium chloride sessile drops with a range of concentrations on different substrates and found mean supersaturations of between 1.1 and 1.5 in terms of wt%, equivalent to $1.11 \leq S_{g/L} \leq 1.65$.

In the previous section it was shown that there have been many studies of sodium chloride aerosols. Of these Na *et al.*[242] measured $S_m = 2.31$ which can be converted to $S_{g/L} = 1.98$, Cohen *et al.*[214] measured concentrations as high as 13.6 mol kg^{-1} for which $S_{g/L} = 1.90$ while Tang *et al.*[241] measured concentrations of 13 mol kg^{-1} for which $S_{g/L} = 1.84$. More recently Gregson *et al.*[246] used modelling of surface enrichment in conjunction with aerosol experiments to determine a critical supersaturation $S_c = 2.04$ (units of concentration g L^{-1}) by determining the threshold that would give the best fit to the observed crystallisation time for evaporating sodium chloride aerosols at different starting concentrations. Given that this is the critical supersaturation it is a larger number than the mean supersaturations calculated here and by others. The other critical supersaturation reported comes from Naillon *et al.*[244] who experimented with circular microcapillaries and found mean supersaturations of 1.4. Then in numerical simulations

they determined that S_c to be 1.45 (1.56 in molalities) but as this is lower than even some of my mean supersaturation measurements it does not seem to hold widely.

6.6.2 Equilibriated Droplets

As discussed above, the relative humidity did not appear to lead to any trend in mean supersaturation in Figure 6.11. This is problematic in the case of droplets which were above the *ERH* and so did not crystallise. Any concentration inhomogeneities that may have developed during drying should have been able to equilibriate during droplet lifetimes of many minutes.

To estimate the time scale for concentration equilibriation the diffusion coefficient for salt in a concentrated droplet is required. The diffusion coefficient for sodium chloride at infinite dilution can be derived from the individual diffusion coefficients for the constituent ions, as for other monovalent ions this can be expressed as[248]

$$D_{\mathrm{NaCl}} = \frac{2}{1/D_{\mathrm{Na^+}} + 1/D_{\mathrm{Cl^-}}}. \tag{6.13}$$

At 25°C, $D_{\mathrm{Na^+}} = 1.33 \cdot 10^{-9}$ m^2 s^{-1} and $D_{\mathrm{Cl^-}} = 2.03 \cdot 10^{-9}$ m^2 s^{-1}, therefore $D_{\mathrm{NaCl}} = 1.61 \cdot 10^{-9}$ m^2 s^{-1}. As the concentration of sodium chloride increases then the solution becomes more viscous, so the $D \propto 1/\eta$ relation from the Stokes-Einstein equation (Equation 5.2) can be applied to get a more reasonable diffusion coefficient for supersaturated droplets. Therefore for a droplet with a typical supersaturation of 1.2 then using the E-AIM model for the density in conjunction with the Chenlo parameterisation[195] for the kinematic viscosity, ν, the dynamic viscosity, $\eta = \nu\rho$, would have increased by a factor of 2.2 compared to a supersaturation of zero.

This diffusion coefficient can be used in the expression for the distance, z, travelled by a particle following a random path in three dimensions due to Brownian motion given by Equation 4.7. Substituting z for the diameter of an inkjet-printed

droplet and rearranging for t means a molecule would diffuse across the diameter of the droplet in only 0.8 seconds, meaning diffusion would be expected to homogenise any sodium chloride concentration gradient in a droplet that did not crystallise within nearly six minutes.

Therefore the mean supersaturations calculated for droplets above the *ERH* (which did not crystallise) should be more effective at describing the state of a droplet than in the other cases as diffusion would even out any present concentration gradients. From this result the black markers in the top right plot of Figure 6.11 were expected to be clustered at lower S as a mean composition would be more reflective of the less salt-rich bulk. However this was not the case, the non-crystallising droplets show just as much scatter in supersaturation as those below the efflorescence relative humidity. This is more evidence for the suggestion that the scatter is a result of varying amounts of evaporation at the nozzle.

6.7 Deposits

Having discussed the conditions under which salt droplets crystallised and the dynamics of nucleation, I shall now discuss the structures of the crystal deposits.

During the evaporation of a droplet containing an inorganic salt there can be crystallisation; depending on the drying conditions the supersaturation and droplet geometry can vary which can lead to different crystal structures. These experiments showed that even simple salts can show very different crystal forms. For simplicity only experiments with droplets without particles will be presented; the inclusion of particles did not lead to different efflorescence behaviour, only changing how the contact line pinned. Given the low particle concentrations used, droplets would only partially pin, frequently leading to non-spherical contact lines during droplet evaporation. Deegan *et al.*[28] found that when the droplet contact angle is less than 90° evaporation is fastest towards the contact line, so

nucleation is most likely to occur there. That the droplets did not crystallise above the efflorescence relative humidity limited the range of relative humidities which could be usefully investigated. The literature on the evaporation of salt droplets is almost entirely made up of studies on sodium chloride as it is a well-known and abundant material, making it an ideal candidate for a model system. Other salts have been investigated, including calcium sulfate (gypsum),[160,249] sodium sulfate[227,250,251] and potassium ferrocyanide,[252] however the discussion of the literature in this thesis is restricted to systems containing sodium chloride.

6.7.1 Sodium Chloride Deposits

Sodium chloride, or halite, crystallises in a cubic structure[253] and has been observed to do so in the literature for microlitre sessile drops. My results are the first examples of inkjet-printed picolitre salt sessile droplets. The first reported experiments which included sessile salt drops were undertaken by Rodriguez-Navarro and Doehne,[227] however the first paper to primarily focus on the structure of sodium chloride deposits from sessile drops came from Takhistov and Chang[254]. In their work they studied large microlitre drops. On hydrophobic substrates they found single crystals while on hydrophilic substrates there was a concentration dependence: at high concentrations the deposit was a single ring, below 1 M there were concentric rings and fractal deposits below 0.1 M.

Shahidzadeh-Bonn *et al.*[251] worked with near saturated drops. On hydrophobic substrates they observed the crystallisation of a large cubic crystal surrounded by a "cauliflower-like" outer ring in which a few smaller cubic crystals were embedded, as they precipitated before the ring but after the largest crystal. On a hydrophilic substrate a ring of cubic crystals was deposited, surrounded by a crystallised wetting film. Later the same group[160,226] studied drops of a concentration just below the saturation concentration on substrates with a range of wettabilities; no "cauliflower-like" outer rings were observed. Instead a large

single crystal was found on hydrophobic substrates and a ring of small cubic crystals on hydrophilic substrates. They also proposed that capillary forces moved the large single crystals away from the drop contact line.[66] Fontana *et al.*[255] also found a ring of cubic crystals in experiments with large drops with diameters of 10's of millimetres under microgravity at the International Space Station. Zhong *et al.*[230] deposited droplets with concentrations of 2.5 to 25 wt% on hydrophobic and hydrophilic substrates. Their results were in line with other studies as they also got single cubic crystals from salt drops evaporating on hydrophobic substrates. Sun *et al.*[256] studied the deposits from low salt concentration drops on a hydrophilic substrate and found that their deposits would include a few cubic crystals scattered across the drop's contact area. The inclusion of particles increased the number of crystals in the deposit as they made the surface uneven so that following the first nucleation event the thin liquid film remaining broke up into more sections. Efstratiou *et al.*[257] experimented with 1 M drops on hydrophilic substrates and found deposits in which there were multiple crystals forming an incomplete ring around the drop contact line.

Shin *et al.*[258] did some of the few experiments on superhydrophobic substrates, with different microstructures and roughness. Over 5 to 20 wt% sodium chloride they observed the formation of continuous hollow rings of salt at the contact line that became thicker at higher concentrations. Heating the substrate gave "igloos" made up of many individual cubic crystals aligned along the liquid-vapour interface. If these crystals did not align well and collapsed the result would be a "pebble".

Vázquez *et al.*[259] investigated the crystallisation of $3.5-26$ wt% sodium chloride droplets evaporating on a hot plate at 45°C with IR thermography. Therefore the authors were able to map temperature changes across the droplet and view the evaporative cooling and localised increases from exothermic crystallisation.[260] These experiments gave rise to a wide variety of deposits. At low concentrations

there were many cubic crystals around the centre of the droplet, the number of which decreased as the salt concentration increased. All their drops showed ring like deposits while there were also a number of creeping-type aggregates leading to fan-shapes or spherulite crystals. One of the few numerical papers comes from Zhang *et al.*[261] who modelled the evaporation with molecular dynamics simulations for salt droplets on a smooth platinum substrate. They found increases in contact angle with salt concentration and different deposits depending on the strength of the solid-liquid interactions: clumps for weak interactions and rings for strong interactions (coupled with higher concentrations and slower evaporation).

Other studies have included sodium chloride as a way to add complexity to evaporating droplets containing the polymers sodium poly(styrene sulfonate)[262] or poly(ethylene oxide),[263] or biological components such as albumin,[264,265] lysozyme,[266] starch[267] or gelatin.[268]

Mailleur *et al.*[269] used reactive substrates, in their experiments they deposited pure water drops so the salt came from the drop dissolving the sodium chloride crystal substrate it was deposited on. This lead to the formation of a hollow shell around the contact line with more complete shells for thinner drops. Soulié *et al.*[190] and Lequien *et al.*[191] deposited salt drops on various polished iron substrates while investigating corrosion. For low 0.001 M concentrations they observed dark brown ring deposits of rust. At 1 M concentrations they could observe a ring of cubic crystals on the hydrophilic substrate with some crystals towards the centre and when the deposit was washed away there were clear pits in the surface. In both cases the substrate would be covered with a thin film of micro-crystallites including fingers and fractal-aggregates. This layer partly disappeared in a nitrogen environment in which there would be no oxygen for corrosion of the substrate.

In contrast to the above literature, my salt deposits showed much less cubic character. Possible reasons include the fact that hundreds of droplets of different

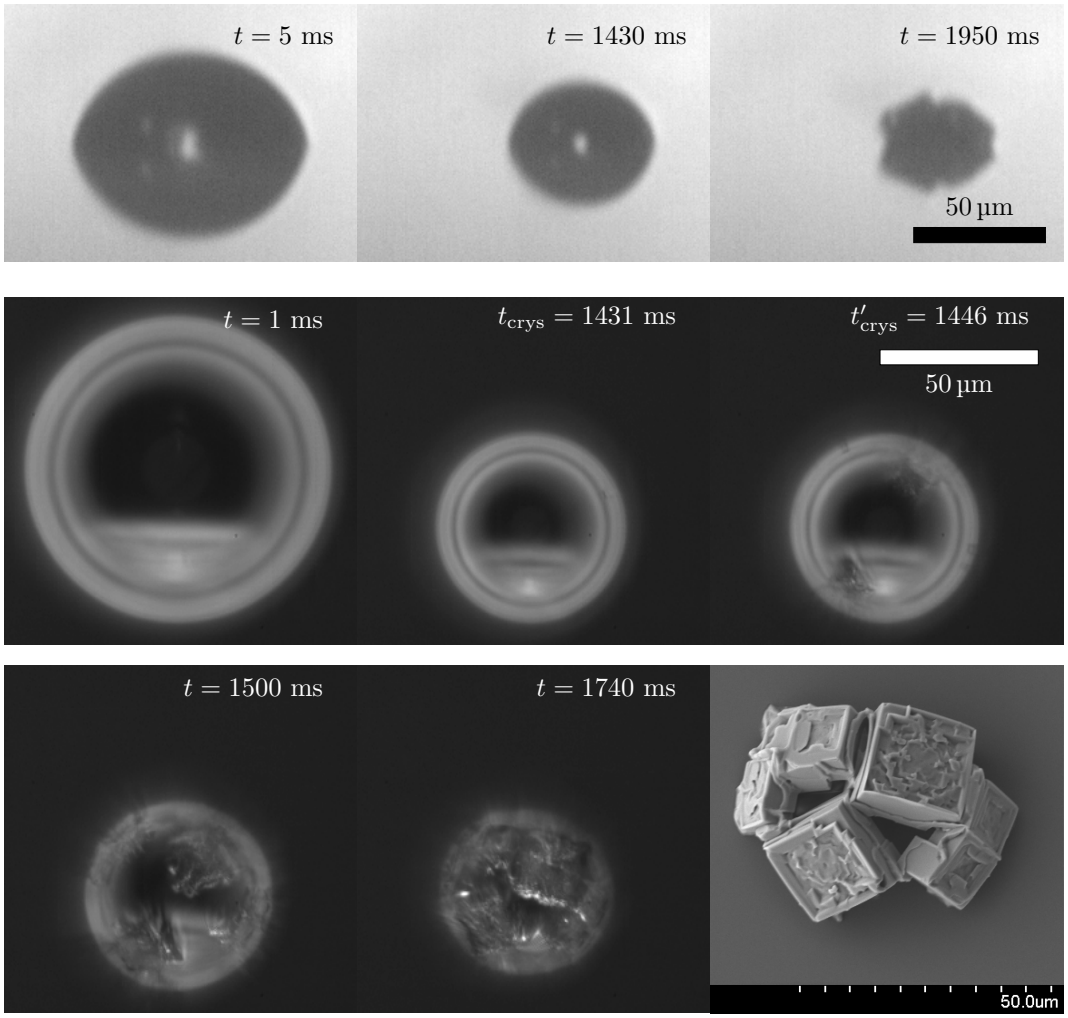

Figure 6.12: Droplet profile and dark-field bottom view images of the evaporation of a 10 wt% NaCl droplet on a HMDS-treated substrate ($RH = 2\%$) with a SEM image of the deposit. t_{crys} is the time at which the first crystal nucleated, t'_{crys} the time at which the first secondary crystal nucleated. The final side-view image gives the time at which the water fully evaporated.

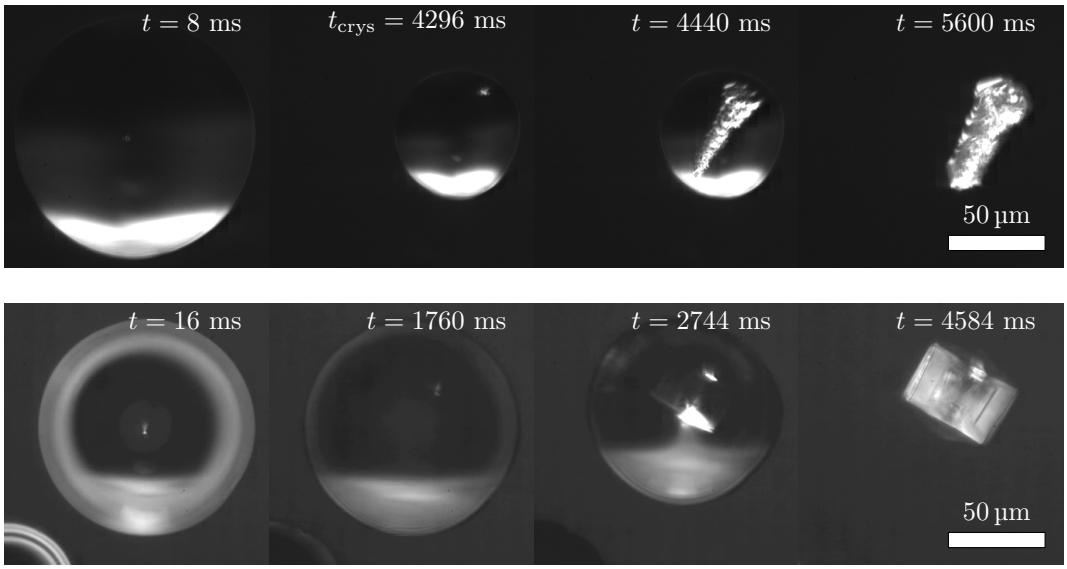

Figure 6.13: Top Row: dark-field bottom view images of a 5 wt% NaCl droplet on a HMDS-treated substrate, $RH = 42\%$. Bottom Row: dark-field bottom view images of a 5 wt% NaCl droplet on a decon-cleaned substrate, $RH = 31\%$.

compositions were imaged at a range of relative humidities on substrates with different treatments, rather than a more limited exploration of experimental variables. Subsequently results were collected where nucleation occurred over a range of supersaturations, meaning I was more likely to stumble across new behaviour. Secondly these experiments looked at a lengthscale closer to that of an individual crystal so it was possible to distinguish between entirely well-ordered cubic crystals and crystals that had flat sides and so only appeared rectangular. It is also possible that having a smaller droplet could have been relevant; while the inkjet-printed sessile droplets were not as small as those in which confinement effects are definitely present[243] the shorter evaporation time compared to microlitre droplets makes kinetically controlled behaviour more possible.

As discussed previously, HMDS-treated substrates were most commonly used so the volume at the moment of nucleation could be more precisely determined by virtue of the larger contact angles. Figure 6.12 gives an example of the types

of deposit seen on such substrates where initial droplet contact angles were in the range of $60 - 70°$. Crystals nucleated at the contact line where the highest salt concentration within a droplet is expected. The growing crystals would then be pulled into the centre of the drop as a result of capillary forces acting to maintain the spherical cap geometry of the droplet. Capillary forces also aligned flat crystal faces against one another. Scanning Electron Microscopy (SEM) images acquired with Yilin Wang showed sodium chloride crystals with rough tops and smooth sides. While NaCl has a face-centred cubic crystal structure, the overall deposit is not cubic throughout. The cores of the crystals appear amorphous as a result of competing fast growth from multiple locations on the crystals at the high supersaturations. It is only when the crystals growth is diffusion limited at late times that the crystal shape is cubic as growth "squares-off" the crystals. That the deposit shape is kinetically controlled is supported by the low frequency of cuboidal crystals from the hundreds of droplets imaged. In addition Figure 6.13 presents some frames from one of few droplets which left a truly cubic crystal deposit. In this example it is clear that the crystal is well ordered as it is virtually invisible in dark-field recordings until the crystal grows in size enough to perturb the liquid-vapour interface because of a lack of scattering of LED light. In contrast the crystal nucleus seen in Figure 6.12 could be noticed when it was on the order of only a micron in size as the internal structure was disordered so any crystal nuclei strongly scattered light. It was only for experiments on OTS-treated substrates that clear crystals with an ordered structure were found to frequently nucleate.

Figure 6.13 also gives an example of an obviously non-cubic structure where the sodium chloride crystal grows more like a needle. In this case the crystal initially grew quickly along a single axis while at later times the crystal grew in all directions with the tips getting "squared-off". These needle-shaped crystals more often appeared in a branched structure with two needles growing from the same nucleus; the resulting needles were much shorter as each branch competed

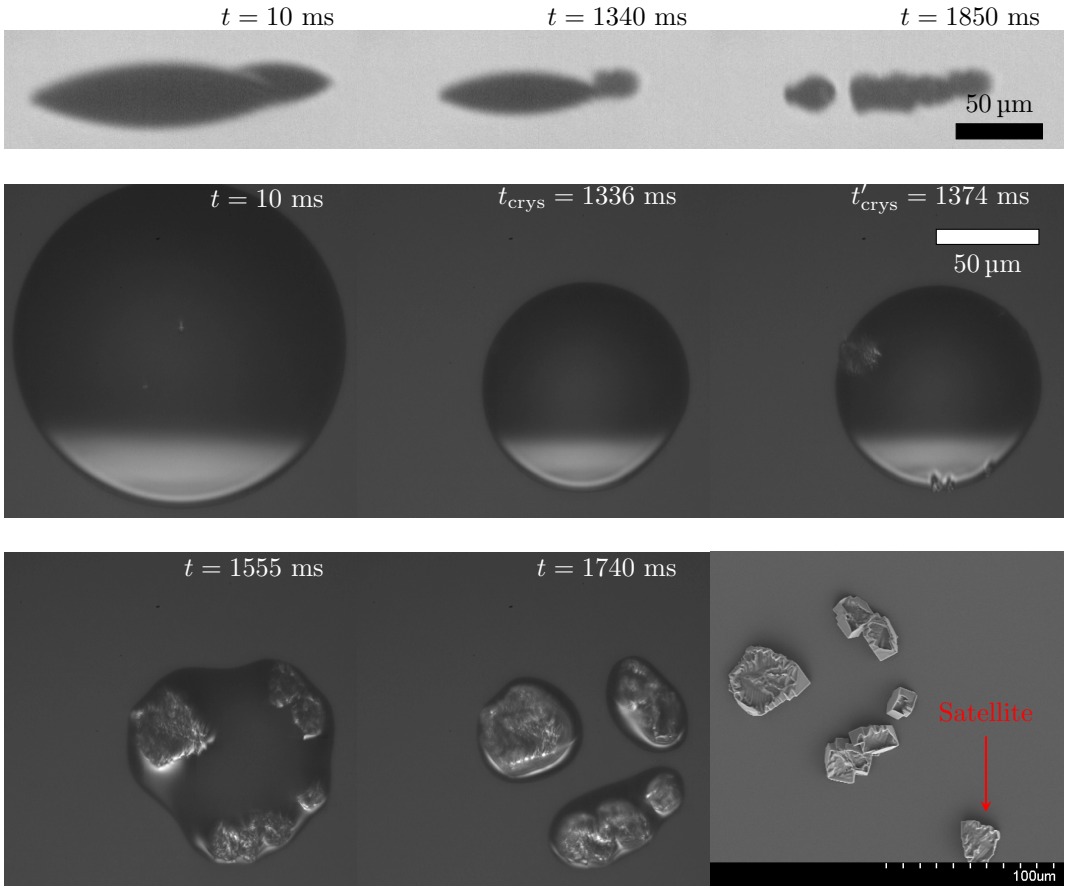

Figure 6.14: Droplet profile and dark-field bottom view images of a 10 wt% NaCl droplet on a plasma-cleaned substrate ($RH = 2\%$) with a SEM image of the deposit.

for salt ions.

In the literature other researchers have observed continuous crystalline rings or a mass of small cubic crystals from microlitre sodium chloride drops. However the inkjet-printed salt droplets here did not show any ring deposits. This may have been a size effect as at low volumes, for a fixed nucleation rate the expected number of crystal nuclei will drop if the volume of fluid is small so there are not enough crystals to form a continuous ring.

On plasma-cleaned substrates the crystals were flatter and were not pulled inwards by capillary forces, unlike on HMDS-treated substrates, possibly due to increased friction with the substrate. As a result the crystal in Figure 6.15 appears less cuboidal at early times as one side is templated by the curved liquid-vapour

interface. These circular sector-type shapes were more common on plasma-cleaned substrates but still observed on the other substrates when the crystal nucleus got stuck at the contact line. However the converse was not true and deposits like those in Figure 6.12 were not found on higher-energy substrates.

The relative humidity was not important to the structure of an individual crystal when below the efflorescence relative humidity. However the deposits overall would differ as multiple nucleation was more likely at low relative humidities. Taking an example of droplets on a plasma-cleaned substrate, for Figure 6.15 the relative humidity was 45%, and there was a single crystal while in Figure 6.14 at $RH = 2\%$ the primary crystal is very similar, except it is a little smaller due to the later nucleation of a number of other crystals on the opposite side of the droplet. Multiple nucleation was still possible at high (but still below the ERH) relative humidities with up to three crystals being seen to nucleate. However all deposits with many crystals (five or more) were found when $RH \leq 20\%$.

There has been discussion in the literature, especially in experiments in capillaries, of sodium chloride nucleating to form hopper crystals at high supersaturations.[270] These are crystals which grow faster at the corners than the centres of the faces leading to chains of interconnected cubic crystals linked at the corners (Figure 6.16A) or square crystals with depressions in the centre of any faces (Figure 6.16B). The former type occurs at high supersaturations in which crystal growth is no longer diffusion-limited but instead limited by the rate at which ions can be incorporated, therefore crystals switch to growing in such a way to maximise the crystal surface area. This supersaturation dependence was also found by Zhang *et al.*;[271] in sodium chloride solution in oil emulsions, a cyclohexane oil phase lead to cubic crystals while adding acetone stabilised the salt droplets, allowing them to reach metastable concentrations from which hopper crystals precipitated.

While the needle-like crystal shapes observed in some of my experiments bear some similarities in shape to hopper crystals, hopper crystals have an ordered

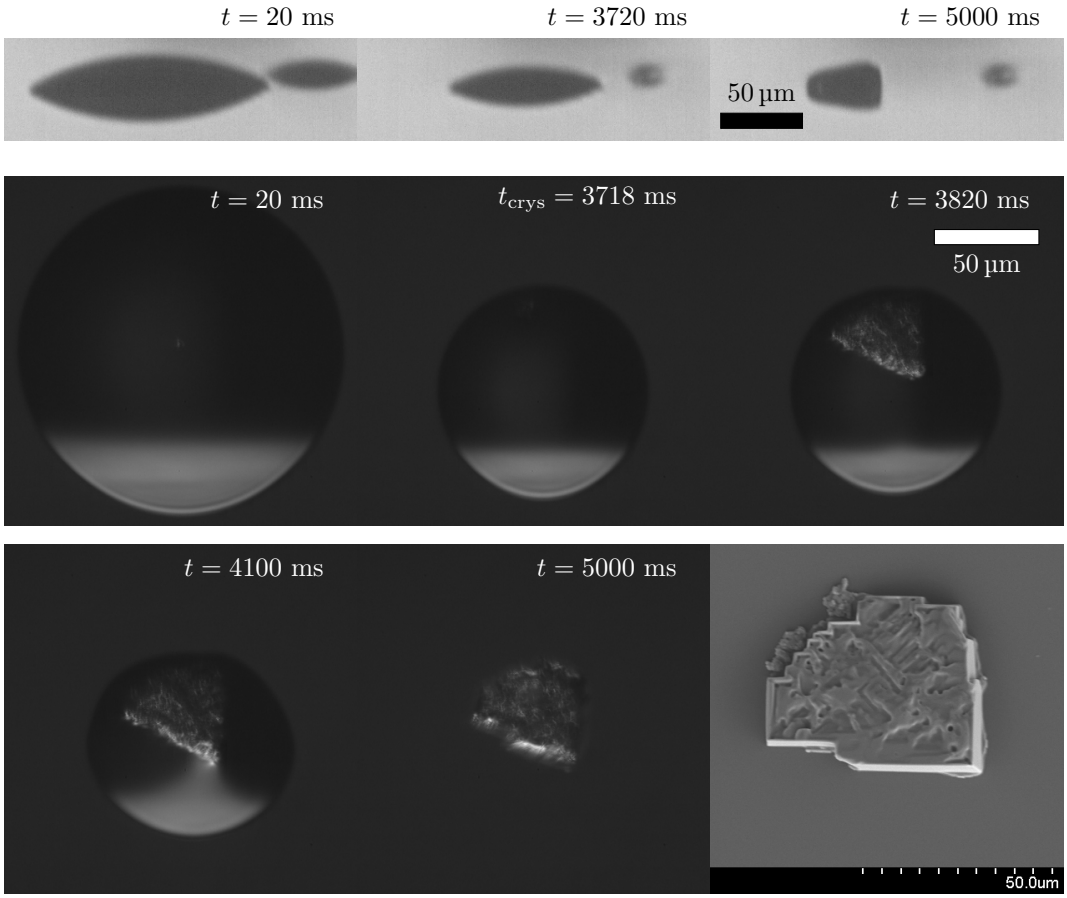

Figure 6.15: Droplet profile and dark-field bottom view images of a 10 wt% NaCl droplet on a plasma-cleaned substrate ($RH = 45\%$) with a SEM image of the deposit.

structure so little scattering in dark-field videos would be expected. However the needle-like crystals are easy to spot even when small suggesting the crystals are macroscopically amorphous rather than hopper-like (and ordered).

In addition where hopper crystals are unbranched then the final crystal in the chain grows the largest as its surroundings will have the highest ion concentration. In contrast Figure 6.13 shows that the needle like crystal is thinnest at the point furthest from the nucleation site, although this could be a result of the crystals nucleating in limited fluid rather than a capillary. A hopper structure would also not well describe crystals of the same shape as those on plasma-cleaned substrates shown in Figures 6.14 and 6.15. In these cases the crystal shape is still not cuboidal and the crystal grows at a similar speed in all directions whereas hopper

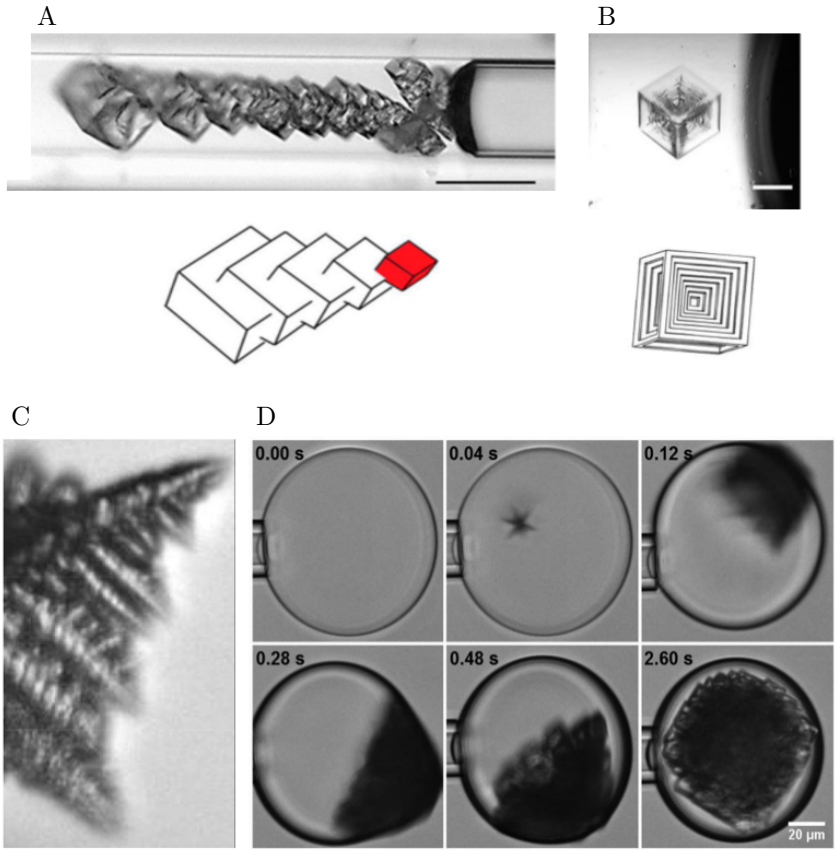

Figure 6.16: A (B) - NaCl Hopper crystals nucleating in capillaries of 100 µm (B: 1000 µm) diameter. Adapted with permission from J. Desarnaud, H. Derluyn, J. Carmeliet, D. Bonn and N. Shahidzadeh, The Journal of Physical Chemistry Letters, 2014, **5**, 890–895. Copyright 2020 American Chemical Society. C - Dendritic (D - Microcrystallite) growth of a sodium chloride solid from a droplet in octanol. Adapted with permission from A. Utoft, K. Kinoshita, D. L. Bitterfield and D. Needham, Langmuir, 2018, **34**, 3626–3641. Copyright 2020 American Chemical Society.

crystals grow more quickly at the corners.

Utoft *et al.*[245] manipulated sodium chloride microdroplets in different organic phases. In their experiments they observed "dendritic" crystals that are closer in appearance to my crystals. In an octanol outer/continuous phase the water has a higher solubility than decane, leading to faster water loss from their droplets (equivalent to a lower relative humidity in my experiments). Therefore while a decane phase led to a cubic crystal at $S = 1.13$, in octanol they observed (Figure 6.16C, D) dendritic structures that resembled the needle-like structure in Figure 6.13 and rough "multi-faceted dendritic structures" like those in Figures 6.14 and 6.15.

While I have attributed the non-cubic macroscopic structures to the high supersaturations achieved in evaporating sessile droplets, cubic crystals are still possible at high supersaturation. Grossier *et al.*'s emulsion droplets at supersaturations of up to 1.97 nucleated to form cubic crystals once agitated by a needle.[243] While Hammadi *et al.*[272] instead used paraffin oil rather than dodecamethylpentasiloxane at lower supersaturations ($S > 1.24$).

6.7.2 Sodium Nitrate Deposits

Sodium nitrate crystallises as a (ditrigonal scalenohedral) hexagonal system, leading to rhombohedral crystals like calcite.[185,273,274] The sodium nitrate crystal shapes I observed after the evaporation of inkjet-printed droplets could be broadly divided into two categories. Figure 6.17 shows the nucleation and crystal growth of the most common type of deposit. Sodium nitrate droplets did not always nucleate at the contact line; in the bottom-view images the bright spot at $t_{\text{crys}} = 3368$ ms is away from the contact line, allowing the crystal to grow in both directions along some axis. Sodium nitrate crystals tended to be longer than they were wide as they would first grow across the droplet from the point at which the crystal nucleated. Once the growing crystal reached the edge of the droplet the crystal

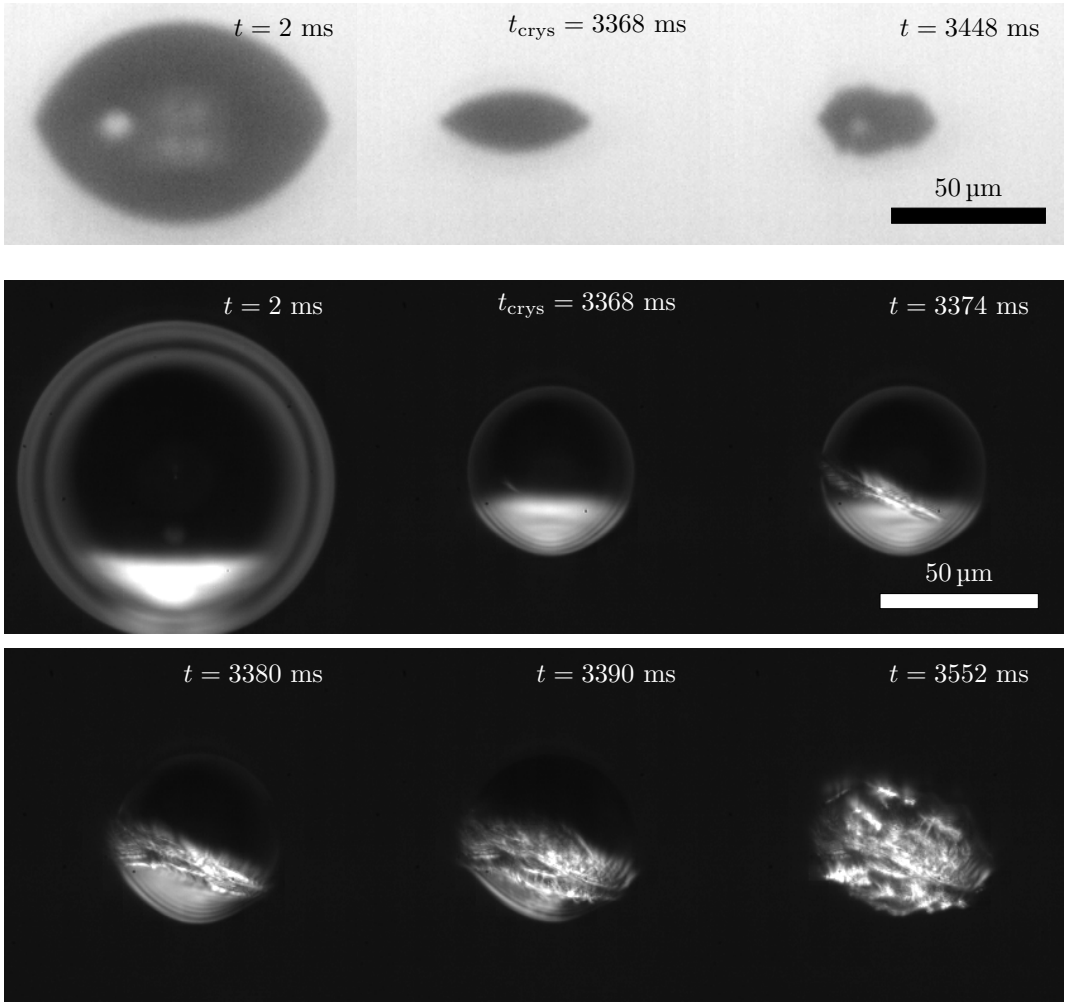

Figure 6.17: Droplet profile and dark-field bottom view images of a 5 wt% $NaNO_3$ droplet on a HMDS-treated substrate, $RH = 29\%$ showing the most common nucleation behaviour observed in these $NaNO_3$ experiments.

would grow more slowly, roughly perpendicular to the main axis. From this basic form the appearance of crystals could vary quite a bit depending on whether the crystal branched or not. Figure 6.18 shows how if the crystal had multiple branches from the critical nucleus then the branches would compete for salt ions, leading to shorter branches and smaller crystal aspect ratios. In other cases, when the crystal branched from a point along the primary axis, rather than from the critical nucleus, the branches were approximately perpendicular to the primary axis, so the growing branch took up the ions in regions of the droplet which were

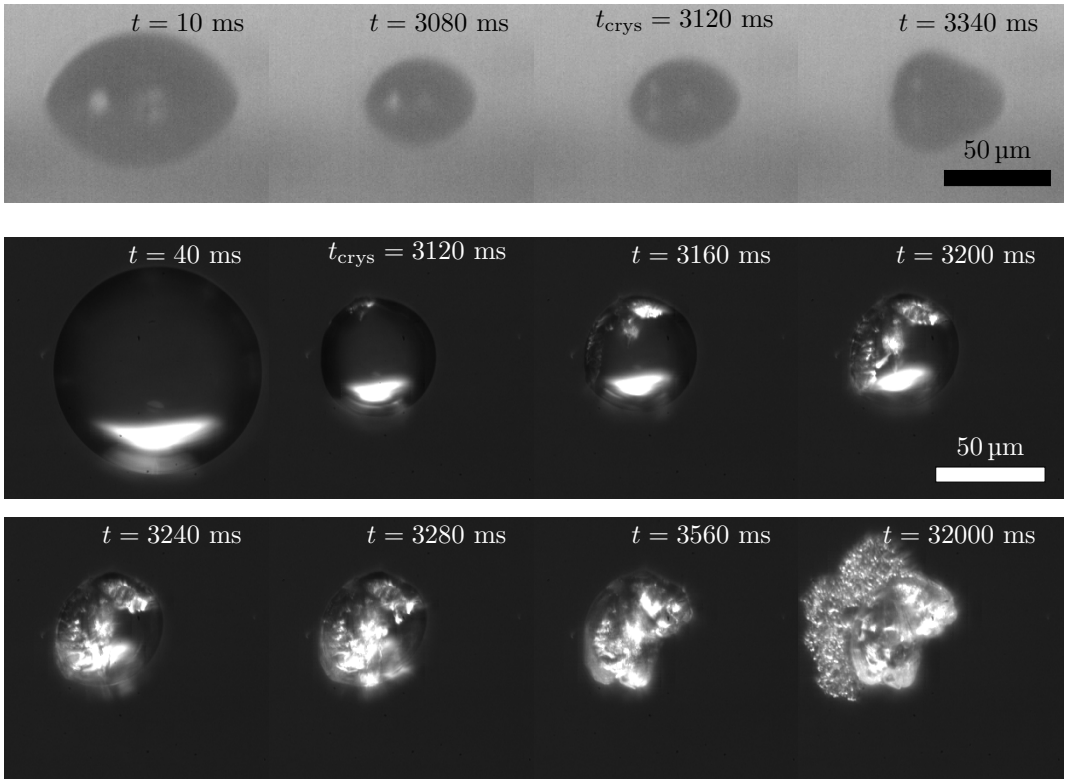

Figure 6.18: Droplet profile and dark-field bottom view images of a 10 wt% $NaNO_3$ droplet on a HMDS-treated substrate, $RH = 33\%$. At long times see crystal growth along the substrate.

not depleted in salt ions. This lead to better defined crystals as there were fewer unincorporated ions at late stages to add to the crystal which would "round-off" distinguishing features.

Another feature of sodium nitrate droplets displayed in Figure 6.18 is the formation of a very thin crystalline layer around the primary crystal on HMDS-treated substrates. In appearance this layer bears similarities to a crystallised wetting layer[251] or the impurities expelled from sodium chloride droplets after multiple crystallisation and deliquescence cycles.[226] Without chemical analysis it is unclear whether my crystalline layer was a result of impurities in the sodium nitrate or some kind of creeping mechanism as is prominent in potassium chromate droplets.[229] The videos show that the crystalline layer forms tens of seconds after nucleation when the remaining film of liquid on nucleated sodium nitrate crystals

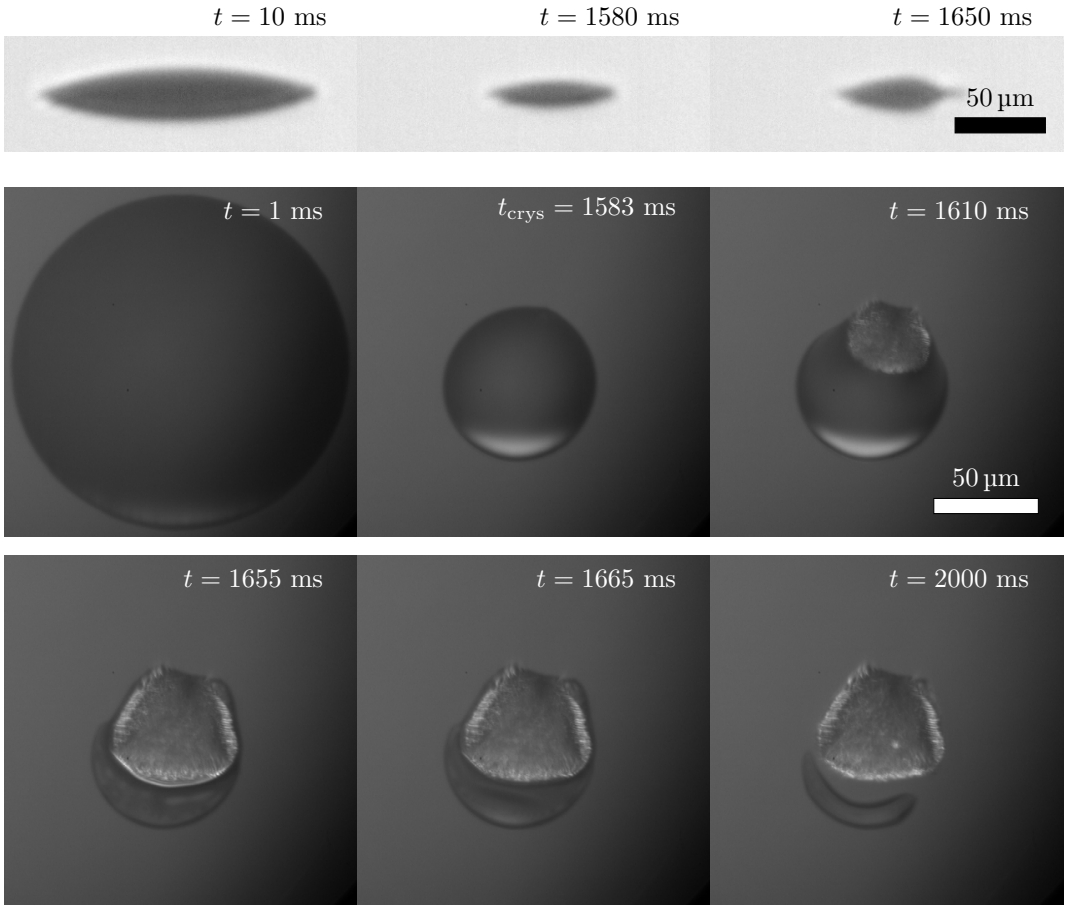

Figure 6.19: Droplet profile and bottom view images (both light and dark-field LEDs used) of a 10 wt% $NaNO_3$ droplet on a plasma-cleaned substrate, $RH = 27\%$.

dewets from the top of the crystal onto the substrate. Once the fluid is in contact with the substrate then the layer grows over a number of seconds until the crystal appears dry. Figure 6.18 shows the growth of the largest crystal layer observed although it is atypical as the thin crystalline phase was normally observed growing more evenly from all sides of the primary crystal, and on areas within the initial footprint of the droplet; these other layers were less visually impactful than the one in Figure 6.18. These crystal layers were found when $RH < 30\%$; they may still occur at higher RH except the slower evaporation delayed any possible formation beyond the limit of the bottom-view camera's memory without adjusting to lower frame rates.

The second category of sodium nitrate crystal structures were found for

droplets evaporating on plasma-cleaned substrates. On these substrates the critical nucleus formed at the contact line and the crystal grew in all directions rather than along a single axis. An example of this behaviour is shown in Figure 6.19 where the crystal grew more slowly ($\approx 0.7\,\mu m\,s^{-1}$) than in the example of unidirectional growth presented in Figure 6.17 ($\approx 2.5\,\mu m\,s^{-1}$ along main axis). Depending on the quality of the plasma-cleaning process there was different behaviour. When using plasma-cleaned substrates upon which 10 wt% droplets had an initial contact angle on the order of 36° then then after nucleation the droplet would remain attached to the crystal. On substrates with an extended cleaning procedure where the initial contact angle was on the order of 16° then droplets were like the one shown in Figure 6.19 where the remaining fluid after the crystal's growth slowed would drain away and form a separate, asymmetric droplet. These particular measurements took place at $RH = 27\%$, within the band of humidities in which most but not all droplets crystallised, this was reflected in how crystallisation of this residue was inconsistent. These were the only incidents in which more than one crystal nucleated from a sodium nitrate droplet as the detached residue's crystal would be separate from the main crystal.

6.7.3 Ammonium Sulfate Deposits

The nucleation of ammonium sulfate crystals and the following growth was very different to the other inorganic salts studied. Ammonium sulfate has a wide range of temperature dependent crystal forms with different magnetic behaviour[275] although at room temperature it is isomorphous with potassium sulfate (β-K_2SO_4)[276] which is orthorhombic.

While nucleation still occurred near the contact line, the crystals grew faster and had different shapes; the AMS deposits always covered the full footprint of the droplet at the moment of crystallisation. Figure 6.20 shows the nucleation of a 10 wt% AMS droplet on a HMDS-treated substrate from the side and below. The

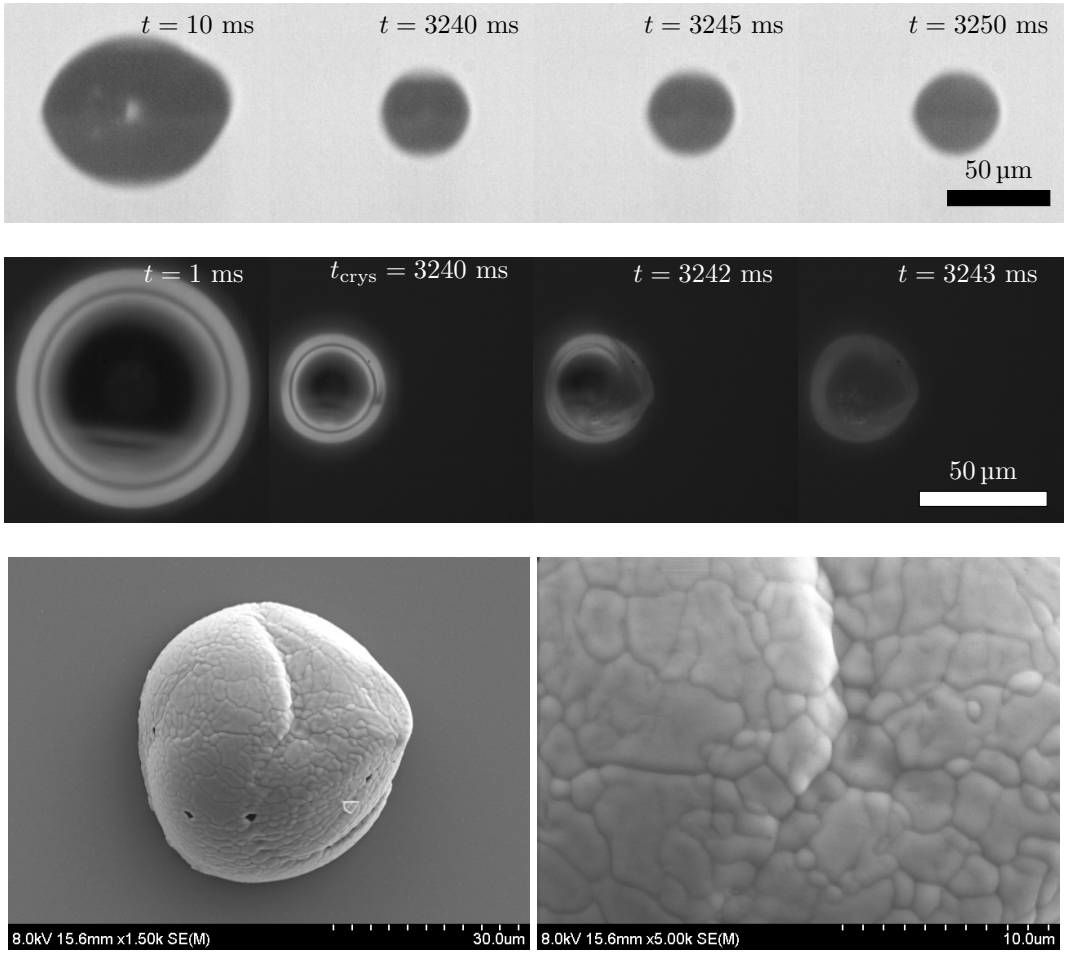

Figure 6.20: Droplet profile and dark-field bottom view images of a 10 wt% AMS droplet on a HMDS-treated substrate, $RH = 32\%$ with SEM images of the deposit.

crystal nucleated at the contact line and the crystal then grew inwards to totally cover the droplet's contact area within ten milliseconds. The SEM image shows a commonly observed feature: that the location at which the droplet nucleated appears slightly pointed. The side-view images show that the droplet profile was nearly identical after crystallisation; the bottom-view videos show that the crystals would slightly change in appearance after this point as the residue water evaporated. Therefore as the crystals grew along the liquid-vapour interface it seems likely that there was some kind of fluid core remaining, which evaporated through the porous structure shown in Figure 6.21.

The SEM images were acquired with Yilin Wang a number of hours after the

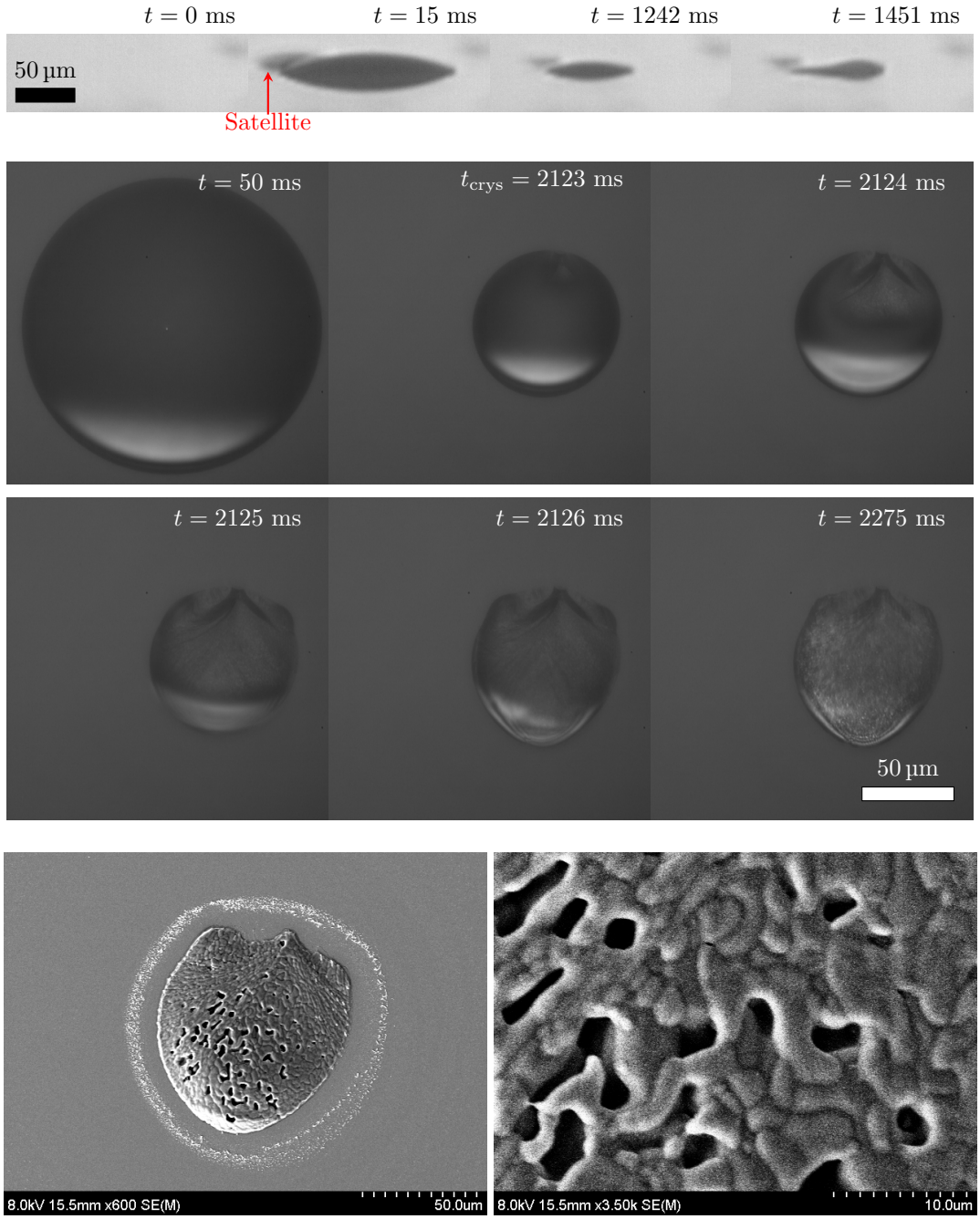

Figure 6.21: Droplet profile and bottom view images (both light and dark-field LEDs used) of a 10 wt% AMS droplet on a plasma-cleaned substrate, $RH = 36\%$ with SEM images of the deposit.

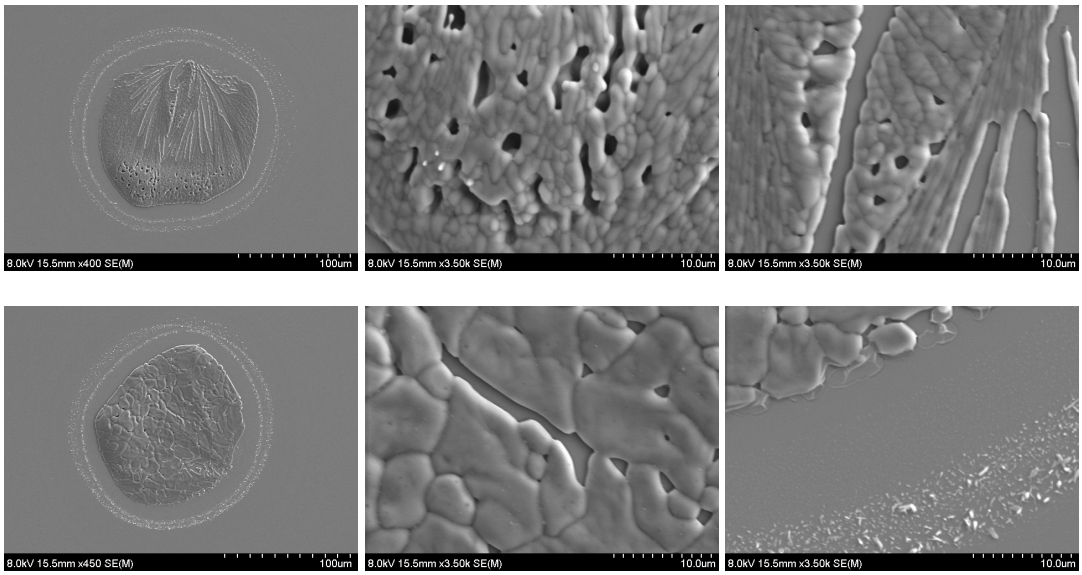

Figure 6.22: SEM images of two 10 wt% AMS droplets dried on a plasma-cleaned substrate, $RH = 34\%$ with higher magnifications of different regions of the deposit.

droplets were printed, by this time any fluid would have evaporated and if it had not then the vacuum within the SEM instrument would totally dry the crystals. If crystals were not mechanically stable then the vacuum could have led to damage, however the lack of change between the SEM and dark-field images suggests that this was not an issue. In the dark-field bottom view images the crystal appears uniformly rough, this is corroborated by the SEM images which show that aside from a few holes (possibly for fluid to evaporate from) the crystal was generally quite homogeneous.

This is in contrast to the appearance of AMS crystals from droplets deposited on plasma-cleaned substrates. These crystals also frequently had a "point" where the droplet had nucleated and there were often "spokes" radiating out from this point into the droplet (see Figure 6.22). Near where the crystal nucleated the SEM images show that the surface of the crystal was similar to those from droplets on HMDS-treated substrates. On the opposite side of the droplet the crystal was much thicker, as can be seen in the droplet profiles in Figure 6.21. This thicker region tended to have the same bumpy appearance as other regions of the

crystal except that the surface would be punctuated by a number of holes. This roughness resulted in these parts of the droplets appearing brighter in AMS dark-field images. Another difference for plasma-cleaned substrates was the appearance of rings of nano-sized crystallites surrounding the deposit. These were not visible in dark-field images and may have been a result of crystallisation within a wetting film surrounding the droplets printed on high-energy substrates.

6.8 Flows

To end this Chapter I relate my investigations of the types of evaporation driven flow in salt droplets and how they compare to the results of others.

6.8.1 Literature Review

The literature on drying salt sessile droplets is dominated by investigations of the deposits. Despite this there are some examples of studies of the internal flows that can arise during the evaporation of such droplets. However due to the small changes in surface tension with increasing salt concentration (Figure 6.1 and Table 6.2) the identity of these flows depends upon the droplet geometry. The mechanism driving these flows is not immediately obvious because for a sessile droplet with a salt-enriched liquid-vapour interface, but particularly enriched towards the contact line, buoyancy-driven and solutal Marangoni flows act in the same direction if the contact angle is below 90°.

The first experimental measurements of the internal flow structure of a salty droplet was undertaken by Kang *et al.*.[62] In their experiments with 1, 5 and 20 wt% sodium chloride sessile drops (with volumes of 3 µL) they observed toroidal vortex flows of fluorescent particles using a side-view ray tracing method that corrected for the curved droplet surface.[147] A hydrophobic Teflon coating on the substrate meant that the contact angle was near 90° so the evaporative flux was

approximately constant across the liquid-vapour interface, as a result they thought that solutal Marangoni flows would be too weak, as would thermal Marangoni flows as no flow structure as a result of evaporative cooling was observed in water drops. Therefore they argued that the flows were buoyancy driven, and found matching scaling with Rayleigh number between experimental with numerically modelled velocities.

Buoyancy driven flows have also been investigated by Pradhan and Panigrahi[277] for 1 M sodium chloride droplets on a hydrophobic substrate. Their experiments showed the presence of buoyancy-driven circulatory internal flows ($u < 20\,\mu\mathrm{m\,s^{-1}}$). In pairs of drops less than a drop diameter apart the flow patterns were asymmetric as a result of suppressed evaporation between the two drops. These researchers later ran experiments of and numerically modelled the evaporation of sessile and pendant sodium chloride droplets on a superhydrophobic substrate.[278] They found that the convective flows went upwards (along the drop's axis of symmetry) in both sessile and pendant cases, although flows were faster in the sessile geometry, whereas if the flows were surface tension driven a reversal would have been expected.

The formation of Shin *et al.*'s igloo deposits needed circulatory flows.[258] As a result of the superhydrophobic substrate solutal Marangoni and buoyancy flows act in opposite directions. Therefore their flows are best explained as arising from a plume of lower density fluid rising below the apex of the drop such that the flows were buoyancy-driven.

Takhistov and Chang[254] were the first to suggest the presence of solutal Marangoni flows in salt droplets, attributing the faster than expected evaporation rates they measured as being a result of increased convection to the contact line. The first measurements of a salt driving a Marangoni flow in a sessile droplet were not done with sodium chloride. Bormashenko *et al.*[252] investigated the drying of < 3 wt% potassium ferrocyanide drops on hydrophobic flat and

textured polypropylene films. These drops gave crown-like deposits the authors argued as being indicative of a Marangoni instability.

Like Takhistov and Chang, Soulié *et al.*[205] also attributed a change in evaporation rates to solutal Marangoni flows. Their model for the evaporation of salt drops was accurate at low concentrations but overestimated the evaporation rate as concentrations approached 1 M on hydrophilic substrates, suggesting salt enrichment towards the contact line suppressing evaporation. When adding particles these authors were then able to view multiple vortices they attributed to solutal Marangoni flow. However droplets with contact angles of 30° or higher were shown to be well described with the model, indicating that a drop having a high salt concentration was not enough in itself to lead to solutal Marangoni flows for a less non-uniform evaporative flux profile.

Despite Soulié *et al.*'s[205] model still being effective at low salt concentrations, other researchers have recently found that low salt concentrations can actually drive solutal Marangoni flows when the droplets evaporate on hydrophilic substrates, which shall be discussed in more detail in later sections.[43,256]

6.8.2 Sodium Chloride

While studies have shown that buoyancy-driven convection is possible in microlitre salty sessile drops[62,277] (and pendant drops[279]), they are not relevant for ink-jet printed droplets[64] due to their small heights. For example assuming a plausible 2% concentration difference between the apex of the droplet and the substrate then the Archimedes number $Ar \sim 10^{-4}$ ($Ar \sim 10^{-5}$ with a hydrophilic substrate) while buoyancy is only relevant when $Ar > 1$, therefore any circulatory flows are surface tension driven. Salts act to increase the surface tension of a solution meaning that a salt-rich contact line has a higher surface tension than the apex, leading to a solutal Marangoni flow from the apex to the contact line acting in the same direction as in ethanol-water and sugar droplets. For experiments on

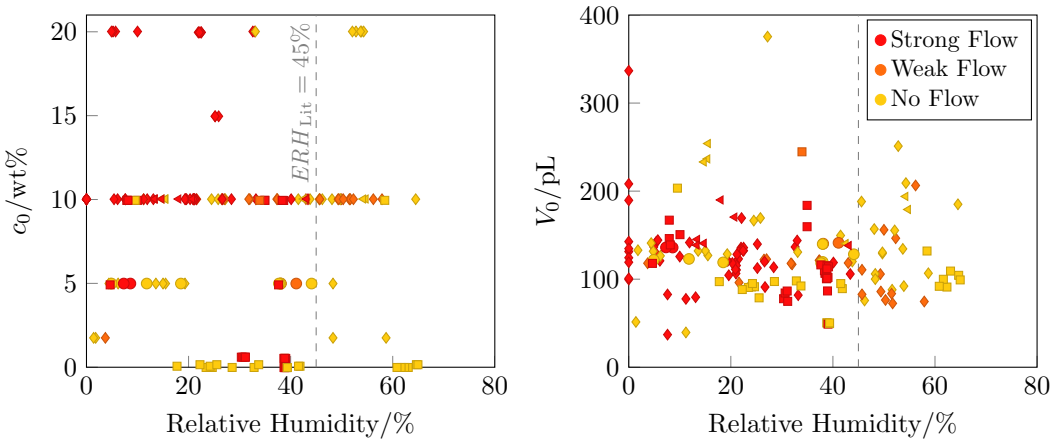

Figure 6.23: Map of experimental space of RH vs NaCl wt% or initial volume for droplets with circular contact lines and containing particles. Marker colour: red - strong recirculation, orange - weak recirculation, yellow - no recirculation. Dashed grey line for literature efflorescence relative humidity for NaCl. Marker shape follows convention of: diamonds for HMDS-treated, squares for plasma-treated and circles for decond-cleaned substrates.

superhydrophobic OTS-treated substrates with initial contact angles on the order of 110°, the circulatory internal flows were reversed, going from the contact line towards the apex, consistent with solutal Marangoni flows.

Solutal Marangoni flows were observed for salt droplets but only under certain environmental conditions, substrate combinations and salt concentrations, mapped out in Figure 6.23. On HMDS-treated substrates there were no solutal Marangoni flows at lower sodium chloride concentrations of 5 wt% or less. At concentrations of 10 wt% Marangoni flows were not consistently found, at higher concentrations flows were expected. If plasma-cleaned substrates were used then solutal Marangoni flows were observed at concentrations of even 2 wt% while lower concentrations are discussed in the following section. The cause of this substrate dependence is related to how thinner droplets have more uneven evaporative flux. Larger droplet radii for the same volume also means that it takes longer for diffusion to erase radial concentration gradients so the gradients that develop can become larger. These effects mean that thinner droplets have greater

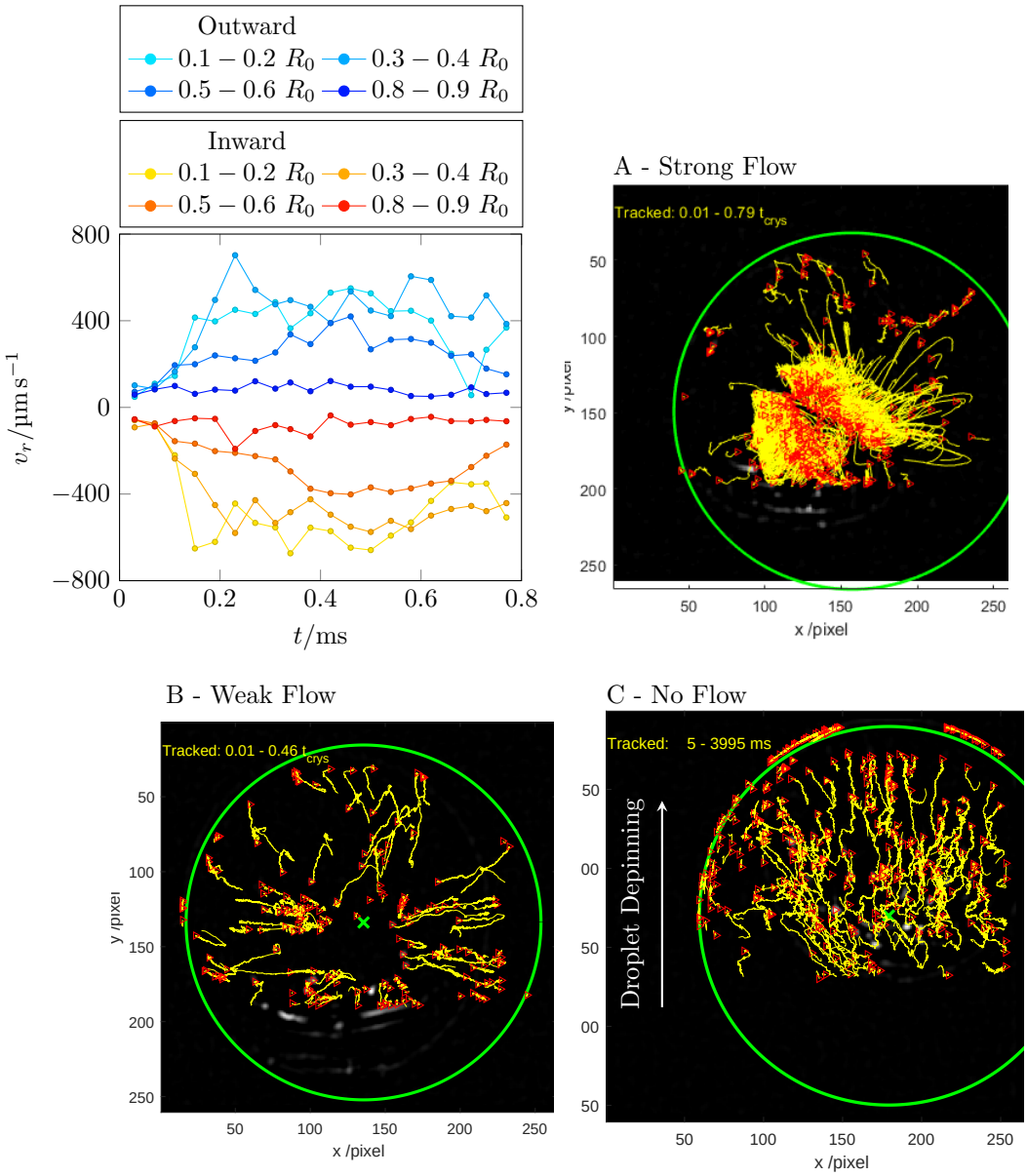

Figure 6.24: Particles tracks for different "strength" solutal Marangoni flows for 10 wt% NaCl droplets on a HMDS-treated substrates. A - Strong Flow $RH = 20\%$ (with PIV results), B - Weak Flow $RH = 28\%$, C - No Flow $RH = 50\%$.

surface tension gradients and so more easily reach a large enough surface tension gradient to drive flow.

In experiments at 10 wt% NaCl on HMDS-treated substrates the solutal Marangoni flows were not fully reproducible, suggesting that the surface tension gradients generated during the evaporation of such droplets were around the cusp of what was required. This was supported by how there was an additional relative humidity dependence for whether droplets exhibited recirculatory flows. Figure 6.23 shows that in 10 wt% droplets the flows became "weak" at high relative humidities. Other results (not included in Figure 6.23 as the droplets had asymmetric contact lines) showed that flows were rarely observed above 50% relative humidity even on plasma-cleaned substrates. In addition Figure 6.23 shows that there was no dependence in droplet volume as to whether there were recirculatory flows for inkjet-printed droplets.

Figure 6.24 helps quantify my flow strength definitions; case A gives an example of "strong" flow where the tracks are unclear because of a period of continuous recirculation of particles in the same area. However when the flows were "weak" a particle would complete a single recirculation loop at most. During weak flow central particles may move a few microns inwards but it was more common to see outward motion of particles near the top of the droplet.[58] This outward particle motion is not a result of the Coffee Ring Effect in which particles move most quickly at the end of drying[45] as the fastest motion in these droplets takes place towards the beginning rather than end of drying. In addition the case C (no Marangoni flow observed) example in Figure 6.24 shows that without pinning the flows would not be radially axisymmetric, instead particles would move with the droplet as the contact line depinned. The velocities found from PIV of the cases B and C also differed. In case C measured velocities were on the order of $50\,\mu\mathrm{m\,s^{-1}}$, equivalent to the noise in the measurements seen in the $0.8 - 0.9\ R_0$ PIV output in Figure 6.24 while for case B when weak flows were present the

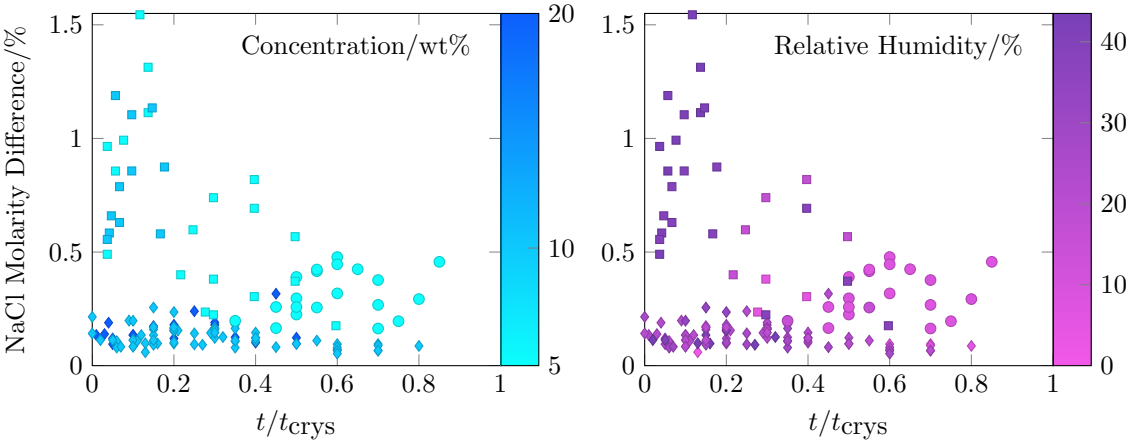

Figure 6.25: Estimated concentration difference for approximately 50 droplets at different times during their evaporation in which axisymmetric solutal Marangoni flows were tracked to estimate du/dn in Equation 1.20.

particle velocities were on the order of $100\,\mu m\,s^{-1}$.

From Appendix B the flow velocity at the interface will be three times the magnitude of the maximum velocity of particles that would move in the opposite direction. i.e. I calculate the flow velocity along the liquid-vapour interface from the maximum inward velocities from PIV. The reduction in volume at a given time was used to calculate the mean droplet concentration so increases in viscosity during drying could be accounted for in Equation 1.20, the surface tension dependence on concentration comes from Bzdek *et al.*[198] (see Table 6.2). Therefore Equation 1.20 could be used to determine the surface tension gradient and so the concentration gradient that would lead to the measured flow velocities. This approach was similar to Efstratiou *et al.*[257] who derived

$$u = \frac{1}{\eta}\frac{d\sigma}{dc}\frac{\Delta ch}{l} \tag{6.14}$$

which differs from our result by a factor of 2 from their lengthscale using the droplet diameter rather than radius.

The estimated concentration differences are given in Figure 6.25. Consistent with plasma-cleaned substrates more easily leading to solutal Marangoni flows,

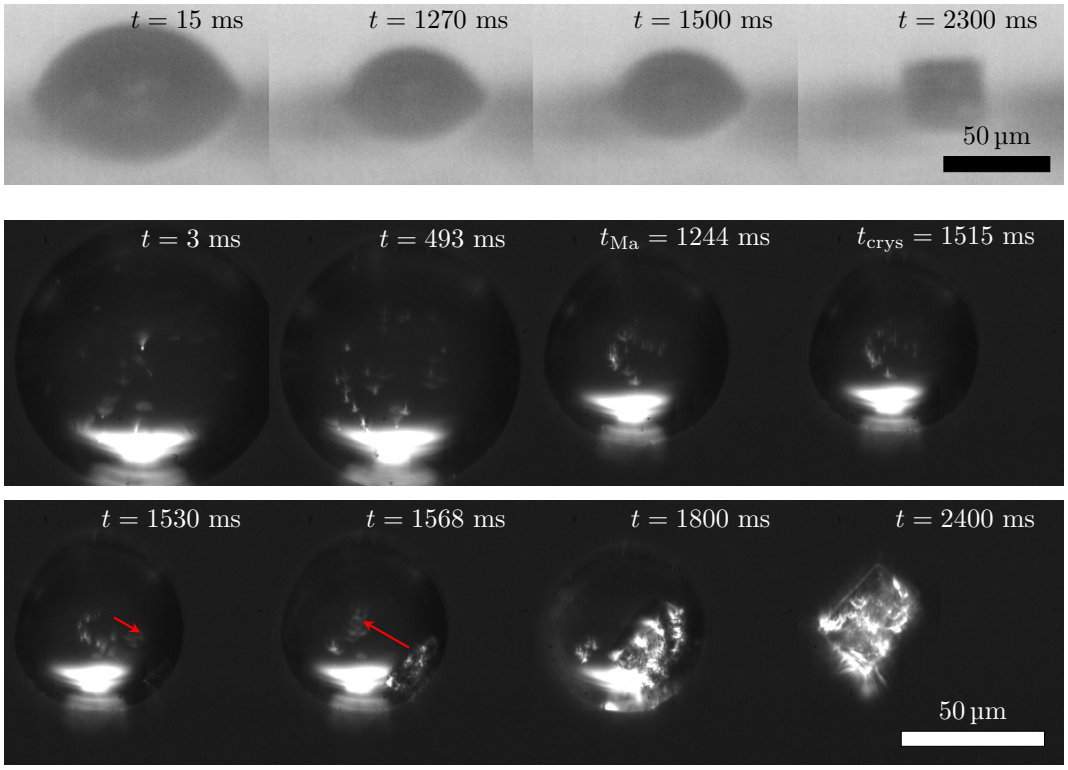

Figure 6.26: Droplet profile and bottom view dark-field images of a 10 wt% sodium chloride droplet containing particles on a HMDS-treated substrate, $RH = 19\%$. Particles migrate to centre and then respond (red arrows) to a local reduction in surface tension around the crystal, moving towards then away from the contact line.

those experiments (given by square markers) exhibited the highest concentration gradients, on the order of 1%. Velocities on plasma-cleaned substrates could only be effectively recorded at early times, for the same reason as for thin droplets of ethanol-water droplets with high ethanol concentrations: the main vortex would break up, becoming asymmetric so a radial velocity would no longer be a useful quantity. The estimated concentration gradients on HMDS-treated substrates were much smaller, typically less than 0.2%. As a result it is surprising that solutal Marangoni flows were not always observed in salty droplets containing particles as if the concentration gradient threshold was so low then more droplets would have been expected to reach such concentration gradients.

The presence of solutal Marangoni flows was not important to the structure

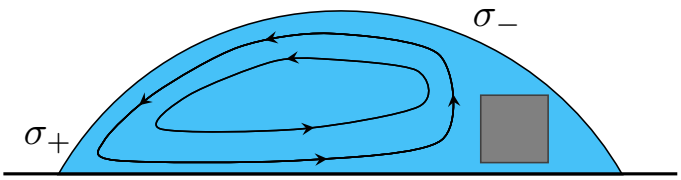

Figure 6.27: Cartoon showing the direction of flow for a single solutal Marangoni flow vortex in salt droplets after crystal growth leading to a local decrease in surface tension.

of the final arrangement of particles in salt droplets. Figure 6.26 shows that the crystal dominated the resulting deposit as crystallisation drove some solutal Marangoni flows. In Figure 6.26 the red arrows mark the movement of particles towards and then away from the crystal. The flow is driven by the growing crystal taking up salt, depleting the surrounding region of ions. Since those ions were increasing the surface tension then the ion-depleted region of liquid-vapour interface nearest the crystal has a lower surface tension than at the far side of the contact line generating a flow with direction given by Figure 6.27. This motion is fast, particles travel from near the centre to the crystal (at the contact line) and back again within a few tens of milliseconds. Thus the particle velocities are greater than $1\,\mathrm{mm\,s^{-1}}$. That the velocities of these solutal Marangoni flows are much larger than those measured at earlier times as a result of evaporation is expected due to the large surface tension difference between salt-rich and salt-depleted fluid at the far and near sides to the crystal in a droplet.

That the crystallisation process introduces a flow has been reported previously. Sun *et al.*[256] noted that particles were repelled (along the liquid-vapour interface) by a growing crystal in a high salt concentration drop while Efstratiou *et al.*[257] focused on how nucleation of crystals lead to jets of fluid (along the substrate) towards nucleating crystals in 1 M drops on a hydrophilic substrate. They also considered whether the Marangoni flows could have been driven by a temperature rather than a concentration gradient as crystallisation is exothermic so could lead

to local increases in temperature[259,260] and decreases in surface tension. As a result a thermally driven flow could act in the same direction but was discounted as infrared thermography revealed no large temperature gradients.

6.8.3 Low NaCl Concentrations

Following the influential main paper describing the coffee ring effect the first author Deegan[48] published a secondary paper focusing on deposits of drops containing surfactants and salts. Results for sodium chloride concentrations of 0.001, 0.01 and 1 mM were presented. A 1 mM concentration had a less well formed ring deposit and Deegan suggested that the difference was a result of differing particle interactions at increasing solution ionic strengths.

Marín *et al.*[43] showed evidence of salty droplets exhibiting enhanced evaporation and solute accumulation at the contact line sufficient to drive solutal Marangoni flows even at very low NaCl concentrations. In 0.8 µL droplets the accumulation of 1.1 µm particles at the contact line could be measured and the growth rate of the ring deposit had a larger exponent than proposed by Deegan *et al.*,[28] which was larger for increasingly salty droplets going from 1 to 10 mM. When they demonstrated the presence of solutal Marangoni flows they did so at a higher concentration (still far below saturation) of 100 mM although the experimental particle velocities were smaller than those in their lubrication model by a factor of more than 40. Their argument that this could be a result of colloidal particles not being good tracers for interfacial flows is not convincing as the disagreement was just as large in the bulk of the droplet where particles were far from the interface.

Recently Sun *et al.*[256] investigated the evaporation of salty droplets with a concentration of 0.9 wt% (to match blood plasma), equivalent to a concentration of about 150 mM NaCl. A piranha solution-cleaned substrate was used so the contact angles were low, however in contrast to the study from Marín *et al.*,[43] the

Chinese group found that the presence of sodium chloride retarded the growth of the ring deposit and that the particles in the deposit ended up more loosely packed.

I attempted to verify Marín *et al.*'s results[43] however my experiments were not a perfect replication as I worked with inkjet-printed droplets rather than microlitre volume drops, this meant that while my droplets were much smaller than those of Marín *et al.*, the particles were of a similar diameter. Therefore even at much higher particle fractions there were not enough particles in the actual droplet to form a continuous ring deposit[15] and so verify their power law exponents for the growth of the ring deposit. Despite this I could still test whether there were any Marangoni flows in low NaCl concentration droplets on plasma-cleaned substrates (~15° in Marín *et al.*'s experiments vs $10-25°$ in these experiments) at $RH = 40\%$.

My experiments with NaCl corroborated Marín *et al.*'s result that recirculatory flows were present in 100 mM NaCl droplets at $RH = 40\%$. Figure 6.28 shows that the Marangoni flows did not develop immediately for 100 mM droplets, this is reminiscent of the low concentration lactose experiments (see Figure 5.11) in which the droplet had to become more concentrated before the concentration gradient grew to a level sufficient to drive circulatory flows.

On the plasma-cleaned substrates the flows were only axisymmetric for a short time at the start of drying, droplets tended to depin unevenly due to incomplete ring deposits (of particles) forming before the droplets became very thin. This was recorded in the particle tracks in Figure 6.28, at the start particles moved radially although at late times wandering paths near the contact line were recorded. At concentrations of 100 mM, circulatory flows were only present on plasma-cleaned substrates; on HMDS-treated substrates where the initial contact angles were about 72° no flows were observed. If the relative humidity was high, $RH \approx 50-60\%$ then the droplets on plasma-cleaned substrates did not exhibit

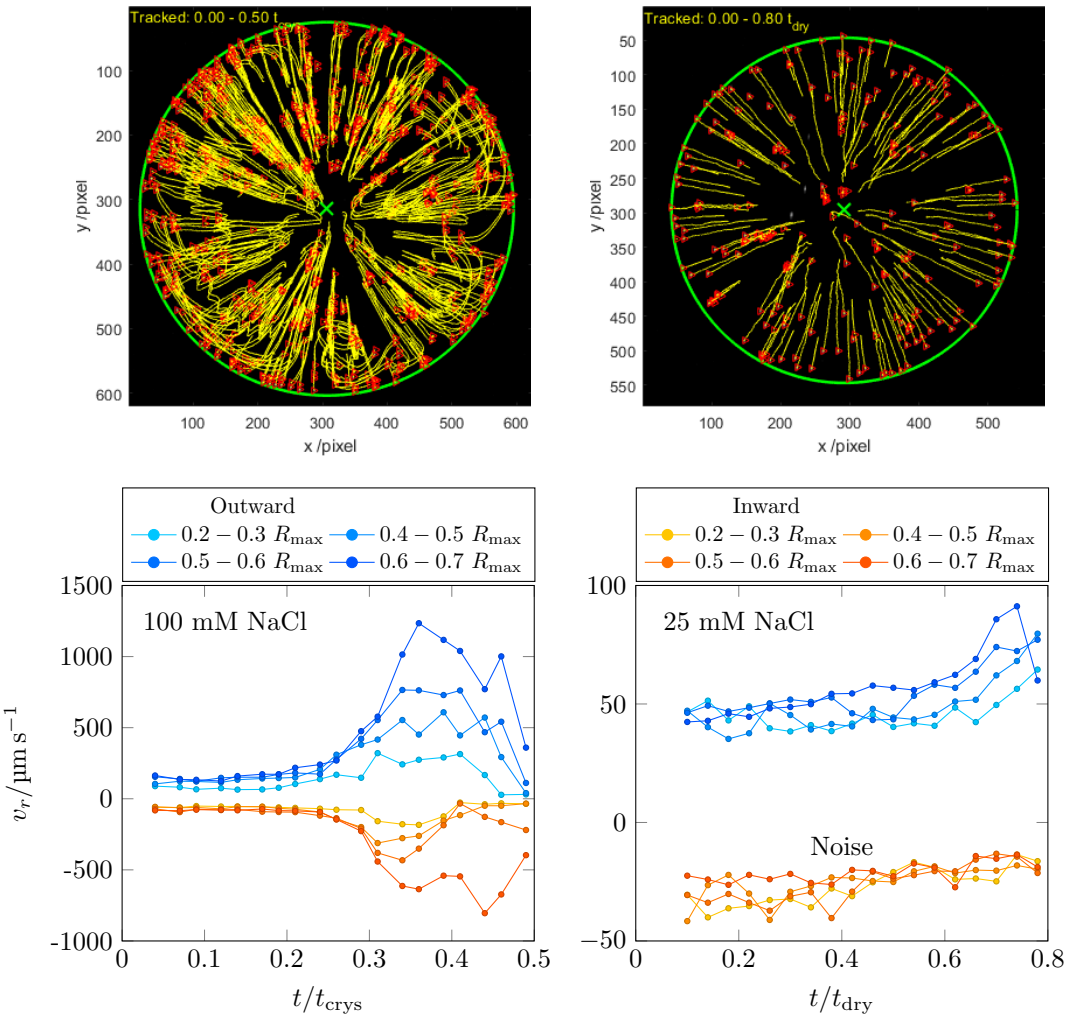

Figure 6.28: Particle tracks and measured radial velocities for 100 mM and 24 mM NaCl droplets on plasma-cleaned substrates at $RH \approx 40\%$, $V_0 \approx 180$ pL. Compared to at 100 mM when Marangoni recirculation is observed, there is only convective flow at 25 mM.

recirculatory flows.

In experiments with lower NaCl concentrations of 10, 25 or 40 mM no circulatory flows were recorded, even when the relative humidity was lowered to 25% (given that too high a relative humidity had been found to reduce the incidence of recirculatory flows, see Figure 6.23). The right side of Figure 6.28 shows that at NaCl concentrations of 25 mM, only slow, outward convective flow consistent with the coffee ring effect was observed. The inward velocities and velocity measurements at early times in this figure are a result of noise.

In the previous section, Figure 6.25 showed that on plasma-cleaned substrates the estimated concentration differences driving solutal Marangoni flows were on the order of 1%. Relating this back to the low concentration droplets, after the initial short spreading stage the droplet contact radii did not vary, therefore the evaporation rate can be approximated as constant as at such low concentrations the water activity at the surface would not vary significantly over time. At such low concentrations $t_{\mathrm{dry}} \approx t_{\mathrm{crys}}$ so at the measured peak in particle velocities in Figure 6.28, at around one third of the way through drying, the concentration would be approximately 50% greater. Therefore with an initial concentration of 100 mM the concentration difference across the droplet surface would be on the order of 1.5 mM. A difference of 1.5 mM is similar to the absolute concentration difference of several millimoles per litre of solution found for higher NaCl concentration droplets on other substrates, for example if $c_0 = 10$ wt% ≈ 2 M NaCl then if the gradient is about 0.1% for a HMDS-treated substrate (Figure 6.25) then the concentration difference would be about 2 mM. This seems to be the magnitude of the required salt enrichment threshold, which means that if the initial salt concentration was any lower then droplets would not have reached the threshold for strong solutal Marangoni flows in which particles recirculated multiple times.

Therefore it seems possible that Marín *et al.* were unable to measure such weak flows which was why they demonstrated the presence of flows at concentrations two orders of magnitude higher than the rest of their measurements. Given that solutal Marangoni flows developed in inkjet-printed droplets late even at 100 mM concentrations then droplets would have already dried to a thin film for $1-10$ mM concentrations by the time that there was a large enough concentration gradient to induce solutal Marangoni flow. Despite this flaw, their central argument that there was a flow along the interface at lower than expected salt concentrations was verified by confocal microscopy.

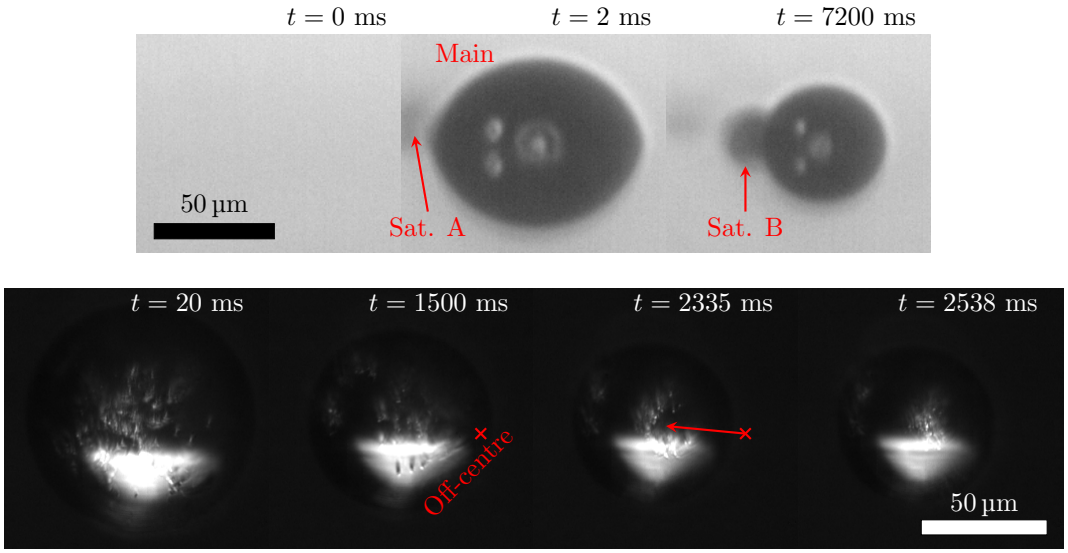

Figure 6.29: When a 20 wt% $NaNO_3$ droplet was printed on a HMDS-treated substrate with multiple satellites nearby, the circulatory flows were off-centre at the start but became more axisymmetric after the smaller satellites finished evaporating. $RH = 43 \pm 2\%$.

6.8.4 Sodium Nitrate and Ammonium Sulfate

Compared to sodium chloride, sodium nitrate has a smaller change in surface tension with concentration while ammonium sulfate has a larger change. Therefore it was expected that it would be harder to observe flows in sodium nitrate droplets and easier in ammonium sulfate droplets. This was broadly correct, the vast majority of experiments with AMS droplets containing particles showed Marangoni flows.

As sodium nitrate is much more soluble than sodium chloride it was possible to start with more concentrated droplets without experiencing significant crystallisation at the nozzle. It was thought that using more concentrated droplets would lead to a greater magnitude of surface tension gradients which would counteract how sodium nitrate changes the surface tension less than sodium chloride. However the flows in sodium nitrate droplets were unreliable; in over 100 videos of sodium nitrate droplets of various concentrations with particles there were inconsistencies in when flows were observed as flows would no longer be observed

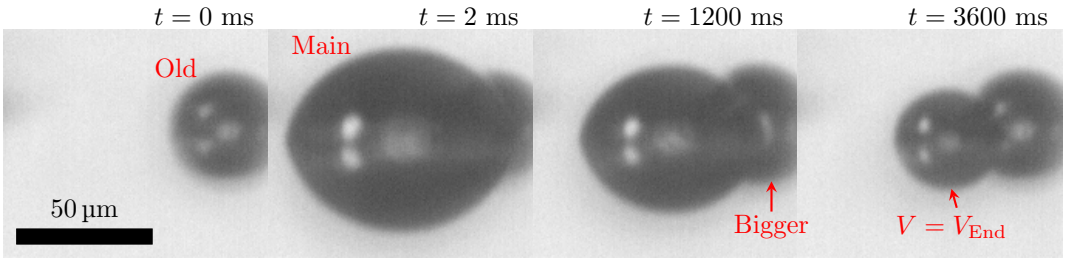

Figure 6.30: Growth of a previously printed droplet (Old) upon deposition of a new 10 wt% $NaNO_3$ droplet (Main) on a HMDS-treated substrate, $RH = 44 \pm 2\%$. After deposition the Old droplet becomes bigger due to a local increase in water vapour leading to condensation on the Old droplet. The scalebar is only accurate in the plane of focus of the telescopic lens.

or suddenly appear in the next droplet printed with no change in method (such as a delay prior to printing), substrate or relative humidity. On the occasions in which there were continuous, near axisymmetric particle flows, migration towards the centre of the droplet was recorded (see Figure 6.29).

From the results in Section 6.8.3 circulatory flows were expected on high energy surfaces given the minimum sodium nitrate concentration used was 5 wt%. This was indeed the case and it was only on plasma-cleaned substrates that solutal Marangoni flows were always observed.

One potential cause of the inconsistencies considered was the environment of the droplet on the substrate. Compared to sodium chloride, sodium nitrate is much more hygroscopic which contributes to its less defined efflorescence transition. Therefore printing too near a previous droplet which had since crystallised could change the evaporation of the droplet by the crystal acting as a vapour sink, enhancing evaporation on only one side of the droplet. Despite Lu *et al.*[225] using FTIR-ATR to show that the crystals would take up water despite their appearance not appreciably changing, the presence of crystals did not appear to be relevant upon testing. However at higher relative humidities when sodium nitrate droplets did not crystallise then "old" supersaturated droplets were able to act as vapour sinks as water vapour could condense onto a low water activity

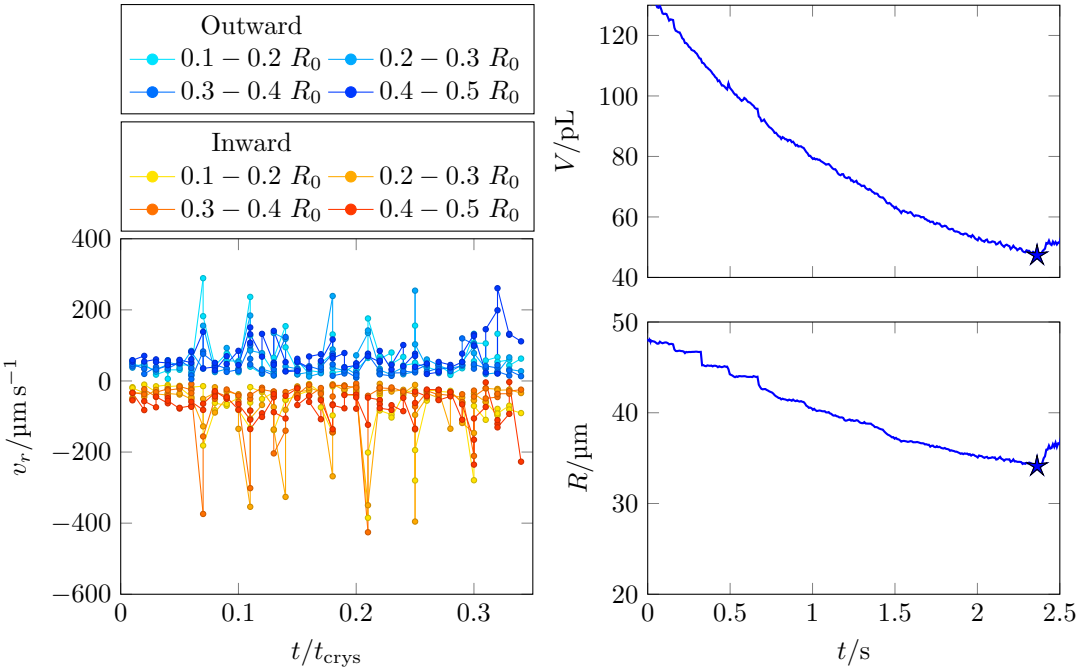

Figure 6.31: Stop and start solutal Marangoni flows during the evaporation of a 30 wt% $NaNO_3$ droplet on a HMDS-treated substrate, $RH = 29 \pm 2\%$. The "jerky" flows coincide with steps in the droplet radius in the bottom right plot.

interface as illustrated in Figure 6.30 where an older droplet near the freshly printed droplet is seen to grow larger as a result of condensation.

A common origin of a driving force for internal flows was the presence of smaller satellite droplets deposited at the same time of printing near the main droplet. These would evaporate and so lower the evaporative flux across the near side of the main droplet. Figure 6.29 presents an example of a droplet on a HMDS-treated substrate where flows were very off-centre at the beginning but became nearly axisymmetric later on. This would be consistent with the evaporation of the main droplet being influenced by a satellite which would finish evaporating first, leaving the main drop with an axisymmetric evaporative flux at late times.

When investigating sodium chloride droplets, where I classed the flow as "weak" there was occasionally what what looked like normal recirculatory flow, except the flow would suddenly end after a single cycle, occasionally restarting for another cycle. These stop-start flows have not been discussed previously in the

sessile drop literature and were more common in sodium nitrate droplets than the other salt droplets investigated. Figure 6.31 displays some particle tracking data in which the particles were seen to be near stationary before suddenly moving and stopping again after approximately completing one loop of a Marangoni streamline. When the flows paused the particles came to an abrupt stop leading to the motion appearing "jerky". As in droplets of other solutes which increase the surface tension, solutal Marangoni flows were directed inwards along the interface. These suddenly appearing flows led to stick-slip contact line motion where Figure 6.31 shows that at early times there were steps in the droplet radius. These flows were not related to experiments where droplets were interacting with satellites as the transient flows were axisymmetric; instead these flows were likely symptomatic of the difficulties in reproducibly generating solutal Marangoni flows under these conditions. Given the presence of solute only leading to very small changes in surface tension then the surface tension gradients generated were around the cusp of what was required to actually lead to regular circulatory flow. Therefore for these droplets, we suggest that mixing as a result of the Marangoni flows dissipates the driving concentration gradient leading to periodic behaviour.[108]

The main motivation for the ammonium sulfate experiments was to test the salt's efflorescence behaviour. Therefore only limited measurements took place with droplets containing particles for $c_0 = 10$ wt%, $28\% \leq RH \leq 48\%$, on HMDS-treated and plasma-cleaned substrates. Under these conditions solutal Marangoni flows were reliably generated at low contact angles where there would be a larger surface tension gradient, outward radial velocities peaked around $800\,\mu\mathrm{m\,s^{-1}}$ while inward radial velocities up to around $500\,\mu\mathrm{m\,s^{-1}}$ were measured. On HMDS-treated substrates the flow behaviour was dependent on whether there was a nearby satellite droplet. In Figure 6.32 when a satellite droplet was present then there were strong, non-axisymmetric solutal Marangoni flows where the centre of the flows had moved in the direction of the satellite droplet. When tracing these

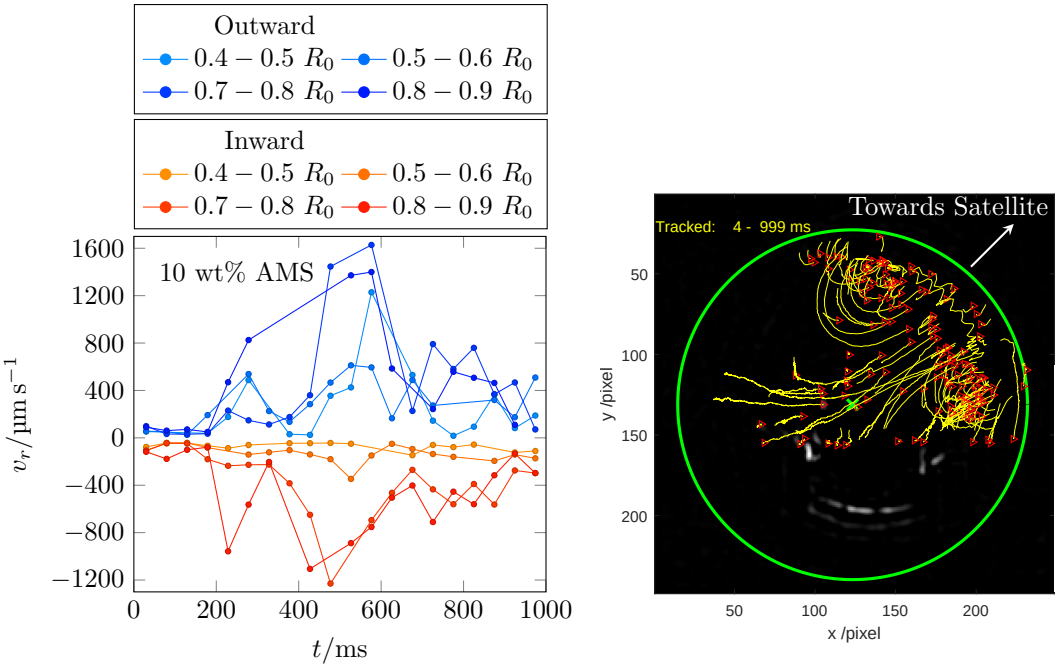

Figure 6.32: Particle tracks and measured radial velocities for a 10 wt% AMS droplet, $V_0 = 155$ pL on a HMDS-treated substrate at $RH = 42 \pm 2\%$. The Marangoni recirculation primarily occurred at the side of the droplet nearest to its satellite.

off-centre flows the particles moved even more quickly than on plasma-cleaned substrates, reaching outward radial velocities of 1.6 mm s^{-1} and inward radial velocities of up to around 1.2 mm s^{-1}. This suggests suppression of evaporation into the region between the main and satellite droplets is very significant, even when those satellites were multiple droplet radii away. In contrast when there were no satellite droplets then there was stop-start behaviour, similar to that observed in some sodium nitrate droplets. This stopping and starting of the flows should follow the same mechanism in both cases, that because of the high contact angles the surface tension gradients are small and grow slowly enough that mixing from Marangoni flow is able to refresh the surface and destroy the concentration gradient driving it.

6.9 Conclusions and Future Directions

To summarise, many salt droplets of different concentrations were printed on hydrophilic and hydrophobic substrates under a range of relative humidities. The sets of conditions which would lead to solutal Marangoni flows were identified and a volume-averaged model applied to attempt to quantify the evaporation rate as the droplets increased in salt concentration.

The relative humidity was varied systematically and aerosol-like behaviour found as sodium chloride and ammonium sulfate would not crystallise above the so-called efflorescence relative humidity. Compared to aerosol literature values these measured *ERH*'s were slightly higher, we suggest this increase is a result of heterogeneous nucleation at the substrate. Sodium nitrate droplets did not have a clear *ERH* which is consistent with results in the literature that nucleation is a stochastic process and some probability of $NaNO_3$ droplets will not crystallise even at low relative humidities. Aside from the value in showing that efflorescence behaviour persists between sessile and aerosol droplets the results for ammonium sulfate have wider value. AMS is commonly added as a component to agrichemical formulations so knowledge of the conditions which would impact a plant's uptake of the salt, due to it getting locked away in a crystal at low *RH*, is of value in determining optimum conditions for spraying crop fields. Given that the efflorescence relative humidity was examined there is an opportunity for future experiments to test if there is any, unexpected, shift in the deliquescence relative humidity. Such experiments would involve humidity cycling and could also be of value by further probing the efflorescence of sodium nitrate to see whether certain droplets repeatably nucleate during cycles which would be indicative of impurities present in the droplets rather than stochastic nucleation behaviour.

The volume-averaged model could be utilised with physical properties data calculated from the E-AIM model for high salt concentrations for all the salts chosen for study. Compared to solvent and sugar droplets the model did not

perform well, good agreement of evaporation rates with experiment was only found for low humidities ($< 10\%$) and even then only in the early stages of drying. At higher humidities the calculated evaporation rates were too fast, with the disagreement increasing at higher *RH*. The model for salt droplets did not have a modification to take into account crystallisation so the model was stopped at the experimental crystallisation time, further work to integrate Classical Nucleation Theory could be of value by allowing comparisons between predictions and experiment. For sodium chloride and ammonium sulfate droplets with relative humidities above the *ERH* the model gave similar results to EG-water or sugar droplets as a plateau was reached. Like with these other systems the modelled volume at which these salt droplets plateaued was much lower than experiment. Like the other systems we suggest that the disagreements between the model and experiment are a result of the non-uniform composition within the droplet: if the surface is enriched in salt then the water activity at the surface is suppressed and the evaporation rate will be lower.

The flow behaviour of salt droplets was quite different to solvent mixtures or sugar solution droplets as the presence of solutal Marangoni flows was inconsistent and there were multiple variables controlling whether they were present: substrate (plasma-cleaned preferred for flow to be present), concentration (high preferred) and relative humidity (low *RH* preferred). When Marangoni flows were present they acted in the same direction as sugar droplets although flows were faster, and there was also particle migration towards the centre of the droplet although any collected group was always displaced by the nucleating crystal. On HMDS-treated substrates there were examples for all the salts of "jerky" motion: when there was weak solutal Marangoni flow the observed recirculation would sometimes pause, allowing the surface tension gradient to build up again due to evaporation across the droplet interface which would restart the Marangoni flow. Going forwards these systems might be particularly interesting to determine the conditions under

which Marangoni flow are observed as the experiments are close to the edge-case of when flows are present. The presence of satellite droplets also appeared important near this cut-off of whether flows were present as evaporation would be suppressed between the droplets, generating a larger surface tension gradient. In future work it could be valuable to play with this effect by deliberately printing secondary droplets with a second nozzle at controlled distance from the primary droplet. Investigations of Marangoni flows at low NaCl concentrations on plasma-cleaned substrates showed that Marangoni flows could still be observed at around 100 mM concentrations although at even lower concentrations we were unable to verify the work of Marín *et al.*[43].

Unlike the other systems studied in the rest of this thesis there was crystallisation from the droplets, crystallisation effects dominated over whatever the particles had been doing before as the process created large surface tension gradients that disrupted particle deposition. Therefore this chapter focused on the deposition of salt crystals rather than suspended tracer particles.

The crystal deposits were analysed and the conditions, primarily the substrate choice, which lead to each deposit feature described. SEM images and dark-field videos of droplet drying showed that sodium chloride did not always nucleate as single cubic crystals as high supersaturations allowed for fast crystal growth from multiple sites on a crystal, creating amorphous deposits. The most common type of deposit was a set of two to four ”blocky” crystals that were not well ordered internally and so scattered a lot of light from the LEDs. The number of crystals increased, and so their mean size decreased, at lower relative humidity. Often the crystals were only ”blocky” on one side as if the crystal remained close to the contact line during its growth then its shape was templated by the droplet liquid-vapour interface to become curved. This was possible on both HMDS-treated and plasma-cleaned substrates but much common in the latter case. In contrast, the crystal deposits from sodium nitrate or AMS were clearly

different between HMDS-treated and plasma-cleaned substrates and nucleation from multiple sites was not observed. On HMDS-treated substrates a long crystal of sodium nitrate would nucleate and grow to reach opposite sides of the droplet before growing more slowly near perpendicular to the main growth axis. On plasma-cleaned substrates the crystal would nucleate from the contact line and grow in all directions, leaving a much flatter, wider crystal. AMS droplets on HMDS-treated substrates nucleated in a particularly interesting way as it was the only case where it was hard to notice that nucleation had occurred from side-view videos as the crystal had the same shape as the droplet. The crystal would grow from one point near the contact line to completely cover the liquid-vapour interface and the entire droplet footprint. As a result the crystal is likely hollow as there would still have been some fluid remaining just after nucleation. On plasma-cleaned substrates AMS crystals would also grow to cover the entire droplet footprint, being thicker at the side of the droplet opposite to the nucleation location. SEM also showed that these deposits were also surrounded by rings of microcrystallites that could not be observed using scattered light at the printing rig. In terms of future work there are clear avenues to experiment with different salts with new crystal habits, as well as choosing salts with more accessible (than NaCl) polymorphs. It would also be beneficial to run experiments to break the AMS crystals that nucleated on HMDS-treated substrates to verify that they were hollow.

To extend the work presented here it is clear that the delay before printing a droplet needs to be much more tightly controlled to improve reproducibility. By the end of this work an approach was taken in which the arm upon which the inkjet nozzle was mounted was motorised so that the nozzle could be moved between experiments more easily. This allowed the user to print continuously in a location far away on the substrate to refresh the fluid at the nozzle, before calling it back to the correct position in view of the cameras for the real experiment.

However this approach was not straightforward to automate as the crystal deposits were of interest. Therefore the distance that the nozzle would be moved between experiments needed to be extended for every experiment otherwise the crystal deposits would be dissolved and so could not be taken for SEM analysis. A more thorough automation using LabView would be advantageous although it was difficult to remodel the experiment while it was in use most days by multiple users. Such an improvement would help reduce differences between the model and experiment and hopefully reduce the scatter in supersaturation data to help uncover more subtle trends.

Aside from developments in the method it would be interesting to look at droplets containing multiple salts to investigate changes in the efflorescence behaviour. Whether the crystals nucleated separately or together could also be tested as in aerosol experiments the more stable salt can use the crystal of the first salt to nucleate as a surface for heterogeneous nucleation.[213] However in a sessile droplet heterogeneous nucleation is possible at the substrate so crystals may be separate, allowing their identity to be probed using Raman Spectroscopy techniques[280] such as Raman Imaging.[281]

Chapter 7

Particle Migration

In this Chapter I will draw results from across the previous Chapters to better discuss the possible mechanism driving the particle migration observed.

In Section 1.5 the Stokes number was used to verify that the particles were expected to follow flow streamlines. Instead we observed particle migration when there were solutal Marangoni flows with the direction given in Figure 7.1 for the different systems. In this Chapter I discuss potential mechanisms depending on particle interactions or the action of fluid flow that drive this particle migration.

7.1 Potential Mechanisms

Collision-based mechanisms[282] are not viable: there is particle depletion towards the contact line so as the edge of the collected group contracts there are no outer particles outside the group to collide and induce continual migration.

Diffusion of particles across streamlines does not make sense as a mechanism as such migration would not be directional.

Talbot[88] ruled out thermophoresis as a result of temperature gradients arising from evaporative cooling towards the contact line by running experiments on sapphire substrates with much higher thermal conductivity than glass. In these experiments any temperature gradients would be reduced as a greater amount

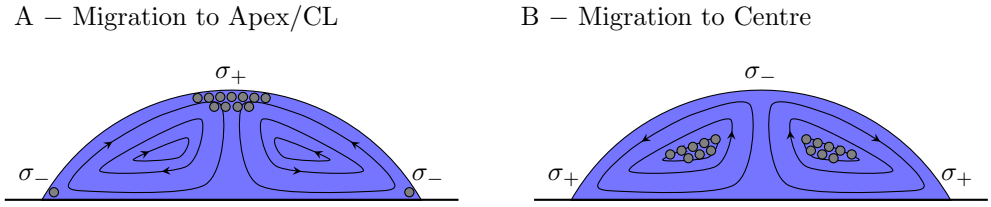

Figure 7.1: The directions of Marangoni flows in response to surface tension gradients where the contact line region has A - a lower surface tension, or B - a higher surface tension, than at the apex. Grey tracer particles have been added to show the position to which particles migrated to under each flow direction.

of the heat lost during evaporation could be replenished by heat conducted from the substrate; however no reduction in particle migration was found with this approach. They also ruled out density-based mechanisms with deuterated fluids. In such systems the particles would be less, rather than more dense, than the surrounding ethanol-water mixture and so experience a buoyancy force in the opposite direction compared to undeuterated droplets, however no change was recorded. I tested for second order density effects in experiments with binary mixtures of deuterated ethanol and high-purity (i.e. undeuterated) water droplets to reduce the density difference between ethanol and water but found no measurable (considering inherent variability in experiments) difference in such systems.

Given the inconclusive independence between the direction of the solutal Marangoni flows and the migration direction it is plausible that the migration is shear-induced, during migration to the centre of the droplet the particles travel towards quiescent regions of the droplet, in the same direction as the concentration gradient.

However there are pieces of evidence that do not fit a shear induced migration interpretation; firstly the droplet systems with migration towards the centre: ethanol-water, EG-ethanol, EG-water with ethanol vapour and sugar and salt solutions all have different evaporation timescales and flow velocities yet can still have remarkably similar particle distributions at the end of Marangoni flows.

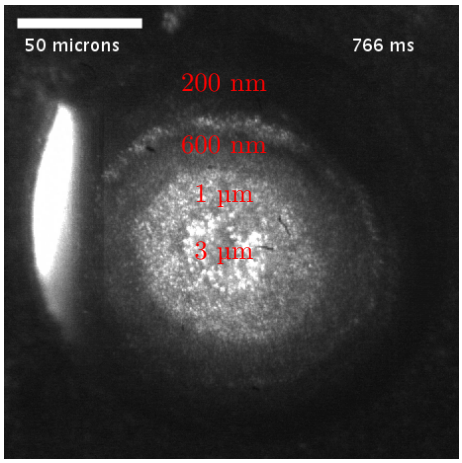

Figure 7.2: End of solutal Marangoni flows in an ethanol-water droplet containing sterically stabilised PS particles of different sizes: 0.5%v 200 nm, 0.05%v 600 nm, 0.01%v 1 µm, and 0.5%v 3 µm. Copyright E. Talbot 2014.[88]

While this does not particularly support a diffusiophoretic mechanism either, in a shear mechanism the lower shear rates in the slower flows in sugar or salt solutions would be expected to lead to different outcomes. Secondly, and more significantly, shear migration towards the quiescent region should always be towards the centre of the droplet so do not explain the reversal of migration direction for ethanol vapour or EG-water experiments where migration was towards the apex, away from the low shear region. In addition it would also be unclear why the hole in ethanol-water droplet collected groups would fill in a little before the Marangoni flows end.

Finally there were problems with how the migration scales with particle size. Figure 7.2 displays a frame from one of Talbot's experiments[88] where she added particles of different sizes (200 nm, 600 nm, 1 µm and 3 µm) within the same ethanol-water droplet. It is clear that the particles migrated different distances, with the smallest particles migrating much less than the large ones. In a shear-induced mechanism this general trend is expected, a large particle will be exposed to a greater number of flow streamlines and so experience a greater shear. However

if the radii of the collected groups were fitted as a function of the particle radius, a_p, the dependence is very weak, with $R_g \sim a_p^{1/4}$.

In established shear mechanisms in the literature the scaling with particle radius is much more significant. According to Faxén's Law, at low Reynolds number a particle in a collection of particles experiences a hydrodynamic force giving a velocity that scales with a_p^2.[283,284] Rubinow and Keller[285] demonstrated that a particle spinning in a viscous fluid experiences a force orthogonal to its direction of motion (F scales with a_p^3) giving a velocity that scales with a_p^4. It is also well known that in parabolic Poiseuille flow through pipes, rigid particles experience a lift force perpendicular to the direction of flow that leads to focusing away from the walls.[286] Saffman[287] found expressions for this lift, deriving leading drift velocity terms that scaled with a_p^3. Based upon these examples the lack of agreement between the $a_p^{1/4}$ scaling of the collected group radius and that of the particle velocities in shear-induced mechanisms with strong strong particle radius scaling, suggests the migration is not shear-induced. This leads to our tentative endorsement of diffusiophoresis as the driving mechanism of the particle migration.

7.2 Diffusiophoresis

Diffusiophoresis is our current mechanism driving the particle migration as while it is not perfect it at least can explain the change in migration direction in ethanol-water droplets with the addition of ethanol vapour.

Diffusiophoresis is the induced motion of particles as a result of diffuse interactions with a concentration gradient in the surrounding fluid. The concentration gradient results in a chemical potential gradient at a particle's surface which is realised as an osmotic pressure difference that propels the particle.[288,289] There are many possible origins for such a chemical potential gradient such as van der

Waals interactions, repulsive steric exclusions, electric or temperature fields, or asymmetric particles (e.g. Janus self-swimmers[290]). The development of microfluidic technology has drawn attention to the phenomenon of diffusiophoresis as it has become easier to generate large, stable concentration gradients.[289–294]

The relevant equations were first derived by Derjaguin *et al.*[295] who introduced diffusiophoresis to explain the enhanced deposition of latex at high salt concentrations, further details are given in Appendix E.

For a "neutral solute" (such as a binary mixture of ethanol and water) the diffusiophoretic velocity, u_{DP}, is given by[295,296]

$$u_{\mathrm{DP}} = \frac{k_{\mathrm{B}}T}{\eta} L^2 \nabla c \int_0^\infty y \left(\exp \frac{-\phi(y)}{k_{\mathrm{B}}T} - 1 \right) \tag{7.1}$$

where L is the length scale of the interaction, y is the distance from the particle and $\phi(y)$ is the interaction potential; in experiments this velocity is on the order of a few microns per second.

For a solvent mixture this interaction potential is not well defined,[294,297] as a result the bulk of the studies in literature focus on electrolytes where the interaction is known and the lengthscale is the Debeye length; although there is an additional "chemiphoretic" term that appears due to different ion mobilities induce an electric field up or down the concentration gradient to maintain electroneutrality. The sum of these terms gives a velocity where terms can be grouped into the following simplified form[298]

$$u_{\mathrm{DP}} = D_{\mathrm{DP}} \, \nabla \ln \frac{c}{c^*}, \tag{7.2}$$

where c^* is the reference concentration chosen for the chemical potential. The dependence of the induced electric field is the origin of the different concentration difference dependence compared to Equation 7.1.

Paustian *et al.*[293] ran experiments with ethanol-water mixtures rather than electrolytes and found that for solvent mixtures the diffusiophoretic velocity was

better fit by

$$u_{\mathrm{DP}} = D_{\mathrm{DP}} \nabla \ln x \tag{7.3}$$

where x was the mole fraction of solute (ethanol) rather than the concentration as for the electrolyte systems.

An example of a practical application is the work of Kabalnov and Wennerström[128] who wanted to understand the migration induced banding of carbon black pigment within an inkjet printer head (containing an ink with water and polyethylene glycol). To do this they derived a steady-state model with evaporation from a capillary joined to a reservoir where the fluid contained an involatile solute and particles. Within their chemical potential formalism these particles had a thermodynamically preferred solvent driving migration away from the interface enriched with the non-volatile solvent. This particle migration opposed the replenishing flow from the fluid reservoir and so led to concentrated bands of particles that moved away from the nozzle aperture over time and so would reduce skin formation at the interface such as in inkjet printheads.

7.3 Experiments

7.3.1 Direction of Migration

In Chapter 4 I showed that during the evaporation of ethanol-water droplets the particles added as flow tracers migrated across flow streamlines towards the centre of the droplet. However rather than migrating exactly towards the centre, there was a hole in the toroidal flow vortex (see Figure 7.3). This suggests that the particles migrated to the quiescent ring within the vortex where fluid elements had the highest effective distance from the liquid-vapour interface. While a position directly below the apex close to the substrate (rather than at the substrate, as there will be a stagnant layer from the no-slip boundary condition) will be furthest from the liquid-vapour interface, Marangoni flows mean that a fluid element near

the substrate will spend some time at the interface during a recirculation cycle.

Evaporation caused the surface to become deficient in the more volatile ethanol, therefore the migration is towards higher ethanol concentrations. The micron diameter polystyrene particles used are sterically-stabilised by polymer (PEGMA) chains attached to their surfaces which prevent aggregation, these chains provide the diffuse layer of interactions necessary for diffusiophoresis. The concentration gradients are also large enough for migration to be feasible. Paustian *et al.*[293] measured velocities of about $2\,\mu m\,s^{-1}$ for an ethanol-water concentration gradient on the order of $0.03 - 0.06$ M/µm ($\Delta c = 5$ or 10 M across a 150 µm channel). Diddens's simulations of ethanol-water drops[39] showed that the interface typically has an ethanol concentration a few mass percent lower than the bulk. Using this concentration gradient $\Delta c \approx 0.2$ M which will act over $5-10\,\mu m$ (about half a droplet height). This gives a gradient of $0.02 - 0.04$ M/µm, comparable to Paustian *et al.*'s system.

In experiments with water or ethanol-water droplets in an environment enriched with ethanol vapour, the particles accumulated at the contact line and apex (see Figure 7.3). Considering the condensation of ethanol on the droplets, the ethanol concentration will be higher along the liquid-vapour interface (i.e. closer to the vapour source), being greatest at the contact line. Therefore the collection of particles towards the interface is still consistent with particle migration towards higher ethanol concentrations. The particles collecting at the contact line and apex were carried by solutal Marangoni flows where they then jammed at the higher particle concentrations from the particles migrating against the flows to stay at higher ethanol concentrations.

For mixtures containing ethylene glycol, EG-water droplets had the same flow direction as in the ethanol vapour experiments and similar migration to the apex. As ethylene glycol is much less volatile than water the interface is EG rich so migration is towards higher EG concentrations than the bulk. For EG-

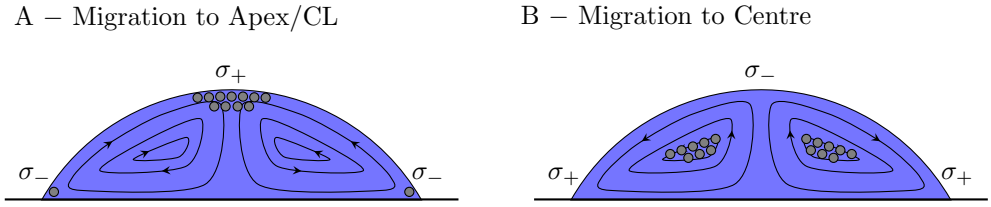

Case A − Migration to Apex/CL
(Ethanol-Water in Ethanol Vapour)

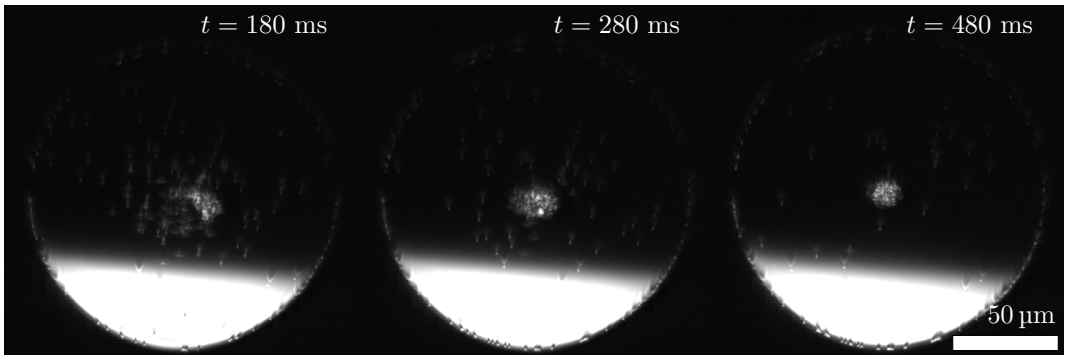

Case B − Migration to Centre
(Ethanol-Water)

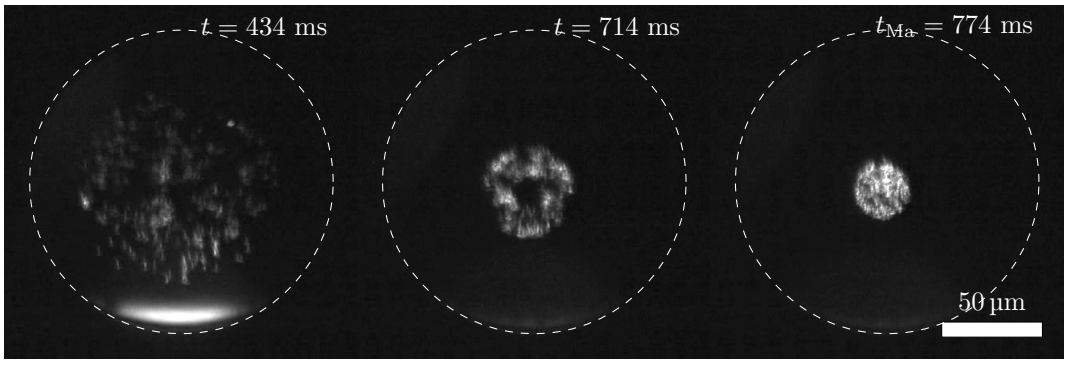

Figure 7.3: Reminder of directions of Marangoni flows in response to surface tension gradients between the apex and contact line and the direction of migration in each case with examples of ethanol-water droplets with and without ethanol vapour from Chapter 4.

ethanol droplets the flows were in the same direction as ethanol-water droplets and migration was towards the centre of the droplet. During evaporation the interface would be depleted of ethanol due to its faster evaporation, meaning that the migration was in the direction of higher ethanol concentrations. This is in contrast to Paustian *et al.*[293] who observed migration towards lower ethanol concentrations although the direction is dependent on the particles used; for example different research groups have found migration towards higher[293] and lower[299] sodium chloride concentrations.

These experiments set up a series of preferred neutral solvents for the direction of particle migration: ethanol, then ethylene glycol and then water. This motivated experiments with ternary droplets of all three components; in ternary mixtures the ethanol evaporated first, then the water, leaving a long lasting EG rich droplet. The solutal Marangoni flows went in stages, first like at ethanol-water droplet, then an EG-water droplet, therefore particles first migrated to the centre before moving to the apex. During experiments with EG-water droplets in ethanol vapour (which dissipated) there was EG-water like, then EG-ethanol like flow with corresponding migration to the apex and then the centre of the droplet. Therefore the above series of particle preference was not violated.

For the involatile solutes chosen for experiments, the sugars sucrose and lactose, and the salts sodium chloride, sodium nitrate and ammonium sulfate any migration was towards the centre of the droplet. For the salts this makes intuitive sense. The particles were sterically-stabilised so would experience an entropic penalty at high salt concentrations as the polymer chains attached to the particle surface would reduce in extension to minimise unfavourable interactions with the fluid. In regards to sugar droplets the fact that particles (outside the collected group and away from the contact line) appeared to move towards lower solute concentrations after the end of Marangoni flows (see last two frames in Figure 5.12 for a sucrose droplet) is also a supportive piece of evidence for a diffusiophoretic mechanism.

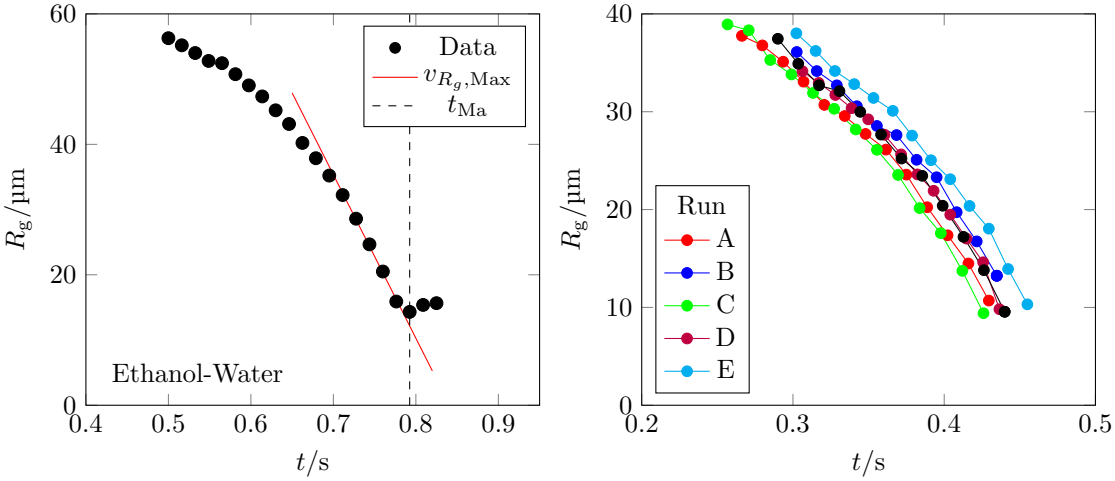

Figure 7.4: Characteristic shape of the change in R_g with time: the radius reaches a minimum as the solutal Marangoni flows end. The gradient of this curve, v_{R_g} reaches it's maximum value at the same time. The right plot shows the reproducibility of this shape in consecutive ethanol-water droplet experiments on Decon-cleaned substrates, $RH \approx 40\%$.

7.3.2 Measuring the Migration

The method discussed in Section 2.6 to find the radius of the collected group over time was used to quantify the speed of migration towards the centre of a droplet. This measure was useful as it did not appear to vary over the range of low particle concentrations used in experiments; however it was not applicable when the particles migrated to form a raft. In these cases the lack of recirculation meant particles stayed along the interface. Therefore the migration was parallel to the flow at the interface so it was not possible to separate flow and migration velocities. The radius of the raft was also strongly particle concentration dependent as high packing fractions could be achieved, making comparisons across experiments inconsistent.

Figure 7.4 shows the radius of the collected group over time in some ethanol-water droplets. The shape shown with the radius decreasing more quickly towards the end of the solutal Marangoni flows was characteristic and reasonably reproducible (see migration in five consecutive droplets in right-hand plot of Figure

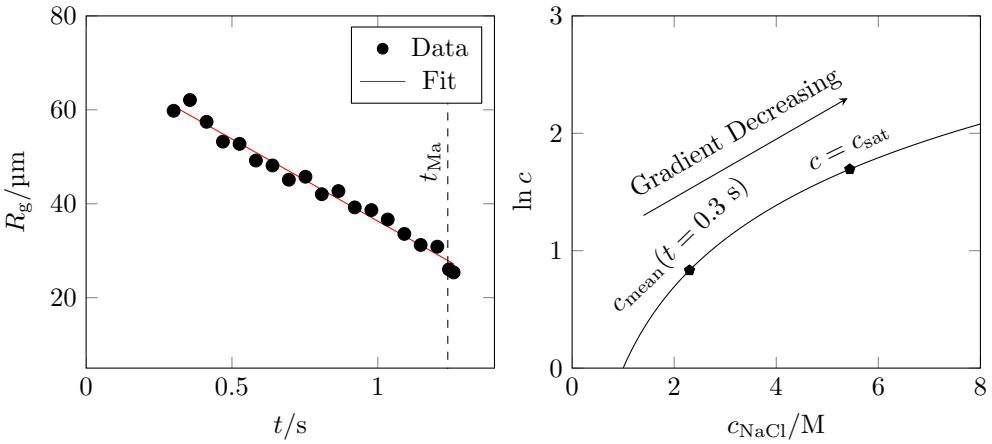

Figure 7.5: Approximately linear decrease in collected group radius for the NaCl droplet from Figure 6.26. The right hand plot shows the functional form of $\ln c$ from which a slow down in migration as the solute accumulated and the gradient of $\ln c$ decreased was predicted.

7.4) for this binary mixture on Decon-cleaned or HMDS-treated substrates.

According to Equation 7.3 the migration velocity is proportional to the gradient of natural logarithm of the mole fraction of solute. This gradient of the natural logarithm is greatest as the mole fraction approaches zero (although at some point the model is expected to break down as otherwise the presence of a single molecule would lead to implausibly large velocities); therefore in experiments where the ethanol is preferentially evaporating the lower ethanol mole fraction towards the end of the solutal Marangoni flows was expected to lead to faster migration. The exact logarithmic dependence was not verified in my results but the speeding up of particle migration as the ethanol concentration decreased was observed.

In the reverse case with migration towards the apex for water or ethanol-water droplets in ethanol vapour Equation 7.3 would predict that droplets without ethanol at the start were expected to have larger concentration gradients and so faster migration. The experiments did not corroborate this prediction although in experiments with ethanol vapour the migration did appear fastest at the beginning of evaporation.

For involatile solutes the concentration would instead increase over time so as

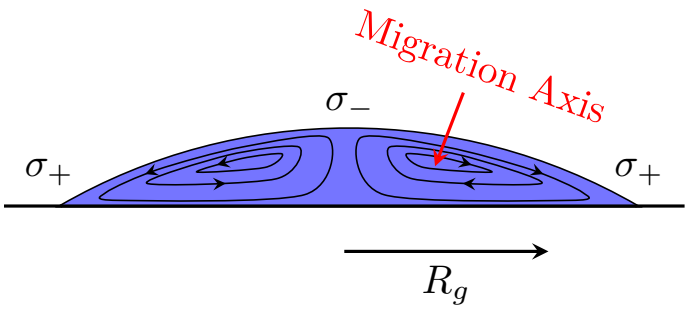

Figure 7.6: Measured collected group radius and the proposed axis (red) along which particles would experience the greatest concentration gradient and so fastest migration for a thin droplet with solutal Marangoni flows arising from having a higher surface tension towards the contact line than the apex.

$\ln c$ changes less at higher c, slower migration was expected towards the end of Marangoni flows. However this prediction was not fulfilled: while the migration in NaCl droplets on HMDS-treated substrates was different to ethanol-water droplets, with R_g linearly decreasing (see left-hnd plot of Figure 7.5), sucrose showed the same characteristic shape as ethanol-water droplets. The curvature in $R_g(t)$ for both ethanol-water mixtures and sucrose solutions persisted, although reduced, on HMDS-substrates so the choice of substrate was not the entire cause of the difference for NaCl droplets. (However the sample size for NaCl was much lower, see fewer marks for NaCl in Figure E.1.) A cause for the lack of quantitative agreement might be that $\nabla \ln c$ is subject to the effective distance between the quiescent region and the interface, in turn dependent on the shape of the evaporating droplet which is important as the droplets for the NaCl results had larger contact angles.

The actual velocity of retraction of the collected group can be quite large, up to about a tenth of the actual flow velocities for the three systems studied so that v_{R_g} could be tens or hundreds of $\mu m\,s^{-1}$, much larger than the $u_{DP} = 1$ or $2\ \mu m\,s^{-1}$ common in the literature. This suggests that the axis taken in the above analysis is incorrect, illustrated by the cartoon in Figure 7.6. Migration approximately

perpendicular to (away from) the interface, where the flow streamlines are most tightly packed with the highest local concentration gradient, could lead to a small migration velocity resulting in large changes in R_g once a particle is carried to the position furthest from the apex along a streamline. However this effect is not large enough to fully explain measuring migration velocities being 100 times those typically found; taking the cartoon for a rough estimate, the aspect ratio of a Marangoni loop might reach a value of 10, which is far off from accounting for the difference in magnitude.

7.4 Challenges for Diffusiophoresis

While diffusiophoresis qualitatively fits as a possible mechanism for the migration the evidence is insufficient to make a definitive conclusion. Therefore it is worth considering where there are problems in considering diffusiophoresis.

One issue with confidently attributing the migration in these experiments to diffusiophoresis is how the radius of the collected group changes in different situations. I previously discussed how the characteristic shape was the same for ethanol-water mixtures and sucrose solutions despite the solute concentration decreasing in one and increasing in the other and so changing $\nabla \ln x$ from Equation 7.3 in different ways over time. This weak match to the diffusiophoresis explanation opens the possibility of the flows being involved in the migration even if a shear-induced mechanism is unable to account for the switch in migration direction.

It is also hard to argue for a diffusiophoretic mechanism because the actual interaction between the particles and an ethanol concentration gradient is unclear. We would be unable to predict which way our particles would migrate in a new neutral solute without experiments.

However the primary challenge to embracing a diffusiophoretic mechanism is

that the end migration location appears correlated to the direction of flow in the droplets. Where there were solutal Marangoni flows from the contact line to the apex migration was towards the apex and contact line; when the flows went from the apex to the contact line migration was towards the centre. In a diffusiophoretic mechanism the particles will move according to the concentration gradient and so should be independent of the Marangoni flow direction. Therefore while this point does not contradict a diffusiophoretic mechanism, the diffusiophoresis explanation would be more compelling if I found an example of migration in droplets with particles moving to the centre with flows from the contact line to the apex, or migration to the interface with flows from the apex to the contact line. Appendix E includes details on the experiments attempted to address this problem although none were satisfactory.

7.5 Conclusions and Future Directions

In summary across the different systems studied where there was solutal Marangoni flow we also observed particle migration. In Case A (see Figure 7.3) when flows were from the contact line to the apex along the liquid-vapour interface, e.g. EG-water or water in ethanol vapour droplet systems, migration resulted in particle rafts forming at the apex. In Case B when flows were from the contact line to the apex along the liquid-vapour interface, e.g. ethanol-water or salt droplet systems, migration resulted in particle migration away from the liquid-vapour interface.

While it is possible that migration and flow are coupled we suggest that the concentration gradients within the droplet are what drive the migration, rather than the flows caused by the concentration gradient along the liquid-vapour interface, meaning that the migration should be independent of the flow direction. This diffusiophoretic migration in response to concentration gradients

across the particle fits better than other mechanisms assessed such as buoyancy-driven migration, thermophoresis, or shear-induced migration (which is unable to explain migration to the apex as the low shear region does not change with flow direction).

Unsuccessful attempts to study the migration of these particles without there being Marangoni flows in cuvettes and capillaries, and difficulties in quantitatively matching my migration velocities in droplets to the scaling from diffusiophoretic theory mean that there are challenges to overcome to conclusively demonstrate that this mechanism is correct.

The argument would be much more convincing if the migration and flow directions were clearly decoupled. Therefore further work is required to find a system where there are new combinations of particle migration direction and solutal Marangoni flow direction by studying new formulations and/or using differently functionalised tracer particles.

It would also be very valuable to use microfluidic devices to quantitatively investigate the particle migration outside of droplet geometries or the presence of solutal Marangoni flows. Data from experiments tailoring the magnitude of the concentration gradient driving particle migration to that present during droplet experiments could also provide powerful evidence for diffusiophoretic migration.

Assuming a diffusiophoretic migration mechanism there is little value in trying to study the effect in microlitre drops where OCT could be used to view particle migration from the side. The migration is driven by the concentration gradient across the interaction lengthscale of the particle. Therefore taking an example 2% concentration difference between the apex and substrate, for a larger drop the distance between these locations is larger so the concentration difference per unit distance and so across a particle lengthscale will be smaller and harder to measure.

Chapter 8

Summary and Future Work

In this final Chapter I summarise the results presented in this thesis, drawing attention to the most interesting points before discussing avenues for future experiments to build on the work presented here.

8.1 Final Summary

It is useful to consider three broad categories to help provide structure when discussing the results:

- Evaporation behaviour and how effectively my volume-averaged multicomponent model based on Popov's equations can describe the evaporation,
- Flow behaviour, whether solutal Marangoni flows were present and if so how fast they were and in which direction they acted,
- The deposit structure of particles (including the effect of particle migration) or salt crystals after the end of drying.

These categories are across solvent mixture droplets made up of combinations of water, ethanol and ethylene glycol with and without ethanol vapour, and solute droplets of sucrose and lactose or the crystallising salts sodium chloride, sodium nitrate or ammonium sulfate.

These categories reflect our aim starting out to learn more about how to control the deposits from inkjet-printed droplets from an understanding of the evaporation process and resulting internal flows.

8.2 Performance of the Model

I developed a volume-averaged model (described in Section 2.9) where each volatile component would evaporate according to its own set of mass loss equations with the activities set by the mean fluid composition. Where the model worked well it could be used to make useful predictions while the breakdown of the model was also useful in assessing the non-uniformity of droplet composition during drying through the divergence between this simple model and experiment.

I found the model fitted the evaporation of ethanol-water droplets well, showing that there was significant mixing from solutal Maranongi flow. The condensation of ethanol onto water or ethanol-water droplets in experiments with ethanol vapour could be qualitatively accounted for in the model. To obtain a quantitative match with experiment the mixed-mode contact angle dynamics need further refinement. For ethylene glycol mixtures (where the EG was assumed to be fully involatile) the modelled droplets evaporated much more than their experimental counterparts at late times, indicating the presence of an EG enriched, viscous, layer that suppressed further evaporation by reducing the local water activity at the interface and hindering the diffusion of water to the interface.

Similar to the EG-water mixtures, modelled droplets containing sugars evaporated much more than in their experimental counterparts at late times. In this case the ”fixing” of tracer particles is strong evidence of the droplet reaching a glassy state. At this point the sugar concentration and viscosity would be high which would suppress the diffusion of water to the interface and the water activity at the interface.

For salt droplets the model could qualitatively predict that the evaporation rate would continuously decrease in response to higher salt concentrations reducing the water activity. However the model performed poorly quantitively, consistently overestimating the evaporation rate even at early times. The model was also unable to account for crystallisation.

8.3 Internal Flows

It is well established that the evaporative flux across a non-hemispherical sessile droplet is uneven. In droplets containing more than one component, each with different volatilities, the non-uniform evaporative flux can generate surface tension gradients across the interface which drove solutal Marangoni flows for all the mixtures studied in this thesis (under certain conditions).

The directions and magnitudes of flow are given in Table 8.1. When the surface tension at the contact line was greater than at the apex (as a result of preferential evaporation of the lower surface tension component, or greater solute concentration) flows went from the apex to the contact line and there was particle migration to the centre of the droplet. When the surface tension at the contact line was lower than at the apex then any Marangoni flows were reversed. It is worth emphasising that the fastest particle velocities were all on plasma-cleaned substrates and that these are all the radial component of a velocity so actual velocities could be even larger.

Among the solvent mixture droplets Marangoni flows were readily observed as the surface tension gradients were large, the exception being at high ethylene glycol concentrations where there was very little evaporation within a 10 second experimental window. In contrast to solvent mixtures, in sugar droplets the flows started later into drying as it took time for a concentration gradient sufficient to drive solutal Marangoni flow to develop. This was because the surface tension of

Table 8.1: Summary of solutal Marangoni flow directions and approximate range of the magnitude of flow velocities in the droplet systems studied, directions of Marangoni flow along the liquid-vapour interface: AC - apex to contact line, CA - contact line to apex. The three component solvent droplets have two flow stages: S1 and S2. EG-Water S2 has "N?" for for whether there is ethanol vapour as we suggested that there should only be one stage if the ethanol vapour did not dissipate.

Droplet Fluid	EtOH Vapour?	Direction	$\lvert v_r \rvert$ /µm s^{-1}	Migration to
Ethanol-Water	-	AC	1000-3000	Centre
Water	Y	CA	150-300	Apex
Ethanol-Water	Y	CA	200-600	Apex
EG-Water	-	CA	150-300	Apex
EG-Ethanol	-	AC	600-2000	Centre
EG-Water S1	Y	AC	100-300	Centre
EG-Water S2	N?	CA	200-500	Apex
EG-EtOH - H_2O S1	-	CA	600-1200	Apex
EG-EtOH - H_2O S2	-	AC	300-500	Centre
Sucrose	-	AC	200-500	Centre
Lactose	-	AC	200-800	Centre
Sodium Chloride	-	AC	100-1200	Centre
Sodium Nitrate	-	AC	200-800	Centre
Ammonium Sulfate	-	AC	200-1600	Centre

the fluid was much less strongly dependent on the concentration of sugar.

The Marangoni flows in salt droplets were more subtle and if there were going to be flows they started quickly, however they could be very weak and end quickly too. Sodium chloride droplets required the most fine tuning of experimental conditions to see strong Marangoni flows and required high energy substrates or combinations of low relative humidity and high solute concentration. Otherwise the flows appeared weaker or not at all. Despite these limitations I found with low NaCl concentrations on plasma-cleaned substrates that Marangoni flows could still be observed down to concentrations of around 100 mM.

The other salts studied, sodium nitrate and ammonium sulfate, increase surface tension more quickly with increasing salt concentration (than NaCl) so those droplets exhibited solutal Marangoni flow a little more readily. Despite this, on HMDS-treated substrates there were examples for all three salts of "jerky"

motion: when there was weak solutal Marangoni flow the observed recirculation could pause, in this time interval the surface tension gradient would build up again due to evaporation across the droplet interface which would then restart the Marangoni flow. This could happen just once, sometimes without a single restart, or repeatedly. This type of Marangoni flow has not been previously reported.

The end of solutal Marangoni flows was related to transitions in the evaporative dynamics. In an ethanol-water system this was when most the ethanol had evaporated. In EG (-water or -ethanol), and sugar droplets, the flows ended once a layer of involatile-component rich fluid built up at the interface that suppressed evaporation of the more volatile component by increasing the local viscosity and hindering transport of volatile molecules to the interface. For salt droplets the end time of the flows was often unclear as the evaporation-driven solutal Marangoni flows got disrupted by the nucleation of salt crystals which induced much larger, asymmetric, surface tension gradients by taking in the local salt ions to grow.

8.4 Deposition from Droplets

Particle migration meant the (Marangoni) flows themselves had less control over the deposition of particles than anticipated. We suggest that this migration is independent of the flows and is diffusiophoretic in nature in response to concentration gradients within the droplet. This proposed mechanism fits better than the others considered including: buoyancy-driven migration, thermophoresis, or shear-induced migration (which is unable to explain migration to the apex as the low shear region does not change with flow direction).

In the literature researchers have frequently designed solutal Marangoni flows to keep particles distributed throughout the droplet to prevent a ring stain forming although migration disrupted this process. For example ethanol-water droplets frequently displayed partial ring deposits where outward convective flow would

unevenly pull apart the collected group of particles in the centre of the droplet (following migration there), these rings would be deposited along wherever the contact line was at late times. The deposition from droplet systems in ethanol vapour was in a pattern with a ring stain, with most the particles in a central raft which typically fractured and moved off-centre in the final milliseconds before complete evaporation of the droplet.

In sugar droplets particle migration meant that the particles were collected in the centre of the droplet. The increase in viscosity by orders of magnitude with drying of the droplets meant that this distribution was effectively ”set” in that position. Therefore the addition of sugars is a new mechanism to allow for the control of particle deposits, where sugar concentrations can be tuned to fix particles in a group at the centre of the droplet.

In salt deposits the particles would get redistributed by the Marangoni flows following nucleation. Therefore within the category of deposition from the droplets we were primarily interested in the structure of the crystals. The high salt supersaturations reached during drying meant that following nucleation crystals could grow rapidly due to a high surrounding concentration of salt ions. For sodium chloride droplets this meant that the deposited crystals were microcrystalline as there was growth from multiple sites on a crystal; well ordered cubic layers would only develop as the droplet nearly finished evaporating when crystal growth was slowed down by the limited availability of ions. Within sodium chloride droplets there were often multiple nucleation sites so that multiple, separate, crystals would be deposited. On HMDS-treated substrates these crystals would all get pulled towards the centre of the droplet by the retreating contact line. Examples of typical NaCl deposits can be seen in Figure 7.3 where it is clear that the deposits on different substrates are quite similar.

The other salts studied, sodium nitrate and ammonium sulfate, had differing crystal habits and so crystallised into different forms and had distinct structures

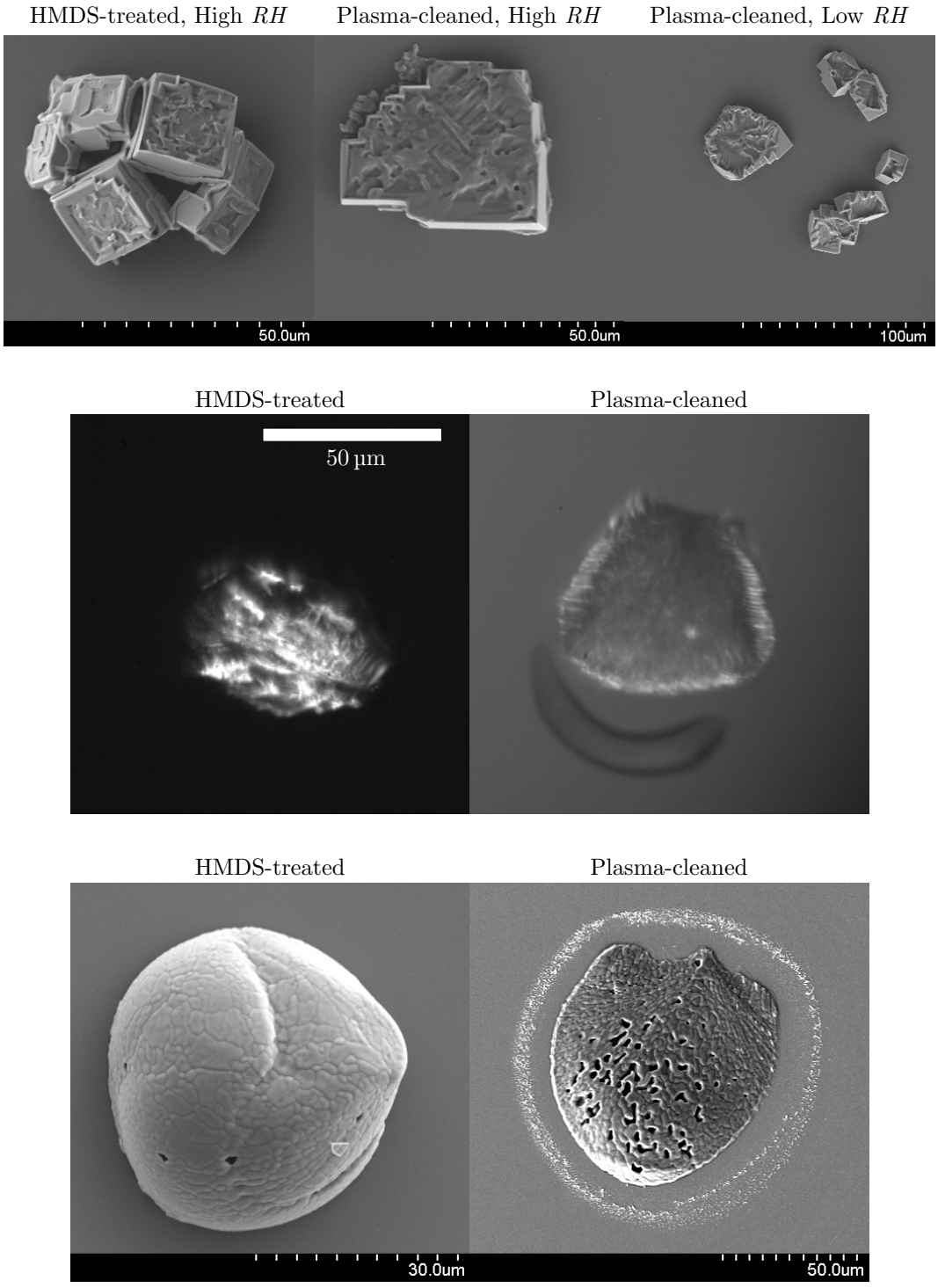

Figure 8.1: Reproduction of salt deposits on differently prepared substrates from Chapter 6. Top row: NaCl $RH = 2 \pm 4\%$ or $35 \pm 2\%$. Middle row: $NaNO_3$ $RH = 28 \pm 2\%$. Bottom row: AMS $RH = 34 \pm 2\%$.

depending on the substrate wettability. On HMDS-treated substrates a long crystal of sodium nitrate would nucleate away from the contact line and grow to reach opposite sides of the droplet before growing more slowly near perpendicular to the main growth axis. On plasma-cleaned substrates the crystal would nucleate from the contact line and grow in all directions, leaving a much flatter, wider crystal. Examples of typical $NaNO_3$ deposits (previously shown in Chapter 6) can be seen in Figure 7.3.

Crystal deposits from ammonium sulfate droplets also showed different structures. On HMDS-treated substrates it was difficult to notice that nucleation had occurred from side-view videos as the crystal had the same shape as the droplet. The AMS crystal would grow from one point near the contact line to completely cover the liquid-vapour interface and the entire droplet footprint. As a result the crystal is likely hollow as there would still have been some fluid remaining just after nucleation. On plasma-cleaned substrates AMS crystals would also grow to cover the entire droplet footprint, being thicker at the side of the droplet opposite to the nucleation location. SEM also showed that these deposits were also surrounded by rings of microcrystallites. Examples of typical AMS deposits can be seen in Figure 7.3.

In systematic studies varying the relative humidity I found that there was little difference in the crystal structures with RH, except that more nucleation events occurred in NaCl droplets at low RH. This was likely because there was only a small window of relative humidities in which nucleation was possible. My experiments provide the first evidence of aerosol-like behaviour in sessile droplets: sodium chloride and ammonium sulfate would not crystallise above the so-called efflorescence relative humidity (48% for NaCl and 40% for AMS) and would instead persist without crystallising despite the concentration being above the saturation concentration. Compared to aerosol literature values these measured ERH's are slightly higher, we suggest this increase is a result of heterogeneous nucleation at

the substrate. Sodium nitrate droplets did not have a well-defined *ERH* which is consistent with results in the literature that there is some probability $NaNO_3$ droplets will not crystallise even at low relative humidities.

8.5 Reflectometry

One of the parts of this thesis with the greatest future potential was the development of a novel experimental setup that applied reflectometry to measure the evolving composition of an evaporating droplet. Ethanol-water droplets with a range of concentrations were printed onto a silica hemisphere of known refractive index; as the ethanol preferentially evaporated, the refractive index difference between the fluid and substrate changed so with the fluid's refractive index's dependence on the ethanol concentration known, that concentration could be extracted by applying Fresnel's Equations. This composition data is very valuable as it is necessary to corroborate models yet such experimental data is sparse in the literature.

A strength of this experiment was that the same droplet would be measured throughout its lifetime (instead of taking measurements from reproducibly printed droplets after different time delays) while the droplets involved are also orders of magnitude smaller than other methods in the literature. However there are limits to when good signals could be obtained towards the end of drying with the cause of my so-called "anomalies" currently unclear.

Reflectometry experiments on ethanol-water binary droplets quantified the residue of ethanol remaining at the end of solutal Marangoni flows and into late stages of drying. This residue was near the substrate as the technique measured the concentration in this region rather than the bulk concentration. This work corroborates Chen *et al.*'s observation of a residue of ethanol persisting after the end of solutal Marangoni flows.[105]

8.6 Future Work

One of the strengths of this thesis is how different systems have been studied and analysed in a systematic way. Therefore there are natural avenues to expand this approach by simply studying more formulations with new solvents and solutes and finding new combinations (for example adding two different salts to the same droplet to see changes in efflorescence behaviour). This would have added benefits in maybe stumbling across a system with new particle migration behaviour to help inform our discussion of the proposed diffusiophoretic mechanism. It would also be valuable for the experiments with salts if a salt with multiple polymorphs was studied in which case different drying conditions could have a greater impact on the resulting deposit. More complex mixtures could involve systems where not all the components were fully miscible so that phase separation could be observed. Experiments with environments enriched in the vapour of solvents other than ethanol could also play a part to add complexity and work towards the number of components that are present in actual inkjet formulations.

A lot of valuable experiments can come from the reflectometry equipment developed in this thesis as so far the technique has only been applied to ethanol-water droplets. One obstacle here is that more work needs to be done to understand the origin of the "anomalies" where the reflectance increased towards the end of evaporation in a way inconsistent with changes in composition (and so refractive index) or laser-heating. Different hemispheres will also be required as solute mixtures, such as sucrose, that higher refractive indices, which would limit the sensitivity of the current apparatus.

There are a number of possible improvements that could be made to improve the function of the reflectometry rig or add features. These include obtaining a PMT with a faster response, setting up additional cameras to view the droplets during evaporation, or moving to using prisms as the substrate rather than hemispheres (so that the same position does not need to be repeatedly printed on).

The next generation of this technique could also involve mapping of the concentrations across a droplet rather than taking the average across a spot by having the reflected beam land across a charge-coupled device.

The reflectometry work showed that inkjet-printed droplets can have inconsistent starting concentrations if the delay between droplets being printed is not strongly controlled. While the general method kept this to less than a second this could be improved upon, especially seeing the scatter in figures throughout the thesis (for example in the volumes at the end of Marangoni flow in ethanol-water droplets in Figure 4.9 or supersaturations of NaCl at nucleation in Figure 6.11). Therefore a very worthwhile improvement would be to develop a more automated system to print droplets. This might involve using LabView to move the arm holding the nozzle away, print a droplet, and then move the nozzle back into location. Other direct improvements to the rig could include the incorporation of a second nozzle near the first, this could allow experiments on coalescence and droplet interactions, for instance the presence of satellite droplets seemed important to whether there were Marangoni flows in some salt droplets and a second nozzle could quantify the distance over which such effects were important. A second nozzle would also have been useful in the experiments with ethanol vapour as it could have held pure ethanol to print and so make it easier to calibrate the concentration of ethanol in the environment between experiments as the main nozzle's fluid would not require replacing.

The current volume-averaged model is useful but could be improved further. Future work on this topic could include reworking the assumptions used when calculating the change of contact angle as a function of droplet composition during mixed modes in which the contact radius and angle both decreased. Experiments also showed that ethylene glycol is not totally involatile and the small volumes of inkjet-printed droplets means that such droplets can evaporate in minutes rather than hours or days. As a result it could be fruitful to run further experiments to

collect data that could be used by the model to get derive predictions of the vapour pressure of ethylene glycol enriched fluids. The complexity required to develop a (finite element) model to handle non-uniform composition within the droplet means that it is difficult to develop if a researcher is not specialised in modelling so it may be more efficient to collaborate with the experienced modellers in the field who have already been working on such problems. A different improvement to the model could be to integrate Classical Nucleation Theory and make predictions on when there would be crystallisation from the droplet.

In order to properly attribute the particle migration observed to diffusiophoresis, experiments with microfluidic devices are needed to test the migration of particles without any Marangoni flow. It would also be good to continue searching for a system with new combinations of flow and migration direction, for example migration to the apex with flows from the apex to the contact line as in ethanol-water mixtures (rather than the reverse as in EG-water mixture droplets).

My attempt to determine the theoretical Marangoni number at the end of the experimental Marangoni flows using reflectometry data for ethanol-water mixtures means that I do not think the number is useful for evaporating droplets and should be reworked by theoreticians as it consistently overestimates experimental flow velocities. In my opinion the idea that the concentration gradient is destroyed by diffusion (i.e. D is in the denominator in Equation 1.22) does not seem effective, the destruction of the concentration gradient arises from the motion of the surface as a result of the flows compared to how quickly the concentration gradient is generated by evaporation. This appears more obvious in inkjet-printed droplets where the shorter timescales involved, due to the smaller volumes, mean that diffusion is too slow to be relevant. An interesting system that could be of use here are the salt droplets on HMDS-treated substrates were there was sometimes "jerky" motion as the flows temporarily paused, meaning that these systems are close to the edge-case of when flows are present.

Appendix A

Optics Derivations

A.1 Laws of Optics

Electromagnetic radiation can be described by orthogonally propagating electric, **E**, and magnetic, **B**, fields while each **E** or **B** field can be described as the superposition of two orthogonal polarisations in which the plane of propagation is unchanged with time. Therefore we can consider linearly polarised, monochromatic light with no loss of generality. For light of wavelength, λ, the **E** field in complex notation ($i = \sqrt{-1}$) is

$$\mathbf{E} = \mathbf{E}_0 \exp[i(\mathbf{k} \cdot \mathbf{r} - \omega t)] \tag{A.1}$$

or more simply

$$\mathbf{E} = \mathbf{E}_0 \cos(\mathbf{k} \cdot \mathbf{r} - \omega_i t). \tag{A.2}$$

where ω_i is the angular frequency of the incident wave

$$\omega = \frac{2\pi}{T}, \tag{A.3}$$

and T is the time period of the oscillation is defined by

$$T = \frac{\lambda}{v}. \tag{A.4}$$

The wavevector, **k**, of the propagating light has the direction direction $\hat{\mathbf{k}}$

$$\mathbf{k} = \frac{2\pi}{\lambda}\hat{\mathbf{k}}, \tag{A.5}$$

while **r** is the position vector in terms of the unit vectors of the (Cartesian) coordinate system and $\mathbf{E}_0$ is the amplitude of the oscillation.

If this light hits an interface between two homogeneous, lossless dielectric materials of refractive indices n_i and n_t we can describe the reflected and transmitted light, while making no assumptions of the origin in time or space, amplitudes, frequencies, directions wavelengths or phases as

$$\mathbf{E}_r = \mathbf{E}_{0r} \cos(\mathbf{k} \cdot \mathbf{r} - \omega_r t + \phi_r) \tag{A.6}$$

$$\mathbf{E}_t = \mathbf{E}_{0t} \cos(\mathbf{k} \cdot \mathbf{r} - \omega_t t + \phi_t). \tag{A.7}$$

Here ϕ_r and ϕ_t are phase constants relative to $\mathbf{E}_i$ introduced because the position of the origin is not unique.

The laws of Electomagnetism define boundary conditions for this problem such that the component of the $\mathbf{E}$ field which is tangential to the interface must be continuous. Following from this the total tangential component of incident and reflected $\mathbf{E}$ fields must equal that of the transmitted $\mathbf{E}$ field on the other side of the interface. Thus, introducing $\hat{\mathbf{u}}$ as the unit vector normal to the interface

$$\hat{\mathbf{u}} \times \mathbf{E}_i + \hat{\mathbf{u}} \times \mathbf{E}_r = \hat{\mathbf{u}} \times \mathbf{E}_t. \tag{A.8}$$

This must hold at all points along the interface, therefore the three waves must share the same dependence across terms with a dependence on time or space

$$\omega_i = \omega_r = \omega_t \tag{A.9}$$

$$\mathbf{k}_i \cdot \mathbf{r} = \mathbf{k}_r \cdot \mathbf{r} + \phi_r = \mathbf{k}_t \cdot \mathbf{r} + \phi_t \tag{A.10}$$

Rearranging Equation A.10 we find

$$(\mathbf{k}_i - \mathbf{k}_r) \cdot \mathbf{r} = \phi_r \tag{A.11}$$

$$(\mathbf{k}_i - \mathbf{k}_t) \cdot \mathbf{r} = \phi_t \tag{A.12}$$

As the dot products do not equal zero that means that the pairs of vectors define a plane, i.e. the end of $\mathbf{r}$ sweeps out a plane perpendicular to $(\mathbf{k}_i - \mathbf{k}_r)$ which is the interface. Therefore these vectors must be parallel to our interface unit vector

$$(\mathbf{k}_i - \mathbf{k}_r) \times \hat{\mathbf{u}} = (\mathbf{k}_i - \mathbf{k}_t) \times \hat{\mathbf{u}} = 0 \tag{A.13}$$

Both the incident and reflected light exist in the same medium, therefore they have the same refractive index, speed, wavelength and hence magnitude of wave

vector

$$k_i = k_r \tag{A.14}$$

Therefore given the definition of the cross product of vectors **a** and **b**

$$\mathbf{a} \times \mathbf{b} = ab \sin\theta \tag{A.15}$$

where a and b are the magnitudes and θ is the angle between the two vectors, and Equation A.13 we find

$$k_i \sin\theta_i = k_r \sin\theta_r. \tag{A.16}$$

Hence we have the Law of Reflection

$$\theta_i = \theta_r. \tag{A.17}$$

By the same approach but without being able to cancel the wavevectors due to the light being in different optical media we find

$$k_i \sin\theta_i = k_t \sin\theta_t. \tag{A.18}$$

which accounting for the fact $\omega_i = \omega_t = \omega$ we can multiply both sides by c/ω to obtain Snell's Law

$$n_i \sin\theta_i = n_t \sin\theta_t. \tag{A.19}$$

A.2 The Fresnel Equations

The above analysis determined the interdependence of $\mathbf{E}_i, \mathbf{E}_r$ and $\mathbf{E}_t$. In what follows the magnitudes $\mathbf{E}_{0i}, \mathbf{E}_{0r}$ and $\mathbf{E}_{0t}$ will be determined although such analysis will be dependent on the polarisation relative to the interface.

s-polarised Light

E is perpendicular to the plane of incidence, therefore **B** is parallel such that

$$\hat{\mathbf{k}} \times \mathbf{E} = v\mathbf{B} \tag{A.20}$$

$$\hat{\mathbf{k}} \cdot \mathbf{E} = 0 \tag{A.21}$$

and the three vectors form a right-handed system. As before we can make use of the boundary conditions such that the tangential component of the **E** field is

continuous across the interface so after cancelling the cosine terms and taking our origin such that the phase constants ϵ_r and ϵ_t disappear

$$\mathbf{E}_{0i} + \mathbf{E}_{0r} = \mathbf{E}_{0t}. \tag{A.22}$$

We now need to apply a further boundary condition, namely that the normal component of the **B** field is continuous across the interface, as is the tangential component of the Magnetic Field Strength, **H**, defined as

$$\mathbf{H} = \frac{\mathbf{B}}{\mu} \tag{A.23}$$

where μ is the magnetic permeability of the medium. This last condition requires that

$$-\frac{B_i}{\mu_i}\cos\theta_i + \frac{B_r}{\mu_i}\cos\theta_r = -\frac{B_t}{\mu_t}\cos\theta_t \tag{A.24}$$

Rearranging and using Equations 3.3, A.20 and that the velocities will be the same on the same side of the interface we obtain

$$\frac{1}{\mu_i v_i}(E_i - E_r)\cos\theta_i = \frac{1}{\mu_t v_t}E_t\cos\theta_t. \tag{A.25}$$

Expanding E_i, E_r and E_t in terms of their cosine forms (Equation A.2), noting that the terms inside the cosines will be the same at the interface and can thus be cancelled and multiplying by c gives

$$\frac{n_i}{\mu_i}(E_{0i} - E_{0r})\cos\theta_i = \frac{n_t}{\mu_t}E_{0t}\cos\theta_t. \tag{A.26}$$

Combining with Equation A.22 and substituting for E_{0t} or E_{0r} we find

$$\left(\frac{E_{0r}}{E_{0i}}\right)_s = \frac{\frac{n_i}{\mu_i}\cos\theta_i - \frac{n_t}{\mu_t}\cos\theta_t}{\frac{n_i}{\mu_i}\cos\theta_i + \frac{n_t}{\mu_t}\cos\theta_t} \tag{A.27}$$

$$\left(\frac{E_{0t}}{E_{0i}}\right)_s = \frac{\frac{2n_i}{\mu_i}\cos\theta_i}{\frac{n_i}{\mu_i}\cos\theta_i + \frac{n_t}{\mu_t}\cos\theta_t}. \tag{A.28}$$

For dielectric materials $\mu_i \approx \mu_t \approx \mu_0$ so these equations are typically reduced to give the amplitude reflection and transmission coefficients for s-polarised light.

$$r_s = \frac{n_i\cos\theta_i - n_t\cos\theta_t}{n_i\cos\theta_i + n_t\cos\theta_t} \tag{A.29}$$

$$t_s = \frac{2n_i\cos\theta_i}{n_i\cos\theta_i + n_t\cos\theta_t}. \tag{A.30}$$

p-polarised Light

In order to determine the amplitude coefficients for p-polarised Light we need to apply the boundary conditions that the tangential components of the **E** and **H** fields are continuous so we find in contrast to Equation A.22 that

$$E_{0i}\cos\theta_i - E_{0r}\cos\theta_r = E_{0t}\cos\theta_t, \tag{A.31}$$

while the continuity of **H** leads to

$$\frac{1}{\mu_i v_i}E_{0i} + \frac{1}{\mu_r v_r}E_{0r} = \frac{1}{\mu_t v_t}E_t, \tag{A.32}$$

$$\frac{n_i}{\mu_i}(E_{0i} + E_{0r}) = \frac{n_t}{\mu_t}E_t. \tag{A.33}$$

As above either E_{0t} or E_{0r} can be substituted for by rearranging Equation A.31 to give

$$\left(\frac{E_{0r}}{E_{0i}}\right)_p = \frac{\frac{n_t}{\mu_t}\cos\theta_i - \frac{n_i}{\mu_i}\cos\theta_t}{\frac{n_i}{\mu_i}\cos\theta_i + \frac{n_t}{\mu_t}\cos\theta_t} \tag{A.34}$$

$$\left(\frac{E_{0t}}{E_{0i}}\right)_p = \frac{\frac{2n_i}{\mu_i}\cos\theta_i}{\frac{n_t}{\mu_t}\cos\theta_i + \frac{n_i}{\mu_i}\cos\theta_t}. \tag{A.35}$$

Which for dielectric materials are reduced to the amplitude reflection and transmission coefficients for p-polarised light.

$$r_p = \frac{n_t\cos\theta_i - n_i\cos\theta_t}{n_t\cos\theta_i + n_i\cos\theta_t} \tag{A.36}$$

$$t_p = \frac{2n_i\cos\theta_i}{n_t\cos\theta_i + n_i\cos\theta_t}. \tag{A.37}$$

While r_s is always positive, r_p starts negative and go goes through zero. This leads to the existence of the Brewster angle where the amplitude of one of the components goes to zero leading to polarised reflections.

A.3 Reflectance

If we imagine a circular beam of light incident on a surface, the power per unit area hitting the surface in a vacuum is described by the Poynting Vector

$$\mathbf{S} = c^2\epsilon_0\mathbf{E}\times\mathbf{B} \tag{A.38}$$

with a flux density (W/m^2) of

$$I = \langle S \rangle = \frac{c\epsilon_0}{2} E_0^2. \tag{A.39}$$

If the beam of light is not in a vacuum

$$I = \frac{v\epsilon_r\epsilon_0}{2} E_0^2 \tag{A.40}$$

where ϵ_r is the relative permittivity of the dielectric medium and is simply a factor if the material is homogeneous.

The beam of light is incident at an angle so if A is the original cross-sectional area, $A\cos\theta_i$ will be the cross-sectional area of the incident beam while the cross-sectional areas of the reflected and transmitted beams respectively will be $A\cos\theta_r$ and $A\cos\theta_t$.

Following from this we can introduce the reflectance, R, as the ratio of reflected to incident power

$$R = \frac{I_r A\cos\theta_r}{I_i A\cos\theta_i} = \frac{I_r}{I_i} \tag{A.41}$$

while the transmittance, T, is defined as the ratio of the transmitted to incident power

$$T = \frac{I_t\cos\theta_t}{I_i\cos\theta_i}. \tag{A.42}$$

For the reflectance each intensity term can be substituted using Equation A.40, taking into account that the incident and reflected light are in the same medium

$$R = \frac{\frac{v_r\epsilon_{rr}\epsilon_0}{2} E_{0r}^2}{\frac{v_i\epsilon_{ri}\epsilon_0}{2} E_{0i}^2} = \left(\frac{E_{0r}}{E_{0i}}\right)^2 = r^2. \tag{A.43}$$

Similarly the transmittance can be determined with simplification from Equation 3.1 to be

$$T = \frac{n_t\cos\theta_t}{n_i\cos\theta_i}\left(\frac{E_{0t}}{E_{0i}}\right)^2 = \left(\frac{n_t\cos\theta_t}{n_i\cos\theta_i}\right) t^2. \tag{A.44}$$

Applying the conservation of energy to the striking of the surface

$$I_i A\cos\theta_i = I_r A\cos\theta_r + I_t A\cos\theta_t \tag{A.45}$$

dividing everything by c we find

$$n_i E_{0i}^2\cos\theta_i = n_r E_{0r}^2\cos\theta_r + n_t E_{0t}^2\cos\theta_t \tag{A.46}$$

and dividing by the LHS gives

$$1 = \left(\frac{E_{0r}}{E_{0i}}\right)^2 + \left(\frac{n_t \cos\theta_t}{n_i \cos\theta_i}\right)\left(\frac{E_{0t}}{E_{0i}}\right)^2 . \tag{A.47}$$

Therefore

$$R + T = 1 \tag{A.48}$$

and because we can reduce the light to two components parallel and perpendicular to the plane of incidence we can introduce component forms of the reflectance in terms of the Fresnel amplitude coefficients

$$R_p = r_p^2 \tag{A.49}$$

$$R_s = r_s^2 \tag{A.50}$$

Appendix B

Marangoni Flow Lubrication Approximation

If our droplets are thin with $R \gg h$ then we can apply a lubrication model[37] in which the height averaged radial velocity at a given radius is zero. At some radius the height dependence of the flow velocity can be approximated by a parabolic

$$u = ah - bh^2 \tag{B.1}$$

where a and b are constants. This velocity goes to zero at the substrate because of a non-slip boundary condition and is at a maximum at the unconstrained liquid-vapour interface.[87] The turning point (u_0, h_0) can be found using

$$\frac{du}{dh} = a - 2bh \tag{B.2}$$

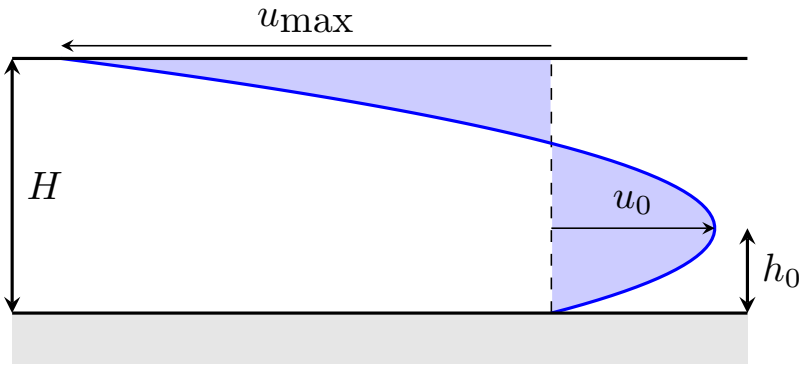

Figure B.1: Parabolic Marangoni flow profile of a droplet under the lubrication approximation.

when the above expression is set to zero we find

$$h_0 = \frac{a}{2b}, \tag{B.3}$$

substituting this into Equation B.1 we find

$$u_0 = a\frac{a}{2b} - b\left(\frac{a}{2b}\right)^2 = \frac{a^2}{4b}. \tag{B.4}$$

As the height averaged flow is zero, the two light blue areas in Figure B.1 must be equal, thus

$$\int_0^H u\, dh = \left[\frac{ah^2}{2} - \frac{bh^3}{3}\right]_0^H = \frac{aH^2}{2} - \frac{bH^3}{3} = 0. \tag{B.5}$$

Hence

$$b = \frac{3a}{2H} \tag{B.6}$$

which can be substituted into Equation B.3 for

$$h_0 = \frac{H}{3}, \tag{B.7}$$

so that

$$u_0 = \frac{aH}{6}. \tag{B.8}$$

The maximum velocity occurs at the interface of the droplet when $h = H$, therefore

$$u_{\max} = -\frac{aH}{2} = -3u_0. \tag{B.9}$$

In the above scheme the turning point occurs at two thirds of the distance between the substrate and liquid-vapour surface. Therefore the mean velocity of fluid moving left is twice that of the fluid moving right in Figure B.1 so that the total velocity across the height is zero .

Appendix C

Solvents

C.1 Binary + Ethanol Vapour

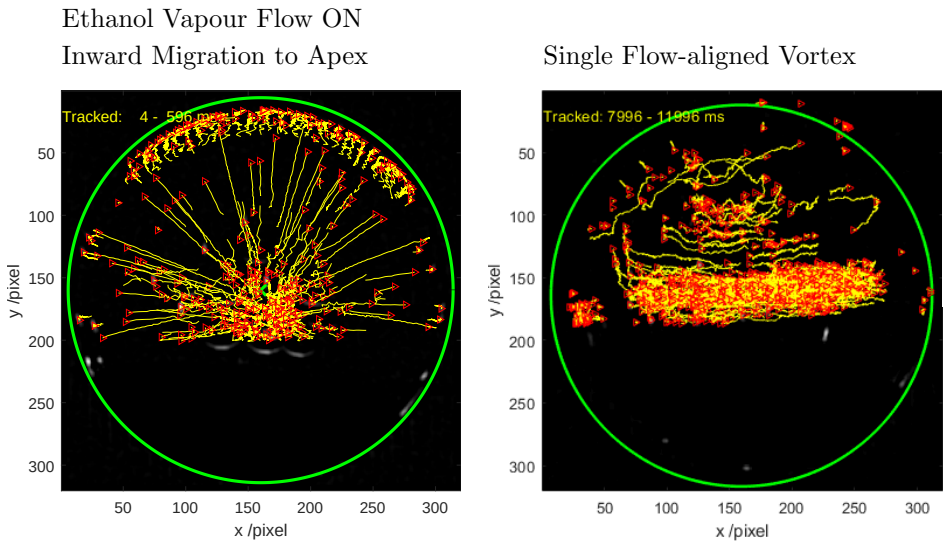

Figure C.1: Particle tracks from 70%v EG-water droplets evaporating in an ethanol rich environment with ethanol flowing into the chamber. At first there is migration towards the apex of the droplet, later on the flows converge into a single vortex from the apex to the contact line nearest the vapour inlet.

In the first 1-2 seconds of evaporation the particles would collect at the apex in identical behaviour to an ethylene glycol-water droplet without ethanol vapour. If the ethanol vapour was still flowing into the chamber at this point then instead of axisymmetric flow with particle migration towards the centre of the droplet (see Figure 4.31) there would be a single vortex roll aligned towards the gas inlet.

Appendix D

Solutes

D.1 Lactose Viscosity

Figure D.1 shows a few viscosity measurements for lactose aerosol droplets, demonstrating that its viscosity dependence is similar to sucrose and other sugars.[172]

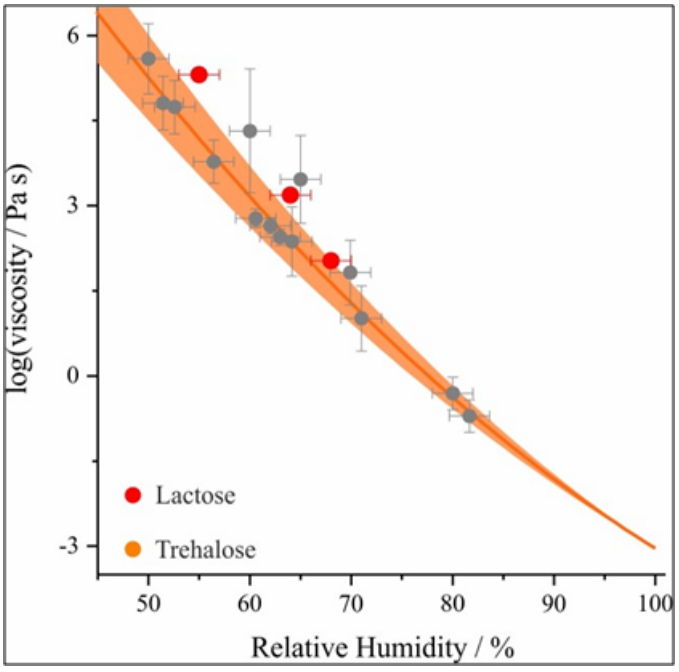

Figure D.1: Viscosity of lactose and trehalose solutions. Reproduced with permission from Young Chul Song from Ref.172, 178

D.2 Sucrose Final Volumes

Figure D.2 shows that experimental final volumes once sugar droplets stopped evaporating over a time frame of tens of seconds were higher than expected. This further supports the formation of a viscous shell of sucrose developing during evaporation, preventing further evaporation and resulting in non-uniform compositions within the droplet, unlike the model.

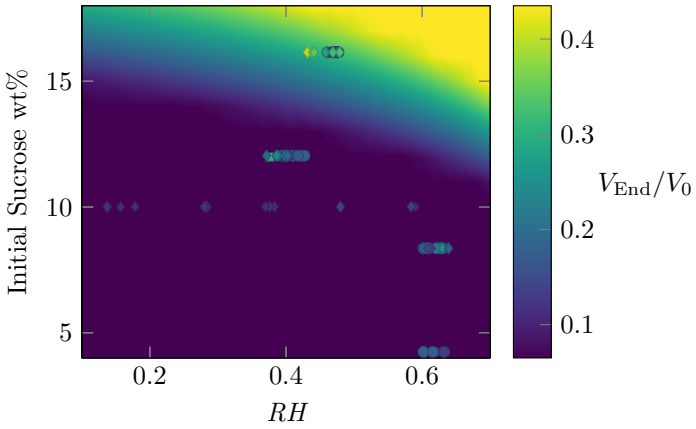

Figure D.2: Theoretical surface of expected remaining volume at the end of evaporation of sucrose droplets for initial sucrose concentration and environmental relative humidity combinations. Markers are for measured end volumes.

D.3 Other Salt Supersaturations

Experiments used 1 and 10 wt% solutions of AMS, however for the lower concentrations the volumes of the droplets at the moment the drops crystallised were too low to measure effectively, therefore Figure D.3 only contains 10 wt% AMS droplets. Different substrates and relative humidities were used and no trend in the supersaturation can be observed in either. The top right plot is can be thought of as experiments under high or low relative humidity, as no trend in humidity was observed the mean supersaturations of droplets which different effloresce were no different to those which did. This range in the differences is reflective of the poor reproducibility of the flows compared to ethanol-water and aqueous sucrose mixtures. The behaviour is similar for the sodium nitrate results presented in Figure D.4.

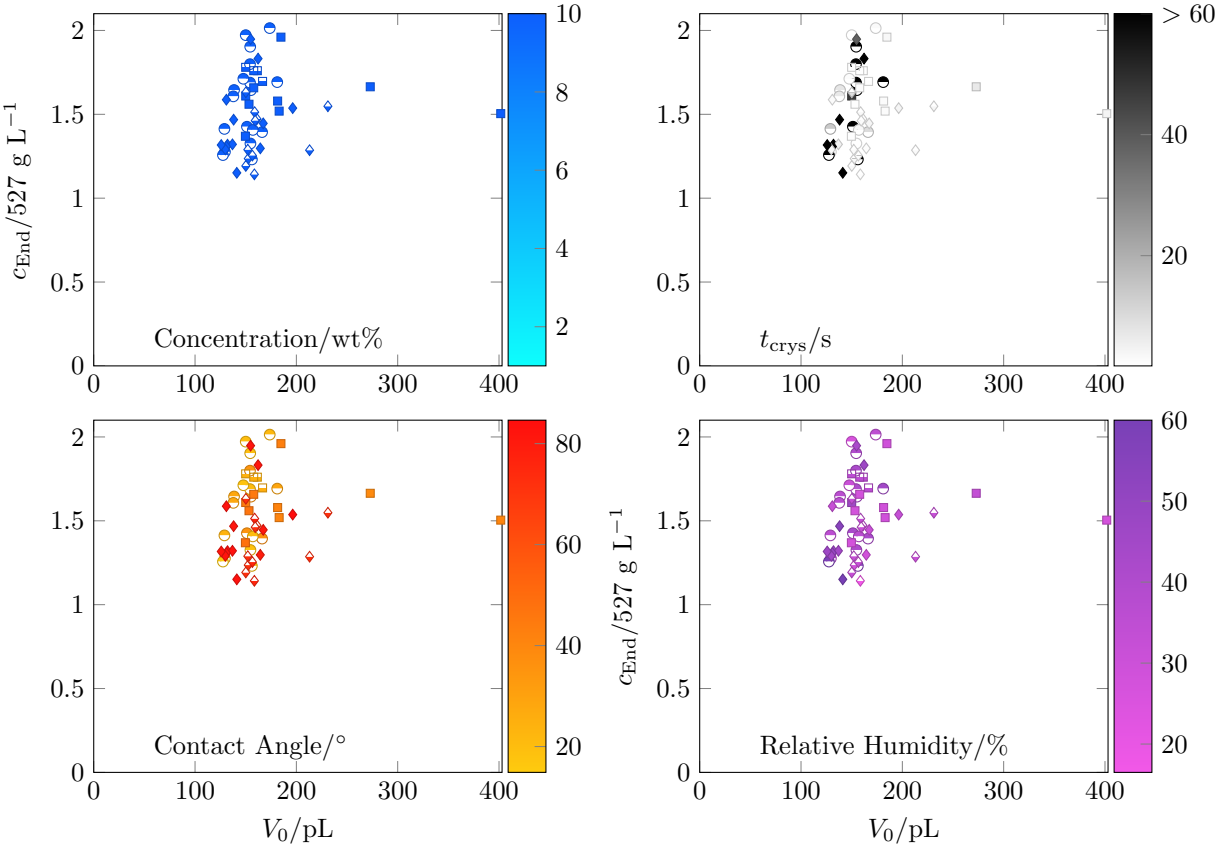

Figure D.3: Supersaturations for AMS droplets as a function of volume with colormap dependence on starting concentration in wt%, relative humidity, initial contact angle or measured crystallisation time. Circle and diamond markers denote Decon or HMDS treated substrates respectively.

D.4 Ammonium Sulfate Efflorescence

Figure D.5 shows that ammonium sulfate droplets had a clear efflorescence relative humidity which did not exhibit any dependence on whether the relative humidity in the chamber had been increased or descreased relative to the previous droplet video saved.

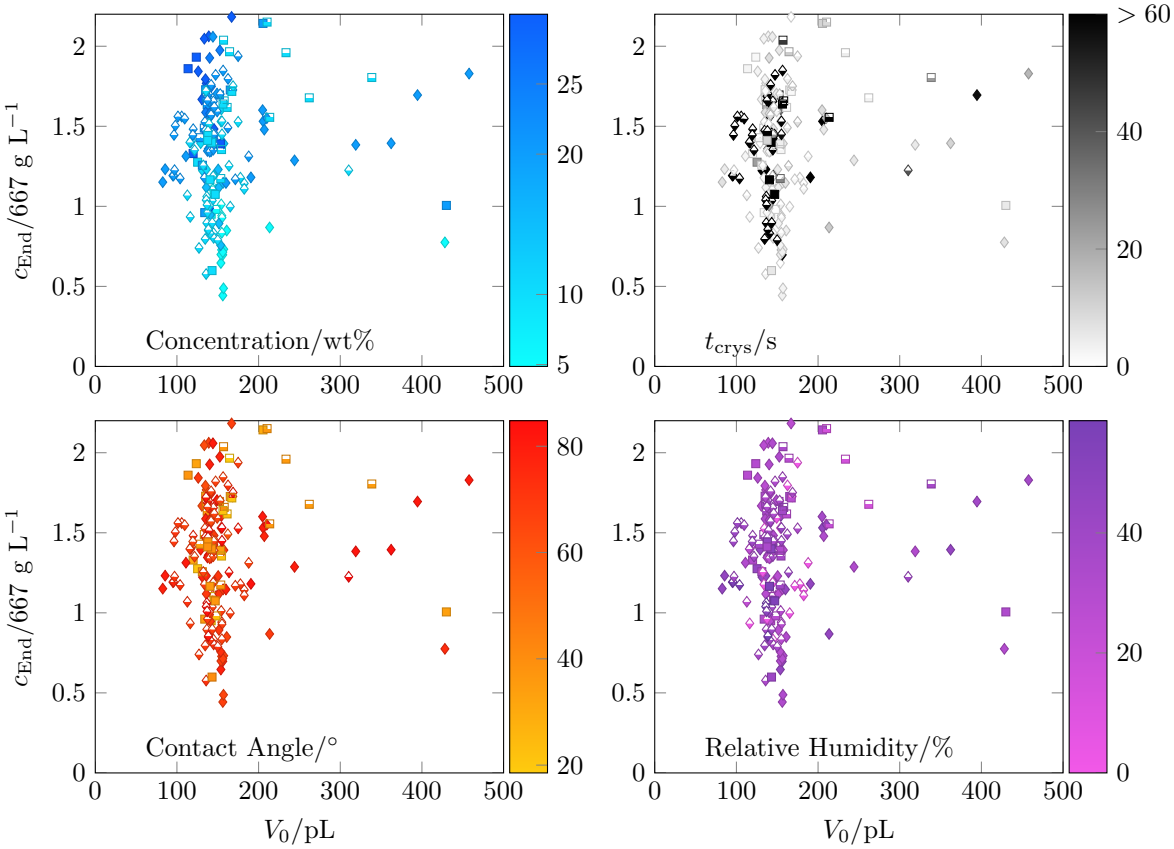

Figure D.4: Supersaturations for $NaNO_3$ droplets as a function of volume with colormap dependence on starting concentration in wt%, relative humidity, initial contact angle or measured crystallisation time. Half-filled markers were without particles. Square and diamond markers denote plasma cleaned or HMDS treated substrates respectively.

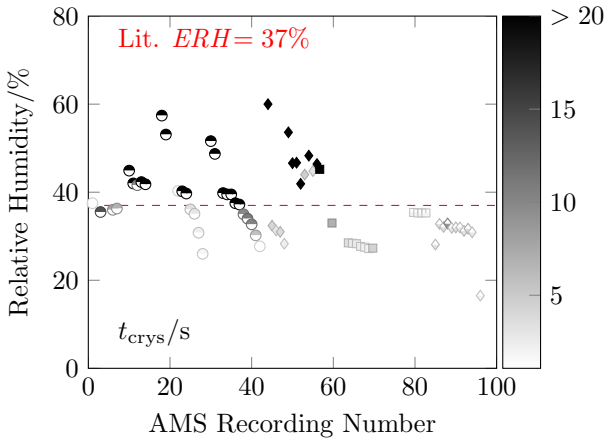

Figure D.5: Crystallisation times for AMS droplets in order of experiment with the relative humidity being varied (as well as substrate and concentration).

Appendix E

Particle Migration

E.1 Theory

Derjaguin *et al.*[295] made the theoretical leap that for a particle there could be a velocity/stress gradient in the Stoke's flow through the interfacial region between a particle and fluid which could lead to particle motion. Across this interfacial lengthscale the osmotic stresses needed to be continuous, while the lengthscale also needed to be an order of magnitude smaller than the particle radius so that stresses would fulfil the necessary boundary condition of being discontinuous in the macro system.

For a salt system the diffusiophoretic velocity including the"chemiphoretic" term is[298]

$$u_{\mathrm{DP}} = \frac{\epsilon}{\eta}\frac{k_{\mathrm{B}}T}{ze}\left(\zeta\frac{D_+ - D_-}{D_+ + D_-} + \frac{4k_{\mathrm{B}}T}{ze}\ln\cosh\frac{ze\zeta}{4k_{\mathrm{B}}T}\right)\nabla\ln\frac{c}{c^*} \tag{E.1}$$

where c^* is the reference concentration chosen for the chemical potential, ϵ is the permittivity, z is the ion charge and $D_\pm$ are the ion diffusivities.

E.2 Migration Velocities

Figure E.1 shows the migration velocities for ethanol-water, sucrose and sodium chloride droplets. These velocities of retraction of the collected group can be quite large, up to about a tenth of the actual flow velocities for the three systems studied so that v_{R_g} could be tens or hundreds of $\mu\mathrm{m\,s^{-1}}$, much larger than the $u_{\mathrm{DP}} = 1$ or 2 $\mu\mathrm{m\,s^{-1}}$ common in the literature.

Some evidence that these migration velocities are impacted by the shape of the

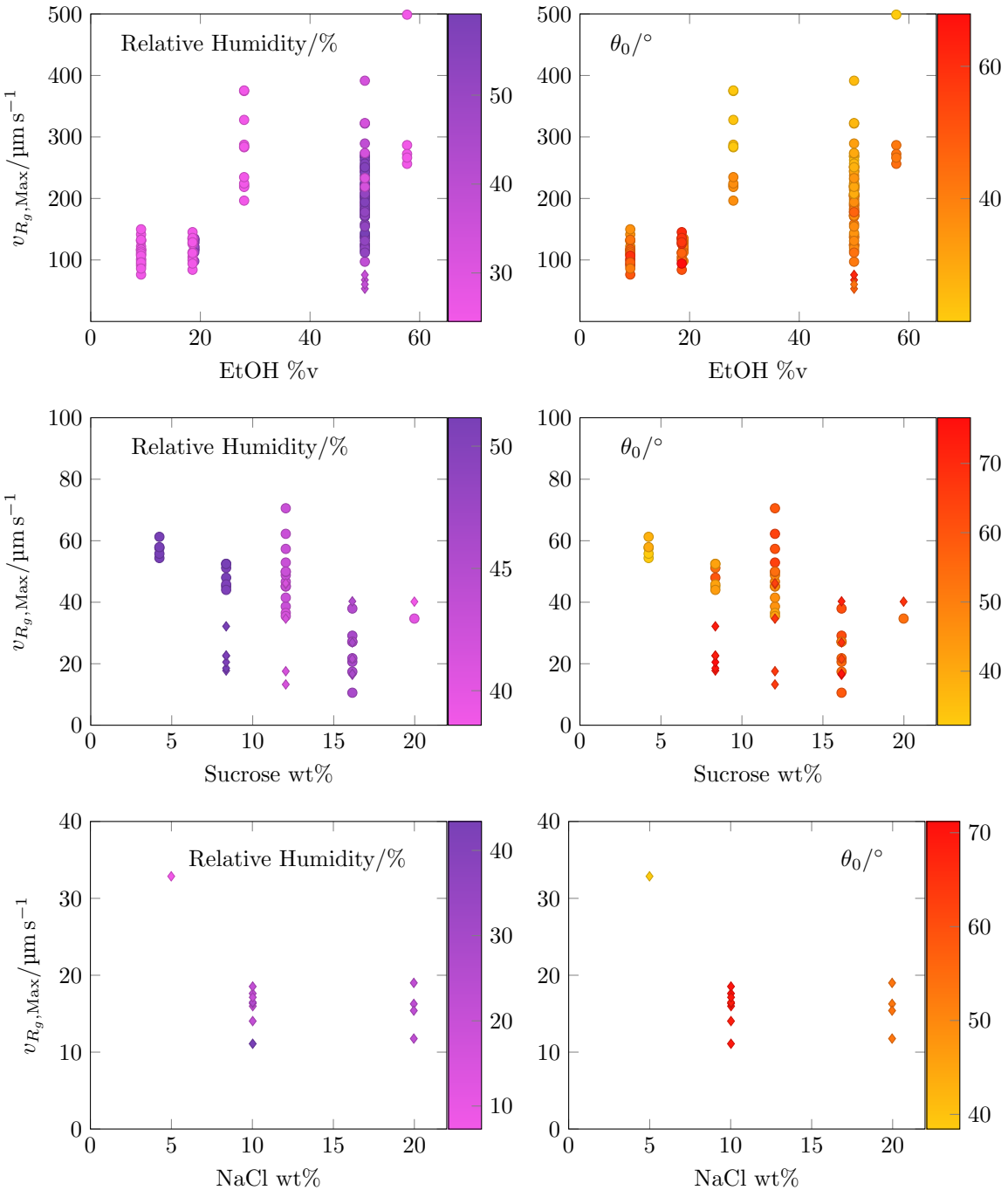

Figure E.1: Maximum retraction speed of the edge of radius of the collected group in particle migration towards the centre of the droplet. The different rows are for different droplet systems in order of migration velocities: top - ethanol-water mixtures, middle - sucrose solutions, bottom - sodium chloride solutions. Left plots show the *RH* dependence while right plots show the dependence with starting contact angle. Circle markers for droplets evaporating on a Decon-cleaned substrate, diamonds for HMDS-treated substrates.

droplets is that the HMDS-treated substrate diamond markers for 50%v ethanol in the top row of Figure E.1 have the lowest v_{R_g}; these droplets would have a higher contact angle and height meaning the concentration difference was across a larger distance.

E.3 Experiments to Verify Diffusiophoric Migration

In order to gather more evidence that our particles followed a diffusiophoretic migration mechanism I ran experiments with different particles and others without droplets and solutal Marangoni flows.

I attempted to find a system with flow from the apex to the contact line along the liquid-vapour interface but with migration to the apex rather than the centre by replacing the sterically-stabilised PS particles with non-functionalised 0.5 µm silica particles that would have different interactions in a diffusiophoretic model. The migration was unchanged across ethanol-water droplets, water droplets in ethanol vapour and sodium nitrate droplets. As these silica particles were hydrophilic it is unclear why they would not prefer water over ethanol, and so migrate in the opposite direction in the systems with ethanol and water.

Kosmulski and Matuevi[300] looked at the motion of 100 nm sulfate-stabilised polystyrene particles in lattices where a layer of ethanol was carefully deposited on top of water, finding solvophoretic migration of particles (diffusiophoresis in response to a neutral solute) towards the shifting boundary layer. I attempted to use this approach to test for diffusiophoretic behaviour from the PEGMA-stabilised PS particles by creating a concentration gradient within a cuvette for absorption spectroscopy. I first added a layer of PS particle rich water (or a ethanol-water mixture) and then pure ethanol (slowly delivering it through a pipette along the side of the cuvette). These results were inconclusive: when I left a series of cuvettes in the lab overnight I observed visibly increased particle densities at the ethanol-water boundary (i.e. particle motion towards higher ethanol concentrations against the direction of sedimentation) that would be consistent with diffusiophoresis. When I tried to actually record the interface, at a low frame rate for 8 hours within a tensiometer setup, then experiments were stymied by the very slow nucleation of bubbles in the aqueous phase that gave rise to Marangoni flows that disrupted the diffuse fluid-fluid interface. Degassing

the particle solution by sonication under vacuum prior to filling cuvettes did not eliminate this issue so I was unable to collect clear videos, despite finding promising snapshots over long times.

Experiments in horizontal and vertical rectangular capillaries containing particle solution were also inconclusive despite seeing increased particle density in the direction of higher ethanol concentrations. Adding ethanol directly into the open end of the capillary or placing an ethanol vapour source (soaked tissue) still induced solutal Marangoni flows so the experiments had the same problem as those with droplets as the migration could not be decoupled from flow.

In another attempt to isolate diffusiophoretic migration outside of droplets I used a three input flow focusing microfluidic device usually used to prepare monodisperse emulsions (with assistance from its usual user Yilin Wang).[301] With the central input containing water and particles, and the side input channels containing ethanol, I hoped to observe greater particle spreading in the outlet in response to the ethanol concentration gradient[291] but the preliminary results showed that there was too much mixing at the focusing junction.

Appendix F

MATLAB Code

F.1 Popov Model Implementation (NaCl)

Model Evaporation of pinned or depinning NaCl droplets.

```
%09/05/19 Jack Goodall
%Use Popov 05 Equation
%Evaporation of pL sodium chloride droplets into a RH controlled chamber

%Pick droplets, input conditions and whether evaporate in CCA or CCR mode.
%If CCR use dtheta equations, if CCA use dm equations but adjust CA based
%on surface tension of fluid.

close all
source = strcat(pwd, '\'); %print working directory
addpath(genpath('myFunctions\'))

%Reasonable assumption if the drop is representative of the prepared fluid
dt_inv = 1000; %time steps per second
dt = 1/dt_inv; %ms timestep

%Read Data
DROP = 9;

if DROP == 1
elseif DROP == 7
    fileIN = fopen('2019_01_18_10wtNaCl_vid16.txt','r');
    %a_envir = 64.5/100; %Experimental
    a_envir = 0.75; %Fitted
    TempC = 23.6 ; %Experimental
    %wt = 9.9; %Experimental
    wt = 10; %Fitted
    time = 16000;
    CL = 1; %pinned CL

elseif DROP == 8
    fileIN = fopen('2019_01_18_10wtNaCl_vid42.txt','r');
    a_envir = 8.5/100; %Experimental
    %a_envir = 0.10; %Fitted
    TempC = 23.6 ; %Experimental
    wt = 9.9; %Experimental
    time = 1300; %tcrys
    CL = 1; %pinned CL

elseif DROP == 9
    fileIN = fopen('2019_01_18_10wtNaCl_vid23.txt','r');
    a_envir = 33.2/100; %Experimental
    %a_envir = 0.47; %Fitted
    TempC = 23.6 ; %Experimental
    wt = 9.9; %Experimental
    %wt = 12; %Fitted
    time = 2800; %tcrys
    CL = 1; %pinned CL
elseif DROP == 10
    fileIN = fopen('2019_01_18_10wtNaCl_vid31.txt','r');
    %a_envir = 19.5/100; %Experimental
    a_envir = 0.33;  %Fitted
    TempC = 23.6 ; %Experimental
```

```
    %wt = 9.9; %Experimental
    wt = 13; %Fitted
    time = 1700; %tcrys
    CL = 1; %pinned CL
end

formatSpec = '%f';
sizeData = [5 Inf]; %rows;
headers = fgets(fileIN); %don't get top line=header in array
Data    = fscanf(fileIN,formatSpec,sizeData);
fclose(fileIN);

%First column is vol fraction water, second is vol fraction ethanol
Result = zeros(1,length(Data));

theta0  = Data(2,1) * pi/180 ; %Contact Angle from degrees to radians
V0      = Data(5,1) ; %Volume pL
R0 = Data(3,1)/2 * 10^(-6) ; %Radius from microns to m

Mr_NaCl = 58.44; %g/mol
m0 = wt/Mr_NaCl/((100-wt)/1000); %if had 100g of solution...
m = m0;

mass_T = NaClDensity_Molality_EAIM(m0)*V0*10^(-12)*1000; %density*(V pL->cm3)
mass_NaCl = wt/100*mass_T; %masses in grams
mass_wat = (100-wt)/100*mass_T;

n_NaCl=mass_NaCl/Mr_NaCl;
M0 = n_NaCl/(V0*10^(-12));

V = V0;
M = M0;
R = R0;
theta = theta0;
ST = NaClsurfacetension_EAIM_m(m);
storeth = [theta0];

n_loop = 1; %as first calculation is after 1 ms has elapsed

for loops=1:time

    %If droplet depins...
    if DROP == 1
    elseif DROP == 7
        if loops == 950
            CL = 0;
        end
    elseif DROP == 8
        if loops == 140
            CL = 0;
        end
    elseif DROP == 9
        if loops == 400
            CL = 0;
        end
    elseif DROP == 10
        if loops == 280
            CL = 0;
        end
    end

    if CL == 0 %UNPINNED CL

        delta_mass_wat = dmdtPopovNaCl_m(m, a_envir, R(end), theta(end), TempC)*
            dt;
        mass_wat = [mass_wat, mass_wat(end)+delta_mass_wat];
        m_old = m;
        m = 1000*n_NaCl/mass_wat(end); %conversion of dividing by g to kg

        density = NaClDensity_Molality_EAIM(m);
        V = [V, (mass_wat(end)+mass_NaCl)/density*1e9];

        if ismember(DROP,[1,6,7,8,11,12])

            %approximate the solid-liquid surface in order to have an increase
            %in CA as the surface becomes richer in NaCl
            costheta = ST*cos(theta)/NaClsurfacetension_EAIM_m(m);
            theta = acos(costheta);
            ST = NaClsurfacetension_EAIM_m(m); %UPDATE surface tension
        end

        R = [R, Rspherical(V(end)* 10^(-15),theta)]; %function needs V in m3

    elseif CL==1 %PINNED CL

        dtheta = dthetadtPopov_NaCl_m(m, a_envir, R(end), theta(end), TempC)*dt;
        theta  = theta+dtheta;
```

```
        V = [V, vspherical(R(end),theta(end))*1e15];

        %new molality
        V1 = V(end-1); %L
        V2 = V(end); %L
        M1 = n_NaCl/(V1*1e-12); %mol/L
        M2 = n_NaCl/(V2*1e-12); %mol/L
        rho1 = NaClDensity_Molarity_EAIM(M1); %g/mL
        rho2 = NaClDensity_Molarity_EAIM(M2); %g/mL
        mass1 = (V1*1e-12)*rho1*1000;
        mass2 = (V2*1e-12)*rho2*1000;

        delta_mass_wat=mass2-mass1;
        mass_wat = [mass_wat, mass_wat(end)+delta_mass_wat];
        m = 1000*n_NaCl/mass_wat(end); %conversion of dividing by g to kg

        R = [R, R(end)];
        ST = NaClsurfacetension_EAIM_m(m); %UPDATE surface tension
    end
    storeth = [storeth theta(end)];
end

m = 1000*n_NaCl./mass_wat; %conversion of dividing by g to kg

Realtime = Data(1,:) ;
RealCA   = Data(2,:) ;
RealVolume = Data(5,:) ;
RealRadius = Data(3,:)/2 ;

MFS = mass_NaCl./(mass_NaCl+mass_wat);
ts = (0:length(R)-1)';
ModelCA = storeth'*180/pi;
ModelR = R'*10^6;
OUTPUT = [ts ModelCA ModelR V' MFS'];

figure(2)
hold on
plot(ts,ModelR);
plot(Realtime,RealRadius,'g');
xlabel(' Time/ms ', 'FontSize',12);
ylabel('Radius/micron','FontSize',12);

figure(3)
hold on
plot(ts,ModelCA);
plot(Realtime,RealCA,'g');
xlabel(' Time/ms ', 'FontSize',12);
ylabel('Contact Angle/degrees','FontSize',12);

figure(4)
hold on
plot(ts,MFS);
xlabel(' Time/ms ', 'FontSize',12);
ylabel('NaCl MFS','FontSize',12);

figure(1)
hold on
plot(ts,V);
plot(Realtime,RealVolume,'g');
xlabel(' Time/ms ', 'FontSize',12);
ylabel('Volume/pL','FontSize',12);
```

Function dmdtPopovNaCl_m

```
function dm_watdt = dmdtPopovNaCl_m(m,a_envir, radius, theta, TempC)
%NaCl Molality (mol/kg) to calculate water activity in the drop, water activity
    of the environment
%drop radius in metres, drop contact angle in radians, temperature in
%degrees celcius

vp_wat_sat  = vp_watT(TempC); %Pa
D_wat       = D_watT(TempC); %m2/s
Mr_wat  = 18.015 ; %g/mol Molecular mass
RT = 8.314 * (TempC+273.15) ; % J/mol,

ANGLEDEP = sin(theta)/(1+cos(theta))+4*PopovIntegral(theta); %angular dependence
     in dm/dt
cp_wat_sat  = Mr_wat*vp_wat_sat/RT ; % g/m^3

a_fluid = NaClActivity_m(m);
dm_watdt      = -pi*radius*D_wat*cp_wat_sat*(a_fluid-a_envir)*ANGLEDEP;

end
```

Function PopovIntegral.m

```
%% Polynomial Fit for the toroidal coordinate integral of A8 and A10
% Y. O. Popov, Phys. Rev. E, 2005, 71, 036313.
% After calculating integral, use a polynomial to save computation

% Popovtheta = 0:pi/100:pi/2 ;
% step   = 0.001 ;
% Ls     = 40 ;
%
% Popovintegral = zeros(1,length(Popovtheta));
% for j=1:length(Popovtheta)
%     for i=1:length(Ls)
%         tau   = step:step:Ls(i) ;
%         Popovintegral(j) = trapz(tau,(1+cosh(2*Popovtheta(j)*tau))./(sinh(2*pi
    *tau)).*tanh((pi-Popovtheta(j)).*tau));
%     end
% end
%
% I = polyfit(Popovtheta,Popovintegral,3);

function Popov1 = PopovIntegral(THETA) %angle in radians
I = [0.0044285     0.010526     -0.070681      0.31706];
Popov1 = polyval(I, THETA);
end
```

F.2 Reflectometry Analysis

Convert PMT output to ethanol composition results.

```
% MATLAB code to analyse Oscilloscope traces and convert to reflectances
% and ethanol compositions
% Written by Jack Goodall 22/3/2020

close all;
clear all;
addpath('C:\Users\User\Documents\MATLAB\Reflectometry\myFunctions\')

%% INPUTS
Composition_inputs % load file information

%% Save settings
fileloc    = 'R:\Jack Goodall\Data\12 - Reflectometry\';
analysisloc    = 'C:\Users\User\Documents\MATLAB\Reflectometry\Analysis\';
FileNameAndLocation = 'C:\Users\User\Documents\MATLAB\Reflectometry\
    Composition_inputs' ;

fileloc    = strcat(fileloc,folder);
addpath(fileloc)

% Analysis_folder = strcat(fileloc,'Analysis');
% if exist(Analysis_folder) == 7
% else
%     mkdir (Analysis_folder)
% end

%Read number of drops from filetitle
filetitle_dropidx = strfind(filetitle,'drop');
for b=filetitle_dropidx:-1:1
    filetitle_b = filetitle(b);
    if filetitle_b == '_'
        break
    end
end
ndrops = filetitle(b+1:filetitle_dropidx-1);

%Read experiment number from filetitle
pre    = [];
for i = 1:length(filetitle)
    if filetitle(i) == '_'
        break
    end
    pre = [pre filetitle(i)] ; %end pre = '1', '2' ... '245' etc.
end

for CHAR=1:26
    outputfolder=strcat(analysisloc, folder, pre, '_', char(64+CHAR));
    if exist(outputfolder) == 7
    else
```

```
        mkdir (outputfolder)
        break
    end

end

inputsfile = strcat(pre,'_', char(64+CHAR),'_inputs.txt') ;%pre, char(64+i),

backupfile  = sprintf(inputsfile,FileNameAndLocation); %eg '_file_1.txt'
currentfile = strcat(FileNameAndLocation, '.m');
backupfile  = strcat(outputfolder,'\',backupfile);
copyfile(currentfile, backupfile);

%% Open File

fileformat = 'txt';
filename = [filetitle,'.',fileformat];
fileIN = fopen(filename,'r');

formatSpec = '%f';
sizeData = [2 Inf]; %rows;
Data     = fscanf(fileIN,formatSpec,sizeData);
fclose(fileIN);

%% Time Average the file and select region of interest

tav = TimeAverage(Data(1,:),TimeAv);
Dataav = TimeAverage(Data(2,:),TimeAv);
DataavErr = TimeAverageErr(Data(2,:),TimeAv);
dt = tav(2) - tav(1);


%% Refractive Index Data
%CRC 2005 concentrative properties
ni = 1.461;
datan = [...
    %MFS    n
    0.00        1.333
    0.005       1.3333
    0.01        1.3336
    0.02        1.3342
    0.03        1.3348
    0.04        1.3354
    0.05        1.336
    0.06        1.3367
    0.07        1.3374
    0.08        1.3381
    0.09        1.3388
    0.10        1.3395
    0.12        1.341
    0.14        1.3425
    0.16        1.344
    0.18        1.3455
    0.20        1.3469
    0.22        1.3484
    0.24        1.3498
    0.26        1.3511
    0.28        1.3524
    0.30        1.3535
    0.32        1.3546
    0.34        1.3557
    0.36        1.3566
    0.38        1.3575
    0.40        1.3583
    0.42        1.359
    0.44        1.3598
    0.46        1.3604
    0.48        1.361
    0.50        1.3616
    0.60        1.3638
    0.70        1.3652
    0.80        1.3658
%     0.90      1.365
%     0.92      1.3646
%     0.94      1.3642
%     0.96      1.3636
%     0.98      1.363
%     1.00      1.3614
    ...
    ];

nt0 = interp1(datan(:,1),datan(:,2),fluidwt);

%% Select Region of Interest
fig1 = figure(1);
hold on

```

```
plot(Data(1,:),Data(2,:),'c');
plot(tav,Dataav,'b');

xlabel(' Time/s ', 'FontSize',12);
ylabel('PMT Signal/V','FontSize',12);
plotheight=ylim;
plotwidth=xlim;

text(plotwidth(1)+(plotwidth(2)-plotwidth(1))*0.5,plotheight(1)+(plotheight(2)-
    plotheight(1))*0.95,...
    'Select Region of Interest');

rect = getrect(fig1); %[xmin ymin width height]
tavin = rect(1);
tavout = rect(1)+rect(3);

tavin_idx = round((tavin-tav(1))/dt);
tavout_idx = round((tavout-tav(1))/dt);
tR = tav(tavin_idx:tavout_idx);
Signal = Dataav(tavin_idx:tavout_idx);
SignalErr = DataavErr(tavin_idx:tavout_idx);

plot(tR,Signal,'k');

%% Find time=0 of printing

tR_grad = tR(1,1:end-1)+dt;

dsignal = Signal(2:end) - Signal(1:end-1);
[gradientmax, idx_t0] = max(dsignal);
t0 = tR_grad(idx_t0-2); %2 may be inaccurate, seemed to fit best on test
tR = tR - t0;

%% Calculate Reflectance
R = (Signal-Voff)/(Von-Voff);
dRtop = sqrt( SignalErr.^2 + dVoff^2);
dRbot = sqrt( dVon^2 + dVoff^2);
dR = sqrt((dRtop./(Signal-Voff)).^2 + (dRbot/(Von-Voff))^2).*R;

fig4 = figure(4);
hold on

plotR  = plot(tR,R,'k');
plotwidth=xlim;
plotheight=ylim;

xlabel(' Time/s ', 'FontSize',12);
ylabel('Reflectance','FontSize',12);
ylim([0 1])


%% Calculate Reflectance for given composition at fixed angle

num_sets = length(datan);
Rp = zeros(3,num_sets);

for i=1:num_sets
Rp(1,i) = FresnelRpGauss(theta_i2,ni,datan(i,2));
Rp(2,i) = FresnelRpGauss(theta_i2+theta_err,ni,datan(i,2));
Rp(3,i) = FresnelRpGauss(theta_i2-theta_err,ni,datan(i,2));
end


%% Refractive Index from Reflectance

nt = interp1(Rp(1,:),datan(:,2),R);
% % % % nt0linear = interp1(Rp,datan(:,2),[R0 Rgrad_Rin]);
% % % % nt_fit = interp1(Rp,datan(:,2),R_fit);
% % %
% % % figure(6)
% % % hold on
% % %
% % % plot(tR,nt,'k');
% % % plot([0,tR(tRin_idx)],nt0linear);
% % % % scatter(tsfit,nt_fit,'b');
% % % % scatter(0,interp1(datan(:,1),datan(:,2),fluidwt),'r');
% % %
% % % xlabel(' Time/s ', 'FontSize',12);
% % % ylabel('Refractive Index','FontSize',12);

%% Ethanol Mass Fraction from Reflectance

wt = interp1(Rp(1,:),datan(:,1),R);

wtNaN = wt;
wtNaN(isnan(wtNaN))=0;
%if wt=NaN then X-wt =NaN so mean = NaN so lose error values
```

```
222
223 %uncertainty due to theta
224 wtplus = interp1(Rp(2,:),datan(:,1),R);
225 wtminus = interp1(Rp(3,:),datan(:,1),R);
226 wtdtheta = [wtplus-wtNaN; wtNaN-wtminus];
227 %wtdtheta2 = [wtplus-wtNaN; wtNaN-wtminus];
228
229 NaNs = isnan(wtdtheta(2,:));
230 for i=2:length(wtdtheta)
231     if NaNs(i) == 1
232         wtdtheta(2,i) = wtdtheta(1,i);
233     end
234 end
235
236 wtdtheta = mean(wtdtheta,1);
237
238 %uncertainty due to R
239 wtdRplus = interp1(Rp(1,:),datan(:,1),R+dR);
240 wtdRminus = interp1(Rp(1,:),datan(:,1),R-dR);
241 wtdR = [wtNaN-wtdRplus ; wtdRminus-wtNaN];
242
243 NaNs = isnan(wtdR(1,:));
244 for i=2:length(wtdR)
245     if NaNs(i) == 1
246         wtdR(1,i) = wtdR(2,i);
247     end
248 end
249
250 wtdR = mean(wtdR,1);
251
252 wtErr = sqrt(wtdR.^2 + wtdtheta.^2);
253
254 % % wt0 = interp1(Rp,datan(:,1),[R0 Rgrad_Rin]);
255 % % wt_fit = interp1(Rp,datan(:,1),R_fit);
256
257 figure(7)
258 hold on
259
260 plot(tR,wt,'k');
261
262 plot(tR,wt+wtErr,'m--');
263 plot(tR,wt-wtErr,'m:');
264
265 xlabel(' Time/s ', 'FontSize',12);
266 ylabel('Ethanol Mass Fraction','FontSize',12);
267 ylim([0 fluidwt])
268
269 % %% Error Plot
270 % figure(8)
271 % hold on
272 %
273 % %
274 % % plot(tR,wtdR*100,'b');
275 % % plot(tR,100*(wtdR+wtdtheta),'r');
276 % plot(tR,dR)
277 %
278 % xlabel(' Time/s ', 'FontSize',12);
279 % %ylabel('Ethanol wt% Error','FontSize',12);
280
281 %% Save Output
282 fluidwt=fluidwt*100;
283 Output = [tR; Signal; R; nt; wt; wtErr]'; %6 columns
284 size_Output = size(Output);
285 outputpath = strcat(outputfolder,'\Output.txt');
286 save(outputpath,'Output','-ascii');
287
288 %writematrix requires 2020
289 columns = string(zeros(1,100));
290 for b=1:26
291     columns(b) = char(64+b);
292 end
293 for b=27:length(columns)
294     v = floor((b-1)/26);
295     columns(b) = strcat(char(64+v),char(64+b-26*v));
296 end
297
298 charin = 2+8*(CHAR-1);
299 charout = 8+8*(CHAR-1);
300
301 xlsrange = strcat(columns{charin},'5:',columns{charout},num2str(4+length(Output)
    ));
302 OutputSpreadsheet = strcat(analysisloc, folder,'_Outputs_auto_',num2str(round(
    fluidwt)),'wt.xlsx');
303
304 %File Information
305 writematrix(filetitle,OutputSpreadsheet,'Sheet',pre,'Range',strcat(columns{
    charin},'1'));
```

```
writematrix(theta_i2,OutputSpreadsheet,'Sheet',pre,'Range',strcat(columns{charin+1},'2'));
writematrix(char(64+CHAR),OutputSpreadsheet,'Sheet',pre,'Range',strcat(columns{charin},'2'));

%Column Headers
writematrix('Time/s',OutputSpreadsheet,'Sheet',pre,'Range',strcat(columns{charin},'3'));
writematrix('Signal/V',OutputSpreadsheet,'Sheet',pre,'Range',strcat(columns{charin+1},'3'));
writematrix('R',OutputSpreadsheet,'Sheet',pre,'Range',strcat(columns{charin+2},'3'));
writematrix('nt',OutputSpreadsheet,'Sheet',pre,'Range',strcat(columns{charin+3},'3'));
writematrix('MFS',OutputSpreadsheet,'Sheet',pre,'Range',strcat(columns{charin+4},'3'));
writematrix('MFS_Err',OutputSpreadsheet,'Sheet',pre,'Range',strcat(columns{charin+5},'3'));

writematrix(Output,OutputSpreadsheet,'Sheet',pre,'Range',xlsrange);

fclose all;

tavfolder = strcat(fileloc,'tav');
if exist(tavfolder) == 7
else
    mkdir (tavfolder)
end

TimeAveragedData = [tav;Dataav]';
tavfilename = strcat(filetitle,'_tav',num2str(TimeAv),'.txt');
tavfolderfull = strcat(tavfolder,'\',tavfilename);
writematrix(TimeAveragedData,tavfolderfull,'Delimiter','tab');
```

Input variables

```
%Composition Inputs for Reflectometry Analysis
%This file gets saved automatically so conditions can be preserved

folder     = '2020_03_20 7030WaterEthanol\';
filetitle  = '13_7030_1drop_500Hz_60V_128_4deg_1stnoprevious';
theta_i2 = 66.13;
theta_err = 0.06;
Von  = -0.976;
Voff = -0.167;
TimeAv = 41;
fluidwt = 0.255;

dVon  = 0.01;
dVoff = 0.005;
```

Function TimeAverage.m

```
function v_cut = TimeAverage(v,n)
%For reflectometry

cut = floor(length(v)/n);
v_cut = zeros(1,cut*n);

if mod(n, 2) == 0
    display('Use odd number for time averaging')
else
    % x is odd
    for i=1+(n-1)/2:n:cut*n
        v_cut(i) = mean(v(i-(n-1)/2:i+(n-1)/2));
    end
    v_cut(~any(v_cut,1)) = [];
end

end
```

Function TimeAverageErr.m

```
function v_err = TimeAverageErr(v,n)
%For reflectometry

cut = floor(length(v)/n);
v_err = zeros(1,cut*n);
%size(v_cut)

if mod(n, 2) == 0
    display('Use odd number for time averaging')
else
    % x is odd
    for i=1+(n-1)/2:n:cut*n
        v_err(i) = std(v(i-(n-1)/2:i+(n-1)/2)); %standard deviation
    end
    v_err(~any(v_err,1)) = [];
end

%standard error
v_err=v_err/sqrt(n);

end
```

Function FresnelRpGauss.m

```
%Jack Goodall 25/3/2020
%Fresnel Equations, only Rp (light parallel to axis of incidence)
%Gaussian convolution

function Rpgauss = FresnelRpGauss(theta_i_deg,ni,nt) %nt must be single valued,
    theta_i can be a 1D array
format long

laser_D = 0.81; %mm
lens_f   = 50;  %mm
NA = laser_D/(2*lens_f); %rad
NA = NA * 180/pi; %deg
angular_step = 0.01; %deg
laser_th = -1.5:angular_step:1.5;
laserI =  exp(-2*laser_th.^2/NA^2);
sumI = sum(laserI);

theta_i = [theta_i_deg-1.5:angular_step:theta_i_deg+1.5]*pi/180;
theta_t = asin(ni/nt * sin(theta_i));
theta_t = real(theta_t);

rp = (nt*cos(theta_i) - ni*cos(theta_t))./(ni*cos(theta_t) + nt*cos(theta_i) );

Rp = rp.^2;
%Rp(imag(Rp) ~= 0) = 1;

Rpgauss = conv(Rp,laserI,'valid')/sumI;
```

Bibliography

[1] R. J. L. Ramsey, G. R. Stephenson and J. C. Hall, *Pesticide Biochemistry and Physiology*, 2005, **82**, 162–175.

[2] D. L. Reichard, *Weed Technology*, 1988, **2**, 82–87.

[3] S. H. Eom, S. Senthilarasu, P. Uthirakumar, S. C. Yoon, J. Lim, C. Lee, H. S. Lim, J. Lee and S.-H. Lee, *Organic Electronics*, 2009, **10**, 536–542.

[4] M. Singh, H. M. Haverinen, P. Dhagat and G. E. Jabbour, *Advanced Materials*, 2010, **22**, 673–685.

[5] W. Shen, X. Zhang, Q. Huang, Q. Xu and W. Song, *Nanoscale*, 2014, **6**, 1622–1628.

[6] G. Hu, J. Kang, L. W. T. Ng, X. Zhu, R. C. T. Howe, C. G. Jones, M. C. Hersam and T. Hasan, *Chemical Society Reviews*, 2018, **47**, 3265–3300.

[7] G. Hu, L. Yang, Z. Yang, Y. Wang, X. Jin, J. Dai, Q. Wu, S. Liu, X. Zhu, X. Wang, T.-C. Wu, R. C. T. Howe, T. Albrow-Owen, L. W. T. Ng, Q. Yang, L. G. Occhipinti, R. I. Woodward, E. J. R. Kelleher, Z. Sun, X. Huang, M. Zhang, C. D. Bain and T. Hasan, *Science Advances*, 2020, **6**, eaba5029.

[8] A. Matavž, R. C. Frunză, A. Drnovšek, V. Bobnar and B. Malič, *Journal of Materials Chemistry C*, 2016, **4**, 5634–5641.

[9] D. Brutin, B. Sobac, B. Loquet and J. Sampol, *Journal of Fluid Mechanics*, 2011, **667**, 85–95.

[10] J. R. Trantum, D. W. Wright and F. R. Haselton, *Langmuir*, 2012, **28**, 2187–2193.

[11] R. Dou, T. Wang, Y. Guo and B. Derby, *Journal of the American Ceramic Society*, 2011, **94**, 3787–3792.

[12] M. Nadgorny and A. Ameli, *ACS Applied Materials & Interfaces*, 2018, **10**, 17489–17507.

[13] O. A. Basaran, H. Gao and P. P. Bhat, *Annual Review of Fluid Mechanics*, 2013, **45**, 85–113.

[14] I. Rodríguez-Ruiz, Z. Hammadi, R. Grossier, J. Gómez-Morales and S. Veesler, *Langmuir*, 2013, **29**, 12628–12632.

[15] X. Shen, C.-M. Ho and T.-S. Wong, *The Journal of Physical Chemistry B*, 2010, **114**, 5269–5274.

[16] M. Taylor, A. J. Urquhart, M. Zelzer, M. C. Davies and M. R. Alexander, *Langmuir*, 2007, **23**, 6875–6878.

[17] E. L. Talbot, A. Berson, P. S. Brown and C. D. Bain, *Physical Review E*, 2012, **85**, 061604.

[18] P. L. Kelly-Zion, C. J. Pursell, N. Hasbamrer, B. Cardozo, K. Gaughan and K. Nickels, *International Journal of Heat and Mass Transfer*, 2013, **65**, 165–172.

[19] W. C. Bigelow, D. L. Pickett and W. A. Zisman, *Journal of Colloid Science*, 1946, **1**, 513–538.

[20] K. S. Birdi and D. T. Vu, *Journal of Adhesion Science and Technology*, 1993, **7**, 485–493.

[21] W. Kwieciński, T. Segers, S. van der Werf, A. van Houselt, D. Lohse, H. J. W. Zandvliet and S. Kooij, *Langmuir*, 2019, **35**, 10453–10460.

[22] D. Lohse and X. Zhang, *arXiv:2005.03782 [cond-mat, physics:physics]*, 2020.

[23] S. Karpitschka, F. Liebig and H. Riegler, *Langmuir*, 2017, **33**, 4682–4687.

[24] R. G. Picknett and R. Bexon, *Journal of Colloid and Interface Science*, 1977, **61**, 336–350.

[25] K. S. Birdi, D. T. Vu and A. Winter, *The Journal of Physical Chemistry*, 1989, **93**, 3702–3703.

[26] H. Gelderblom, A. G. Marín, H. Nair, A. van Houselt, L. Lefferts, J. H. Snoeijer and D. Lohse, *Physical Review E*, 2011, **83**, 026306.

[27] C. Poulard, G. Guéna and A. M. Cazabat, *Journal of Physics: Condensed Matter*, 2005, **17**, S4213.

[28] R. D. Deegan, O. Bakajin, T. F. Dupont, G. Huber, S. R. Nagel and T. A. Witten, *Physical Review E*, 2000, **62**, 756–765.

[29] H. Hu and R. G. Larson, *Langmuir*, 2005, **21**, 3963–3971.

[30] H. Hu and R. G. Larson, *The Journal of Physical Chemistry B*, 2002, **106**, 1334–1344.

[31] Y. O. Popov, *Physical Review E*, 2005, **71**, 036313.

[32] R. Mollaret, K. Sefiane, J. R. E. Christy and D. Veyret, *Chemical Engineering Research and Design*, 2004, **82**, 471–480.

[33] F. Girard, M. Antoni, S. Faure and A. Steinchen, *Langmuir*, 2006, **22**, 11085–11091.

[34] G. J. Dunn, S. K. Wilson, B. R. Duffy, S. David and K. Sefiane, *Colloids and Surfaces A: Physicochemical and Engineering Aspects*, 2008, **323**, 50–55.

[35] H. Hu and R. G. Larson, *Langmuir*, 2005, **21**, 3972–3980.

[36] D. P. Siregar, J. G. M. Kuerten and C. W. M. van der Geld, *Journal of Colloid and Interface Science*, 2013, **392**, 388–395.

[37] A. Oron, S. H. Davis and S. G. Bankoff, *Reviews of Modern Physics*, 1997, **69**, 931–980.

[38] C. Diddens, J. G. M. Kuerten, C. W. M. van der Geld and H. M. A. Wijshoff, *Journal of Colloid and Interface Science*, 2017, **487**, 426–436.

[39] C. Diddens, *Journal of Computational Physics*, 2017, **340**, 670–687.

[40] H. Tan, C. Diddens, P. Lv, J. G. M. Kuerten, X. Zhang and D. Lohse, *Proceedings of the National Academy of Sciences*, 2016, **113**, 8642–8647.

[41] Y. Li, P. Lv, C. Diddens, H. Tan, H. Wijshoff, M. Versluis and D. Lohse, *Physical Review Letters*, 2018, **120**, 224501.

[42] H. Kim and H. A. Stone, *Journal of Fluid Mechanics*, 2018, **850**, 769–783.

[43] A. Marín, S. Karpitschka, D. Noguera-Marín, M. A. Cabrerizo-Vílchez, M. Rossi, C. J. Kähler and M. A. Rodríguez Valverde, *Physical Review Fluids*, 2019, **4**, 041601.

[44] R. D. Deegan, O. Bakajin, T. F. Dupont, G. Huber, S. R. Nagel and T. A. Witten, *Nature*, 1997, **389**, 827–829.

[45] A. G. Marín, H. Gelderblom, D. Lohse and J. H. Snoeijer, *Physical Review Letters*, 2011, **107**, 085502.

[46] C. Monteux and F. Lequeux, *Langmuir*, 2011, **27**, 2917–2922.

[47] T.-S. Wong, T.-H. Chen, X. Shen and C.-M. Ho, *Analytical Chemistry*, 2011, **83**, 1871–1873.

[48] R. D. Deegan, *Physical Review E*, 2000, **61**, 475–485.

[49] L. Shmuylovich, A. Q. Shen and H. A. Stone, *Langmuir*, 2002, **18**, 3441–3445.

[50] A. Shimoni, S. Azoubel and S. Magdassi, *Nanoscale*, 2014, **6**, 11084–11089.

[51] H. Hu and R. G. Larson, *The Journal of Physical Chemistry B*, 2006, **110**, 7090–7094.

[52] L. E. Scriven and C. V. Sternling, *Nature*, 1960, **187**, 186–188.

[53] X. Xu and J. Luo, *Applied Physics Letters*, 2007, **91**, 124102.

[54] W. D. Ristenpart, P. G. Kim, C. Domingues, J. Wan and H. A. Stone, *Physical Review Letters*, 2007, **99**, 234502.

[55] T. Still, P. J. Yunker and A. G. Yodh, *Langmuir*, 2012, **28**, 4984–4988.

[56] W. Sempels, R. D. Dier, H. Mizuno, J. Hofkens and J. Vermant, *Nature Communications*, 2013, **4**, 1757.

[57] A. Marín, R. Liepelt, M. Rossi and C. J. Kähler, *Soft Matter*, 2016, **12**, 1593–1600.

[58] J. Shi, L. Yang and C. D. Bain, *Langmuir*, 2021, **37**, 4091–4101.

[59] L. Cui, J. Zhang, X. Zhang, L. Huang, Z. Wang, Y. Li, H. Gao, S. Zhu, T. Wang and B. Yang, *ACS Applied Materials & Interfaces*, 2012, **4**, 2775–2780.

[60] C. Seo, D. Jang, J. Chae and S. Shin, *Scientific Reports*, 2017, **7**, 500.

[61] H. Kim, F. Boulogne, E. Um, I. Jacobi, E. Button and H. A. Stone, *Physical Review Letters*, 2016, **116**, 124501.

[62] K. H. Kang, H. C. Lim, H. W. Lee and S. J. Lee, *Physics of Fluids*, 2013, **25**, 042001.

[63] A. Edwards, P. Atkinson, C. Cheung, H. Liang, D. Fairhurst and F. Ouali, *Physical Review Letters*, 2018, **121**, 184501.

[64] Y. Li, C. Diddens, P. Lv, H. Wijshoff, M. Versluis and D. Lohse, *Physical Review Letters*, 2019, **122**, 114501.

[65] P. J. Yunker, T. Still, M. A. Lohr and A. G. Yodh, *Nature*, 2011, **476**, 308–311.

[66] J.-Y. Jung, Y. W. Kim and J. Y. Yoo, *Analytical Chemistry*, 2009, **81**, 8256–8259.

[67] L. Nicolaou and T. A. Zaki, *Journal of Aerosol Science*, 2016, **102**, 105–127.

[68] B. Derby, *Annual Review of Materials Research*, 2010, **40**, 395–414.

[69] H. Wijshoff, *Physics Reports*, 2010, **491**, 77–177.

[70] D. Jang, D. Kim and J. Moon, *Langmuir*, 2009, **25**, 2629–2635.

[71] Y. Liu and B. Derby, *Physics of Fluids*, 2019, **31**, 032004.

[72] B.-J. de Gans, P. C. Duineveld and U. S. Schubert, *Advanced Materials*, 2004, **16**, 203–213.

[73] E. L. Talbot, H. N. Yow, L. Yang, A. Berson, S. R. Biggs and C. D. Bain, *ACS Applied Materials & Interfaces*, 2015, **7**, 3782–3790.

[74] S. D. Hoath, S. Jung, W.-K. Hsiao and I. M. Hutchings, *Organic Electronics*, 2012, **13**, 3259–3262.

[75] C. Andrieu, D. A. Beysens, V. S. Nikolayev and Y. Pomeau, *Journal of Fluid Mechanics*, 2002, **453**, 427–438.

[76] W. D. Ristenpart, P. M. McCalla, R. V. Roy and H. A. Stone, *Physical Review Letters*, 2006, **97**, 064501.

[77] S. Karpitschka and H. Riegler, *Physical Review Letters*, 2012, **109**, 066103.

[78] N. J. Cira, A. Benusiglio and M. Prakash, *Nature*, 2015, **519**, 446–450.

[79] R. Malinowski, I. P. Parkin and G. Volpe, *Science Advances*, 2020, **6**, eaba3636.

[80] H. Sadafi, S. Dehaeck, A. Rednikov and P. Colinet, *Langmuir*, 2019, **35**, 7060–7065.

[81] H. N. Yow and S. Biggs, *Soft Matter*, 2013, **9**, 10031–10041.

[82] J. de Jong, G. de Bruin, H. Reinten, M. van den Berg, H. Wijshoff, M. Versluis and D. Lohse, *The Journal of the Acoustical Society of America*, 2006, **120**, 1257–1265.

[83] I. G. Hughes and T. P. A. Hase, *Measurements and their Uncertainties*, Oxford University Press, 2010.

[84] I. Cooper, *Doing Physics with MATLAB*, 2014, http://www.physics.usyd.edu.au/teach_res/mp/mphome.htm.

[85] D. Blair and E. Dufresne, *The Matlab Particle Tracking Code Repository*, http://site.physics.georgetown.edu/matlab/.

[86] J. C. Crocker and D. G. Grier, *Journal of Colloid and Interface Science*, 1996, **179**, 298–310.

[87] E. L. Talbot, *PhD Thesis*, Durham University, 2014.

[88] E. L. Talbot, *Doctoral*, Durham University, 2014.

[89] L. Greenspan, *Journal of Research of the National Bureau of Standards*, 1977, **81A**, 89–96.

[90] S. Armstrong, G. McHale, R. Ledesma-Aguilar and G. G. Wells, *Langmuir*, 2019, **35**, 2989–2996.

[91] D. R. Lide, G. Baysinger, S. Chemistry, L. I. Berger, R. N. Goldberg and H. V. Kehiaian, *CRC Handbook of Chemistry and Physics Internet Version 2005*, CRC Press, Boca Raton, FL, 85th edn., 2005.

[92] E. N. Fuller, P. D. Schettler and J. C. Giddings, *Industrial & Engineering Chemistry*, 1966, **58**, 18–27.

[93] G. A. Lugg, *Analytical Chemistry*, 1968, **40**, 1072–1077.

[94] E. W. Washburn, C. J. West, N. R. C. (U.S.), National Academy of Sciences (U.S.) and International council of scientific unions., *International critical tables of numerical data, physics, chemistry and technology*, Published for the National Research Council by McGraw-Hill, New York, 1st edn., 1926, vol. 3.

[95] G. Brenn, L. J. Deviprasath, F. Durst and C. Fink, *International Journal of Heat and Mass Transfer*, 2007, **50**, 5073–5086.

[96] J. R. Welty, C. E. Wicks, R. E. Wilson and G. L. Rorrer, *Fundamentals of Momentum, Heat and Mass Transfer*, John Wiley & Sons, New York, 5th edn., 2008.

[97] K. Sefiane, L. Tadrist and M. Douglas, *International Journal of Heat and Mass Transfer*, 2003, **46**, 4527–4534.

[98] A. K. H. Cheng, D. M. Soolaman and H.-Z. Yu, *The Journal of Physical Chemistry B*, 2006, **110**, 11267–11271.

[99] C. Liu, E. Bonaccurso and H.-J. Butt, *Physical Chemistry Chemical Physics*, 2008, **10**, 7150–7157.

[100] T. Ozturk and H. Y. Erbil, *Colloids and Surfaces A: Physicochemical and Engineering Aspects*, 2018, **553**, 327–336.

[101] K. Sefiane, S. David and M. E. R. Shanahan, *The Journal of Physical Chemistry B*, 2008, **112**, 11317–11323.

[102] R. J. Hopkins and J. P. Reid, *The Journal of Physical Chemistry A*, 2005, **109**, 7923–7931.

[103] M. D. Raj, D. K. Mandal, S. Navaneethakrishnan and S. Bakshi, *Experiments in Fluids*, 2010, **48**, 715–719.

[104] P. Innocenzi, L. Malfatti, S. Costacurta, T. Kidchob, M. Piccinini and A. Marcelli, *The Journal of Physical Chemistry A*, 2008, **112**, 6512–6516.

[105] P. Chen, M. Toubal, J. Carlier, S. Harmand, B. Nongaillard and M. Bigerelle, *Langmuir*, 2016, **32**, 9836–9845.

[106] Y. Kita, Y. Okauchi, Y. Fukatani, D. Orejon, M. Kohno, Y. Takata and K. Sefiane, *Physical Chemistry Chemical Physics*, 2018, **20**, 19430–19440.

[107] T. Ozturk and H. Y. Erbil, *Langmuir*, 2020, **36**, 1357–1371.

[108] Y. Li, C. Diddens, A. Prosperetti, K. L. Chong, X. Zhang and D. Lohse, *Physical Review Letters*, 2019, **122**, 154502.

[109] A. K. Thokchom, A. Gupta, P. J. Jaijus and A. Singh, *International Journal of Heat and Mass Transfer*, 2014, **68**, 67–77.

[110] E. Dietrich, M. Rump, P. Lv, E. S. Kooij, H. J. W. Zandvliet and D. Lohse, *Journal of Fluid Mechanics*, 2017, **812**, 349–369.

[111] H. Sadafi, R. Rabani, S. Dehaeck, H. Machrafi, B. Haut, P. Dauby and P. Colinet, *Colloids and Surfaces A: Physicochemical and Engineering Aspects*, 2020, **602**, 125052.

[112] M. Jalaal, C. Seyfert, B. Stoeber and N. J. Balmforth, *Journal of Fluid Mechanics*, 2018, **837**, 115–128.

[113] S. Karpitschka, *Journal of Fluid Mechanics*, 2018, **856**, 1–4.

[114] V. Zamora, A. Díez, M. V. Andrés and B. Gimeno, *Optics Express*, 2007, **15**, 12011–12016.

[115] F. Sedlmeir, R. Zeltner, G. Leuchs and H. G. L. Schwefel, *Optics Express*, 2014, **22**, 30934–30942.

[116] J. A. Räty and K.-E. Peiponen, *Applied Spectroscopy*, 1999, **53**, 1123–1127.

[117] J. Räty and K.-E. Peiponen, *Measurement Science and Technology*, 1999, **11**, 74–76.

[118] K.-E. Peiponen, A. Jääskeläinen, J. Räty, O. Richard, U. Tapper, E. I. Kauppinen and K. Lumme, *Applied Spectroscopy*, 2000, **54**, 878–884.

[119] H. Soetedjo and J. Räty, *Applied Spectroscopy*, 2003, **57**, 127–132.

[120] R. Laitinen, J. Räty, K. Korhonen, J. Ketolainen and K.-E. Peiponen, *International Journal of Pharmaceutics*, 2017, **523**, 127–132.

[121] E. Hecht, *Optics*, Addison Wesley, 4th edn., 2002.

[122] I. H. Malitson, *Journal of the Optical Society of America*, 1965, **55**, 1205–1209.

[123] R. A. Campbell, J. P. R. Day and C. D. Bain, *Applied Spectroscopy*, 2005, **59**, 993–1001.

[124] C. Diddens, *Personal Communication*, 2021.

[125] H. Cabrera, J. Akbar, D. Korte, I. Ashraf, E. E. Ramírez-Miquet, E. Marín and J. Niemela, *Applied Spectroscopy*, 2018, **72**, 1069–1073.

[126] R. M. Pope and E. S. Fry, *Applied Optics*, 1997, **36**, 8710–8723.

[127] P. Combis, P. Cormont, L. Gallais, D. Hebert, L. Robin and J.-L. Rullier, *Appl. Phys. Lett.*, 2012, 5.

[128] A. Kabalnov and H. Wennerström, *Soft Matter*, 2009, **5**, 4712–4718.

[129] B. R. Hammond and R. H. Stokes, *Transactions of the Faraday Society*, 1953, **49**, 890–895.

[130] B. Beulen, J. d. Jong, H. Reinten, M. v. d. Berg, H. Wijshoff and R. van Dongen, *Experiments in Fluids*, 2007, **42**, 217–224.

[131] J. de Jong, H. Reinten, H. Wijshoff, M. van den Berg, K. Delescen, R. van Dongen, F. Mugele, M. Versluis and D. Lohse, *Applied Physics Letters*, 2007, **91**, 204102.

[132] M.-J. van der Meulen, H. Reinten, F. Dijksman, D. Lohse and M. Versluis, *Journal of Imaging Science and Technology*, 2016, **60**, 040502.

[133] C. Meinhart and H. Zhang, *Journal of Microelectromechanical Systems*, 2000, **9**, 67–75.

[134] J. R. Castrejón-Pita, S. D. Hoath, A. A. Castrejón-Pita, N. F. Morrison, W.-K. Hsiao and I. M. Hutchings, *Journal of Imaging Science and Technology*, 2012, **56**, 50401.

[135] S. M. Rowan, M. I. Newton, F. W. Driewer and G. McHale, *The Journal of Physical Chemistry B*, 2000, **104**, 8217–8220.

[136] G. Guéna, C. Poulard and A. M. Cazabat, *Colloids and Surfaces A: Physicochemical and Engineering Aspects*, 2007, **298**, 2–11.

[137] J. Park and J. Moon, *Langmuir*, 2006, **22**, 3506–3513.

[138] E. Talbot, A. Berson, L. Yang and C. Bain, *NIP & Digital Fabrication Conference*, 2013, **2013**, 307–312.

[139] C. Diddens, Y. Li and D. Lohse, *Journal of Fluid Mechanics*, 2021, **914**, A23.

[140] A. Pahlavan, L. Yang, C. D. Bain and H. A. Stone, *Physical Review Letters*, 2021, (In Preparation).

[141] J. R. E. Christy, Y. Hamamoto and K. Sefiane, *Physical Review Letters*, 2011, **106**, 205701.

[142] G. Vazquez, E. Alvarez and J. M. Navaza, *Journal of Chemical & Engineering Data*, 1995, **40**, 611–614.

[143] N. G. Tsierkezos and I. E. Molinou, *Journal of Chemical & Engineering Data*, 1998, **43**, 989–993.

[144] MEGlobal, *Monoethylene Glycol MEG Technical Product Brochure*, https://www.meglobal.biz/wp-content/uploads/2019/01/Monoethylene-Glycol-MEG-Technical-Product-Brochure-PDF.pdf.

[145] Z. Wang, X.-F. Peng, A. S. Mujumdar, A. Su and D.-J. Lee, *Drying Technology*, 2008, **26**, 806–810.

[146] P. Gurrala, P. Katre, S. Balusamy, S. Banerjee and K. C. Sahu, *International Journal of Heat and Mass Transfer*, 2019, **145**, 118770.

[147] K. H. Kang, S. J. Lee, C. M. Lee and I. S. Kang, *Measurement Science and Technology*, 2004, **15**, 1104–1112.

[148] J. R. E. Christy, K. Sefiane and E. Munro, *Journal of Bionic Engineering*, 2010, **7**, 321–328.

[149] R. Bennacer and K. Sefiane, *Journal of Fluid Mechanics*, 2014, **749**, 649–665.

[150] X. Zhong and F. Duan, *The European Physical Journal E*, 2016, **39**, 18.

[151] J. Shi, L. Yang and C. D. Bain, *ACS Applied Materials & Interfaces*, 2019, **11**, 14275–14285.

[152] L. Gao and T. J. McCarthy, *Langmuir*, 2007, **23**, 3762–3765.

[153] J. Perelaer, P. J. Smith, C. E. Hendriks, A. M. J. v. d. Berg and U. S. Schubert, *Soft Matter*, 2008, **4**, 1072–1078.

[154] A. H. Persad, K. Sefiane and C. A. Ward, *Langmuir*, 2013, **29**, 13239–13250.

[155] M. Majumder, C. S. Rendall, J. A. Eukel, J. Y. L. Wang, N. Behabtu, C. L. Pint, T.-Y. Liu, A. W. Orbaek, F. Mirri, J. Nam, A. R. Barron, R. H. Hauge, H. K. Schmidt and M. Pasquali, *The Journal of Physical Chemistry B*, 2012, **116**, 6536–6542.

[156] R. Malinowski, G. Volpe, I. P. Parkin and G. Volpe, *The Journal of Physical Chemistry Letters*, 2018, **9**, 659–664.

[157] P. Kabi, R. Pal and S. Basu, *Langmuir*, 2020, **36**, 1279–1287.

[158] O. Hegde, S. Chakraborty, P. Kabi and S. Basu, *Physics of Fluids*, 2018, **30**, 122103.

[159] E. L. Talbot, A. Berson and C. D. Bain, NIP & Digital Fabrication Conference, 2012, pp. 420–423.

[160] N. Shahidzadeh, M. F. L. Schut, J. Desarnaud, M. Prat and D. Bonn, *Scientific Reports*, 2015, **5**, 10335.

[161] C. J. Roberts and P. G. Debenedetti, *AIChE Journal*, 2002, **48**, 1140–1144.

[162] M. Mathlouthi and P. Reiser, *Sucrose: Properties and Applications*, Springer US, 1995.

[163] P. F. Fox, T. Uniacke-Lowe, P. L. H. McSweeney and J. A. O'Mahony, *Dairy Chemistry and Biochemistry*, Springer, 1998.

[164] European Commission, *Milk and dairy products*, 2020, https://ec.europa.eu/info/food-farming-fisheries/farming/facts-and-figures/markets/production/production-sector/animal-products/milk-and-dairy-products_en.

[165] S. Rogers, Y. Fang, S. X. Qi Lin, C. Selomulya and X. Dong Chen, *Chemical Engineering Science*, 2012, **71**, 75–84.

[166] B. Zobrist, C. Marcolli, D. A. Pedernera and T. Koop, *Atmospheric Chemistry and Physics*, 2008, **8**, 5221–5244.

[167] P. G. Debenedetti and F. H. Stillinger, *Nature*, 2001, **410**, 259–267.

[168] C. A. Angell, *Science*, 1995, **267**, 1924–1935.

[169] R. M. Power, S. H. Simpson, J. P. Reid and A. J. Hudson, *Chemical Science*, 2013, **4**, 2597–2604.

[170] H.-J. Tong, J. P. Reid, D. L. Bones, B. P. Luo and U. K. Krieger, *Atmos. Chem. Phys.*, 2011, **11**, 4739–4754.

[171] M. Mathlouthi and J. Genotelle, *Carbohydrate Polymers*, 1998, **37**, 335–342.

[172] Y. C. Song, A. E. Haddrell, B. R. Bzdek, J. P. Reid, T. Bannan, D. O. Topping, C. Percival and C. Cai, *The Journal of Physical Chemistry A*, 2016, **120**, 8123–8137.

[173] E. Landt, *Naturwissenschaften*, 1934, **22**, 809–809.

[174] R. S. Norrish, *International Journal of Food Science & Technology*, 1966, **1**, 25–39.

[175] R. S. Norrish, *Selected tables of physical properties of sugar solutions*, British Food Manufacturing Industries Research Association, Leatherhead, Surrey, Issue 51 of Scientific and Technical Surveys edn., 1967.

[176] D. Pharma, *Lactose - Some basic properties and characteristics*, https://dfepharma.com/-/media/documents/technical-documents/technical-papers/lactose-some-basic-properties.pdf.

[177] R. W. Fessenden, *PhD Thesis*, University of Massachusetts Amherst, 1928.

[178] F. Gregson, Y. C. Song and J. P. Reid, *Personal Communication*, 2018.

[179] R. H. Perry, W. Green and J. O. Maloney, *Perry's Chemical Engineers' Handbook*, McGraw-Hill, New York, 7th edn., 1997.

[180] H. C. Price, J. Mattsson and B. J. Murray, *Physical Chemistry Chemical Physics*, 2016, **18**, 19207–19216.

[181] D. J. Fairhurst, in *Droplet Wetting and Evaporation*, ed. D. Brutin, Academic Press, Oxford, 2015, pp. 295–314.

[182] R. P. Sear, *Journal of Physics: Condensed Matter*, 2007, **19**, 033101.

[183] S. Karthika, T. K. Radhakrishnan and P. Kalaichelvi, *Crystal Growth & Design*, 2016, **16**, 6663–6681.

[184] F. K. A. Gregson, *PhD Thesis*, University of Bristol, 2020.

[185] R. Benages-Vilau, T. Calvet and M. A. Cuevas-Diarte, *Crystallography Reviews*, 2014, **20**, 25–55.

[186] J. Bauer, S. Spanton, R. Henry, J. Quick, W. Dziki, W. Porter and J. Morris, *Pharmaceutical Research*, 2001, **18**, 859–866.

[187] E. Amstad, F. Spaepen and D. A. Weitz, *The Journal of Physical Chemistry. B*, 2016, **120**, 9161–9165.

[188] M. Quilaqueo and J. M. Aguilera, *Food Research International*, 2016, **84**, 143–149.

[189] S. Li and L. H. Hihara, *Corrosion Science*, 2016, **108**, 200–204.

[190] V. Soulié, F. Lequien, F. Ferreira-Gomes, G. Moine, D. Feron, P. Prene, H. Moehwald, T. Zemb and H. Riegler, *Materials and Corrosion*, 2017, **68**, 927–934.

[191] F. Lequien, V. Soulié, G. Moine, A. Lequien, D. Feron, P. Prene, H. Moehwald, H. Riegler and T. Zemb, *Colloids and Surfaces A: Physicochemical and Engineering Aspects*, 2018, **546**, 59–66.

[192] I. N. Tang and H. R. Munkelwitz, *Journal of Geophysical Research: Atmospheres*, 1994, **99**, 18801–18808.

[193] S. L. Clegg, P. Brimblecombe and A. S. Wexler, *The Journal of Physical Chemistry A*, 1998, **102**, 2155–2171.

[194] S. L. Clegg, P. Brimblecombe and S. W. Anthony, *Extended AIM Aerosol Thermodynamics Model*, http://www.aim.env.uea.ac.uk/aim/aim.php.

[195] F. Chenlo, R. Moreira, G. Pereira and B. Bello, *European Food Research and Technology*, 2004, **219**, 403–408.

[196] A. W. Adamson and A. P. Gast, *Physical Chemistry of Surfaces*, Wiley, New York, 6th edn., 1997.

[197] C. L. Henry, C. N. Dalton, L. Scruton and V. S. J. Craig, *The Journal of Physical Chemistry C*, 2007, **111**, 1015–1023.

[198] B. R. Bzdek, R. M. Power, S. H. Simpson, J. P. Reid and C. P. Royall, *Chemical Science*, 2016, **7**, 274–285.

[199] R. Tuckermann, *Atmospheric Environment*, 2007, **41**, 6265–6275.

[200] P. K. Weissenborn and R. J. Pugh, *Journal of Colloid and Interface Science*, 1996, **184**, 550–563.

[201] N. Matubayasi, H. Matsuo, K. Yamamoto, S.-i. Yamaguchi and A. Matuzawa, *Journal of Colloid and Interface Science*, 1999, **209**, 398–402.

[202] N. Matubayasi and R. Yoshikawa, *Journal of Colloid and Interface Science*, 2007, **315**, 597–600.

[203] B. Svenningsson, J. Rissler, E. Swietlicki, M. Mircea, M. Bilde, M. C. Facchini, S. Decesari, S. Fuzzi, J. Zhou, J. Mønster and T. Rosenørn, *Atmos. Chem. Phys.*, 2006, 16.

[204] C. S. Dutcher, A. S. Wexler and S. L. Clegg, *The Journal of Physical Chemistry A*, 2010, **114**, 12216–12230.

[205] V. Soulié, S. Karpitschka, F. Lequien, P. Prené, T. Zemb, H. Moehwald and H. Riegler, *Physical Chemistry Chemical Physics*, 2015, **17**, 22296–22303.

[206] N. Sghaier, M. Prat and S. Ben Nasrallah, *Chemical Engineering Journal*, 2006, **122**, 47–53.

[207] J. Desarnaud, H. Derluyn, J. Carmeliet, D. Bonn and N. Shahidzadeh, *The Journal of Physical Chemistry Letters*, 2014, **5**, 890–895.

[208] M. Volmer, *Zeitschrift für Elektrochemie und angewandte physikalische Chemie*, 1929, **35**, 555–561.

[209] C. Orr, F. K. Hurd and W. J. Corbett, *Journal of Colloid Science*, 1958, **13**, 472–482.

[210] S. T. Martin, *Chemical Reviews*, 2000, **100**, 3403–3454.

[211] I. N. Tang, H. R. Munkelwitz and J. G. Davis, *Journal of Aerosol Science*, 1977, **8**, 149–159.

[212] I. N. Tang, in *Generation of Aerosols*, ed. K. Welleke and A. Arbor, Ann Arbor Science Publishers, Michigan, 1980, pp. 153–167.

[213] C. B. Richardson and T. D. Snyder, *Langmuir*, 1994, **10**, 2462–2465.

[214] M. D. Cohen, R. C. Flagan and J. H. Seinfeld, *The Journal of Physical Chemistry*, 1987, **91**, 4563–4574.

[215] M. D. Cohen, R. C. Flagan and J. H. Seinfeld, *The Journal of Physical Chemistry*, 1987, **91**, 4583–4590.

[216] Y. Gao, L. E. Yu and S. B. Chen, *The Journal of Physical Chemistry A*, 2007, **111**, 10660–10666.

[217] X. Li, D. Gupta, H.-J. Eom, H. Kim and C.-U. Ro, *Atmospheric Environment*, 2014, **82**, 36–43.

[218] C.-T. Lee and W.-C. Hsu, *Journal of Aerosol Science*, 2000, **31**, 189–197.

[219] Y. Liu, Z. Yang, Y. Desyaterik, P. L. Gassman, H. Wang and A. Laskin, *Analytical Chemistry*, 2008, **80**, 633–642.

[220] S.-S. Ma, W. Yang, C.-M. Zheng, S.-F. Pang and Y.-H. Zhang, *Atmospheric Environment*, 2019, **210**, 177–185.

[221] D. Lamb, A. M. Moyle and W. H. Brune, *Aerosol Science and Technology*, 1996, **24**, 263–278.

[222] I. N. Tang and H. R. Munkelwitz, *Aerosol Science and Technology*, 1991, **15**, 201–207.

[223] M. Gysel, E. Weingartner and U. Baltensperger, *Environmental Science & Technology*, 2002, **36**, 63–68.

[224] R. C. Hoffman, A. Laskin and B. J. Finlayson-Pitts, *Journal of Aerosol Science*, 2004, **35**, 869–887.

[225] P.-D. Lu, F. Wang, L.-J. Zhao, W.-X. Li, X.-H. Li, J.-L. Dong, Y.-H. Zhang and G.-Q. Lu, *The Journal of Chemical Physics*, 2008, **129**, 104509.

[226] J. Desarnaud and N. Shahidzadeh-Bonn, *EPL (Europhysics Letters)*, 2011, **95**, 48002.

[227] C. Rodriguez-Navarro and E. Doehne, *Earth Surface Processes and Landforms*, 1999, **24**, 191–209.

[228] K. Zehnder and A. Arnold, *Journal of Crystal Growth*, 1989, **97**, 513–521.

[229] W. J. P. van Enckevort and J. H. Los, *Crystal Growth & Design*, 2013, **13**, 1838–1848.

[230] X. Zhong, J. Ren and F. Duan, *The Journal of Physical Chemistry B*, 2017, **121**, 7924–7933.

[231] D. J. Cziczo and J. P. D. Abbatt, *The Journal of Physical Chemistry A*, 2000, **104**, 2038–2047.

[232] J. F. Robinson, F. K. A. Gregson, R. E. H. Miles, J. P. Reid and C. P. Royall, *The Journal of Chemical Physics*, 2020, **152**, 074503.

[233] N. E. R. Zimmermann, B. Vorselaars, D. Quigley and B. Peters, *Journal of the American Chemical Society*, 2015, **137**, 13352–13361.

[234] D. W. Oxtoby, *Annual Review of Materials Research*, 2002, **32**, 39–52.

[235] D. Nuyttens, K. Baetens, M. De Schampheleire and B. Sonck, *Biosystems Engineering*, 2007, **97**, 333–345.

[236] Q.-N. Zhang, Y. Zhang, C. Cai, Y.-C. Guo, J. P. Reid and Y.-H. Zhang, *The Journal of Physical Chemistry A*, 2014, **118**, 2728–2737.

[237] F. K. A. Gregson, J. F. Robinson, R. E. H. Miles, C. P. Royall and J. P. Reid, *The Journal of Physical Chemistry B*, 2020, **124**, 6024–6036.

[238] M.-J. Lee, H.-J. Jung, H.-J. Eom, S. Maskey, H. K. Kim and C.-U. Ro, *Atmospheric Chemistry and Physics Discussions*, 2011, **11**, 23203–23229.

[239] H. Kim, M.-J. Lee, H.-J. Jung, H.-J. Eom, S. Maskey, K.-H. Ahn and C.-U. Ro, *Atmospheric Environment*, 2012, **60**, 68–75.

[240] A. Baldelli, R. M. Power, R. E. H. Miles, J. P. Reid and R. Vehring, *Aerosol Science and Technology*, 2016, **50**, 693–704.

[241] I. N. Tang, H. R. Munkelwitz and N. Wang, *Journal of Colloid and Interface Science*, 1986, **114**, 409–415.

[242] H.-S. Na, S. Arnold and A. S. Myerson, *Journal of Crystal Growth*, 1994, **139**, 104–112.

[243] R. Grossier, Z. Hammadi, R. Morin and S. Veesler, *Physical Review Letters*, 2011, **107**, 025504.

[244] A. Naillon, P. Duru, M. Marcoux and M. Prat, *Journal of Crystal Growth*, 2015, **422**, 52–61.

[245] A. Utoft, K. Kinoshita, D. L. Bitterfield and D. Needham, *Langmuir*, 2018, **34**, 3626–3641.

[246] F. K. A. Gregson, J. F. Robinson, R. E. H. Miles, C. P. Royall and J. P. Reid, *The Journal of Physical Chemistry B*, 2019, **123**, 266–276.

[247] R. Grossier, V. Tishkova, R. Morin and S. Veesler, *AIP Advances*, 2018, **8**, 075324.

[248] E. L. Cussler, *Diffusion: Mass Transfer in Fluid Systems*, Cambridge University Press, Cambridge ; New York, 3rd edn., 2009.

[249] S. A. McBride, S. Dash and K. K. Varanasi, *Langmuir*, 2018, **34**, 12350–12358.

[250] K. Morinaga, N. Oikawa and R. Kurita, *Scientific Reports*, 2018, **8**, 12503.

[251] N. Shahidzadeh-Bonn, S. Rafai, D. Bonn and G. Wegdam, *Langmuir*, 2008, **24**, 8599–8605.

[252] E. Bormashenko, Y. Bormashenko, R. Pogreb, O. Stanevsky and G. Whyman, *Journal of Colloid and Interface Science*, 2007, **306**, 128–132.

[253] G. P. Brewington, *Physical Review*, 1934, **46**, 861–864.

[254] P. Takhistov and H.-C. Chang, *Industrial & Engineering Chemistry Research*, 2002, **41**, 6256–6269.

[255] P. Fontana, D. Pettit and S. Cristoforetti, *Journal of Crystal Growth*, 2015, **428**, 80–85.

[256] H.-H. Sun, W.-B. Li, W.-J. Ji, G.-L. Dai, Y. Huan, Y.-R. Wang and D. Lan, *Chinese Physics B*, 2020, **29**, 014701.

[257] M. Efstratiou, J. Christy and K. Sefiane, *Langmuir*, 2020, **36**, 4995–5002.

[258] B. Shin, M.-W. Moon and H.-Y. Kim, *Langmuir*, 2014, **30**, 12837–12842.

[259] P. Vázquez, C. Thomachot-Schneider, K. Mouhoubi, G. Fronteau, M. Gommeaux, D. Benavente, V. Barbin and J.-L. Bodnar, *Infrared Physics & Technology*, 2015, **71**, 198–207.

[260] J. Schmid, I. Zarikos, A. Terzis, N. Roth and B. Weigand, *Experimental Thermal and Fluid Science*, 2018, **91**, 80–88.

[261] J. Zhang, M. K. Borg, K. Sefiane and J. M. Reese, *Physical Review E*, 2015, **92**, 052403.

[262] D. Kaya, V. A. Belyi and M. Muthukumar, *The Journal of Chemical Physics*, 2010, **133**, 114905.

[263] Y. Msambwa, A. S. D. Shackleford, F. F. Ouali and D. J. Fairhurst, *The European Physical Journal E*, 2016, **39**, 21.

[264] Y. Y. Tarasevich and A. K. Ayupova, *Technical Physics*, 2003, **48**, 535–540.

[265] G. Chen and G. J. Mohamed, *The European Physical Journal E*, 2010, **33**, 19–26.

[266] H. M. Gorr, J. M. Zueger, D. R. McAdams and J. A. Barnard, *Colloids and Surfaces B: Biointerfaces*, 2013, **103**, 59–66.

[267] M. D. Choudhury, T. Dutta and S. Tarafdar, *Colloids and Surfaces A: Physicochemical and Engineering Aspects*, 2013, **432**, 110–118.

[268] M. D. Choudhury, T. Dutta and S. Tarafdar, *Soft Matter*, 2015, **11**, 6938–6947.

[269] A. Mailleur, C. Pirat, O. Pierre-Louis and J. Colombani, *Physical Review Letters*, 2018, **121**, 214501.

[270] J. Desarnaud, H. Derluyn, J. Carmeliet, D. Bonn and N. Shahidzadeh, *The Journal of Physical Chemistry Letters*, 2018, **9**, 2961–2966.

[271] J. Zhang, S. Zhang, Z. Wang, Z. Zhang, S. Wang and S. Wang, *Angewandte Chemie International Edition*, 2011, **50**, 6044–6047.

[272] Z. Hammadi, R. Grossier, S. Zhang, A. Ikni, N. Candoni, R. Morin and S. Veesler, *Faraday Discussions*, 2015, **179**, 489–501.

[273] R. W. G. Wyckoff, *Physical Review*, 1920, **16**, 149–157.

[274] D. L. Rousseau, R. E. Miller and G. E. Leroi, *The Journal of Chemical Physics*, 1968, **48**, 3409–3413.

[275] K. Hasebe, *Journal of the Physical Society of Japan*, 1981, **50**, 1266–1274.

[276] R. H. Chen, Y.-C. Chen, C. S. Shern and T. Fukami, *Solid State Ionics*, 2009, **180**, 356–361.

[277] T. K. Pradhan and P. K. Panigrahi, *Colloids and Surfaces A: Physicochemical and Engineering Aspects*, 2016, **500**, 154–165.

[278] T. K. Pradhan and P. K. Panigrahi, *Colloids and Surfaces A: Physicochemical and Engineering Aspects*, 2017, **530**, 1–12.

[279] R. Savino and R. Monti, *Journal of Crystal Growth*, 1996, **165**, 308–318.

[280] K. Linnow, M. Steiger, C. Lemster, H. De Clercq and M. Jovanović, *Environmental Earth Sciences*, 2013, **69**, 1609–1620.

[281] A. Pineiro-Romero, *PhD Thesis*, Durham University, 2018.

[282] J. R. Brown, E. O. Fridjonsson, J. D. Seymour and S. L. Codd, *Physics of Fluids*, 2009, **21**, 093301.

[283] G. K. Batchelor, *Journal of Fluid Mechanics*, 1976, **74**, 1–29.

[284] L. Durlofsky, J. F. Brady and G. Bossis, *Journal of Fluid Mechanics*, 1987, **180**, 21–49.

[285] S. I. Rubinow and J. B. Keller, *Journal of Fluid Mechanics*, 1961, **11**, 447–459.

[286] G. Segré and A. Silberberg, *Nature*, 1961, **189**, 209–210.

[287] P. G. Saffman, *Journal of Fluid Mechanics*, 1965, **22**, 385–400.

[288] J. L. Anderson, *Annual Review of Fluid Mechanics*, 1989, **21**, 61–99.

[289] D. Velegol, A. Garg, R. Guha, A. Kar and M. Kumar, *Soft Matter*, 2016, **12**, 4686–4703.

[290] I. Buttinoni, J. Bialké, F. Kümmel, H. Löwen, C. Bechinger and T. Speck, *Physical Review Letters*, 2013, **110**, 238301.

[291] B. Abécassis, C. Cottin-Bizonne, C. Ybert, A. Ajdari and L. Bocquet, *Nature Materials*, 2008, **7**, 785–789.

[292] S. Shin, E. Um, B. Sabass, J. T. Ault, M. Rahimi, P. B. Warren and H. A. Stone, *Proceedings of the National Academy of Sciences*, 2016, **113**, 257–261.

[293] J. S. Paustian, C. D. Angulo, R. Nery-Azevedo, N. Shi, A. I. Abdel-Fattah and T. M. Squires, *Langmuir*, 2015, **31**, 4402–4410.

[294] J. L. Anderson and D. C. Prieve, *Separation and Purification Methods*, 1984, **13**, 67–103.

[295] B. V. Derjaguin, G. P. Sidorenkov, E. A. Zubashchenko and E. V. Kiseleva, *Kolloidn. Zh.*, 1947, **9**, 335–347.

[296] J. L. Anderson, M. E. Lowell and D. C. Prieve, *Journal of Fluid Mechanics*, 1982, **117**, 107–121.

[297] J. T. Ault, S. Shin and H. A. Stone, *Soft Matter*, 2019, **15**, 1582–1596.

[298] D. C. Prieve, J. L. Anderson, J. P. Ebel and M. E. Lowell, *Journal of Fluid Mechanics*, 1984, **148**, 247–269.

[299] S. Shin, J. T. Ault, P. B. Warren and H. A. Stone, *Physical Review X*, 2017, **7**, 041038.

[300] M. Kosmulski and E. Matuevi, *Journal of Colloid and Interface Science*, 1992, **150**, 291–294.

[301] Y. Wang, R. Deng, L. Yang and C. D. Bain, *Lab on a Chip*, 2019, **19**, 3077–3085.